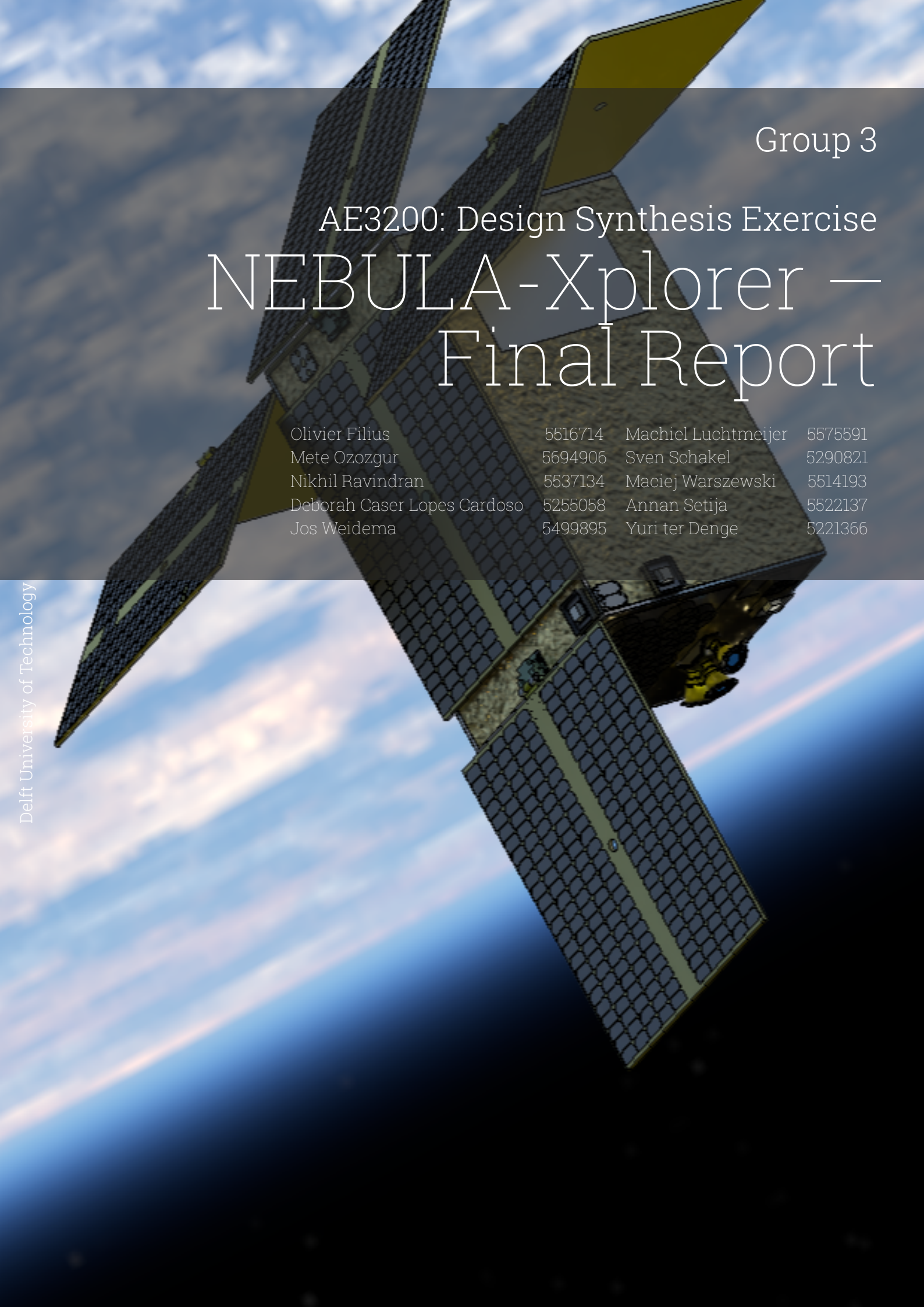

Group 3

AE3200: Design Synthesis Exercise

NEBULA-Xplorer — Final Report

Olivier Filius	5516714	Machiel Luchtmeijer	5575591
Mete Ozozgur	5694906	Sven Schakel	5290821
Nikhil Ravindran	5537134	Maciej Warszewski	5514193
Deborah Caser Lopes Cardoso	5255058	Annan Setija	5522137
Jos Weidema	5499895	Yuri ter Denge	5221366

Delft University of Technology

Acknowledgements

The NEBULA-Xplorer team who worked on this report would like to first express our sincere gratitude to all individuals who contributed to the successful completion of this report.

First and foremost, we would like to thank our tutor Iklim Akay for her continuous support and guidance during this DSE project. We are very thankful for the time she dedicated to giving us constructive and insightful feedback with helped with our development both as individual professionals and as a team.

Next, we would like to thank David Jameux for being such a dedicated mentor. His advice about industry practices, teamwork, technical decision-making, and general expertise was invaluable. His enthusiasm was a strong source of motivation and inspiration for all of us, and we are very grateful for all of his input.

To our coaches Fazlur Rahman and Philip Wurzner, thank you for taking the time to support us through all the challenges and uncertainties, and for offering comments and recommendations that helped us make the best work possible.

We are grateful for our client, Martin Grim, for his guidance and advice throughout the project. His dedication for the mission inspired all of us to fully engage with the project objectives.

We would also like to thank Ben Ricketts, for his expertise and input on the scientific targets.

An additional thank you to our TA, Antonio Minafra, for his consistent support in recent weeks and providing practical advice and helpful insights.

Finally, the team would like to thank the many professors and industry professionals who provided expert advice and significantly improved the quality of this work. In particular, we thank Mr van den Bos and Mr Atherstone for assistance with CATIA, Ines Uriol Balbin for support with the TCS, Jadon Wolfgang for guidance on payload data handling and the CPDU, Niels van der Pas (Sparkwing) for input on the solar panel configuration, Dr Stefano Speretta and Prof. Dr A. Cervone for their insight into space propulsion, Michel van Pelt for his advice on the cost analysis, and Tjaard Sijpkes for valuable guidance on risk assessment. We also thank the previous and current NEBULA-Xplorer team members. Their collective expertise, support, and enthusiasm were essential to the success of this work.

TABLE OF CONTENTS

LIST OF ABBREVIATIONS

AGN Active Galactic Nuclei
AIT/AIV Assembly, Integration & Test/Verification
AKE Attitude Knowledge Error
AOCS Attitude and Orbit Control System
APE Absolute Pointing Error

BER Bit Error Rate
BH Black Hole

C&DH Command and Data Handling
CAMs Collision Avoidance Manoeuvres
CBS Cost Breakdown Structure
CCSDS Consultative Committee for Space Data Systems
CER Cost Estimating Relationships
CFRP Carbon Fiber Reinforced Polymer
CME Coronal Mass Ejection
CoG Center of Gravity
CoM Centre of Mass
ConOps Concept of Operations
COTS Commercial Of The Shelf
CPDU Central Payload Data Unit
CPU Central Processing Unit
CSDA Continuous Slowing Down Approximation

DET Direct Energy Transfer
DoD Depth of Discharge

ECSS European Cooperation for Space Standardization
EEE Electrical, Electronic, Electromechanical
EM Engineering Model
EMI Electromagnetic Interference shielding
EOL Beginning-Of-Life
EOL End-Of-Life
EPS Electrical Power System
ESA European Space Agency
ESD Electro Static Discharge
EUV Extreme Ultra Violet

FDIR Fault Detection, Isolation and Recovery
FEC Forward Error Correction
FEM Finite Element Method
FM Flight Model
FMEA Failure Modes and Effects Analysis
FS Flight Spare

GCR Galactic Cosmic Rays
GND Ground
GNSS Global Navigation Satellite System
GSE Ground Support Equipment

HBLM Heritage Based Likelihood Metric
HEXI High Energy X-ray Instrument
HKTM Housekeeping Telemetry
HPBW Half-power Beam Width

IFP Instrument Focal Plane
IRU Instrument Readout Unit
ISS International Space Station
ITO Indium Tin Oxide

LDPC Low-Density Parity-Check
LEO Low Earth Orbit
LEOP Launch and Early Operations
LET Linear Energy Transfer
LEXI Low Energy X-ray Instrument
LoS Loss of Signal
LV Launch Vehicle

MIB Minimum Impulse Bit
MLI Multi-Layer Insulation
MMOI Mass Moment of Inertia
MMU Mass Memory Unit
MNS Mission Need Statement
MOO Modes Of Operations
MPPT Maximum Power Point Tracking
MTQ Magnetorquers

NASA National Aeronautics and Space Administration
NIST National Institute of Standards and Technology
NS Neutron Star

OBC On Board Computer

PCDU Power Conditioning and Distribution Unit
PCU Propulsion Control Unit
PCU Power Conditioning Unit
PD Proportional-derivative
PFM Protoflight Model
PGF Pyrolytic Graphite Film
PM Prototype Model
PM/FM Prototype/Flight Model

POS Project Objective Statement
PROP Propulsion
PU Processing Unit

QPE Quasi-Periodic Eruption
QSL Quasi-Static Loading

RAAN Right Angle of Ascending Node
RAM Random Access Memory
RAMS Reliability Availability Maintainability and Safety
RF Radio Frequency
RMS Root-mean-squared
RPM Rotation Powered Millisecond-pulsars
RSS Root-sum-squared
RW Reaction Wheel

S/C Spacecraft
SAA South Atlantic Anomaly
SADA Solar Array Drive Assembly
SEB Single Event Burnout
SEE Single Event Effects
SEL Single Event Latch-up
SEP Solar Energetic Particles
SER Solar Electromagnetic Radiation
SEU Single Event Upset
SoC State of Charge
SPDT Single-pole Double-throw
SRON Space Research Organization Netherlands
SRP Solar Radiation Pressure

TC Telecommands
TCS Thermal Control System
TID Total Ionizing Dose
TRL Technology Readiness Level
TRRs Test Readiness Reviews
TSI Total Solar Irradiance
TT&C Telemetry, Tracking and Command

UL Unit Load
UV Ultraviolet

V&V Verification and Validation
VMPP Maximum Power Point Voltage
VRRs Validation Readiness Reviews

WD White Dwarf

XRB X-Ray Binary

1 Executive Overview

The NEBULA-Xplorer Mission (Netherlands Educational Satellite for Exploration of Binary-Linked Astrophysics) is a space mission initiated by Space Research Organization Netherlands (SRON) and carried out by students from Dutch educational institutes with the support of other industrial partners from the Netherlands. The scientific goal of the project is to observe X-ray binaries to better understand the universe and gather information that can help solve the mysteries of one of the most controversial topics in the history of science: black holes. X-Ray binaries are combinations of an extremely compact object, such as a black hole or a neutron star, and a companion star. The compact object extracts matter from the companion star, which releases great amounts of energy that can be observed using X-ray sensors. SRON has intentionally assigned the conceptual mission design to a student team as part of its objective to support the development of future space engineers and strengthen the Dutch space engineering ecosystem. This provides students with the opportunity to contribute to a mission with real scientific relevance while working within a professionally guided environment. As a result, the project has both scientific and educational purposes, which frame the scope and risk exposure in this early design phase.

Observational satellites currently observing X-ray binaries are approaching their End-Of-Life (EOL), with the final mission estimated to last until 2028. The planned future missions will only launch in the second half of the 2030s, creating a scientific gap in the observation of X-ray binaries. This critical gap can be filled with the NEBULA-XPlorer Mission with a 2030 launch date. The lack of other missions adds significant scientific value to the NEBULA-XPlorer. The mission is categorised as an European Space Agency (ESA) Mini-F Rideshare Mission. The Mini-F class encompasses small satellites with a mass range of 200-400 kg, and spacecraft mass is directly proportional to Mission and Launch Costs. As the spacecraft is a mini-satellite with very high scientific value, the mission's total value is magnified enormously. It is also worth noting that ESA is increasingly interested in low-cost, high-return scientific missions, which align well with the NEBULA-Xplorer mission.

Another critical aspect of the mission is its aim to support and contribute to the independence of Europe's Space Industry. While outlining the mission, the launch vehicle chosen was specifically a European launch vehicle. The Vega-C launch vehicle was selected as suitable for this mission after research into the options. Currently, Vega-C is launched only from the Guiana Space Centre in French Guiana. Therefore, this is assumed to be the only option for the NEBULA-Xplorer Mission, because a European launch site will be used. Furthermore, during the design process, European Cooperation for Space Standardization (ECSS) standards have been used to comply with the regulations for European space missions. These requirements have been extensively studied and implemented during the early design stages to prevent any complications that can occur during the adoption of the NEBULA-Xplorer Mission by ESA.

The mission definition began with a set of user requirements provided to the student design team, reflecting the scientific objectives, operational constraints, and overall mission context of NEBULA-Xplorer. These user requirements were primarily driven by the mission's nature, namely the need to perform sustained, high-quality X-ray observations of binary systems within the constraints of a Mini-F class spacecraft and a rideshare launch profile. Based on these inputs, a structured requirements engineering approach was applied to derive a consistent, traceable set of mission-, system-, and subsystem-level requirements, ensuring that the spacecraft design aligns with the intended scientific return while remaining technically feasible and compliant with European standards and constraints.

For this project, an iterative design process was adopted to converge on a feasible and robust baseline spacecraft configuration within the constraints of a Mini-F rideshare mission. Multiple subsystem design options

were initially defined and combined into system-level concepts, which were refined through successive iterations until a trade-off selected the baseline design, supported by a sensitivity analysis to confirm its robustness. Reliability was identified as a key design driver, and a redundancy philosophy was therefore applied to ensure mission-critical functions remain resilient to credible failure cases, with Failure Modes and Effects Analysis (FMEA) introduced as a structured method for identifying dominant failure modes and allocating redundancy where required.

Firstly, the mission environment was extensively analysed, as it directly determines the radiation and debris conditions that drive key performance and survivability requirements, while simultaneously shaping subsystem sizing and operational constraints throughout the spacecraft design. Several candidate operational orbits were investigated, after which a final baseline orbit was selected with an inclination of 45 degrees and an altitude envelope of 475 to 550 km. Within this environment, the South Atlantic Anomaly (SAA) was identified as the dominant contributor to spacecraft radiation exposure, leading to the definition of dedicated radiation mitigation measures during SAA crossings and the implementation of a corresponding operational protection strategy.

In parallel, the debris environment was assessed to quantify collision likelihood and to support the selection of an orbit that provides a favourable balance between maximising science observation time and minimising exposure to the most populated orbital shells. To support this assessment, ESA debris mitigation tools were applied to evaluate orbital lifetime behaviour, collision avoidance requirements, and end-of-life disposal performance, including the prediction of re-entry characteristics and the resulting on-ground casualty risk for uncontrolled re-entry scenarios. The selected orbital inclination was found to provide improved observation efficiency compared to alternative inclinations, while the altitude range was optimised to meet operational lifetime objectives without imposing additional stress on other subsystems, particularly propulsion, power, and thermal margins.

Following the definition of the mission environment and operational orbit, the spacecraft architecture was developed by establishing subsystem designs that collectively satisfy the derived performance requirements while remaining compatible with the volume and interface constraints imposed by the Vega-C rideshare launch configuration. The spacecraft structure provides the primary load-bearing framework required to maintain structural integrity throughout launch and operations, while enabling the mechanical integration of all subsystems within the available envelope. The baseline structural concept utilises an X-braced frame enclosed by high-stiffness Carbon Fiber Reinforced Polymer (CFRP) sandwich panels with a honeycomb core, while a web-stiffened base panel interfaces with the launcher and distributes launch loads efficiently. Structural verification is performed using Finite Element Method (FEM) analysis, including stress, strength, buckling, and dynamic response assessments to ensure compliance with launch load conditions and to verify sufficient structural margins across all load cases.

The propulsion subsystem provides the mission ΔV capability required for orbit injection corrections, Collision Avoidance Manoeuvres (CAMs) execution, and a single re-boost manoeuvre, while also supporting the flexibility required to respond to short-notice conjunction events throughout the operational lifetime. A customised Dawn SatDrive bi-propellant system is selected, consisting of four B20 thrusters, self-pressurised N_2O/C_3H_6 tanks, and an integrated feed-and-valve manifold with associated control electronics, enabling high-thrust, time-critical burns while maintaining operational robustness. The propulsion system is sized using a Python-based ΔV budget model including ESA margins, and pulse-mode accuracy analyses support the use of two-thruster burns combined with trimming capability to ensure manoeuvre precision and repeatability under realistic execution uncertainties.

The Attitude and Orbit Control System (AOCS) subsystem is designed to meet the mission pointing, knowledge, and slew requirements while ensuring spacecraft survivability and operational stability in the Low Earth Orbit (LEO) environment, particularly under conservative disturbance conditions and during transitions between science and safe operational states. Sizing is performed using worst-case disturbance torque estimation, resulting in an architecture that combines reaction wheels for disturbance rejection and pointing performance, and magnetorquers for momentum management and long-term angular momentum control. A four-wheel pyramidal configuration is selected to provide redundancy and continuous control authority, supported by a sensor suite including star trackers, gyroscopes, magnetometers, coarse sun sensors, and radiation sensors, with additional

Global Navigation Satellite System (GNSS) capability included to support orbit determination and operational requirements.

The Electrical Power System (EPS) is responsible for power generation, storage, regulation, and distribution, and is sized based on predicted mission power consumption profiles, thermal conditions, and expected degradation over the operational lifetime. The selected configuration employs deployable fold-out solar panels as a lightweight and high-Technology Readiness Level (TRL) solution, combined with a heritage ABSL battery pack to provide robust energy storage during eclipse operations and peak load cases. The power management architecture is based on an unregulated bus with independent Maximum Power Point Tracking (MPPT) trackers, while system robustness is ensured through redundancy and fault protection measures implemented at both hardware and control levels to support safe and autonomous operation across all mission modes.

The Thermal Control System (TCS) controls spacecraft heat distribution and dissipation to maintain all components within their operational temperature limits while minimising payload thermal fluctuations that may affect science performance. The thermal concept combines passive measures, including Multi-Layer Insulation (MLI), radiators, and thermal straps, with active control via distributed temperature sensors and electrically powered heaters, both governed by the TCS processing unit. These approaches are used in combination to ensure stable thermal performance across all operational modes, while accounting for eclipse-driven cycling, internal dissipation, and the radiative environment associated with the selected orbit.

The Telemetry, Tracking and Command (TT&C) subsystem enables downlink of Housekeeping Telemetry (HKTM) and payload data while providing uplink capability for telecommands required for spacecraft operation, autonomy recovery, and mode control. The baseline design uses S-band transceivers and low-gain patch antennas to provide reliable communications coverage over a wide range of spacecraft attitudes, with emphasis placed on maintaining sufficient link performance for routine operations and safe-mode recovery.

The Command and Data Handling (C&DH) subsystem is responsible for onboard data handling, command distribution, and payload data management, including processing, storage, and transfer between subsystems. The baseline architecture includes the main On Board Computer (OBC) and a Central Payload Data Unit (CPDU) for payload data processing and handling, with low-rate subsystem communications implemented via RS485 buses and a high-rate SpaceFibre link between payload storage and TT&C to reduce downlink duration and minimise time spent in communications-constrained operational states. Redundant buses are implemented to improve reliability, enabled by the relatively low mass impact of the data handling architecture while supporting the overall redundancy philosophy applied throughout the spacecraft design.

Having established the subsystem designs, the spacecraft architecture is finalised through the definition of interface design, which governs the integration and functionality of the complete system and ensures consistency between mechanical, electrical, thermal, and operational interfaces. Mechanical interfaces define the physical mounting, alignment, and load transfer between subsystems and the primary structure, while operational interfaces are captured through the definition of mission operational modes and transition logic. A set of operational modes is therefore established to structure spacecraft functionality, reduce subsystem-level requirements where appropriate, and serve as the basis for the flight software state machine, supported by mode flags that enable verification of the mission time budget and operational lifetime compliance.

Finally, the baseline spacecraft design is consolidated through CAD-based visualisation and subsystem placement rationale, supported by mass and power budgets to demonstrate overall feasibility and confirm compatibility with Mini-F constraints. A technical risk assessment methodology is applied using qualitative likelihood and severity metrics to identify unacceptable risks, define mitigation actions, and assign residual risk indices, supported by contingency planning considerations to ensure design robustness in this early development stage. In addition, a verification and validation approach is defined based on mission classification and cost constraints, resulting in a model philosophy consisting of an Engineering Model, a Protoflight Model, and a Flight Spare, with lifecycle planning across Phases A–E to identify the critical reviews and verification activities required to support mission development and compliance demonstration.

2
Mission Overview

In this chapter, the key elements of background and motivations for the mission are detailed. First, the project objectives and scientific target overview are discussed, focusing on the scientific motivation and needs. Next, a payload description is included. At last, the market analysis and sustainable development strategy will be discussed.

2.1. Project Objectives

Since the early days of the Babylonians and the ancient Egyptians, astronomy has been an important part of humankind's scientific pursuits. Bright stars like Polaris and Sirius were identified and utilised for many purposes, like predicting the flooding of the Nile [136]. With the invention of the telescope, many mysteries about these stars got unravelled, among which was the discovery of Sirius being a binary star – a system of two stars [24]. Even later, in June 1962, a group of scientists in New Mexico launched an Aerobee rocket through Earth's atmosphere [95]. The launcher carried a small X-ray detector, and even though it remained in space for less than six minutes, a single source was detected: Scorpius X-1. Just like Sirius, Scorpius X-1 was a binary star, but not an ordinary one: it was the earliest discovery of an X-ray binary, which consists of a compact object, like a black hole or neutron star, that orbits a star. The project leader of the Scorpius discovery, Riccardo Giacconi, received a Nobel Prize for his contributions on the discovery of cosmic X-ray sources [58], and research on X-ray binaries is still of great value.

Nevertheless, a scientific gap is about to form for this type of research, with the amount of X-ray observatories currently in space starting to diminish: NASA's Chandra and NICER are both about to be decommissioned soon, and JAXA's XRISM is expected to be end of life by 2028 [8]. Besides this, ESA's XMM is the only other X-ray observatory in space, though it is not able to observe bright objects [8]. As such, the SRON has initiated a student project to design and launch a new X-ray observatory into Low Earth Orbit (LEO) at 550 km altitude in the early 2030s, where it shall remain for at least five years. The launch will be performed at the Guiana Space Centre (CSG) as part of a Mini-Fast rideshare mission by the European Space Agency (ESA). Because of this, it is already known that the spacecraft will be inserted into orbit by a Vega-C launcher.

The spacecraft itself, named the NEBULA-Xplorer (which is an acronym for Netherlands Educational Satellite for Exploration of Binary-Linked Astrophysics), will investigate multiple X-ray binaries with the use of two instruments: the Low Energy X-ray Instrument (LEXI) and the High Energy X-ray Instrument (HEXI). To fill the scientific knowledge gap and realise the goal of getting the NEBULA-Xplorer into its intended orbit, a Mission Need Statement (MNS) and a Project Objective Statement (POS) are followed throughout the design:

MNS: *The critical observational gap in continuous long-duration spectral timing monitoring of X-ray binaries during the early 2030s must be filled.*

POS: *Design a LEO-satellite for the NEBULA-Xplorer instrument that is compatible with the European Vega-C launcher and scheduled for launch in 2030.*

Over the past few years, multiple student groups have worked on various aspects of the design of the NEBULA-Xplorer and related systems; this report focuses on the conceptual design of the spacecraft (Phase 0 by ESA standards [46]). With the conceptual design, many constraints and requirements are introduced, as well as key drivers on which the design should focus: a high TRL of components, preferably higher than eight, a nominal science time goal of 72.5 ± 2.5 % margin, are excerpts of important stakeholder requirements that have an effect on the design options.
Previously during this design phase, a Project Plan [64], a Baseline Report [62] and a Midterm Report [63]

have been written; this report focuses on the final detailed design for the conceptual design phase, containing a description of the operations and logistic concept, the design process and its trade-off, the subsystem and interface design and a final design including budgeting. Besides this, a sustainability and cost analysis is performed, along with a technical risk assessment and a Verification & Validation (V&V) plan. Ultimately, recommendations for future work on this mission can be concluded.

2.2. Scientific Target Overview

A thorough understanding of the locations, observation modes, and times of the scientific targets is critical to the design of the spacecraft subsystems and to time budget allocation. The scientific targets of the NEBULA-Xplorer cannot be fully characterised in advance due to their unpredictable nature, though conclusions can be drawn from likely sources. The primary targets are transient outbursts: temporary bursts of energy which can be produced by different sources. By looking at historical outbursts, some information can be inferred about their probable location and preferred observation time to maximise scientific value. Secondary targets, classified with a lower priority, can also be assessed in the same manner.

The majority of NEBULA's scientific targets will be located within the Galactic Plane, clustered toward the Galactic Centre. These will primarily consist of X-Ray Binary (XRB) systems, including Black Hole (BH), Neutron Star (NS), and White Dwarf (WD) systems. Other targets are Active Galactic Nuclei (AGN) and Rotation Powered Millisecond-pulsars (RPM), rapidly rotating neutron stars. Not all targets lie in the Galactic plane. In particular, AGN are distributed evenly across the sky. Targets are classified as primary or secondary, based on the flexibility of their observation. For example, AGN are considered secondary targets because they do not have strict observation timing constraints, as science return can be maximised by observing these targets "every couple of days, most likely for around 1-2k kiloseconds (1000-2000 seconds) at a time" [110].

The targets are classified according to priority, observation time and other relevant parameters in Table 2.1.

Table 2.1: Summary of NEBULA Scientific Target Classes and Observation Characteristics

Primary Targets	**Observation Time**	**Likely Sky Location**	**Observation Mode**
Microquasars (XRB systems with relativistic jets)	3–14 days continuous	Galactic plane, clustered toward the Galactic Centre	Continuous observation during outburst
Other BH XRB systems	3–14 days continuous	Galactic plane, clustered toward the Galactic Centre	Continuous observation during outburst
Rotation-powered Millisecond Pulsars (magnitised NS)	~100–500 ks total	Galactic plane	Long integrations, distributed over months to years
Secondary Targets			
Other persistently accreting (NS and WD) XRB systems	~10–50 ks total	Galactic plane	Grouped observations; short gaps acceptable
Changing-look AGN	1–2 ks per visit	Isotropic (full sky)	Repeated short observations every 1–2 days
AGN with X-ray Reverberation	~300 ks total	Isotropic (full sky)	Quasi-continuous or successive-orbit observations
Quasi-Periodic Eruption (QPE) AGN)	Weeks-long campaign; 1–2 ks per visit	Isotropic (full sky)	Frequent interval observations (0.5–1 day cadence) scheduled in advance ($\approx$ 200 days)

2.3. Payload Description

Previously in Section 2.1, the instruments on board of the NEBULA-Xplorer, LEXI and HEXI, were mentioned. Due to their importance to the mission, a more elaborate description of this payload is provided in this section. As the HEXI payload is currently still in development, only an initial description is available at this stage.

2.3.1. LEXI

As the name suggests, the Low Energy X-ray Instrument (LEXI) will focus on the observation of low-energy X-rays. X-ray observations use a different approach from optical telescopes, since X-rays can only be reflected at very shallow angles. Therefore, this influences the layout of the LEXI and thus the spacecraft design. As seen in Figure 2.1, LEXI will make use of multiple X-ray concentrators instead of a single large telescope, so that the design can remain compact while achieving sufficient sensitivity. Each concentrator then focuses the incoming X-ray on a detector in the focal plane [132]. Each concentrator and its corresponding detector work as a single instrument, but only if they remain aligned with each other. Therefore, the payload structure must

be designed to keep them aligned through all mission phases. This means surviving launch loads and limiting structural deformations, for instance. This shows how the payload drives the design, as consequently, thermal stability and structural stiffness will become critical design drivers.

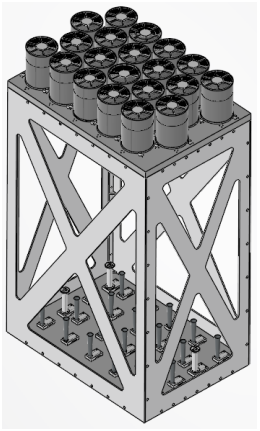

Figure 2.1: Isometric view of LEXI

Table 2.2: LEXI characteristics [126]

Subsystem	Parameter	Value
Optical Payload	Concentrators	20
	Detectors	24
	Height	1350 mm
	Length	650 mm
	Width	450 mm
	Mass	70 kg
	Sun shield	100 mm
Electronics	Housing dim.	140×140×100
	Mass	2 kg
	Peak power	250 W
	Data rate	5 Mbit/s
	Storage	45 Gbyte

2.3.2. HEXI

As previously mentioned, HEXI is currently still in development, meaning that a final design is unavailable at the moment. Nevertheless, an early representation of HEXI can be used for the design. In contrast to LEXI, HEXI operates without input optics, consisting primarily of a detector plate assembly positioned in a similar configuration as the LEXI detectors. This assembly is designed to accommodate four detector units, for which three options are still considered: NuSTAR, Cadmium Tellurium (CdTe), and Coded Mask. At the current design iteration, the CdTe detector is considered the most favourable candidate. Despite the absence of optical concentrators, HEXI is driven by the same critical design drivers as LEXI, regarding thermal stability and structural stiffness. Due to the current maturity level of the instrument, the spacecraft has been designed according to estimated payload characteristics provided by SRON, as summarised in Table 2.3.

Table 2.3: HEXI payload characteristics [126]

Parameter	Value
Input optics	None (baseline)
Detectors	4 (NuSTAR-type)*
Height	Same as LEXI*
Length	160 mm*
Width	160 mm*
Mass	10 kg*
Sun shield height	100 mm

(a) Optical Payload

Parameter	Value
Housing dimensions	140 × 140 × 60 mm
Mass	1 kg
Peak power	80 W
Total data rate	4 Mbit/s (20 Crab)
Data storage	6 Gbyte

(b) Electronics

2.4. Market Analysis

In this section, the market context and stakeholder environment of NEBULA-Xplorer are analysed. Since the mission is not a commercial product, the focus lies on establishing the scientific need, particularly the upcoming observational gap in X-ray astronomy, and on understanding how different stakeholders shape the mission's objectives and constraints. The analysis, therefore, considers the timing of current and future missions, the expectations of key stakeholders such as SRON, ESA, and industry partners, and the implications for mission requirements, performance, cost, and the development timeline.

2.4.1. Market Need

As previously discussed in Section 2.1, this mission was chosen because a critical X-ray observation gap arises, during which NEBULA-Xplorer could be the only mission capable of monitoring these astrophysical occurrences [8]. This gap in X-ray astronomy represents a clear unmet need within the scientific community. High-energy astrophysics depends on long-duration and uninterrupted monitoring, as many X-ray binary sources evolve rapidly. Continuous observations are essential for studying state transitions, burst activity and accretion cycles. Current high-spectral missions are unable to provide this type of monitoring because they are multi-purpose observatories or are constrained by instrument limitations that restrict long, uninterrupted observations[92]. In addition to these scientific considerations, the broader mission purpose is shaped by strategic factors such as scientific relevance, agency prioritisation, ESA funding programmes and the availability of rideshare launch opportunities, as these elements influence the conditions under which the mission can be realised. Without a mission such as NEBULA-Xplorer, the scientific community would likely miss valuable insights into binary evolution, compact object physics, and the behaviour of strong-field gravity. This absence would also create a technological setback and reduce educational and inspirational opportunities for future space science efforts. At the same time, the mission can provide this capability at a relatively low cost compared to large-agency missions [9].

2.4.2. Identifying Market Gap

To determine whether a dedicated X-ray binary monitoring mission is justified, the current landscape of X-ray astronomy missions must be reviewed. The operational status, performance characteristics and expected lifetimes of existing missions indicate which observational needs are currently fulfilled and where significant gaps remain. Chandra launched in 1999 and is experiencing declining efficiency, with uncertainty about long-term funding [90]. NICER is ISS-constrained and not XRB-specific, also affected by a motor-issue since mid-2025 [92]. XRISM is not intended for long-duration monitoring, and the mission lifetime is limited by cryogen depletion expected around mid-2026 [94]. NewAthena is significantly delayed, with launch expected no earlier than 2037 [53].

These missions collectively show that none are dedicated exclusively to X-ray binaries, none provide continuous timing observations, and none will be operational during the anticipated observational gap. To visualise this clearly, a mission timeline was constructed, shown in Figure 2.2. Solid lines indicate confirmed past and ongoing operations. Dashed lines denote periods of uncertainty or future planned availability. This representation highlights not only the operational overlap between missions but also the absence of any dedicated X-ray timing capability in the early 2030s.

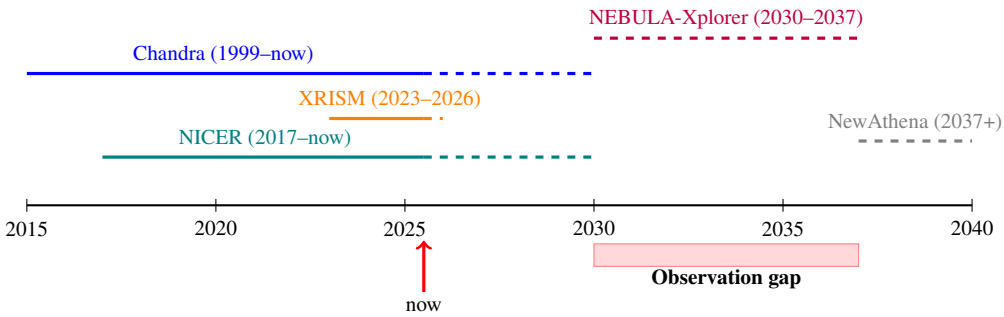

Figure 2.2: Timeline of past, current and future X-ray astronomy missions.

Although NEBULA-Xplorer is not a commercial mission, several strategic factors reinforce its relevance. ESA's mini-F rideshare initiative demonstrates a growing interest in agile, low-cost scientific missions, targeting a Cost-at-Completion below € 50 M [56]. This aligns well with the scale and purpose of NEBULA-Xplorer. Europe will lack an independent X-ray observation capability throughout the gap, and the mission directly enables continuity in high-energy astrophysics research. Furthermore, the project contributes to the development of young engineers, which is one of SRON's central motivations for assigning the conceptual design to a student team. Overall, NEBULA-Xplorer delivers high scientific value at a modest cost under € 50 M and addresses a clearly defined, time-critical need within the astrophysical community.

The SWOT analysis in Figure 2.3 summarises the internal and external factors that influence the NEBULA-Xplorer mission. The strengths and weaknesses describe characteristics of the mission concept and its development approach, while the opportunities and threats reflect the broader scientific and programmatic environment. Together, they clarify how NEBULA-Xplorer fits within the X-ray astronomy landscape and why the mission is well-positioned during the upcoming observational gap.

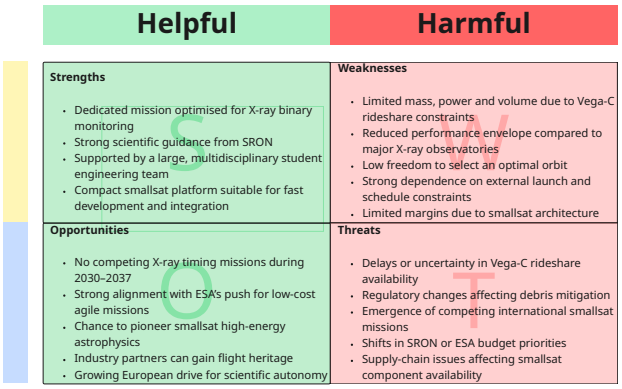

Figure 2.3: SWOT analysis of the NEBULA-Xplorer mission.

2.4.3. Stakeholder Analysis

The key stakeholders associated with this mission include SRON, ESA, the scientific community and industrial partners involved in subsystem development. SRON, the Netherlands Institute for Space Research, acts as the mission owner and scientific lead, defining the primary science objectives, data needs and instrument accommodation. ESA influences requirements related to launch compatibility, debris mitigation and the use of the Vega-C ride-share framework. Because the mission is not commercial, the stakeholder landscape remains relatively straightforward, and the user requirements already capture most relevant constraints such as mass, cost, schedule and environmental conditions. SRON also has an educational objective: the design is intentionally assigned to a student team, which shapes the scope and acceptable risk level of the design phase.

Stakeholder Identification

The stakeholder identification process for NEBULA-Xplorer began by mapping all groups involved in or affected by the mission. Because this is an early-phase preliminary design developed by a student team under SRON guidance, particular attention is given to stakeholders who influence the scientific objectives, technical feasibility, mission architecture and the practical constraints under which the mission must operate. After identifying all relevant actors, each stakeholder was classified according to their influence on mission design and requirements, as well as their interest in the mission's scientific success and data return. This distinction results in two categories: active stakeholders directly shape the mission by defining objectives and requirements, or by controlling key resources and constraints (e.g. funding, launch opportunities, or regulatory approval). Passive stakeholders do not set requirements themselves, but they still influence the design through external constraints and enablers, such as available technologies, subsystem/-operational limitations, procurement realities, and the regulatory environment. This classification helps to prioritise stakeholder needs during requirement derivation and supports design trade-off decisions when objectives conflict.

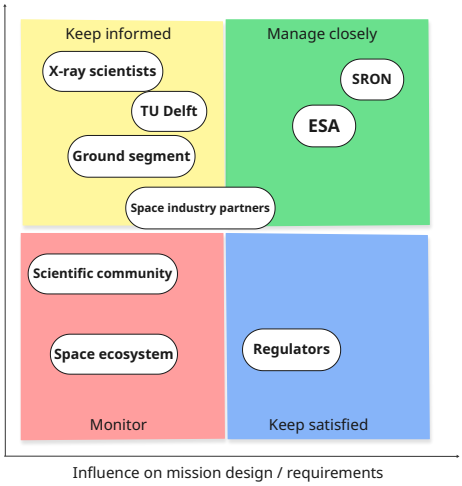

Figure 2.4: Stakeholder influence-interest map

Stakeholder map

The identified stakeholders were positioned on an influence–interest grid in Figure 2.4 to visualise their relative importance for the preliminary design phase. Stakeholders in the upper-right quadrant (high influence, high interest) must be managed closely, as they directly drive mission-level requirements. Stakeholders with strong influence but low interest (upper-left quadrant) must be satisfied through compliance with their constraints. Stakeholders with high interest but low influence (lower-right quadrant) should be kept informed to ensure their scientific and operational needs are addressed effectively. The remaining stakeholders in the lower-left quadrant have minimal influence and indirect interest, yet they still provide contextual value to the mission. Table 2.4 summarises the stakeholders identified in the process, their key needs and their level of influence on the mission design. This structure provides the basis for deriving mission requirements from stakeholder expectations. The NEBULA-Xplorer student teams are not treated as external stakeholders. They form the internal project or-

ganisation that executes the conceptual design within constraints defined by SRON, ESA, and TU Delft. Their interests are represented indirectly through SRON's educational objectives and TU Delft's academic framework.

Table 2.4: Stakeholders, their key needs, and influence on the mission design.

Stakeholder	Key Needs	Influence
Active stakeholders		
SRON	Continuous X-ray monitoring during the observational gap; feasible mission with strong scientific value; educational value for students.	Very high
ESA	Vega-C rideshare compatibility; compliance with safety and debris rules; fit with low-cost small-mission programmes.	High
X-ray scientists	Long, uninterrupted observations; good timing and spectral capabilities; easy access to data.	Medium
TU Delft	Alignment with academic learning objectives; well-coordinated student design process.	Medium
Passive stakeholders		
Regulators	Full compliance with debris mitigation guidelines and safety standards.	High
Arianespace	Provides the launch vehicle and sets constraints on the rideshare schedule and vehicle interface.	Medium-high
Space industry partners	Clear subsystem interfaces; use of hardware within qualification limits; manageable procurement timelines.	Medium
Ground segment providers	Feasible downlink rates and schedules; operations that work with existing infrastructure.	Medium
Scientific community (broader)	Possibility to use data for other research topics.	Low
Space ecosystem (NL/EU)	Educational value, outreach and strengthening of regional space capabilities.	Low

Derivation of mission requirements

Following the stakeholder identification in Section 2.4.3, the next step is to translate the identified stakeholder needs into concrete mission requirements. Rather than defining requirements independently, each mission requirement is derived from a specific stakeholder need or constraint. This ensures that the requirements set are justified, traceable, and aligned with the mission's scientific, regulatory, and operational objectives. The derivations of the most influential stakeholder requirements are summarised below.

Launch compatibility (REQ-MIS-C-001): ESA, as the launch provider, imposes strict compatibility constraints for Vega-C rideshare payloads. These include limitations on mass and volume, dynamic loads during launch, mechanical interfaces and safety standards. REQ-MIS-C-001 is therefore derived directly from ESA's mandatory launch constraints.

Orbit (REQ-MIS-C-002): SRON and the X-ray science community require an orbit that enables continuous or frequent observations of X-ray binaries during the anticipated observational gap. This drives REQ-MIS-C-002, which constrains the orbit in terms of inclination, altitude, and geometry, ensuring sufficient visibility of target sources while remaining compatible with the ESA-provided rideshare orbit.

Mission lifetime (REQ-MIS-O-003): To deliver meaningful scientific value, the satellite must operate reliably for a duration covering the expected observation gap in X-ray astronomy. SRON and the scientific community, therefore, require several years of sustained operation. REQ-MIS-O-003 captures this need and influences subsystem sizing and reliability requirements across AOCS, EPS, propulsion and thermal control.

Launch schedule (REQ-MIS-O-004): The mission schedule must align with both the Vega-C rideshare manifest and academic project timelines. ESA defines available launch windows, while SRON and TU Delft define internal planning milestones for the student-led design process. These constraints together motivate REQ-MIS-O-004.

Cost limit (REQ-MIS-C-005): SRON and ESA emphasise a low-cost, small-satellite mission philosophy consistent with programmes such as Mini-F. REQ-MIS-C-005 sets an upper bound on the allowable mission cost, promoting the use of COTS subsystems and limiting unnecessary design complexity.

Debris mitigation and end-of-life strategy (REQ-MIS-F-006): Regulatory authorities, including ESA's Space Debris Office and national licensing bodies, require all missions to demonstrate a compliant disposal strategy. This requirement strongly affects propulsion capability, drag augmentation considerations and operational planning. REQ-MIS-F-006 is therefore derived directly from mandatory debris mitigation regulations.

Science data collection (REQ-MIS-F-007): X-ray scientists require continuous high-quality data from long-duration observations. To ensure that no data is lost during periods without ground contact, REQ-MIS-F-007 requires that the spacecraft autonomously collect and buffer scientific measurements.

Onboard data storage (REQ-MIS-F-008): Ground segment providers impose limits on downlink bandwidth and contact frequency. As a result, REQ-MIS-F-008 defines the required onboard storage capacity to retain all science data until it can be successfully downlinked.

Downlink capability (REQ-MIS-F-009): To return mission data at a rate compatible with both scientific expectations and ground station availability, REQ-MIS-F-009 specifies the minimum downlink performance needed for routine operations and timely data delivery.

Uplink capability (REQ-MIS-F-010): REQ-MIS-F-010 ensures that uplink capacity is sufficient to support routine commanding, health monitoring and safe-mode recovery. This requirement reflects the needs of ground operators to reliably interact with the spacecraft.

Instrument accommodation (REQ-MIS-F-011): SRON's scientific instrument imposes mechanical, thermal and electrical interface constraints, while ESA constrains the payload volume available in the rideshare configuration. REQ-MIS-F-011 ensures that the spacecraft accommodates the instrument within both SRON's needs and ESA's rideshare constraints.

Overall, this stakeholder-driven derivation ensures that the mission requirements are justified, traceable and prioritised according to stakeholder influence and interest. It provides a consistent basis for subsystem design, trade-off analyses and verification planning.

2.4.4. Stakeholder Benefits

The mission offers distinct benefits to the stakeholders mapped in Figure 2.4.3. For SRON and the wider X-ray science community, NEBULA-Xplorer provides access to continuous X-ray timing data during a period in which no comparable missions will be available, enabling new insights into high-energy astrophysics and strengthening the scientific relevance of the Dutch research landscape. ESA benefits from the demonstration of a compact, low-cost science mission that aligns with the objectives of the Mini-F rideshare programme and supports the usage of Vega-C launch capacity. Space industry partners gain opportunities to demonstrate subsystem performance and flight heritage, supporting future space missions. The mission also contributes to the Dutch and European space ecosystem by offering students a hands-on engineering experience within a realistic mission framework, thereby supporting career development and academic training.

2.4.5. Summary of Findings

NEBULA-Xplorer addresses a clear scientific need created by the 2030–2037 observational gap in X-ray astronomy: neither current nor planned missions can provide long-duration X-ray binary monitoring during this period, and the market analysis indicate that NEBULA-Xplorer would meet global demand for continuous X-ray timing. The SWOT analysis reinforces this position, combining a focused objective, SRON guidance and alignment with ESA's interest in small, low-cost science missions, while acknowledging constraints from the rideshare architecture and regulatory requirements. The stakeholder analysis identifies SRON and ESA as the dominant drivers of mission-level constraints, setting the scientific objectives, launch compatibility, regulatory compliance and cost envelope. X-ray scientists define performance expectations, TU Delft sets the feasible scope of the student-led design, and passive stakeholders define key operational, technological, and procurement boundaries. Overall, the analyses show NEBULA-Xplorer fulfils an otherwise unmet scientific need and provides a solid, stakeholder-driven basis for the next design phases, delivering scientific, educational and programmatic value within the Dutch and European space sectors.

2.5. Sustainable Development Strategy

This section outlines the sustainable development strategy adopted for the mission. The analysis addresses emissions associated with the rideshare launch, and a life-cycle assessment on the spacecraft was performed. In addition, broader sustainability considerations are discussed, including space debris mitigation, responsible use of the radio-frequency spectrum, and the potential role of in-orbit refuelling in extending mission lifetime and reducing long-term environmental impact.

2.5.1. Rideshare Emissions

Fuel Emissions

The Vega-C vehicle employs three solid rocket stages and a liquid-propellant upper stage, with a total propellant mass of 191,189kg [20]. The solid propellant used in the first three stages is composed of 69% ammonium perchlorate, 19% aluminium powder, and 12% hydroxyl-terminated polybutadiene(HTPB). As ammonium perchlorate and aluminium powder contain no carbon, HTPB represents the sole source of carbon contributing to CO2 emissions during the solid propellant combustion. The total mass of the HTPB in the Vega-C rocket is 22,943kg.
Based on this composition and assuming complete combustion, it was estimated that the Vega-C launch vehicle produces approximately 74.7 tonnes of CO_2 from solid propellant combustion alone. Additionally, ammonium perchlorate combustion produces gases such as nitrogen, oxygen and hydrochloric acid. Hydrochloric Acid is a significant pollutant that can contribute to acid rain and cause corrosion. Therefore, the estimated CO_2 emissions represent only a partial measure of the environmental footprint of solid-propellant launch vehicles.

Material

At liftoff, the launcher has a total mass of 210,000 kg, consisting primarily of 191,189 kg of propellant, a dry mass of 15,511 kg, and a payload mass of 3,300 kg according to the Vega-C User's manual [20]. The structural components of the launcher are manufactured using a combination of carbon fibre–reinforced polymer (CFRP) and aluminium. A material composition assumption of 60% CFRP and 30% aluminium was applied. The aluminium content of the propellant is 19%. To quantify the environmental impact of these materials, carbon intensity data were sourced from the IDEMAT database [130]. The total emissions of structural materials and fuel emissions are shown in Table 2.5.

Table 2.5: Material mass and associated CO_2e emissions

Metric	CFRP (structure)	Aluminium (structure)	Aluminium powder (propellant)	HTPB (propellant)	Total
Mass [kg]	9 307	4 653	36 326	22 943	**73 229**
CO_2e [kg]	186 549	40 382	315 257	-	**616 887**

Rideshare fraction

The Vega-C launcher that will place the spacecraft in its final orbit is designed to support rideshare missions. This shared-launch approach distributes the embodied emissions of the launch vehicle across multiple payloads, thereby reducing the effective carbon footprint per satellite and improving overall sustainability compared to dedicated single-payload missions. Given a total payload capacity of 3,300 kg and a conservative estimate of 400 kg for the satellite mass, the NEBULA mission accounts for approximately 12% of the total launch mass. Based on this, the Vega-C launch results in an estimated CO_2 emission of 74.8 tons for the mission.
This analysis excludes the emissions associated with the manufacturing and transportation of the launch vehicle. In addition, the assessment assumes a single-use launch system, with no material recycling at end of life.

2.5.2. Screening Life-Cycle Assessment

To quantify the total environmental impact of the satellite design, a screening life-cycle assessment (LCA) was conducted for the main components of each subsystem. The purpose of this assessment is to obtain an order-of-magnitude understanding of the main environmental contributors and to enable comparison between subsystems, and it focuses on the material production impacts of the major components. Environmental impacts were quantified using carbon dioxide equivalent (CO_2e) emissions and the ReCiPe impact indicator. CO_2e and ReCiPe values for the materials used in the spacecraft's main components were obtained from the IDEMAT database [130]. For each component, the primary material and its associated mass were assumed. Secondary materials were not included. While this approach likely underestimates the absolute environmental impact, it is sufficient to identify key drivers within the spacecraft design.
The resulting CO_2e emissions and ReCiPe impact scores per subsystem are summarised in Table 2.6.

Table 2.6: CO_2e and ReCiPe results by subsystem

Metric	EPS	PROP	AOCS	TCS	TTC	CDH	STUC	Total
CO_2e	1364.05	594.55	823.57	275.90	23.46	6.48	2130.49	**5218.50**
ReCiPe	43.50	22.37	19.16	7.35	0.58	1.51	49.16	**143.62**

The screening LCA results show that the structural subsystem (STUC) is the dominant contributor to the overall environmental impact, accounting for approximately 41% of the total CO_2e emissions. This is primarily attributed to the high mass of structural components and the use of energy-intensive materials, such as aluminium alloys, which are known to have significant production impacts. The electrical power subsystem (EPS) represents the second-largest contributor, contributing roughly 26% of total CO_2e emissions, which is mainly driven by the solar panels and batteries.
The geographic location of manufacturing facilities and the specific manufacturing processes of individual components are not known at this design stage. As a result, emissions associated with manufacturing processes and transportation logistics are not included in the results.

Fuel Emissions

As mentioned in Chapter 8, the propulsion system uses a bi-propellant combination of nitrous oxide (N_2O) and propylene (C_3H_6), with a total onboard quantity of approximately 8.25 L nitrous oxide and 1 L propylene. The ideal, stoichiometrically balanced reaction for this propellant combination is given by:

$$C_3H_6 + 9\,N_2O \rightarrow 3\,CO_2 + 3\,H_2O + 9\,N_2 \tag{2.1}$$

During nominal operation, the propellants are intended to react completely. In this case, the carbon content of the propylene is oxidised to carbon dioxide, resulting in an estimated 1.7 kg CO_2e released over the full mission lifetime. Additionally, water and nitrogen (N_2) are formed, which are both harmless to the environment. The CO_2 contribution is negligible compared to the launch emissions.
A worst-case scenario would involve the release of unreacted nitrous oxide. According to IDEMAT [130], N_2O has a high global warming potential of 273, meaning it causes 273x more warming than CO_2. System design minimizes leakage and venting, however, and no routine release of N_2O is planned during operations.

End-Of-Life

In this analysis, it's assumed that every part will either burn up during reentry or will not be recovered. There's some risk that high-melting-point or composite materials, such as titanium or CFRP, may partially survive reentry and reach the Earth's surface. An end-of-life (EOL) analysis was performed in Section 17.6.4 to analyse the causality risk associated with surviving reentry debris.

2.5.3. Space Debris Mitigation Framework - SDMF

The amount of orbital debris and active spacecraft in Launch and Early Operations (LEOP) continues to grow year over year [54]. In recent years, the space sector has increasingly adopted stricter requirements to limit the generation of space debris, which poses a growing threat to current and future missions. As a result, sustainability has become a key consideration in the design of space missions. In alignment with TU Delft's sustainability policy and the European Space Agency's Zero Debris approach [55], a Space Debris Mitigation Framework is incorporated into the design of the NEBULA-Xplorer mission. The requirements in Table 2.7 are extracted from ESA Space Debris Mitigation Requirements - ESSB-ST-U-007 Issue 1 [48] because this also means compliance with the ECSS: "The compliance with the standard ESSB-ST-U-007 ensures compliance also with the standard ECSS-U-AS-10C Rev."[48]. Only the requirements applicable in the context of the NEBULA-Xplorer (LEO region / Phase 0) are selected and the requirement IDs given correspond to the IDs in the original document. In Section 4.7.1, a collision risk assessment is performed and the annual ΔV required for collision avoidance is shown. The orbit propagation is displayed in Section 4.7.5 and in Section 17.6.4, a causality risk assessment is performed.

Table 2.7: Key requirements for Space Debris Mitigation Strategy falling under ESSB-ST-U-007 Issue 1. [48]

Requirement ID	Title	Requirement
5.3.3.1	Collision risk assessment during design	The developer of a spacecraft or launch vehicle orbital element operating in Earth orbit shall quantify the probability that space debris or meteoroid impact causes the spacecraft or launch vehicle orbital element to break-up, including: 1) Impacts with space debris and meteoroids larger than 1 mm and smaller than 1 cm 2) Impacts with space debris and meteoroids larger than 1 cm 3) A free drift trajectory after orbit injection, end of mission, and disposal, and during normal operations, until re-entry or up to 100 years

Requirement ID	Title	Requirement
5.3.3.2	Collision avoidance implementation	A spacecraft operating in near Earth orbit shall have a recurrent manoeuvre capability if: 1) It is injected into an orbit crossing the LEO protected region with a natural orbit decay duration longer than 5 years 2) Its cumulative collision probability with space objects larger than 1 cm is above 10^{-3} through to its end of life
5.3.3.2	Collision avoidance implementation	The developer of a spacecraft or launch vehicle orbital element injected into near Earth orbit shall quantify, during normal operations and after end of life until re-entry or up to 100 years: 1) The expected number of conjunctions at 10^{-4} and 10^{-6} collision probability threshold 2) The estimated number of collision avoidance manoeuvres triggered thereby on other spacecraft
5.3.3.3	Collision risk management during operations	During the normal operations of a spacecraft in the LEO protected region with a recurrent manoeuvre capability, on an orbit with an average density of space debris larger than 1 cm above 10^{-7} km^{-3}, the acceptable collision probability threshold shall be the lower of: 1) 10^{-4} 2) The collision probability value such as to reduce the annual collision probability by at least 90%
5.4.2.3	LEO protected region clearance	The orbit clearance of a spacecraft or launch vehicle orbital element from the LEO protected region shall satisfy an orbit lifetime less than 5 years starting from the end-of-life epoch.
5.3.2.2	Accidental break-up caused by an on-board source of energy	Spacecraft operating in Earth orbit shall be passivated before the end of life unless a successful controlled re-entry is performed.
5.5	Re-entry	The expected number of casualties per re-entry of a spacecraft or launch vehicle orbital stage shall be less than 10^{-4}.
6.2.a	Verification and Validation Requirements – Models	The space debris and meteoroid environment models used shall be in compliance with ECSS-E-ST-10-04. The ESA MASTER model is compliant.
6.2.b	Verification and Validation Requirements – Models	The 1 cm size space debris population used shall use the latest available calibration epoch at the time of analysis.
6.2.g	Verification and Validation Requirements – Models	For the orbit lifetime assessment, the following confidence level shall be used: 1) 50th percentile for eccentricity below 0.3 at end of life 2) 90th percentile for eccentricity above 0.3 at end of life

2.5.4. Efficient Bandwidth Use and Electromagnetic Compatibility

Sustainable and efficient bandwidth use is essential to prevent congestion on the Radio Frequency (RF) spectrum [73]. By limiting occupied bandwidth to what is strictly necessary for mission requirements, interference with other satellites and services is reduced, and long-term access to orbital and frequency resources is preserved. In Section 12.4.2, occupied bandwidth was a key parameter in the trade-off between forward error correction (FEC) and modulation schemes. Furthermore, bandwidth occupation constraints specified in the ESA PSS-04-105[47] standard were adhered to, ensuring compliance with regulatory requirements and responsible use of the RF spectrum.

Electromagnetic Compatibility (EMC) further contributes to the reliable and sustainable operation of spacecraft systems. EMC refers to the ability of electronic equipment to operate correctly within its electromagnetic environment without causing or suffering unacceptable electromagnetic interference. To verify compliance, EMC performance should be assessed through dedicated testing, including measurements conducted in specialised electromagnetic compatibility test chambers such as the ESTEC Maxwell Test Chamber.

2.5.5. In-orbit Refueling

For the propulsion system, the B20 thrusters developed by Dawn Aerospace are selected. Since 2025, these thrusters are delivered with a standardised Docking and Fluid Transfer (DFT) port, enabling in-orbit refuelling and servicing capabilities [105]. At present, no operational refuelling services are available. However, it is anticipated that the LOOP Network will become operational before 2030. In-orbit refuelling has the potential to significantly extend the satellite's operational lifetime, thereby increasing the mission's return on investment (ROI). It could also provide additional collision-avoidance manoeuvres. Furthermore, the presence of a docking interface allows for post-mission debris removal operations, contributing to the mitigation of space debris in LEO. Reliance on in-orbit refuelling during operations is not recommended, however, due to increased risk to the mission. Nevertheless, refuelling after the nominal end of life (EOL) could be considered to extend the mission duration. In addition, debris removal services enabled by the docking port may be utilized post-EOL as a contingency measure if controlled re-entry fails.

3 Requirements

This chapter discusses the driving used during the design process. It identifies the most driving requirements, which have the largest impact on selecting the baseline design. So it serves as input for Chapter 6. The requirement changes are also documented and discussed at the end of this chapter.

3.1. Driving requirements

During the baseline phase of the design, a set of requirements was generated. From this set, the most driving requirements were identified. These requirements were used in the system-level design trade-off before the detailed design phase and can be found in Table 3.1. The subsystem requirements can be found in the subsystem design sections. The full set of requirements can be found in a separate document[32].

Table 3.1: Driving requirements used in the system-level trade-off

Requirement ID	Parent ID	Requirement	Rationale
REQ-LAUN-C-LAUN005-006	REQ-LAUN-C-MIS001-005	The spacecraft height should be less than 1800 mm	Stated by the Vega-C launcher manual [19]
REQ-LAUN-C-LAUN005-007	REQ-LAUN-C-MIS001-005	The spacecraft diameter should be less than 1500 mm	Stated by the Vega-C launcher manual [19]
REQ-LAUN-C-MIS001-011	REQ-MIS-C-001	The spacecraft wet mass shall be between 200kg and 400kg	Stated by the Vega-C launcher manual [19]
REQ-SYS-F-MIS007-009	REQ-MIS-F-007	The mission shall operate payload HEXI and payload LEXI simultaneously for at least 72.5 ± 2.5 % per orbit.	Client wants to maximise operation time
REQ-EPS-F-MIS007-001	REQ-MIS-F-007	The EPS shall supply a continuous power of at least 438 W until the EOL	During science mode, the payload and supporting subsystems have a peak power consumption of 438 W, science mode shall be possible throughout the entire orbit therefore, the EPS shall deliver continuous power of 438 W
REQ-MIS-C-002	N/A	The science operations orbit shall be a quasi-circular LEO with an initial altitude of 550 km and an inclination between 45 and 60° .	Optimal orbit range for maximising observation time and minimising radiation exposure above the poles
REQ-MIS-O-003	N/A	The nominal mission lifetime shall have a duration of at least 5 years.	Given by client, indicator of ESA mission type classification

The requirements above are considered to be driving because they have a high impact on the design. The first three are constrained directly from the launcher manual; exceeding these limits will result in not being able to launch the spacecraft. Requirement REQ-SYS-F-MIS007-009 defines the availability of the payload. Previous studies have concluded that compliance with this requirement is not likely to be feasible [22]. It is therefore expected to strain the design process and have consequences for all subsystems and the frequency of operations. This translates directly into REQ-EPS-F-MIS007-001, which translates operating the payloads into a power generation need. Even though it is the result of a driving requirement, it is considered a driving requirement on its own because the size of the EPS subsystem shall have a large impact on other subsystems, such as the AOCS and the structure. Requirements REQ-MIS-C-002 and REQ-MIS-O-003 are listed as driving requirements because they define the environment that the spacecraft is exposed to and the duration for which it is exposed to these conditions. This results in reliability requirements that will increase the mission reliability such that the operational lifetime is reached. Additionally, the mission lifetime classifies the mission as an ESA class type III mission [65]. The mission class indicates the applicable ECSS standards, the level of risk that

is acceptable, qualification levels and documentation required. For a class III mission, ESA approaches relatability as 'Finding the best compromise between risk and cost to deliver the mission' [65]. This requirement, therefore, impacts all subsystems in their reliability design.

3.2. Requirement changelog

Between the preliminary design and the final design, some requirements were added or changed. A major change to single out is that of requirement REQ-SYS-F-MIS007-009. The requirement first stated that the mission shall operate payload HEXI and payload LEXI simultaneously for at least 75% per orbit. During the preliminary design, it was found that the design was not compliant with this requirement and that it was unlikely to be feasible. After contact with the client about this non-conformance, the requirement was relaxed to 72.5 % ±2.5 %. REQ-LAUN-O-LAUN011-012 stating: the spacecraft wet mass should be between 200 [kg] and 250 [kg] was changed to a 'should' statement as it was a wish from the client but unlikely feasible.

3.3. Compliance Matrix

After the design, a compliance matrix was generated containing all requirements, their verification methods and whether the design complies with the requirements. This matrix was excluded from the report since the user requirements, driving requirements and driving subsystem requirements can be found throughout the report in their respective sections. The full compliance matrix was delivered as a separate file to the tutor, coaches and the client [32]. All non-compliances are documented within this document below with NCR ID's for future reference.

NCR-REQ-01: REQ-LAUN-C-007 stating that the spacecraft wet mass shall be between 200 [kg] and 400 [kg] was met with a spacecraft total mass of 310.73 [kg]. Including margins for cots components this becomes 344.71 [kg]. ESA's standards on mass margin[82] mandates an extra 20% margin to be added. This would result in a mass of 412.65 [kg] resulting in non-compliance. However, the requirement does not state anything about margins. Considering the spacecraft components are mostly Commercial Of The Shelf (COTS) a lot of uncertainty is already removed. Therefore, using a margin of 15% on top of the total mass is proposed resulting in 396,42 [kg] compliant with the requirement.

NCR-REQ-02: REQ-MIS-C-005 stating: The spacecraft cost without the instrument shall be less than 4M€, was not met. This non-compliance is not considered as a direct mission failure, as the client indicated that budget is not their most limiting factor. It is proposed to change the budget to 9.5M€ as this should be attainable for this mission.

NCR-REQ-03: REQ-TCS-C-LAUN004-008 was not verified and can therefore not be marked as compliant. This should still be executed in subsequent mission phases.

4
Space Environment and Astrodynamics

The spacecraft environment is one of the most important considerations of any space mission. It directly affects the spacecraft's performance and survivability, defines the radiation and debris environment, and represents the medium in which the satellite operates. An inaccurate or incomplete assessment of this environment can have serious consequences, including mission failure. The nature of these environmental effects depends strongly on the spacecraft orbit and mission profile. Given the baseline altitude and inclination of the NEBULA-Xplorer in LEO, an investigation into the operational environment is conducted.

4.1. Orbital Regime

"The science operations orbit shall be a quasi-circular LEO with an initial altitude of 550 km and an inclination between 45 and 60 degrees." - REQ-MIS-C-002

A quasi-circular initial orbit with 550 km altitude at a 45° inclination is selected for the NEBULA-Xplorer mission. The spacecraft's orbit is determined by the stated requirement, and it is allowed to lose altitude, which relaxes the station-keeping requirements. The mission has a 7-year lifetime goal. An operational envelope of 475-550 km is selected, which ensures 7 years of nominal operations. The spacecraft is allowed to drift freely from the initial orbit, but at lower altitudes, it experiences drag, disturbance torques, and an increase in the eclipse fraction. Hence, a lower limit of 475 km is selected, which does not require additional solar array area to meet the mission's power requirements within the 7-year mission goal. Furthermore, the disturbance torques resulting from drag are much lower at this lower altitude, which relaxes the requirements on the AOCS. Finally, the spacecraft can stay in this envelope with one re-boost performed during the first 5 years and it is expected to reach the lower limit of the envelope at 7 years from where it will undergo an un-controlled de-orbit within 5 years, this decreases the total ΔV required to keep the mission operational rather than staying at a constant altitude and decreases the total required ΔV substantially.

The main reason for selecting 45° inclination is that it results in less time spent in high-radiation zones, where the spacecraft must enter radiation protection mode. These zones include the SAA and the polar radiation zones. The time lost to scientific observations in these regions due to rough conditions is detailed in Section 14.5. Overall, 45° inclination covers less area of the SAA and intersects the outer boundaries of the polar radiation regions only briefly. This inclination also results in a lower population of surrounding debris than higher inclinations. The appropriate population graphs comparing these regions are presented in Section 4.5, and the coverage of the radiation zones can be interpreted from Figure 4.3. As a result, a quasi-circular 45° orbit within the altitude envelope of [475, 550 km] is chosen for the nominal operational time-frame of 7 years for the NEBULA-Xplorer mission. The resulting orbital periods for the boundaries of the envelope can be calculated using the equation:

$$T = 2\pi\sqrt{\frac{a^3}{\mu_E}} \tag{4.1}$$

where a is the semi-major axis in km and μ_E is the gravitational parameter of Earth with the value $\mu_E = 3.986 * 10^5 km^3/s^2$. Hence, the orbital periods at 550 km and 475 km are 95.6 min and 94.1 min, respectively.

4.2. Radiation

Even with a selected LEO for the mission, the spacecraft will still experience dangerous levels of radiation that must be accounted for in the final design. This section will describe the types and effects of radiation, with initial estimates of expected levels.

Table 4.1: Radiation environment and associated effects in LEO

Category	Name	Energy / Dose Range	Primary Effects
Radiation Type	Trapped Protons	1–10 krad/year (unshielded)	Ionizing dose increase; Single Event Upset (SEU); concentrated in the SAA
	Trapped Electrons	10 keV – 1 MeV, ∼1–50 rad/year	Surface and internal charging
	Galactic Cosmic Rays (GCR)	GeV energy range, ∼1–10 rad/year	Single Event Latch-up (SEL), Single Event Burnout (SEB)
	Solar Energetic Particles (SEP)	Highly variable	Increased ionizing dose; enhanced surface charging
	Plasma Radiation	Low-energy ionospheric plasma	Surface charging; plasma wakes
	Solar Electromagnetic Radiation (SER)	Ultraviolet (UV), Extreme Ultra Violet (EUV), X-ray	Material degradation
Radiation Effects	Total Ionizing Dose (TID)	Cumulative over mission lifetime	Long-term electronic degradation
	Surface Charging	Particle dependent	Electrostatic discharge; surface potential build-up
	Internal Charging	High-energy particle penetration	Dielectric breakdown; internal discharges
	SEU	Single particle interaction	Transient logic errors
	Single Event Effects (SEE)	High LET events	Permanent damage including SEL and SEB

4.3. Atomic Oxygen

Atomic oxygen, formed in Earth's thermosphere, is one of the key mechanisms driving the material degradation in LEO. As stated by NASA's report titled "Low Earth Orbital Atomic Oxygen Interactions With Spacecraft Materials" [87], the resulting interactions can change the morphology and decrease the thickness with the development of textured surfaces on all materials with volatile oxidation products. This mechanism greatly affects hydrocarbon polymers, which will affect the design choices and protective measures put in place to reduce the negative effects as explained in Chapter 11.

4.4. Solar Conditions

For LEO, temporal variations in the environmental conditions are to be expected both during orbit and the entirety of the mission lifetime. Due to the elliptical nature of Earth's orbit and variations in the Sun's activity, solar irradiance levels will fluctuate.

4.4.1. Beta Angle

During Earth's movement along its orbital path, the Sun's angle with respect to spacecrafts orbital plane will vary, which is called the beta angle. This will impact the time spent in Eclipse. Figure 4.1 shows the progression of solar beta angle and eclipse fraction for both 475 and 550 km altitude over the span of 5 years. The maximum eclipse fraction for 550 km is estimated at around 0.372 with no eclipse periods taking place around 1.5 times a year as seen in Figure 4.1b. A similar graph was produced for EOL altitude of 475 km, shown in Figure 4.1a. The maximum eclipse fraction is larger at higher altitudes, around 0.381, with the minimum around 0.035.

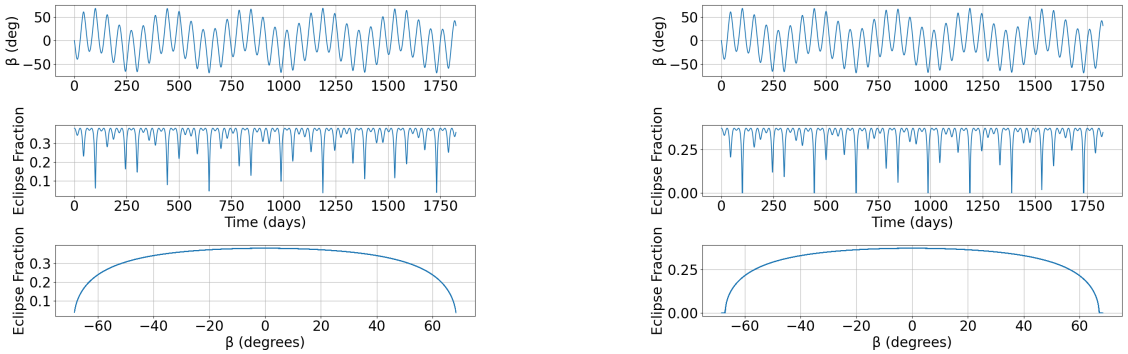

(a) 475 km altitude

(b) 550 km altitude

Figure 4.1: Solar beta angle and eclipse fractions over 5 years

4.4.2. Solar Radiation

Variations in the sun's magnetic field generate different types of solar events like flares, coronal mass ejections, sunspots, and bright faculae. Coronal Mass Ejection (CME) is a large expulsion of plasma and magnetic field from the Sun's corona, and Earth-directed CMEs can cause intense geomagnetic storms[98]. Solar flares are explosions on the sun that suddenly release tremendous amounts of energy in a burst of electromagnetic radiation [57]. A large part of the variations in solar flux can be attributed to the sunspot and faculae regions. Sunspots are darker areas on the surface of the sun where magnetic forces are very strong [96]. On the other hand, faculae are bright areas on the sun's surface that emit more radiation [96]. The facular and sunspot contributions usually do not fully compensate each other, and the resulting imbalance is a major source of the solar flux variability [114].

Solar activity varies with an 11-year cycle in which there is a high uncertainty in predicting the solar flux level at a given point in time [137]. Despite this, the average over an extended time period is well known, and the total solar irradiance over the 11-year cycle changes by only about 0.1% [114]. The Total Solar Irradiance (TSI) is the integrated solar energy arriving at Earth and is historically referred to as the solar constant with a value of 1361 W/m^2. Despite its historical name, which results from the phenomena described above regarding the sun and the Earth's elliptical orbit, the TSI is actually a variable.

Solar Flux

Changes in solar flux over the 11-year cycle greatly influence the atmosphere the spacecraft experiences. During solar maxima, periods of increased solar activity, atmospheric particles become more energised, leading to an expansion of the upper atmosphere and an increase in the drag acting on the spacecraft. This increase in drag can shorten the spacecraft's operational lifetime and amplify disturbance torques, particularly for missions operating at low altitudes within the LEO region. Variations in solar flux levels and their effects on the overall design necessitate predicting solar flux levels for the NEBULA-Xplorer Mission.

The solar radio flux at 10.7 cm wavelength is an excellent indicator of solar activity, often called the F10.7 index. The F10.7 correlates well with the sunspot number as well as a number of UV and visible solar irradiance records[99]. ESA predictions of the solar flux levels have been used for orbit predictions and drag modelling of the NEBULA-Xplorer. The graph illustrating the best/worst case predictions for the solar flux is shown in Figure 4.2 and paired with the geomagnetic effect predictions form a baseline for lifetime analysis and drag modeling of the spacecraft. Note that solar activity data is in $10^{-22} W/m^2/Hz$ units (solar flux units, sfu). The table indicating the solar and geomagnetic predictions and the corresponding atmospheric density at noon for the solar minima and maxima for the NEBULA-Xplorer mission are also provided in Table 4.2. This table is generated using a Python program implementing the NRLMSISE-00 model is created that can estimate conservative values for the atmospheric density by using the estimated worst case solar flux and geomagnetic indices. In the table geomagnetic activity is provided using the geomagnetic planetary A-index (A_p). The categorisation of values (>100, 50-99, 30-49, 16-29, 8-15, 0-7) corresponds respectively to Severe-, Major-, Minor storm, Active, unsettled and quiet. This means that no geomagnetic storm is expected during the lifetime of the NEBULA-Xplorer. Lastly, for the solar and geomagnetic predictions, the 50th percentile data has been used in line with the ESA requirement ESSB-ST-U-007-6.2-g. Best and worst case estimates are provided for each day in the dataset and the absolute minimum and maximum values have been chosen for the solar minimum and maximum.

Table 4.2: Atmospheric density values estimated using solar flux and geomagnetic activity predictions of ESA and the NRLMSISE-00 atmosphere model.

Date	Solar Flux (F10.7)	Geomagnetic Activity (Ap)	Atmospheric Density at 475 km	Atmospheric Density at 550 km
Nov/2030 (Solar minimum)	67 – Min estimate	5 – Min estimate	$\rho = 2.83 \times 10^{-13}$ (kg/m^3)	$\rho = 7.01 \times 10^{-14}$ (kg/m^3)
Mar/2034 (Solar maximum)	261 – Max estimate	17 – Max estimate	$\rho = 8.28 \times 10^{-12}$ (kg/m^3)	$\rho = 3.51 \times 10^{-12}$ (kg/m^3)

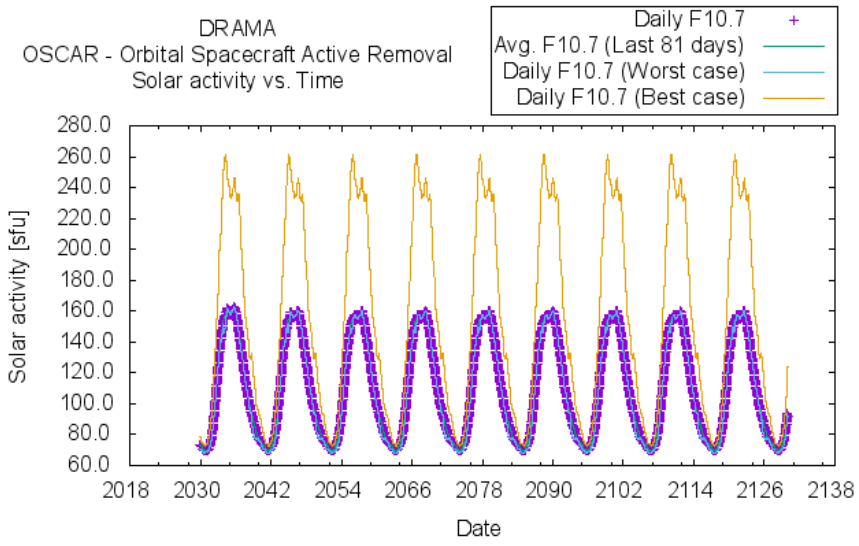

Figure 4.2: Solar flux predictions from the ESA Database obtained on 01/01/2026.

4.4.3. South Atlantic Anomaly and the Polar Radiation Zones

The SAA is a region of weakened Earth's magnetic field that allows energetic charged particles to penetrate to lower altitudes than elsewhere. As a result, passages through the SAA expose LEO satellites to elevated levels of ionising radiation and charged particle flux - protons, electrons, and ions. If a spacecraft and its components are not radiation-hardened or adequately shielded, the radiation effects discussed in Section 4.2 may occur, leading to degradation or failure of onboard systems and, in extreme cases, total mission failure. The primary concern within the SAA is the presence of high-energy protons, which are particularly difficult to shield against.

In addition to the SAA, spacecraft operating in LEO are also exposed to enhanced radiation levels in the polar radiation zones. Near the polar regions, Earth's magnetic field lines are open, allowing energetic charged particles from the solar wind and magnetosphere to precipitate into the upper atmosphere. As a result, satellites in high-latitude or polar orbits experience increased fluxes of energetic electrons. Even though the mission's inclination is 45°, the magnetic and geographic poles do not coincide, and the spacecraft scrapes the polar radiation zones where electron flux is increased.

The SAA is a critical zone for the NEBULA-Xplorer mission where the radiation levels will be among the highest. To mitigate the risk of SEEs, the spacecraft will be completely turned off through SAA passages, and therefore it is important to define a boundary for this region. The increased flux of trapped protons and electrons is mapped using ESA's Space Environment Information System (SPENVIS) tool. To obtain a conservative estimate of the maximum charged-particle flux, the AP-8 proton model is used at solar minimum because, at solar maximum, the increase in atmospheric density means fewer protons reach lower altitudes. For the trapped electrons, the AE-8 electron model is also used at solar maximum, as this gives the maximum flux. The flux graphs at 550 km for trapped protons and electrons with different particle energy thresholds are shown in Figure 4.3. Radiation levels decrease with altitude, but only the case for maximum flux levels is shown in the graphs, since the spacecraft will spend the most time near this altitude.

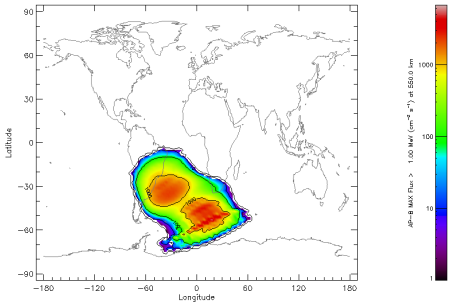

(a) Trapped proton flux in SAA for particle energy higher than 1 MeV

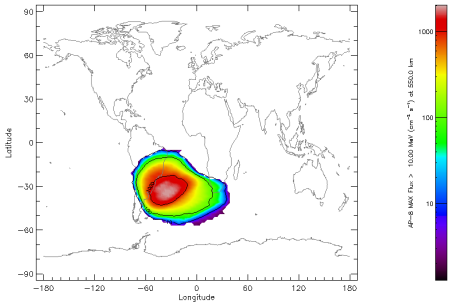

(b) Trapped proton flux in SAA for particle energy higher than 10 MeV

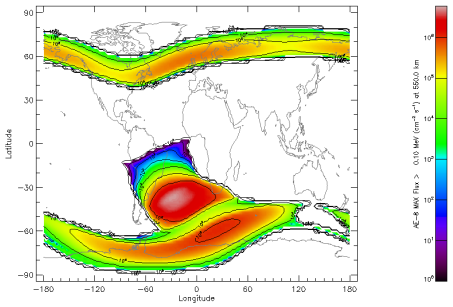

(c) Trapped electron flux for particle energy higher than 100 keV

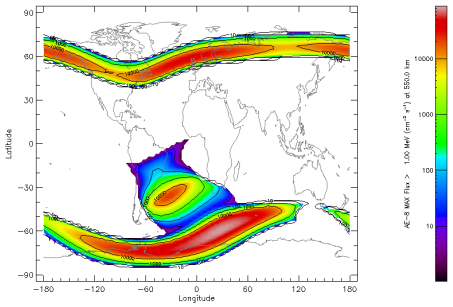

(d) Trapped electron flux for particle energy higher than 1 MeV

Figure 4.3: Trapped particle fluxes in LEO for the SAA and polar radiation zones. The top row corresponds to trapped proton flux, and the bottom row corresponds to trapped electron flux.

4.5. Debris Environment

Orbital debris is any non-operational object in space. These include fragments from earlier missions, such as paint flakes and broken components, launch vehicle bodies, and non-operational satellites. There is also the flux of meteoroids and other active spacecraft that need to be avoided. The average relative velocity in LEO between orbital objects is 9-10 km/s with maximum values above 14 km/s [137]. This means that even an object with a few centimetres in diameter can have catastrophic effects on the spacecraft's subsystems. For instance, using the equation for kinetic energy - $E_k = \frac{1}{2}mv^2$ - with a velocity of 10 km/s and mass of 100 g, the total kinetic energy of the object is 5 MJ. In comparison, 1 kg of TNT approximately releases 4.184 MJ of energy.

It is very likely for a spacecraft to encounter micrometeoroids and orbital debris during its lifetime, especially for the given altitude range of the NEBULA-Xplorer mission. It is also important to quantify this risk and discuss the protection methods. There are two main methods to prevent this debris. Passive protection, where shielding and redundancy or minimising collision cross-sectional area can be included in the design, and/or active protection by performing collision avoidance manoeuvres. The ECSS requirements are an important guideline for setting risk thresholds and determining which method(s) to use for the mission. The associated risk profile of collision avoidance is explained in more detail in Chapter 17.

As a result of the SDMF, the spatial density of debris larger than 1 cm and in the 1 mm - 1 cm range is of particular importance. This directly influences the collision risk and avoidance strategies and is an essential factor of the Delta V budget. As previously explained, this also influenced the mission's orbit selection. The average spatial density graphs for the defined orbital regime are presented for the time frame of November 2030 to November 2036 and for declinations between -60 and 60 degrees, as this area also encompasses the operational inclination of 45° for comparison. The time frame is limited to the given bounds because the future population data is annual and does not extend beyond 2036. The spatial density graphs are generated using ESA's MASTER software and are displayed in Figure 4.4.

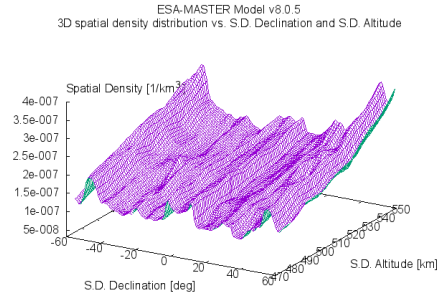

(a) Spatial Density Distribution of objects with diameter > 1 cm for Nov/2030-Nov/2036 using the 2016 FUTURE MASTER DATASET.

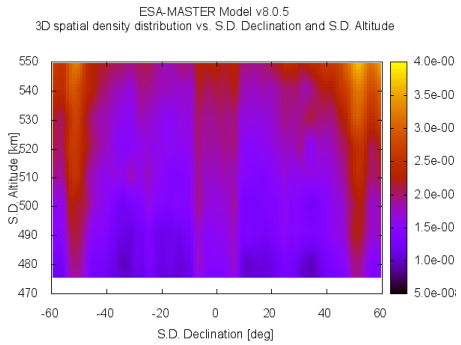

(b) Spatial Density Heat map of objects with diameter > 1 cm for Nov/2030-Nov/2036 using the 2016 FUTURE MASTER DATASET.

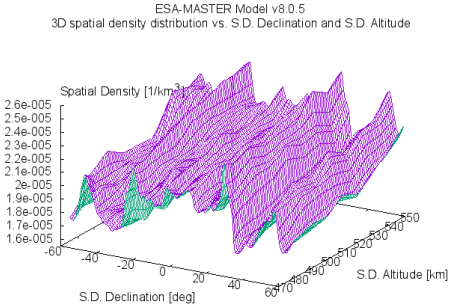

(c) Spatial Density Distribution of objects with diameter 1 mm - 1 cm for Nov/2030-Nov/2036 using the 2016 FUTURE MASTER DATASET.

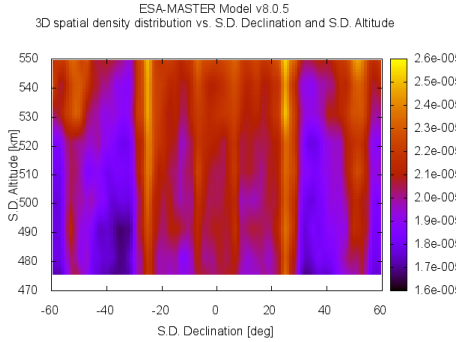

(d) Spatial Density Heat map of objects with diameter 1 mm - 1 cm for Nov/2030-Nov/2036 using the 2016 FUTURE MASTER DATASET.

Figure 4.4: Spatial Density of objects with diameter 1 mm - 1 cm, and > 1 cm for Nov/2030-Nov/2036 using the 2016 FUTURE MASTER DATASET.

4.5.1. Debris Population Validation

The SDMF require the usage of the latest available calibration epoch for the simulations. Unfortunately, at the time of analysis, the only available future debris population is the November 2016 epoch. The more recent August 2024 epoch, at the time of writing, has not yet been published with future population data. It is recommended that, once the Future Debris Population Data is made publicly available, the related simulations be updated accordingly. Although the MASTER tool is validated by ESA, the population datasets are relatively old and may not be representative of the orbital regime of the NEBULA-Xplorer mission. Therefore, an assessment of the orbital regime using the most recent data (August 2024 - Historic Dataset) has been decided upon before implementing the spatial density and flux of these objects in the risk and ΔV analyses.

Although the future dataset shows a clear upward trend overall, compared with the 2024 data, there is a discrepancy specifically at the operational regime of the NEBULA-Xplorer. This is the result of unforeseen fragmentation events, such as the Cosmos-1408, and the deployment of the Starlink Constellation at an altitude of around 550 km. There are currently more than 9,000 Starlink satellites in orbit, with about 4,400 in this region [121]. The number of satellites is planned to be increased to 12,000 [113]. SpaceX has stated its interest in increasing this number to 42,000 in the long term. The orbital altitude of the satellites in the 550 km region is planned to be lowered to 480 km in the future[121], but this remains within the orbital regime of the NEBULA-Xplorer. With the expectation of growth in the-Starlink network, and even the current estimates surpassing the predictions made using the MASTER population data. It is decided that, until a new dataset is published, the results for object flux cannot be used for risk analysis and collision avoidance strategies, as they will be significantly underestimated. For comparison, the average spatial density values for the 1 mm - 1 cm and > 1 cm range are provided for the operation altitude envelope of [475, 550 km] and inclinations of 45 and 60 degrees in Table 4.3. The population of objects that could have catastrophic consequences for the mission in case of collision is smaller for the 45° inclination orbit.

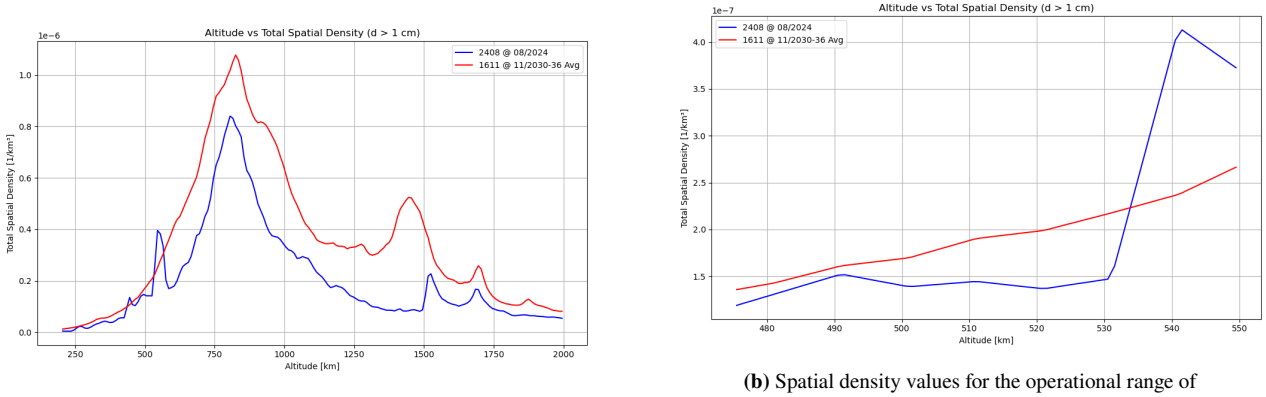

(a) Spatial density values for LEO.

(b) Spatial density values for the operational range of NEBULA-Xplorer.

Figure 4.5: Comparison of spatial density values for objects larger than 1 cm, derived from the updated MASTER historic population (August 2024) and the legacy MASTER future population (averaged over 2030–2036).

Table 4.3: Comparison of the average spatial density values in $\mathbf{km}^{-3}$ for the altitude envelope of 475–550 km, using historic (08/2024) and future MASTER population data (2030–2036 average).

Inclination	**08/2024 (1 mm–1 cm)**	**08/2024 (>1 cm)**	**2030–2036 Avg (1 mm–1 cm)**	**2030–2036 Avg (>1 cm)**
45°	1.804×10^{-5}	1.716×10^{-7}	2.053×10^{-5}	1.623×10^{-7}
60°	1.831×10^{-5}	1.909×10^{-7}	2.052×10^{-5}	1.730×10^{-7}

4.6. Orbital Trajectory and Lifetime Analysis

The mission's lifetime must be analysed to verify that the spacecraft meets both the mission lifetime and the 5-year de-orbiting requirements. To perform this assessment, the launch epoch and key aerodynamic parameters affecting orbital decay must first be defined. A 2030 mission start date was stated in the requirements. The launch date affects orbital lifetime due to variations in solar activity, as changes in solar flux influence atmospheric density and, in turn, drag. In this analysis, November 2030 is selected as the design launch date. This date meets the 2030 requirement and represents a conservative choice for lifetime prediction, as launches earlier in the year yield longer predicted lifetimes. In addition, future population data snapshots were originally available only at November epochs, making a November launch preferable when selecting consistent dataset inputs. Although these population data were later deemed unrepresentative, the November epoch was retained as the design case, since shifting the launch date to December had only a minimal effect on the predicted lifetime. The main design parameter influencing lifetime is the ballistic coefficient, defined as:

$$\beta = \frac{m}{A_{eff} C_D} \tag{4.2}$$

where m is the spacecraft's mass, A is the effective area, and C_D is the drag coefficient. The C_D is 2.2 on average for box-shaped satellites[137]. The spacecraft's mass is obtained from the mass budget in Section 15.3. The effective area represents the projected surface area normal to the incoming flow and is therefore highly dependent on spacecraft attitude. Since the precise operational attitude profile can not be fixed at this design phase, an average projected area is adopted for the design case. Determining the average projected area of the spacecraft requires calculating its cross-sectional area at different attitudes. For this purpose, a 3D model of the spacecraft is created using ESA's CROC tool, and the average deployed cross-sectional area is calculated by simulating the spacecraft's attitude at all possible orientations.

In addition to the design parameters, the orbital lifetime is strongly influenced by environmental variability, primarily changes in solar flux and geomagnetic activity. Increased solar activity enhances atmospheric heating, increasing atmospheric density and, in turn, drag. Similarly, geomagnetic storms can cause short-term density enhancements that increase orbital decay rates.

Table 4.4: Effect of shifting the launch date on the free-drift lifetime of the satellite from a quasi-circular initial orbit at 550 km altitude and 45 degrees inclination.

Mass (kg)	Area (m^2)	C_D	Altitude (km)	Eccentricity	Inclination	**Begin Date**	Ballistic Coefficient	**De-Orbit Pred**	**Lifetime with +5% Margin**
323.5	3.62	2.2	550	1.00×10^{-4}	45°	01/01/2030	40.62	**19/06/2036**	**6.79 yrs**
323.5	3.62	2.2	550	1.00×10^{-4}	45°	01/11/2030	40.62	**26/07/2036**	**6.02 yrs**
323.5	3.62	2.2	550	1.00×10^{-4}	45°	01/12/2030	40.62	**30/07/2036**	**5.94 yrs**

Lifetime simulations are performed using ESA DRAMA's OSCAR tool, applying the latest available prediction settings and solar/geomagnetic input datasets from 01/01/2026. Validation studies of OSCAR indicate that it underestimates orbital lifetime by approximately 10% on average[23], therefore providing a conservative basis for satisfying the mission lifetime requirements Furthermore, an example for the effects of shifting the launch date is provided in Table 4.4. This table confirms that for an earlier launch date in 2030, the lifetime increases, but for a later launch date, it decreases.

Sensitivity Analysis

Due to the changing design in Phase 0, the results of the lifetime simulations are presented as a sensitivity study. This includes variations in spacecraft mass, effective area, drag coefficient, and environmental conditions with the trend shown in Figure 4.6. The detailed list of the different cases considered can be found in Table 4.5. The lifetime for the design case is the last entry in the table, with the average cross-sectional area as the effective area. For the post-mission disposal phase, de-orbiting is expected to occur under higher drag conditions if the spacecraft presents a larger cross-sectional area to the flow. However, to remain conservative, a random tumbling scenario using the average projected area is also evaluated to confirm compliance with the 5-year de-orbiting requirement.

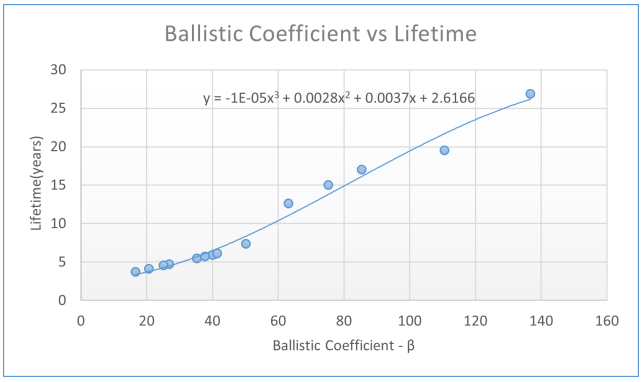

Figure 4.6: Ballistic Coefficient vs Lifetime graphs for November 2030 epoch starting from an initial altitude of 550km at an inclination of 45 degrees.

Table 4.5: Lifetimes for different ballistic coefficients for the same initial orbit of 550 km, 45° inclination, 1×10^{-4} eccentricity, and 01/11/2030 begin date.

CASE	**Mass (kg)**	**Area (m^2)**	**C_D**	**Ballistic Coefficient**	**De-orbit Date**	**Lifetime (yrs) with +5% Margin**
A_av, M_ite4	323.5	3.62	2.2	40.62	26/07/2036	6.02
A_min, A_y, M_ite4	323.5	1.33	2.2	110.56	29/05/2049	19.50
A_max, M_ite4	323.5	5.47	2.2	26.88	25/04/2035	4.70
A_x, M_ite4	323.5	4.17	2.2	35.26	20/01/2036	5.48
A_z, M_ite4	323.5	3.67	2.2	40.07	30/06/2036	5.94
M_max, A_av	400	3.62	2.2	50.23	05/11/2037	7.36
M_min, A_av	200	3.62	2.2	25.11	04/03/2035	4.55
M_min, A_max	200	5.47	2.2	16.62	18/05/2034	3.72

Continued on next page

CASE	Mass (kg)	Area (m^2)	C_D	Ballistic Coefficient	De-orbit Date	Lifetime (yrs) with +5% Margin
M_max, A_min	400	1.33	2.2	136.71	29/05/2056	26.85
M_c, A_av	300	3.62	2.2	37.67	07/04/2036	5.70
M_c,A_av, C_D_max	300	3.62	4.0	20.72	14/10/2034	4.15
M_c, A_av, C_D_min	300	3.62	2.0	41.44	31/08/2036	6.12
M_rand, A_min	250	1.33	2.2	85.44	11/01/2047	17.00
M_min, A_min, C_D_min	200	1.33	2.0	75.19	21/02/2045	15.02
M_rand, A_rand	250	1.80	2.2	63.13	04/11/2042	12.61
Design	**310**	**3.62**	**2.2**	**38.93**	**24/06/2036**	**5.93**

4.7. Delta V Budget

ΔV budgeting is an integral part of the spacecraft design, requiring detailed analysis and conservative estimates. A representative ΔV budget is essential to satisfy mission requirements and ensure that the spacecraft can deliver the necessary velocity increments to perform collision-avoidance manoeuvres, satisfy regulations such as the 5-year de-orbiting requirement, extend the operational lifetime, or inject the spacecraft into its initial orbit. For the NEBULA-Xplorer, the client specified that there is no need to maintain a constant orbit, and the spacecraft is allowed to drift freely from the orbit in which it is injected. Hence, there is no need to implement any station-keeping ΔV, and instead, a one-time re-boosting strategy will be used within the predefined orbit envelope to ensure a 7-year operational lifetime. Collision avoidance is another major element of the ΔV due to the sharp increase in the number of objects in recent years around the orbit of NEBULA-Xplorer.

4.7.1. Collision Avoidance

Collision avoidance requires probabilistic analysis and represents one of the most complex contributors to the overall ΔV budget. To define a collision-avoidance approach, a suitable manoeuvre strategy must first be adopted. This can either be a short- or long-term strategy, depending on the expected time-to-conjunction with a potential object of interest. In addition, the Accepted Collision Probability Level (ACPL) must be selected, which represents the maximum allowable probability of collision before an avoidance manoeuvre is triggered. Although space debris larger than approximately 10 cm is routinely tracked, the available orbital data remains uncertain, and the exact location of these objects cannot be determined with complete accuracy. Furthermore, there is the possibility of detecting a potential conjunction late. During a discussion with space propulsion expert A.Cervone [26], it was highlighted that it may not be possible to confirm whether a collision will occur until the final orbital revolution. Following the deployment of large mega-constellations such as Starlink and amid increasing uncertainty in the debris environment, it was deemed necessary to adopt a fast, short-term collision-avoidance strategy. This approach reduces the risk of catastrophic collisions, particularly in the densely populated operational environment expected for the NEBULA-Xplorer.

The ESA OSCAR–ARES tool can be used to estimate collision probability, the expected number of conjunctions, and the associated ΔV requirements for a spacecraft in a given orbit using the MASTER population dataset. However, as previously discussed, the MASTER dataset is not representative of NEBULA-Xplorer's orbital regime, and the probability threshold required to guarantee a 90% annual reduction in collision risk cannot be reliably computed. Therefore, an ACPL of 10^{-4} is adopted as a conservative threshold for the regression analysis. ARES is subsequently used in this work to estimate the mean number of required manoeuvres and the associated ΔV for a fast avoidance action initiated within one orbital revolution. Example output from ARES for November 2024 is shown in Figure 4.7, and the same data is generated for a 10-year period (2014-2024), for which historical data exists.

A logarithmic regression model is applied to predict the future evolution of the CAMs. Various regression models have been compared, including exponential and polynomial regression. Even though these models provide a better fit to the historical data for interpolation, their extrapolated projections yield less physically meaningful results, and logarithmic regression was therefore selected. ESA currently performs on average 3–4 CAMs per spacecraft in LEO [51]. When extrapolated to 2037, the exponential regression model yields an unrealistic CAMs frequency of 38.32, whereas the second-order polynomial and logarithmic regressions yield 19.96 and 7.54 manoeuvres, respectively. Considering the population of Starlink satellites described in Section 4.5.1, and taking into account that by the end of 2024 the constellation comprised more than 7,000 satellites [129], a conservative assumption is made that approximately half of this population resides within

the sub 550km altitude band, based on comparison with the population distribution described in Section 4.5.1. Scaling this assumption to the planned constellation size of 12,000 satellites yields an expected population increase factor of 1.71 relative to the 2024 baseline. The estimated number of collision avoidance manoeuvres resulting from simulations for 2024 is 3.32, which, when scaled by this factor under the assumption that the primary driver of CAMs growth is the expansion of the Starlink constellation, results in an expected value of 5.68 manoeuvres per year. The 19.96 manoeuvre frequency is only reasonable if SpaceX can reach their long-term goal of 42,000 satellites until the launch of the Nebula Xplorer, which is unrealistic.

This scaled estimate is closely reflected only by the logarithmic regression model, whereas the exponential and polynomial regressions significantly overpredict future manoeuvre rates. Furthermore, considering that Starlink satellites are themselves capable of performing collision avoidance manoeuvres and that additional uncertainties such as fragmentation events exist, the logarithmic regression model is considered to provide a conservative and physically realistic projection. This evolution also remains consistent with the current ESA record, as an increase in manoeuvre frequency by a factor of five or ten would be difficult to justify without the occurrence of major disruptive events. The predicted number of manoeuvres and the corresponding annual ΔV are presented in Table 4.6.

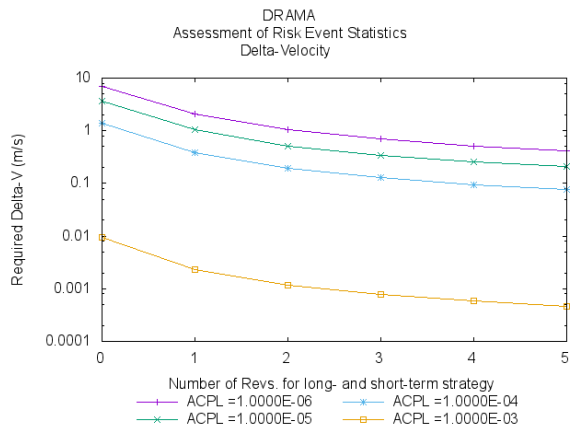

(a) Number of orbital revolutions until conjunction vs required ΔV at different ACPLs for the orbital regime of NEBULA-Xplorer.

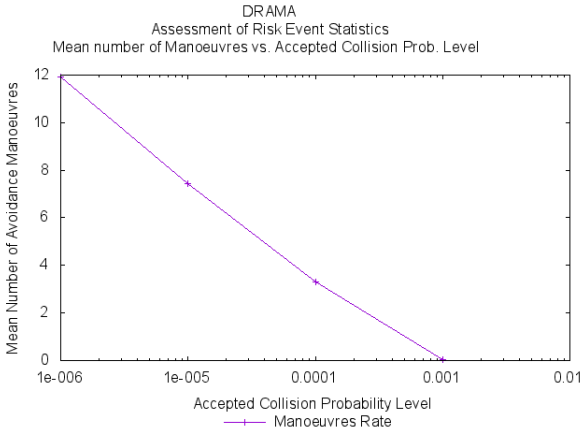

(b) ACPL vs Mean No. of Manoeuvres for the orbital regime of NEBULA-Xplorer at Nov 2024.

Figure 4.7: ARES example output for collision avoidance ΔV and mean number of manoeuvres (at 11/2024) for various ACPLs.

Table 4.6: Predicted number of collision avoidance manoeuvres and total ΔV (2030–2036)

Year	**2030**	**2031**	**2032**	**2033**	**2034**	**2035**	**2036**	**Total**
No. of Manoeuvres	5.07	5.42	5.78	6.13	6.48	6.84	7.19	43.26
Total ΔV [m/s]	1.67	1.79	1.91	2.03	2.15	2.27	2.39	14.21

4.7.2. Orbit Injection

Due to injection uncertainties associated with Vega-C, an additional ΔV margin must be included in the mission budget, as specified in the Vega-C user manual. While the client does not impose strict requirements on inclination, eccentricity, or RAAN injection errors, the possible error in injected altitude is significant (up to ±15 km). This altitude injection error is critical, since deployment below the nominal orbit will result in a reduced orbital lifetime due to increased atmospheric drag, and must therefore be accounted for. Conversely, injection above the target altitude is beneficial, as no orbit-raising manoeuvre would be required and the remaining ΔV margin can be allocated to other mission activities. The worst-case ΔV occurs when the spacecraft is injected into an initial orbit at 535 km altitude. The required ΔV is therefore calculated assuming a Hohmann transfer manoeuvre from 535 km to the nominal operational altitude of 550 km using the equations:

$$\Delta V_1 = \sqrt{\frac{\mu}{r_1}}\left(\sqrt{\frac{2r_2}{r_1 + r_2}} - 1\right) \tag{4.3}$$

$$\Delta V_2 = \sqrt{\frac{\mu}{r_2}}\left(1 - \sqrt{\frac{2r_1}{r_1 + r_2}}\right) \tag{4.4}$$

$$\Delta V_{\text{total}} = \Delta V_1 + \Delta V_2 \tag{4.5}$$

where r_1 and r_2 are the semi-major axes of the initial and final altitude as the orbits are (quasi-)circular. The result is ΔV_{inj} = 8.225 m/s.

4.7.3. Re-Boost and De-orbit

The design case with the mission begin date 01/11/2030 from Table 4.5, is expected to arrive at the lower limit of the altitude envelope around 09/05/2035. Then, with a re-boost up-to 540 km, the spacecraft is expected to lower to 476 km altitude around 01/11/2037. From there, it will de-orbit within 5 years on 26/10/2042. If the maximum cross-sectional area can be turned into the drag on 01/11/2037, which is the expected end-of-mission under a 7-year lifetime goal, then the spacecraft is expected to de-orbit on 28/05/2040, under 3 years. As the time to de-orbit in the random tumbling case is less than 5 years, and this can be further reduced if a maximum drag area is employed after nominal operations, the 5-year de-orbiting requirement will be satisfied. Hence, no Delta V will be included for the de-orbiting. The ΔV for the re-boost can be calculated in the same way for the orbit injection using equations 4.3 - 4.5 and is found to be $\Delta V_{re-boost} = 35.91 m/s$.

4.7.4. Delta V Budget Breakdown

The final Delta V budget breakdown, including a 5% margin [82], is provided in Table 4.7.

Table 4.7: Delta V breakdown of NEBULA-Xplorer.

Type	Collision Avoidance	Orbit Injection	Re-Boost	Total
ΔV [m/s]	14.92	8.64	37.71	**61.27**

4.7.5. Orbit Propagation

The expected orbit propagation of the spacecraft is displayed in Figure 4.8. The orbital decay rate is 16.6 km/year until the re-boost manoeuvre. Then, this is 26.18 km/year for the second phase until the mission end. Finally, for the de-orbiting phase, the decay is 71.68 km/year, corresponding to the spacecraft's average cross-sectional area. The increased decay rate in the second phase is due to higher solar flux, which increases atmospheric density. The dramatic increase in the decay rate during the last phase is mainly due to higher atmospheric density at lower altitudes.

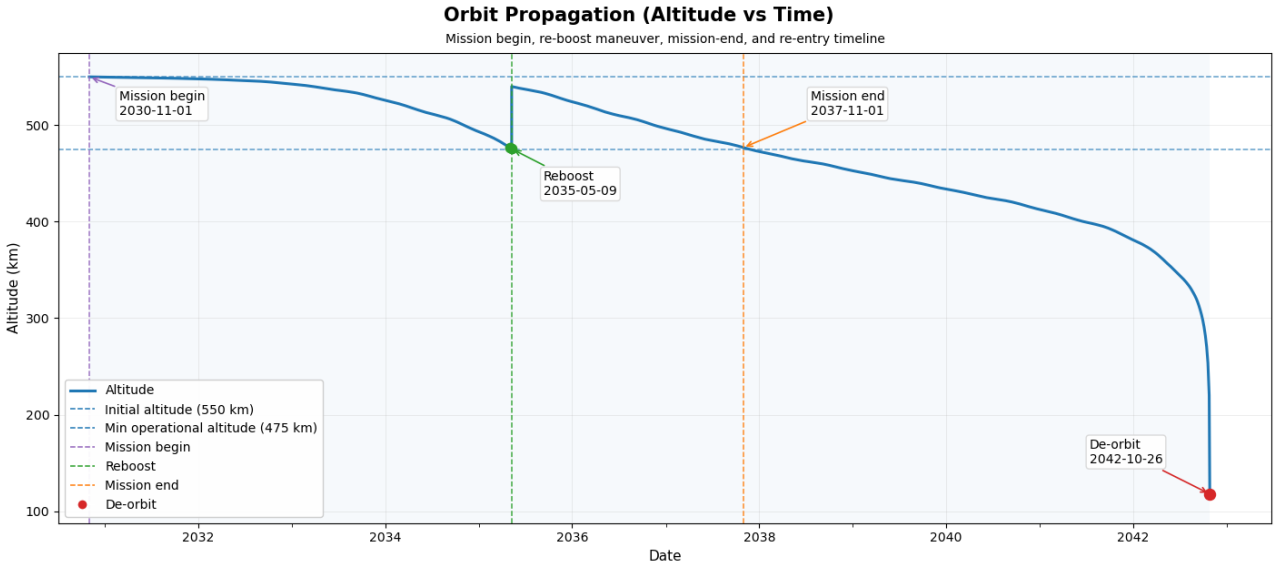

Figure 4.8: Propagated orbit and expected lifetime cycle of the design case for NEBULA-Xplorer with a ballistic coefficient of 38.93.

5
Operations and Logistic Concept Description

The purpose of this chapter is to describe how the NEBULA-Xplorer system operates throughout its entire mission lifetime, from launch to end-of-life disposal. This includes defining the mission phases and the associated spacecraft functions. Since not all subsystems are required in every phase and many functions repeat throughout the mission lifetime, spacecraft functionality is organised into operational modes, each defining which subsystems are active for a specific operational purpose and enabling power-efficient and safe operations. The chapter also explains how the spacecraft interacts with the ground segment and how the mission fits within Leaf Space's existing operational infrastructure. Together, these elements form the Operations and Logistic Concept Description, providing a high-level operational analysis that links the mission architecture, spacecraft behaviour, and supporting ground systems.

5.1. Mission Architecture

The NEBULA-Xplorer mission architecture is organised around three segments: the space segment, the launch segment, and the ground segment. The space segment comprises the spacecraft bus and the X-ray payload, supported by the core subsystems required for orbital operation. A propulsion subsystem is included to enable collision avoidance manoeuvres, the single planned re-boost, and the end-of-life disposal sequence. The launch segment provides orbital insertion using Vega-C. The ground segment comprises ground stations, mission operations, and end users of the science data. It provides the command-and-control loop throughout the mission, including routine commanding and health monitoring. These mission segments are displayed together with details in Figure 5.1.

This architectural overview clarifies the key operational links and the subsystem dependencies that must be supported throughout the mission. Based on these segment interfaces and operational dependencies, the mission can now be described as an operational progression from launch through end-of-life, structured into mission phases.

5.2. Mission Phases Overview

This section describes the mission's operational progression by defining the mission phases, the main functions associated with each phase, and the interactions among the ground, launch, and space segments. These mission phases collectively form the high-level Concept of Operations (ConOps), outlining how the spacecraft is intended to operate from launch until EOL. Following the ConOps framework defined in the JIP [22], the mission is divided into five phases: LEOP, Commissioning, Nominal Operations, Extended Life and Decommissioning.

LEOP is the critical initial phase focused on spacecraft survival and basic functionality, in which the spacecraft stabilises its attitude, becomes power-positive, and establishes first contact with the ground. Operationally, this phase involves continuous ground-station support and initial orbit determination. It takes place during the first five days after launch.

Commissioning is a longer activation and verification phase focused on calibration and validation after the spacecraft has reached a stable, safe state. During this phase, subsystems are brought to full operational configuration, functional tests are performed, and software updates may be uploaded. The X-ray instruments are then enabled and calibrated for scientific use, supported by repeated health checks and dedicated ground operations including multiple uplinks to configure subsystems, retrieve housekeeping data and validate payload performance. This phase is expected to take up to 30 days.

Nominal operations account for the primary five-year science mission. In this period, long, uninterrupted observations are conducted. Science data is collected, stored and downlinked during visibility windows with Leaf Space ground stations. Orbit determination and maintenance manoeuvres are performed, the spacecraft switches modes every orbit, for example, to radiation protection mode during South Atlantic Anomaly crossings and mission planning activities occur on a regular basis.

Extended life, if resources allow, provides up to two additional years of reduced-intensity science operations. During this phase, science observations continue but with a lower duty cycle, fewer downlink passes and reduced operator workload. The ground segment supports a simplified operations scheme aimed at maximising remaining science return while preserving system health.

Decommissioning marks the end of the mission and involves passivating all subsystems and executing the controlled de-orbit to meet debris-mitigation requirements. Operational activities include planning and executing the de-orbit manoeuvre. The ground segment closes operations and collects all mission data.

These five phases form the operational framework of the mission and define when key spacecraft activities and ground-segment interactions take place. Figure 5.2 provides a visual overview of how the phases follow one another along the spacecraft's orbital lifetime. The strategy of doing a single re-boost at 475 km and using no propellant for de-orbiting has been explained in Section 4.7.3.

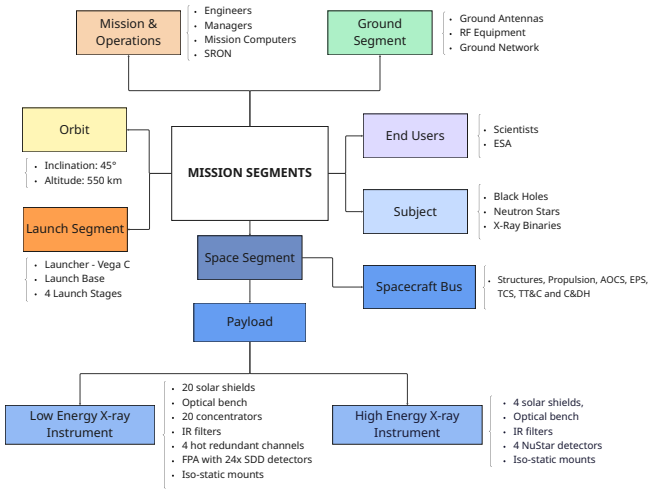

Figure 5.1: Mission Architecture

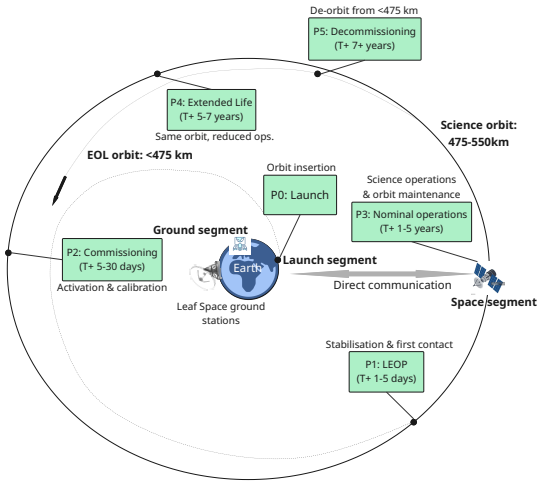

Figure 5.2: Visualisation of the mission phases.

5.3. Modes of Operation

For the spacecraft to perform its mission, not all subsystems need to be active during all mission phases. The spacecraft cannot begin observing science targets immediately after launch vehicle separation during the LEOP phase. Instead, initial operations are dedicated to sun acquisition, solar panel deployment, and establishing contact with the ground segment. During this phase, the spacecraft executes a limited set of essential functions. Activating additional functionality, such as enabling the payloads, would provide no operational benefits and increase the power budget. Functionality, however, is not only related to mission phases as phases follow each other sequentially, but also during the entire mission lifetime, as the need for a function is repeated. Therefore, the spacecraft's functionalities will be separated into operational modes. This is further explained in Section 14.4.

5.4. Ground Segment Operations & Logistics

Leaf Space has been selected as the mission's ground station network. This choice is recommended in the ConOps report cite ConOps, and Chapter 12 presents an analysis of its compatibility with the mission requirements.

For the selected mission orbit at an altitude between 475 km and 550 km and an inclination of 45°, the ground contact characteristics were analysed using the General Mission Analysis Tool (GMAT). 9 suitable ground stations of the Leaf Space network are used. Using the network and assuming a minimum elevation angle of 5°, an average contact duration of 7.74 minutes per pass is achieved. To support the downlink of HKTM and payload data, as well as the uplink of Telecommands (TC), a minimum of 12 ground contacts per day is required. This corresponds to an average of 0.8 contacts per orbit, assuming an orbital period of 95.6 minutes (approximately 15 orbits per day).

Spacecraft operations are coordinated through a Mission Operations Centre (MOC) and a Science Operations Centre (SOC). The MOC is responsible for spacecraft health and safety, commanding, and advising the SOC if the primary target is a smart one. Additionally, it's responsible for the data pipelines to the SOC. The SOC is responsible for providing the MOC with a primary target and secondary targets, and for deciding when the target should change. This decision-making process relies on a daily review of downlinked data. Both operation centres are located at SRON and will be in direct contact with each other. A detailed description of data handling and the end-to-end data pipeline from the spacecraft to mission stakeholders and the scientific community is provided in the ConOps document [22].

Leaf Space offers two options for contact scheduling: an automatic scheduler and on-demand booking. The automatic scheduler uses mission constraints to autonomously select suitable contact windows. On-demand booking allows operators to retrieve a list of available passes for the next 3 days and manually select the desired contacts. In the event of anomalies, additional contacts can be scheduled using this feature, which is particularly relevant during LEOP, when the likelihood of early anomalies is highest. Additional information on contact planning and scheduling is provided in the ConOps report [22].

During LEOP, high-frequency contacts are typically required to rapidly establish communication and verify spacecraft health. Leaf Space guarantees continuous on-deck support during the first 48 hours after separation, with their support team available throughout this period via the Leaf Space Support Platform.

6
Design Process

This chapter summarises the process during the preliminary design phase and how it leads to the final design.

6.1. Design Iterations

For this project, an iterative design process was used. This process was initiated by first outlining many possible design options on a subsystem level. These options were first evaluated individually, and some were eliminated immediately due to their poor fit to the mission (i.e. nuclear-based concepts). Early filtering is justified when alternatives fail to meet mission requirements, operational constraints, or practical programmatic considerations. The remaining design options were combined into multiple realistic system-level options, which are evaluated using the trade matrix. The design process aims to narrow down the options. This was performed iteratively as subsystem sizing matured. Early iterations used conservative, first-order estimations to narrow down the options. Later iterations used refined values and updated criteria, such as the science observation time, as the mission understanding improved. Figure 6.1 is an example of the trade matrix, where each criterion can be traced to a key requirement, which can be found in Table 3.1.

Iteration 3	Requirement	REQ-LAUN-C-MIS001-011	REQ-SYS-O-MIS011-016	REQ-SYS-F-MIS007-009	REQ-MIS-C-005	REQ-MIS-F-007
System option	Option Description	Mass (kg)	Volume (m3)	Power (W)	Cost (€)	Observation Time (% per orbit)
3	EPS	65.570	0.078		771440.000	Typical orbit: 75% ; Comms orbit: 59%
	AOCS 1	11.860	0.055	43.000	410000.000	
	TT&C 3	1.145	0.015	24.200	66000.000	
	PROP 2	38.700	0.176	80.000	600000.000	
	TCS 2	5.100	0.022	12.000	50000.000	
	C&DH 1	1.400	0.001	40.000	250000.000	
	STUC 1	84.400	-	-		
	PLD	90.000	0.581	330.000		
	Total	298.175	1.114	425.000	2147440.000	
6	EPS	67.530	0.078		771440	Typical orbit: 75% ; Comms orbit: 59%
	AOCS 2	15.880	0.008	56.000	520000.000	
	TT&C 5	1.701	0.001	24.200	100000.000	
	PROP 2	38.700	0.176	80.000	600000.000	
	TCS 2	5.100	0.022	12.000	50000.000	
	C&DH 1	1.400	0.001	40.000	250000.000	
	STUC 1	84.400	-	-		
	PLD	90.000	0.581	330.000		
	Total	304.711	1.040	438.000	2291440.000	

Figure 6.1: Part of the system level trade matrix showing options 3 and 6.

6.2. Trade-Off

A weighted trade-off was performed on the final three system-level options, which remained after the iterative design process. To score the options consistently, 7 trade-criteria are defined. These are mass, volume, power, cost, observation time, reliability, and complexity. The weights are shown in Figure 6.2. Reliability and complexity are assessed qualitatively. Along with these criteria, TRL is tracked as an iteration characteristic, but not directly weighted to avoid overconfidence in early TRL estimations. The chosen baseline design (option 6) performed the best overall, as can be seen in Figure 6.2. Each option is scored on a 4-point scale and multiplied by the weight of the criterion. The scores are, however, closely matched, and a sensitivity analysis is conducted in Section 6.3 to determine the robustness of the design choice.

	Mass 20/100	Volume 10/100	Power consumption 15/100	Cost 5/100	Science time 25/10	Reliablility 15/100	Complexity 10/100	Score
Option 3	317.19	0.959	425	2665442	73.93%	Unacceptable	Excellent	3.20
Option 6	299.1984	0.960	438	2893104	73.93%	Excellent	Excellent	3.25
Option 8	328.6508	0.951	474	2856384	75%	Excellent	Complient	3.05

Unacceptable	1
Complient	2
Good	3
Excellent	4

Figure 6.2: Final system level trade-off

6.3. Trade-Off Sensitivity Analysis

In order to assess the robustness of the trade-off, a sensitivity analysis was performed by evaluating how changes in the trade-off criteria and their corresponding weights influence the selected system-level option. By varying the weights, the analysis evaluated how stable the final decision is under assumptions and different stakeholder priorities.

The first approach removed one criterion at a time while redistributing its weight among the remaining criteria, keeping the total weight constant. This approach showed that Option 6 is generally the preferred option, except for when reliability is excluded; in this case, Option 3 was the winner. This therefore highlights reliability as a key differentiator between the two options and also the stakeholder's preference for high-TRL, reliable technology. The second approach, a Monte Carlo weight sampling analysis, also supported this finding. In this analysis, Option 3 was selected 50% of the cases, while Option 6 was crowned the winner in around 30%, mostly when reliability was heavily weighted. This confirms the strong influence of stakeholder emphasis on reliability.

6.4. Reliability and Redundancy Philosophy

This section aims to describe the reliability considerations used in the design of the NEBULA-Xplorer. It goes over how mission lifetime and environment contributed to the allocation of different redundancies.

6.4.1. Reliability as a Design Driver

Redundancy is introduced to prevent mission failure in the presence of component faults. The decision to implement redundancy is driven by both the severity of a potential failure and its likelihood of occurrence. Components with a high probability of failure or a high impact on mission success are therefore prioritised for redundancy, while low-risk components may remain non-redundant. Spacecraft components cannot be repaired or replaced, which results in the need for a very high reliability. Before a description of how reliability will be achieved for the NEBULA-Xplorer mission, it is important to note what reliability implies. According to SMAD [137], a distinction can be made between basic reliability and mission reliability. Basic reliability is described by "the probability that a device will function without failure over a specified time period or amount of usage". When this is changed to "without failure that impairs the mission", it defines mission reliability, which is the more relevant topic for designing a space mission. As described by this definition, the specified time period and operational conditions are key parameters in defining reliability. For a spacecraft, these parameters are directly driven by mission requirements, including mission lifetime and operational environment. In the case of the NEBULA-Xplorer mission, the need for reliability, its required type and level of redundancy are mostly driven by the mission lifetime requirement and the selected operational orbit, as defined by requirements REQ-MIS-O-003 and REQ-MIS-C-002:

REQ-MIS-O-003

The requirement REQ-MIS-O-003 states that the "nominal mission lifetime shall have a duration of at least 5 years". It clearly states the lifetime of the spacecraft that should be designed for. To illustrate the role of reliability in achieving this designed for lifetime, Figure 6.3, depicting the design life and its relation to reliability, is shown.

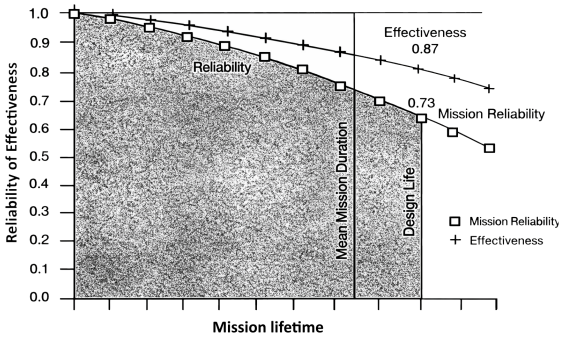

Figure 6.3: Frequently Used Reliability Concepts, from SMAD[137], page 767. Illustrating the mission reliability curve

Figure 6.3 can be used to indicate the effect of mission reliability on design life. It can be seen that a longer mission is deemed to have a lower reliability. The mission reliability calculated at the design life is lower than 1.0. Therefore, the expected life will be lower than the design life. This is often called the Mean Mission Duration (MMD) and can be calculated according to Equation 6.1:

$$MMD = \int_0^{T_d} T dR \tag{6.1}$$

Here, T is a horizontal time line, and dR is the associated increment in reliability. The integral is taken from 0 to T_d to calculate the MMD for a certain design life. From this, it can be concluded that for a more reliable design, the MMD lies closer to the design life. Reliability is therefore a key driver for compliance with REQ-MIS-O-003. Additionally, the five years life time requirement classifies the mission as an ESA class III mission, as earlier stated in Section 3.1. This classification imposes specific expectations regarding acceptable risk, qualification philosophy and system robustness.

REQ-MIS-C-002
REQ-MIS-C-002 states: "The science operations orbit shall be a quasi-circular Low Earth Orbit (LEO) with an initial altitude of 550 km and an inclination between 45 and 60 degrees". The selected science orbit, defined in REQ-MIS-C-002, introduces a LEO environment characterised by radiation exposure, thermal cycling, eclipse periods, and atmospheric drag effects. All these factors drive the type and level of reliability measures to be taken. Specific environmental factors increase the likelihood of certain types of failures occurring. As such, these act as a tool for implementing the appropriate redundancy measures for the specific mission.

6.4.2. Quantifying Reliability

The quantification of reliability can be achieved by assessing the probability that an item will operate without failure during a specified time period. Through this method, the reliability can be calculated with the equation below [137]:

$$R = e^{-\lambda t} \tag{6.2}$$

In Equation 6.2, λ denotes the item failure rate and t the time period the item is used for. In Equation 6.2, only two outcomes are taken into account: success and failure. To extend Equation 6.2 to a spacecraft made out of n non-redundant components, the probabilities of operating without failure of the components are multiplied according to Equation 6.3 below:

$$R_s = \prod_{i=1}^{n} R_i = e^{-\Sigma \lambda_i t} \tag{6.3}$$

Here, R_s is the series reliability where R_i and λ_i are the component reliability and failure rates, respectively. From Equation 6.2 it can be concluded that the reliability of a component can have a maximum theoretical value of 1.0. This would mean that either the time a component is used or the failure rate has to be equal to zero. Combining this result with Equation 6.3, it can be concluded that an increase in the number of components

in series makes for a less reliable system. As mentioned in Section 6.4.1, there is a distinction between basic reliability and mission reliability, which means that a spacecraft component can fail without mission failure. Therefore, a series reliability value of all components of a spacecraft would not result in the mission reliability. To include this parallelism into the calculation, Equation 6.4 can be used.

$$R_p = 1 - \prod_{i=1}^{n} (1 - R_i) \tag{6.4}$$

Where R_p is the reliability of n components or systems arranged in parallel. Reliability can be further increased by adding components or subsystems in parallel that share a function or a part of a function within the system. This ensures that the functionalities of these components can be kept after failure of one or more components. The addition of such parallel elements is known as redundancy. There are several types of redundancies in a system that have a different impact on the overall redundancy. Looking at Figure 6.4, four different models of redundancy implementations can be seen combined with their impact on reliability.

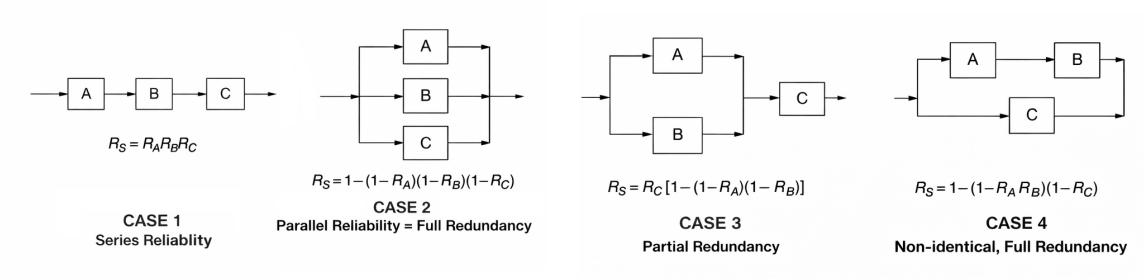

Figure 6.4: Different models for system reliability by combining components or subsystems in series or parallel [137]

The redundancy cases described in Figure 6.4 can be seen as the spacecraft or system. Each block could either be a subsystem or a component fulfilling a function for the mission. For each redundancy case, it could be assessed what the impact of the structure is on the reliability and what would happen if one of the components or subsystems in the diagram fails.

- **Case 1 – Series system**:The system reliability is the product of the individual reliabilities.
- **Case 2 – Fully redundant (parallel) system:**:Failure of one block does not result in mission failure, reliability increases with redundancy.
- **Case 3 – Partially redundant system:** Redundancy of A/B improves reliability, C is sill in series. Reliability is a combination of series and parallel components.
- **Case 4 - Alternative fully redundant system:**: Subsystem C must remain functional when either A or B fails. Again reliability is a combination of series and parallel components.

While exact reliability values cannot yet be quantified since failure rates of components are unknown, the analytical comparison of series and parallel architectures demonstrates that redundancy structurally increases system reliability.

6.4.3. Redundancy Implementation Techniques

Building on the reliability models introduced in the previous section, this section discusses how redundancy is realised in spacecraft system design. According to the ECSS-S-ST-00-01C glossary[34], redundancy is defined as 'The existence of more than one means for performing a given function with the intention of increasing reliability.' This definition provides the framework within which the redundancy techniques described in the following subsections are classified.

Same Design Redundancy

A common approach to achieving a more reliable system is the addition of identical components that perform the same function as illustrated before in Case 2 in Figure 6.4. An example of this is the addition of a fourth reaction wheel, where only three reaction wheels are required to achieve 3-axis control. The fourth wheel is

added to ensure attitude control in the event that one of the wheels fails. This way, an AOCS failure is prevented, which in turn prevents mission failure. The same design redundancy offers good protection against random failures and does not rely on a knowledge of failure modes for the subsystem [137]. It is however, limited against design deficiencies such as improper lubricant selections for the bearings or a wrong controller design. If one of the wheels fails due to such deficiencies, it is likely that the other wheels will also fail shortly after. Another disadvantage of this approach is that it comes with added costs. Besides the actual cost in money, the extra components add weight, take up volume and consume power depending on how it is operated.

Diverse Design Redundancy

A diverse design redundancy is the implementation of two or more different components that both realise the same function. For example, multiple dissimilar sensors can be used to obtain attitude determination for a spacecraft. Star trackers could be the primary attitude sensors because of their high accuracy. However, sun sensors and magnetometers (in LEO) can also achieve the same functionality with lower performance [78]. Including the sun sensors and magnetometers in parallel with the star trackers can thus serve as a backup option in the event that the star trackers fail. This makes the design less susceptible to common mode failures such as blinding of a star tracker or algorithmic errors affecting a specific sensor type. In other words, the advantage of this redundancy technique is that it reduces the probability that the same fault mechanism affects all redundant elements and mitigates systematic design errors and common-cause failures that would defeat same design redundancy. Nevertheless, a large disadvantage is the added logistic costs: besides the extra components, additional test specifications are needed[137]. For this reason, diverse design redundancy is typically implemented when the primary design choice is considered to carry a higher level of risk, for example, when it is intended to demonstrate or validate low TRL components. Therefore, the diverse design redundancy is most economical when the backup unit is already flight proven and has had sufficient testing before.

Functional Redundancy

Functional redundancy is the realisation of a functionality by diverse means and can be easily confused with diverse design redundancy. Functional redundancy focuses on maintaining a function through alternative subsystem responsibilities, which differs from diverse design redundancy, where dissimilar designs are used to realise the same functionality. Often however, a diverse design redundancy can be used to implement a functional redundancy, making the two implementations overlap. An example of a functional redundancy which is not a diverse design redundancy, is using the spacecraft's main OBC as a backup for the AOCS processor in case the latter fails. The OBC and the AOCS processor were not designed to perform the same functionality, but the OBC could be capable of performing the same functionality, which is why a task reallocation can prevent mission failure after an AOCS processor failure. This application often requires cross wiring of subsystems as well as fault detection and isolation logic, which makes the system more complex, which could be considered a disadvantage. An advantage of this technique is that it does not require extra components to the same extent as for same design and diverse design redundancies, which leads to fewer 'penalties' in terms of weight and costs.

Temporal Redundancy

Failed operations can also result into mission failure. A deployment failure of the solar array for instance, might make it impossible to become power positive. To prevent a single deployment failure from endangering the mission success, a temporal redundancy can be used. This type of redundancy is based on repeating unsuccessful operations. It is most effective when a thorough analysis is made about the retry interval and the optimum conditions to increase the probability of a successful operation. For switching on a power supply, this would be reducing the connected loads and pointing the solar array to the sun for maximum power generation. This type of redundancy is often implemented by software, which makes it relatively low in costs compared to hardware-based redundancy solutions. However, effective use of temporal redundancy requires retries being planned in advance. The spacecraft must be able to remain operational long enough to attempt one or more retries while improving the conditions for the operation. Execution of temporal redundancy can be performed autonomously onboard or initiated by the ground segment. For this type of redundancy, it is essential to incorporate mechanisms – sometimes referred to as 'hooks' – that allow for automatic or ground-initiated retries [137].

Hot and Cold Redundancy

Besides added components or shared functionalities as described in the above two sections, a distinction between hot and cold redundancies can be made. For example, the extra reaction wheel discussed in the Same Design Redundancy subsection could be running in parallel to the other wheels, or it could be kept inactive until failure of one of the wheels occurs. Keeping the redundant component active before a failure event is called a hot redundancy. A downside of this is that keeping the component active increases the power consumption and it makes the redundant component more prone to wear and tear. An example of a cold redundancy is a spare memory unit for data storage, which is only activated after the primary memory unit has failed. A common failure mode for onboard data storage is radiation induced damage. By keeping the redundant memory unit turned off, its exposure to radiation effects is reduced, which will lower the likelihood that it fails before the primary unit[84].

6.4.4. Redundancy Allocation and Fault Tolerant Design

In principle, a system should be designed with a fault avoidance approach. It should be the case that all subsystems are designed to withstand the environment they have to operate in. Another approach is a fault tolerant design. In this approach, a system is designed where failure of components or faults do not result into mission failure, which can increase the overall mission reliability. To make a (fault avoidant) design fault tolerant, redundancies are used. As mentioned in Section 6.4.3, adding these redundancies comes with a cost. Therefore, to make a fault tolerant design feasible, it is essential to do an analysis on where to allocate redundancy and assess the appropriate redundancy implementation technique.

Failure Modes Effect Analysis

A FMEAis used as a systematic tool to identify critical failure modes and guide the allocation of redundancy within the spacecraft architecture. A FMEA is usually executed at part level, where the failure modes and causes are analysed. Besides looking at the effects of the failure modes, it is also important to take into account what the probability of said failures occurring is. Combining the likelihood of a failure mode happening with its impact on the mission is called criticality and is also a driving parameter in allocating redundancies. Failure modes with a high probability of occurrence but low mission impact might not justify extensive redundancies and are instead addressed through operational contingencies or monitoring. On the other hand, failure modes with low probability but with severe mission impact are generally mitigated through robust design measures, including hardware redundancies, fault tolerance, and protective architectures. The criticality is assessed in Chapter 17 and will thus be used for allocating redundancy measures throughout the spacecraft.

Due to project constraints, a full-part level FMEA in accordance with standards defined in the ECSS-Q-ST-30[50] is considered to be outside of the scope of this Phase 0 study. To reduce the associated technical risks, it is recommended that all Electrical, Electronic, Electromechanical (EEE) components used in the NEBULA-Xplorer shall comply with the requirements and guidelines defined in ECSS-Q-ST-60[49], in addition to the before mentioned risk analysis that is done in Chapter 17. Compliance with the ECSS standards will ensure appropriate procedures for component selection, qualification, screening, derating, and traceability, thereby reducing the likelihood of failure modes occurring. However, it should be noted that this recommendation can not substitute a full FMEA since it does not eliminate the associated risks for EEE components. Therefore, this is considered to be a risk-minimisation measure to reduce risk in the stage of the mission design. A full FMEA should be conducted in a later mission phase.

7 Structures

In this chapter the design for the spacecraft structure of the NEBULA-Xplorer is described. As the structure forms the basis of the spacecraft design and largely determines whether the spacecraft is in conformity with the Vega-C launcher constraints, the structure subsystem is being treated first. In Section 7.1 and Section 7.2, the key requirements and assumptions made are set in order to properly design the structure. Section 7.3 describes the final design, consisting of the primary structure carrying the loads and the secondary structures, each serving its own purpose. In Section 7.4, the structural analysis is performed as a requirements compliance check. At last, Section 7.5 and Section 7.6 treat the risk and redundancy of the structures subsystem.

7.1. Key requirements

The design of the spacecraft structure is driven by a couple of key requirements. Chapter 3 showed all requirements, where the ones labelled with 'STUC' or 'LAUN' are relevant for the structures design. However, only six of them drive the design process. These six can be seen in Table 7.1. All of these requirements are derived from the Vega-C launcher constraints [19].

Table 7.1: Key requirements for structures design

Requirement ID	Requirement text
REQ-LAUN-C-LAUN005-007	The spacecraft diameter should be less than 1500mm
REQ-STUC-C-LAUN002-001	The spacecraft shall sustain ±3g lateral quasi-static loads w.r.t launch direction
REQ-STUC-C-LAUN002-002	The spacecraft shall sustain ±8.5g longitudinal quasi-static loads w.r.t launch direction
REQ-STUC-C-LAUN002-003	The spacecraft shall have a natural frequency higher than 30Hz in lateral direction w.r.t launch direction
REQ-STUC-C-LAUN002-004	The spacecraft shall have a natural frequency higher than 60Hz in longitudinal direction w.r.t launch direction
REQ-STUC-C-LAUN002-007	The static imbalance along the body fixed Y-axis of the spacecraft (y_G) shall be less than 30mm

The table contains four load requirements which determine the structural integrity. REQ-LAUN-C-LAUN005-007 and REQ-STUC-C-LAUN002-007 both have a closely linked requirement, namely REQ-STUC-C-LAUN005-006 and REQ-LAUN-C-LAUN002-006, which do not appear in the table. That is because these two requirements were found to be non-limiting. The same goes for all other "STUC"-labelled requirements, which do need to go through a compliance check, but have had no effect on decisions made in the design process.

Besides the requirements mentioned in Chapter 3, there are a lot more launcher requirements which can be found in the Vega-C manual [19]. These are requirements for verification logic, safety factors, static tests, sine- and acoustic vibrations, shock and compatibility with the electric field. These requirements are beyond the scope of this project, as a design phase 0 is performed. However, it is highly recommended to include these requirements for the following design phases.

7.2. Assumptions

Besides driving requirements, some assumptions were made for the structures design, which are stated in Table 7.2 below. The assumptions made for the structural analysis are stated in Table 7.6 in Section 7.4.

Table 7.2: List of assumptions made during preliminary structure design

Assumption ID	Assumption/input	Justification	Design Impact	Consequences if Invalid
ASSU-STUC-1	For the structure design, a mathematical model description is given together with a structural analysis in the form of a stress and strength-, dynamic response and buckling analysis	The ECSS standards on Phase 0 structure design state a mathematical model description is required, without going into detail of bolting or other joining methods [37] [38]	The design is worked out up to a certain level, leaving the detailed design of most secondary structures to further design stages	The type of analysis cannot be invalid, as it is a theory.
ASSU-STUC-2	The NEBULA-Xplorer team of the Falcon-9 design have correctly validated their design, meaning the structural design is compliant with the Falcon-9 constraints [132]	As SRON has checked and authorised the document, this is considered a valid assumption. Also, the framework approach aligns with ECSS structural requirements for spacecraft, confirming the structure's load resistance [38]	The structural components used and their configuration are largely based on the Falcon-9 design of NEBULA-Xplorer. This assumption provides the reasoning for why the structural architecture and components were chosen. See Section 7.3.1 for further explanation	A more optimal solution exists in terms of structural performance or mass, which should be investigated
ASSU-STUC-3	The bus structure of the spacecraft can only be placed next to the payload	See Spacecraft height calculation	The spacecraft is designed with the bus next to the payload instead of under it	A spacecraft with the bus structure below the payload must be investigated
ASSU-STUC-4	The outgassing requirements (REQ-STUC-C-LAUN010-012 & 013) are met	All materials selected for this design are standard space-mission materials with extensive flight heritage. Therefore, compliance with outgassing requirements is justified by similarity to previously qualified data [43]	No extra measures have to be taken to comply with the outgassing materials	Requirements are not met, which could result in molecular contamination

Spacecraft height calculation

The assumption mentioned in Table 7.2 is that the bus structure of the spacecraft is placed next to the payload. This assumption resulted in REQ-LAUN-C-LAUN005-006 not being a driving requirement, as mentioned in Section 7.1. The assumption was derived as follows:

To estimate the spacecraft bus structure volume, the Falcon 9 design was used as a reference, as it is equivalent from a system-level point of view [132]. Here, the bus structure volume is about a third of the payload volume. Considering an extra payload in the form of HEXI is added for this design, the bus structure volume could increase and make this ratio bigger. In terms of volume, the HEXI is less significant compared to LEXI (ratio of 1:64), but in terms of power consumption, it could indeed require a higher bus volume (ratio of 1:3).

Calculating the bus structure volume with the new payload dimensions (1345 mm x 760 mm x 535 mm) results in a volume of 0.18 m^3. The payload has to stand upright in the launcher to fit within the 1500 mm diameter circle limit, meaning that if the bus structure were placed under the payload (below the detector plate), the spacecraft's height would increase. With this bus volume assumption, the spacecraft height would become 1793 mm, with REQ-LAUN-C-LAUN005-006 stating the spacecraft height cannot exceed 1800 mm. This is considered too risky a margin to design for. Therefore, it seems more feasible to place the spacecraft bus structure next to the payload.

7.3. Final Design

Before describing the final design, a reference frame is set to keep consistency throughout the entire design description. An axis system is chosen with its origin in the mounting plane of the launch adapter, with the positive z-axis in launch direction and the positive x-axis in flight direction (direction of orbit manoeuvrers). The Vega-C launcher requires a reference frame with its origin in the mounting plane and the z-axis in launch direction [19]. The x-axis is chosen for convenience.

7.3.1. Primary Structure

As mentioned in Section 7.2, the same structural components as the Falcon-9 design are chosen [132]. As the launcher requirements of the Falcon-9 are similar to Vega-C's, the design is likely to comply with its current

requirements [123]. Also, as SRON demands high TRL's for all components of the NEBULA-Xplorer, the chosen architecture provides a high baseline maturity. At last, the re-usage of structural architecture and components allows for engineering resources to be more focused on the critical design drivers, such as the launch vehicle adapter and the accommodation for a larger payload.

X-braced panels

The structural frame of the NEBULA-Xplorer is formed by X-braced panels, which have the purpose of transforming torsional and bending stresses into axial loadings, and as such increasing the stiffness-to-weight ratio of the structural frame. The material for these X-braces is aluminium 6061-T6, chosen for its high strength-to-weight ratio and low cost. Table 7.3 showcases the main properties of the used aluminium alloy, which are useful to take into account during the structural design phase.

Table 7.3: Important mechanical properties of Aluminium 6061-T6 used for the stress simulations and analyses. All values taken from [70].

Mechanical Property	Density [kg/m^3]	Young's Modulus [GPa]	Tensile Yield Strength [MPa]	Shear Modulus [GPa]	Shear Strength [MPa]
Aluminium 6061-T6	2700	68.9	276	207	26

Sandwich panels

The panels of the NEBULA-Xplorer are sandwich panels, consisting of a 15 mm thick aluminium 5056 honeycomb core and 1.92 mm thick CFRP face sheets on both sides. The main functions of these sandwich panels are to stiffen the structural frame and provide mounting for subsystems. For the honeycomb core, a cell size of 3.2 mm was chosen, staying in line with the material choice for the Falcon-9 Baseline Design [123] (though the thickness was increased after performing Quasi-Static Loading (QSL) and dynamic loading tests in accordance with Vega-C requirements in Section 7.4). As for the orientation of the honeycomb panel, a distinction can be made between the side panels (on the xz- and yz-plane) and the top panel (on the xy-plane). The longitudinal direction of a honeycomb core (i.e. parallel to the cor ribbons) has stronger shear properties than the transverse direction (perpendicular to core ribbons), as showcased in the 5056 aluminium honeycomb material properties in Table 7.4. As such, the following choice was made for the honeycomb panel orientations:

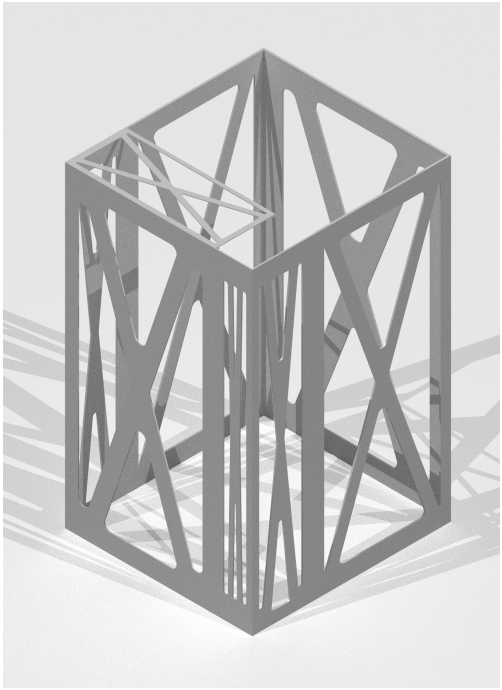

Figure 7.1: Naked X-brace structural frame

- Side panels: longitudinal properties in z-direction, due to high QSL of ±8.5g during launch (REQ-STUC-C-LAUN002-002). This means that the panels have transverse honeycomb properties in lateral directions.
- Top panels: longitudinal properties in y-direction, due to the main internal mounting panel being placed in the yz-plane. Nevertheless, for the structural analysis simulations, both x- and y-directions of the top panel will have transverse honeycomb properties, as per ASSU-CAD-05 in Table 7.6.

As for the CFRP facesheets, a symmetric 16 ply lay-up is used for each side (with each ply having a thickness of 0.06 mm), with the same lay-up as in the Falcon-9 Design [123], which are then doubled through adhesive bonding: $[0°/+45°/-45°/90°/0°/+30°/-30°/90°]_s$

Table 7.4: Important mechanical properties of 5056 honeycomb (cell size 3.2 mm) used for the stress simulations and analyses. All values taken from [107].

Mechanical Property	Density [kg/m^3]	Young's Modulus [GPa]	Tensile Yield Strength [MPa]	Shear Modulus [GPa]	Shear Strength [MPa]	Poisson's Ratio [-]
5056 Honeycomb Longitudinal (L) Direction	32	$7.7 \cdot 10^{-5}$	0.01	0.185	0.96	0.464
5056 Honeycomb Transverse (W) Direction		$1.85 \cdot 10^{-4}$	0.011	0.09	0.586	

Launch Adapter Panel

For the connection between the spacecraft and the launcher, a launch adapter has to be designed which is able to withstand all the loads induced through the launch adapter, as this is the point that puts a constraint on the movement of the NEBULA-Xplorer during launch. As lateral and longitudinal quasi-static loads of ±3g and ±8.5g respectively have to be sustained, as per REQ-STUC-C-LAUN002-001 and REQ-STUC-C-LAUN002-002, a thick and strong launch adapter panel is of the utmost importance for the structural integrity of the spacecraft. For the material of this bottom panel, aluminium 6061-T6 was chosen just like for the X-braced panels (with the material properties once again visible in Table 7.3). Once again this allows for a high strength-to-weight ratio and a low cost, both of high importance for the NEBULA-Xplorer design. In order to save some weight, a web structure was used for the bottom panel as visible in the bottom panel 3D design in Figure 7.2. These webs have the same height of 20 mm as the launcher panel, while the pockets between the webs are 10 mm thick. The web thickness for the final design is 16 mm, and the two circular web areas are placed at the center with a diameter of 592 mm to 620 mm for the outer web to attach the launch adapter to, and an inner web with diameter 252 mm to 300 mm, to allow for load redistribution. Besides the design of the launch adapter panel itself, a choice on the launch adapter also has to be made.

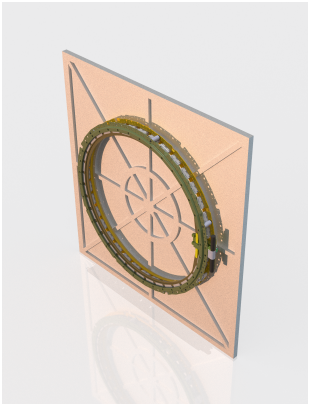

Figure 7.2: Bottom panel design including the launch adapter

Launch Adapter Trade-off

As the NEBULA-Xplorer is designed to be launched in a Vega-C launch vehicle, a launch adapter in compliance with said launcher has to be chosen. For the Vega-C, two launch adapters can be chosen: a decision between the RUAG PAS 610S and the MLB MkII 24" has to be made. Comparing the values in terms of total adapter mass, the adapter mass after separation, the heights of both adapters, the success rates of the adapters and their TRLs, it becomes evident that the differences between both adapters are small. Both having 100% success rates and 9 TRL level, they only show a difference in mass and height. Therefore, the choice was made to use the MLB MkII 24", due to the lower mass before separation (5.1 kg against 5.8 kg), which was one of the factors to be minimised for the design.

7.3.2. Secondary structures

Isostatic Mounts

The isostatic mounts form the attachment of the payload to the spacecraft. Their design is based on the two functions they should perform: clamping the payload without over-constraining it and thermally isolating the payload from the rest of the spacecraft.

A widely used configuration for high precision measurement instruments in aerospace is bipod mounts [101]. These typically involve three A-shaped bipod sub-assemblies, each consisting of two adjustable legs connected to the payload in the same point and two separate points on the spacecraft. The 3-2-1 principle describes how to place these bipods in such a way that the body is constrained in six degrees of freedom (along three translational axes and three rotational axes). Ideally, the single force containing all six constraints should pass through the cog of the instrument. This kinematic mounting method prevents the payload from being over-constrained, which can lead to stresses and deformation [101].

As can be seen in Figure 7.3, the configuration is such that the six degrees of freedom are constrained. Also, the single force is aligned with the Center of Gravity (CoG), as the triangle between the payloads' connection points contains the CoG.

The placement of the nodes (connection points to the structure and the payload) is done such that structural integrity is maintained. This means that the nodes are placed on the stiffest parts of the structure. On the payload, these are the short sides of the concentrator- and detector plate and on the spacecraft structure, these are the corner points of the X-braced panels. The bottom bipod is oriented towards the -xy-direction of the spacecraft, as the structure is more stiff due to internal panelling.

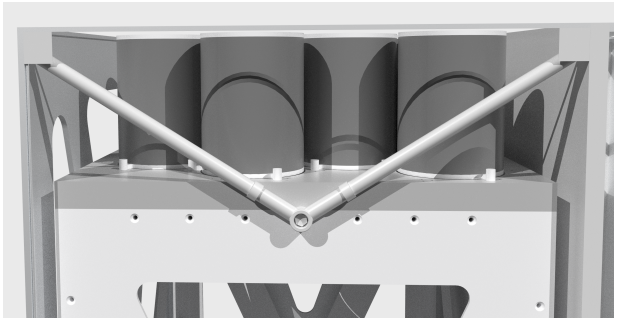

(a) LEXI side mounts

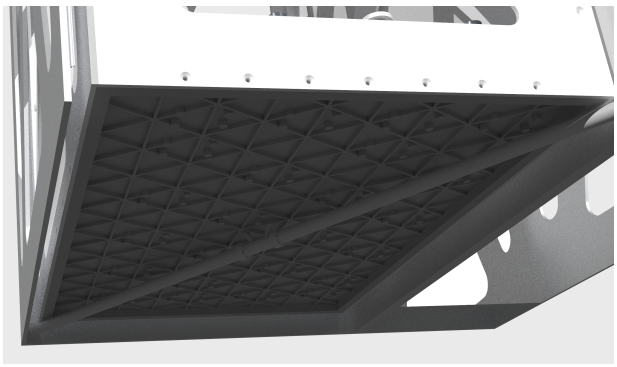

(b) LEXI bottom mount

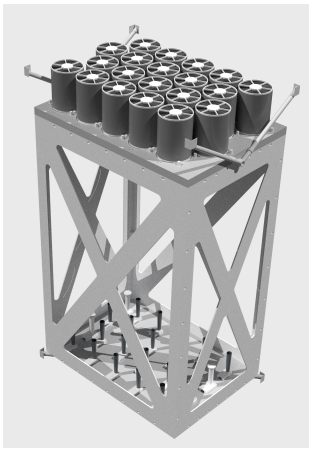

(c) LEXI mounts configuration

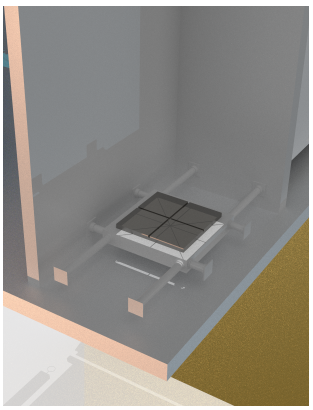

(d) HEXI mounts configuration

Figure 7.3: Isostatic mounts

The second function, thermally isolating the payload, is achieved by making the mounts of titanium rods with 18 mm diameter. Titanium has low thermal conductivity, making it a suitable material for the bipods [132].

Note that due to this isostatic mount design, the LEXI can be considered to be a floating box within the spacecraft. The space reserved around it is a main driver for the total spacecraft dimensions.

Sunshades

The sunshades assembly is another structural component which is essential for the payload's functioning. It is however not a major load bearing component and is thus kept similar to the Falcon-9 design proposal [132]. The main goal of the sunshades for LEXI, is to protect the concentrators from radiation, to assure high-contrast measurements and prevent thermal loads. As HEXI does not have concentrators, the sunshades serve as protection for the detector plate.

The sunshades are made of 0.56 mm thick CFRP plates, placed as a circle above each LEXI concentrator and above HEXI (Figure 7.6). They are mounted on a 5 mm thick Ti-6Al-4V baseplate for low thermal expansion. This titanium baseplate is bolted to the top sandwich panel.

The Falcon-9 design proposal uses the same kind of sunshades as the NICER mission, which is already operative on the International Space Station (ISS) [92]. However, the assembly experienced some damage, forcing National Aeronautics and Space Administration (NASA) to patch some of the sunshades to prevent sunlight from entering the instrument [91]. Henceforth, for further design phases, it is recommended to reconsider using the same sunshades assembly as the NICER mission.

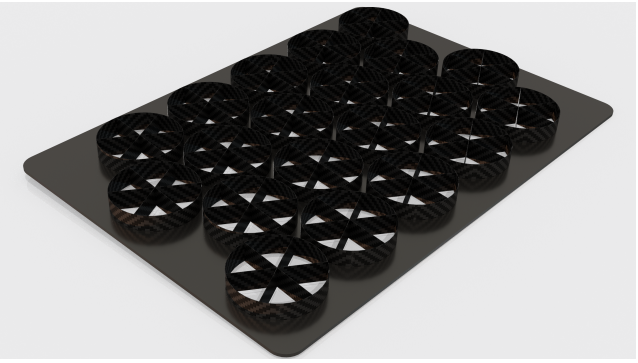

Figure 7.4: LEXI

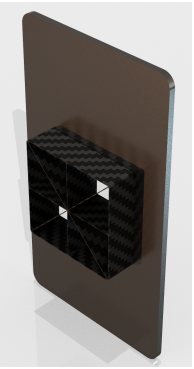

Figure 7.5: HEXI

Figure 7.6: Sunshades

Radiation Shielding

The main radiation environment for the mission is driven by trapped electrons and protons, particularly during SAA passages. The radiation tolerance of the selected components cannot be fully verified, as some key information is classified or unavailable. The most vulnerable subsystems are the spacecraft electronics, which are especially sensitive to SEEs and therefore require additional protection. Although OBCs are commonly protected using an additional aluminium layer, the remaining uncertainty introduces a risk that cannot be accepted for this mission. For this reason, a dedicated radiation vault is implemented around the internal spacecraft components to provide extra shielding and reduce the total radiation exposure. The payload is a sensitive instrument designed by an external supplier and is assumed to be radiation hardened. It will not be placed inside the radiation vault, as additional shielding or structural modifications to the payload could lead to altered measurements.

Several candidate shielding materials were assessed for this analysis: low-Z (Atomic Number) polyethylene (PE), medium-Z aluminium (Al), and high-Z tantalum (Ta). These materials were chosen due to their common use in aerospace applications and their availability for integration. A graded-Z shielding approach–a laminate of materials with different atomic numbers–can improve shielding effectiveness by optimising mass, protection, and cost. While higher-Z materials can shield higher-energy radiation more effectively at a given thickness, they also introduce a significant mass penalty. Tantalum was initially considered due to its high density and shielding capability. However, it was discarded because of its increased mass penalty and would also lead to increased Bremsstrahlung X-ray production when exposed to trapped electrons. Furthermore, tantalum's extremely high melting point would allow the vault to better survive atmospheric re-entry, which is not desirable for the mission's EOL and compliance objectives.

The final radiation vault adopts a PE–Al–PE sandwich panel architecture. The initial PE layer reduces the energy of incoming charged particles before interaction with the Al layer, thereby limiting Bremsstrahlung X-ray production [21]. The intermediate Al layer provides the required structural stiffness and mechanical support, while the final PE layer attenuates secondary radiation and residual charged-particle flux. Shielding performance is evaluated using Continuous Slowing Down Approximation (CSDA) ranges obtained from the National Institute of Standards and Technology (NIST) database [97]. The adopted areal densities of 0.1441 g/cm² (PE) – 0.2699 g/cm² (Al) – 0.1441 g/cm² (PE) ensure protection against electrons up to 1 MeV and protons up to 10 MeV. Operationally, a threshold proton flux at 10 MeV of 10 $cm^{-2}s^{-1}$ is used to define entry into radiation protection mode at the SAA boundary.

Table 7.5: Radiation vault graded-Z shielding configuration and stepwise CSDA attenuation

Case	Layer	Material	Areal density [g/cm^2]	E_{in}	CSDA range at E_{in} [g/cm^2]	Residual / E_{out}
Electron stopping (1 MeV)	1	PE	0.1441	1.0 MeV	0.4155 (PE)	Residual CSDA: 0.4155–0.1441 = 0.2714 $\Rightarrow$ $E_{out} \approx$ 0.8 MeV
	2	Al	0.2699	0.8 MeV	0.4206 (Al)	Residual CSDA: 0.4206–0.2699 = 0.1507 $\Rightarrow$ $E_{out} \approx$ 0.4 MeV
	3	PE	0.1441	0.4 MeV	0.1213 (PE)	Since 0.1441 > 0.1213, electrons are **fully stopped** in final PE layer
Proton stopping (10 MeV)	1	PE	0.1441	10 MeV	0.1132 (PE)	Since 0.1441 > 0.1132, protons are **fully stopped** in first PE layer

7.4. Structural Analysis

In order to comply with the requirements mentioned in Table 7.1, a structural analysis has to be performed. With the design currently being in Phase 0, hand calculations for structural sizing give a rather limited image of the design. Therefore, it was decided to use CAD simulations as the main method for structural sizing and checking of compliance with the set launcher requirements. Nevertheless, due to limited modelling resources, these simulations need to be simplified to preserve Random Access Memory (RAM) space, which is why several assumptions have been made, as noted in Table 7.6.

Table 7.6: List of assumptions made during the preliminary design for the structural analysis simulations

Assumption ID	Assumption / input	Justification	Design Impact	Consequences if Invalid
ASSU-CAD-01	The launch adapter is fully rigid.	The launch adapter is designed and validated by a third party. As such, structural analysis of the adapter is outside the scope of this design.	Allows for the necessary simplification of the simulation model.	A realistic, non-rigid launch adapter would cause a slightly uneven load distribution over the launcher panel, resulting in stress concentrations during launch.
ASSU-CAD-02	Very localized stress concentrations in 3D simulations can be neglected.	The engineer running the simulations can decide whether localized stress concentrations are simulation inaccuracies (this can be checked) or actual structural risks in Phase 0 design. See Section 7.4.1 for a broader explanation.	Allows for the necessary simplification of the simulation model.	Stress concentrations can cause yielding of structural components, though the introduction of brackets and stiffeners in future design phases should prevent this.
ASSU-CAD-03	CFRP is considered isotropic.	The CFRP used in the real model is quasi-isotropic, and for Phase 0 design, CFRP can be simplified using isotropic properties.	Allows for the necessary simplification of the simulation model.	Simulation results are slightly inaccurate due to partially anisotropic behaviour. This can be further researched in later design phases.
ASSU-CAD-04	Calculated natural frequency through simulations will be lower than the natural frequency of the actual spacecraft.	Inclusion of stiffeners and brackets is limited in the simulation model due to memory constraints, which would increase the natural frequency for the flight model.	Allows for the necessary simplification of the simulation model	If $f_{n_{true}} \leq f_{n_{sim}}$, REQ-STUC-C-LAUN002-003/004 might not be met. As such a margin is placed on the simulated natural frequency.
ASSU-CAD-05	Honeycomb structure only carries lateral loads in transverse direction and longitudinal loads in longitudinal direction	The honeycomb panels on the sides are orientated with the longitudinal properties in z-direction, and transverse properties along x- and y-directions (see Section 7.3. While this assumption does not completely hold up for the top panel, both the longitudinal and transverse properties are structurally tested for this panel.	Allows for the necessary simplification of the simulation model	Significant out-of-plane loads can cause local failures, which should be tested upon during later V&V stages.
ASSU-CAD-06	Subsystem components with no assigned materials in CATIA have a coinciding centroid and CoG.	Most components affected by this assumption either have a uniform mass distribution or are small enough to not have a big effect on CoG shifts.	Simplification of CoG calculation, slight difference between true CoG and calculated CoG.	Slight increase or decrease in reaction wheel dimensions and placement, which should be iterated upon in future design phases.
ASSU-CAD-07	Possible stress concentrations due to fasteners can be ignored.	Structural analysis performed focuses on the global load paths, stress concentrations due to fasteners e.a. are more applicable for the later stages of the design.	Allows for the necessary simplification of the simulation model	If, after analysis, stress concentrations due to fastener are expected to have a significant effect on the load distribution, the structure needs to be strengthened near these fasteners.
ASSU-CAD-08	The structure behaves linearly elastic with small deformations under the applied load cases.	The structure will not be designed for plastic deformation, and with the implemented margins, only small deformations should be present.	Enables the use of linear structural validation.	Stresses can be underestimated and wrong representations of load distributions can appear in case of non-linear behaviour or large deformations.

7.4.1. Finite Element Analysis and Stress Concentration Inaccuracies

As mentioned in ASSU-CAD-02 in Table 7.6, very localized stress concentrations might be neglected for the structural analysis, as decided upon by the CAD-engineers performing the simulations. As this can be interpreted as a dangerous assumption to make for the structural integrity of the spacecraft, an elaboration on this assumption was deemed useful.

As the structural subsystem of the NEBULA-Xplorer consists of different components with different dimensions and materials (and hence different mechanical properties), a difference in mesh sizing of the components

is a logical consequence. As mesh sizes are usually determined by the smallest dimensions on a component, slender components usually have smaller meshes. While these smaller meshes do usually give a more accurate representation, they also come with two major problems. First of all, decreasing the mesh sizing means that the number of meshes per component will be increased, hence increasing the number of calculations that will need to be performed by the program, which increases both simulation time and required simulation memory. Secondly, stress singularities have the behaviour to keep increasing the more a mesh is refined – the stress would theoretically diverge to infinity if refined enough [2]. For the structural analysis, this implies that sharper corners are susceptible to higher stress concentrations according to the simulations. Focusing on sections like these is deemed to be outside the scope of a Phase 0 design and are thus neglected in the structural analysis (stress concentrations that take place over a larger area are still taken into consideration). These small stress concentrations are also usually also susceptible to a lower simulation accuracy, hence making their stress values less accurate.

As an example of these simulation inaccuracies, Figure 7.7 and 7.8 can be consulted: while a maximum stress of 843 kPa is visible in Figure 7.7, this stress component is at the same time present at a location with a very low simulation accuracy of 2.39%, as visible in Figure 7.8. An example of a stress concentration that is not ignored for the stress analysis is visible in Figure 7.9. Here, the stress concentration is spread over a large area, for which structural considerations can be made during Phase 0 design: the stress concentration takes place at the intersection of the mounting panels between LEXI, HEXI and the spacecraft bus, directly above the launch adapter (where loads are induced as this panel is clamped).

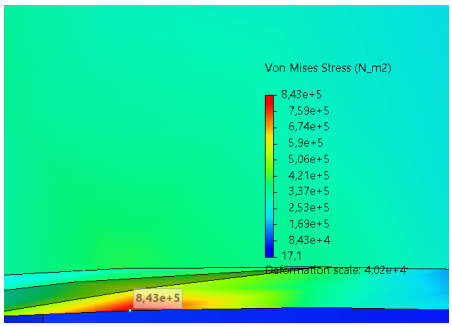

Figure 7.7: Local maximum Von Mises Stress of 843 kPa for the simulation of a sharp-edged component of the NEBULA-Xplorer

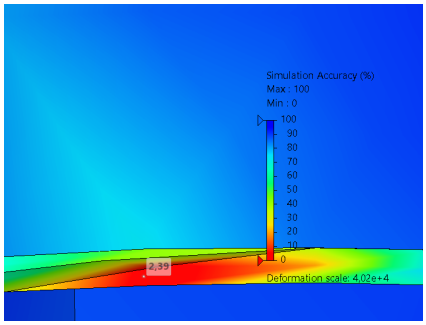

Figure 7.8: Simulation accuracy of 2.39% for the 843 kPa Von Mises Stress component showcased in Figure 7.7

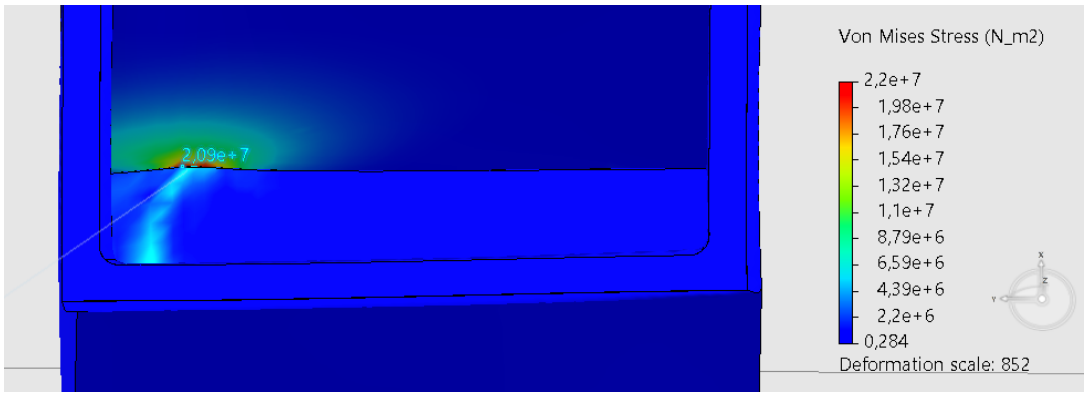

Figure 7.9: A more accurate Von Mises Stress calculation of an FEA-simulation of the NEBULA-Xplorer (taken from stress analysis scenario 6 (see Table 7.7): at the intersection of two mounting panels (only one visible), directly above the load-inducing launch adapter

7.4.2. Design loads

As the structural analysis mainly focuses on requirements REQ-STUC-C-LAUN002-001 to REQ-STUC-C-LAUN002-004, a distinction between static loads and dynamic loads can be made. The static loads can then

be subdivided into a general stress analysis, as described in Section 7.4.3, and buckling loads, as described in Section 7.4.4. Conversely, for the dynamic loads analysis, Section 7.4.5 describes the spacecraft compliance with the natural frequency compliances during launch. Besides a division in analysis between static and dynamic loading, all different load cases are also subdivided into different scenarios, due to both limitations in the honeycomb material properties, as well as combinations of different load cases. Table 7.7 shows all the tested loading scenarios.

Table 7.7: Table of different structural loading scenarios simulated

	Stress Analysis		Buckling Analysis		Dynamic Loading Analysis	
Scenario Number	**Honeycomb properties**	**Load case and direction**	**Honeycomb properties**	**Load case and direction**	**Honeycomb properties**	**Boundary conditions**
1	Longitudinal (L)	+z-direction (8.5g)	Longitudinal (L)	+z-direction (8.5g)	Longitudinal (L)	Clamped launch adapter
2	Transverse (W)	+x-direction (3g)	Transverse (W)	+x-direction (3g)	Transverse (W)	Clamped launch adapter
3	Transverse (W)	+y-direction (3g)	Transverse (W)	+y-direction (3g)	Longitudinal (L)	Clamped top and bottom panel
4	Transverse (W)	+x-direction (2.12g); +y-direction (2.12g)	Transverse (W)	+x-direction (2.12g); +y-direction (2.12g)	Longitudinal (L)	Clamped sides
5	Longitudinal (L)	+x-direction (3g); +z-direction (8.5g)	Longitudinal (L)	+x-direction (3g); +z-direction (8.5g)	Transverse (W)	Clamped top and bottom panel
6	Longitudinal (L)	+y-direction (3g); +z-direction (8.5g)	Longitudinal (L)	+y-direction (3g); +z-direction (8.5g)	Transverse (W)	Clamped sides
7	Longitudinal (L)	+x-direction (2.12g); +y-direction (2.12g); +z-direction (8.5g)	Longitudinal (L)	+x-direction (2.12g); +y-direction (2.12g); +z-direction (8.5g)	N/A	N/A

7.4.3. Stress and Strength Analysis

As previously mentioned, the stress and strength analysis checks if the spacecraft structure survives the launcher requirements for the conceptual design: the load cases in Table 7.7 are quantified and simulated with the use of SIMULIA, as visible in Figure 7.10. Through analyzing the results, Von Mises stress values are assessed, and the structural design is improved if necessary, i.e. dimensions are increased in case of failure or decreased in case of unreasonable over-design, in order to save weight. It was decided to include a a safety margin of 5 on the maximum stress values, due to the structure still being in an early design phase and the exclusion of the payload and other subsystem components in the design. After simulating all the general stress loading scenarios, values for the maximum Von Mises stress can be acquired and iterated upon. The maximum stress values for the final design are shown in Table 7.8. With a maximum stress for scenarios 5 to 7, the structure is still safely within limits, even when taking the safety factor into account. If however, future design requires the structure to be lighter, Table 7.8 should help indicate that it is best not to spare weight in the mounting panel between LEXI, HEXI and the spacecraft bus, as this is where the highest stress values are reached.

Table 7.8: Maximum Von Mises stress values for stress analysis scenarios laid out in Table 7.7

Scenario Number	**1**	**2**	**3**	**4**	**5**	**6**	**7**
Maximum Von Mises Stress[1] [MPa]	14.7	15.5	2.97	10.8	20.9	20.9	20.9
Location Maximum Stress	Bottom panel	Bottom panel	Mounting panel	Bottom panel	Mounting panel	Mounting panel	Mounting panel

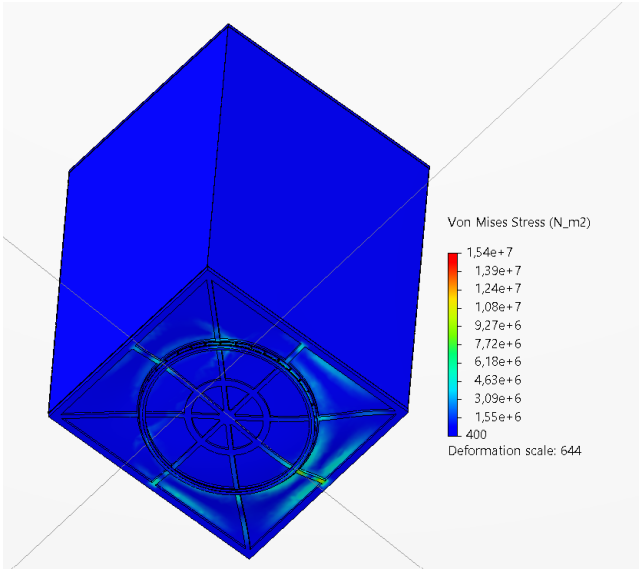

Figure 7.10: Bottom view of a structural stress simulation of the NEBULA-Xplorer. Note the deformation scale of 644: this implies that all visible deformations in the results analysis are exaggerated by a factor of 644, to better visualize the relative deformations.

7.4.4. Buckling

The buckling analysis is quite similar to the general stress analysis, in the sense that the quasi-static loads induced by the launch vehicle are simulated on the structure. This is also visible in the columns regarding the stress analysis and buckling analysis in Table 7.7. However, the difference between both analyses is the output: whereas the stress analysis computes the maximum Von Mises stress (among others), the buckling analysis outputs a safety factor – viz., a safety factor of 5 for a load of 3g would imply that buckling would start to occur at a QSL of $5 * 3g = 15g$. Due to the exclusion of subsystems and payload from the buckling simulations, along with all the made assumptions in Table 7.6 for the simulations, a minimum buckling safety factor of 3 was used as a constraint for the simulations, meaning that the structure would only start to buckle at three or more times the applied loads. As is visible in Table 7.9, the minimum buckling safety factor present is 6.696 for scenario 5 (longitudinal honeycomb properties with a longitudinal QSL of 8.5g and a lateral QSL of 3g in +x-direction). This buckling is also shown in Figure 7.11 (note that the displacement is normalized and thus does not geometrically represent the deformation). Both in Table 7.9 and Figure 7.11 it is evident that in the event that buckling occurs, it is most likely to occur in the mounting panel – more specifically between LEXI and the spacecraft bus, as there are no longitudinal x-braces placed here, and has a large thickness-to-area ratio. While some buckling safety factors seem inaccurate, they were still included here: as the spacecraft is clamped to bottom panel through the launch adapter, most lateral loads occur on this side. However, as a high thickness is required for the longitudinal loads, buckling is not likely to occur here either way.

Table 7.9: Maximum Von Mises stress values for buckling analysis scenarios laid out in Table 7.7

Scenario Number	**1**	**2**	**3**	**4**	**5**	**6**	**7**
Absolute Buckling Safety Factor	10.015	1044.741	1981.874	996.924	6.696	6.843	6.771
Buckling Location	Mounting panel	Bottom panel	Bottom panel	Bottom panel	Mounting panel	Mounting panel	Mounting panel

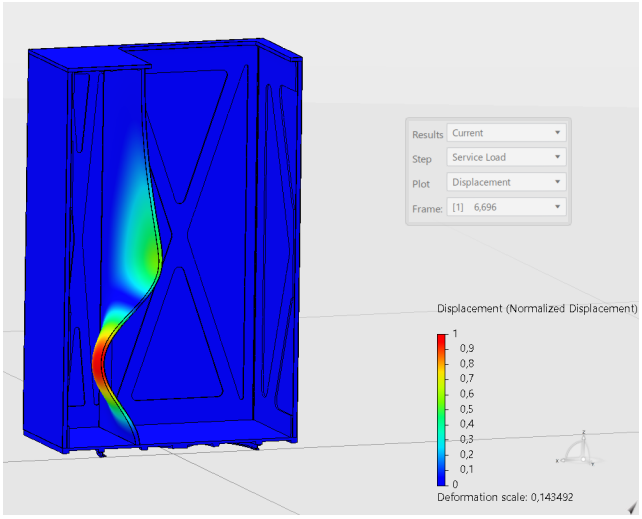

Figure 7.11: Cut view of buckling scenario 5, with a safety factor of 6.696. As can be seen, the buckling is mainly dictated by the mounting panel in this scenario. Note that the visible buckling displacement is normalized and then scaled.

7.4.5. Dynamic loading

In order to meet the dynamic loading requirements, the structure needs to be designed such that the lateral and longitudinal eigenfrequencies of the spacecraft are above 30 Hz an 60 Hz respectively. Due to the nature of SIMULIA natural frequency simulations – the program itself does not make a distinction between lateral and longitudinal eigenfrequencies – and the only boundary condition of the spacecraft during launch being the launch adapter, true lateral and longitudinal natural frequencies are hard to simulate. As such, it was decided to consider six different scenarios for which the spacecraft should have a compliant eigenfrequency, as visible in Table 7.7: simulations 1 and 2 can be viewed as the most realistic representation of launch conditions, with the spacecraft being clamped just to the launch adapter, and as such, are the most leading for the design with respect to the dynamic loads. Nevertheless, as these simulations do not make a distinction between longitudinal and lateral frequencies, the choice was made for both the simulation using longitudinal honeycomb properties (scenario 1) and the simulation using transverse honeycomb properties (scenario 2) to be designed for a natural frequency higher than 60 Hz, to make sure that the dynamic loading requirements were complied with. Besides this, a safety factor of 2 was applied in this phase of the design, meaning that the minimum eigenfrequency would have to be larger than 120 Hz.

To get a better picture of the eigenfrequencies, four more scenarios were implemented to simulate merely the lateral natural frequency (scenarios 3 and 5) and longitudinal natural frequency (scenarios 4 and 6). Though these last four scenarios are far from an accurate representation of the eigenfrequencies of the spacecraft, these simulations were still performed to get a better visualization of the dynamic loading of the spacecraft in merely one direction and help detect weak points in the structure.

In order to increase the natural frequency of the structure and meet the minimum, self-imposed eigenfrequency of 120 Hz, several stiffeners have been added along the top edges near the X-braces of the spacecraft. Besides this, an extra X-brace was added on the top side of the top side of the spacecraft bus, as shown in Figure 7.1. With these structural upgrades, the simulated natural frequencies were raised above 120 Hz, as visible in Table 7.10, with the lowest natural frequency being 126.414 Hz; frequency simulation scenario 1 (shown in Figure 7.12), with a clamped launch adapter and longitudinal honeycomb properties.

Table 7.10: Natural frequencies for dynamic loading scenarios laid out in Table 7.7

Scenario Number	**1**	**2**	**3**	**4**	**5**	**6**
Eigenfrequency [Hz]	126.414	466.16	126.647	126.912	591.433	268.795
Leading Location for Eigenfrequency Value	Mounting panel	Back panel (LEXI side)	Mounting panel	Mounting panel	Back panel (LEXI side)	Bottom panel

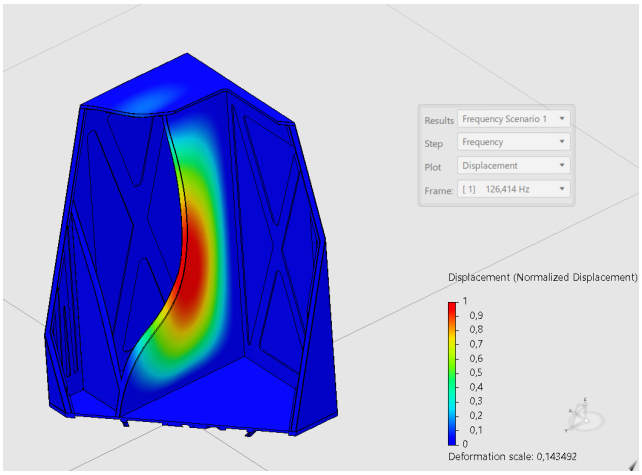

Figure 7.12: Cut view of dynamic loading scenario 1, with an eigenfrequency of 126.414 Hz. As can be seen, the eigenfrequency is mainly dictated by the mounting panel for this scenario. Note that the visible displacement is normalised and then scaled.

7.5. Risk Assessment

Table 7.11 shows the FMEA of the structures subsystem. R-SUB-STUC-001 till 004 had an influence on how the structural analysis was performed. Furthermore, the mitigation plans presented include recommendations for further design phases.

Table 7.11: Risk Log

Risk ID	Failure Mode	Effect	Cause	L	S	Risk	Mitigation
R-SUB-STUC-001	Structure collapse or rupture	Loss of structural integrity, payload misalignment and potential collision with the launcher fairing	The ultimate strength of the materials is exceeded, too high stress concentrations are created or insufficient material strength or thickness	A	5	A5	Perform thorough structural analysis (FEM) and conduct load testing. Apply safety factors during both according to ECSS standards [38].
R-SUB-STUC-002	Structure yield	Payload misalignment and potential collision with the launcher fairing	Yield strength of materials is exceeded, thermal distortion or insufficient material strength or thickness	A	4	A4	Perform thorough structural analysis (FEM) and conduct load testing. Apply safety factors during both according to ECSS standards [38].
R-SUB-STUC-003	Structure buckling	Structure rupture or internal damage to subsystems	Insufficient stiffness, geometrical imperfections or defects	A	5	A5	Perform buckling analysis, usage of honeycomb panels, addition of stiffeners
R-SUB-STUC-004	Dynamic coupling	Amplification of loads leading to structure collision, damage to electronics or optics	Insufficient stiffness	A	5	A5	Perform dynamic loading analysis and conduct testing. Apply safety factors during both according to ECSS standards [38].
R-SUB-STUC-005	Crack propagation	Propagation of pre-existing flaws (cracks, voids, delamination) to a critical size, causing collapse or rupture	Manufacturing defects	C	5	C5	Inspection and implementing Safe Life, meaning undetected flaws cannot propagate to failure
R-SUB-STUC-006	Fatigue failure	Crack initiation or propagation or functional degradation during lifetime	Cyclic loading during service life (testing, transport, launch)	C	4	B4	Perform fatigue analysis and tests

As can be seen, R-SUB-STUC-005 and 006 have a high risk score. As Section 17.4 mentions, these risks need to be managed, which is highly recommended for further design stages.

7.6. Redundancy

The implementation of redundancy is quite different for the structures subsystem for multiple reasons: if the structure fails, it will most likely occur during launch and immediately lead to mission failure. Also, the struc-

ture's functionality is very stand-alone, meaning no other subsystems or components would be able to take over its function. Also, adding redundant components in the structures design has a major impact on total mass.

However, despite these complications, a certain amount of redundancy methods can be incorporated in the structures design. The most important one being the load path redundancy. By adding multiple structural components carrying the same load, a component failure does not immediately transfer into subsystem failure. This is done with the combination of X-braced panels and sandwich panels. This can be seen as a hot diverse design redundancy (see Section 6.4) as both components are designed to carry the launch loads. A more 'zoomed-in' example is the usage of CFRP, which has built-in redundancy. If a few fibres break, the load is transferred to the other fibres. This is a hot same design redundancy (Section 6.4)

The other form of redundancy is mentioned in the mitigation plans in Table 7.11. By using safety factors, extra strength is added, acting as a buffer against uncertainties.

Recommendations for further design phases on how to implement redundancy would be to add redundant bolts or stiffeners (same design redundancy). Also, as mentioned in Table 7.11, the usage of Safe Life by already assuming cracks or material imperfections, is a form of redundancy implementation.

7.7. Requirements compliance check

As Section 7.4 proves, key requirements REQ-STUC-C-LAUN002-001 till 004 are met. Compliance with REQ-STUC-C-LAUN005-007 can be seen in Figure 7.13. Do note that this figure does not yet contain the externally placed subsystem components that will be discussed in the coming chapters. Chapter 15 will however show these components will not exceed the launcher envelope dimensions. On the other hand, REQ-STUC-C-LAUN002-007 is indeed affected by other subsystems and will therefore be checked for compliance in Chapter 15.

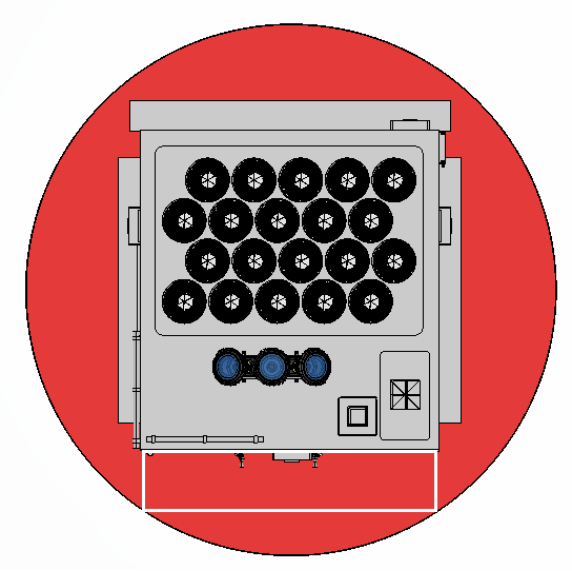

Figure 7.13: Top view of the spacecraft within the launcher dimensions

From Figure 7.13, the sensitivity of exceeding the launcher envelope diameter can be reduced. As the LEXI and HEXI stay constant, the bus structure has maximum dimensions. As this configuration of the bus structure next to LEXI is chosen, its width (in y-direction) cannot increase. The figure shows that the length (in x-direction) can increase by 157 mm. These derived constraints result in spatial requirements for other subsystems. The propulsion system design is most affected by this requirement. Figure 7.13 thus also shows the reserved envelope for the propulsion system, spanning 663 mm in width and 414 mm in length. This envelope is derived from the requirement that the propulsion system has to be aligned with the CoG. As the y-coordinate of the CoG is aimed to be zero, the propulsion system envelope is located in the middle of the bus structure.

8 Propulsion

The propulsion subsystem is responsible for providing all manoeuvres required throughout the mission. Its primary role is to enable CAMs in response to conjunction warnings with space debris, thereby ensuring more spacecraft safety throughout its mission lifetime. In addition, it will support the orbit maintenance strategy by performing a strategic re-boost to lengthen the operational lifetime while still complying with ESA's debris mitigation requirements [48]. The AOCS subsystem is designed to be fully responsible for attitude control and momentum management, so the propulsion system does not need to be designed to fulfil that function. The ΔV budget required to fulfil these functions has been defined at the mission level in Section 4.6 and is used as an input for the propulsion system design and sizing.

8.1. Key requirements

Table 8.1 shows the key requirements that were used to size the propulsion subsystem.

Requirement ID	Requirement Text	Rationale
REQ-PROP-C-SYS017-001	The propulsion system shall provide 14.93 m/s ΔV to perform all required space debris CAMs during the entire mission lifetime.	To ensure spacecraft safety by enabling timely avoidance of conjunction events with space debris. Following ECSS space debris rules. More on the debris environment in Section 4.5.
REQ-PROP-C-SYS019-002	The propulsion system shall provide 8.64 m/s ΔV to perform an injection error correction in case the Vega-C put us below the desired 550 km orbit.	To ensure that the increased drag below 550 km does not decrease our orbit too much within the nominal operations phase. The amount of ΔV comes from the injection error of the Vega-C.
REQ-PROP-O-MIS002-003	The propulsion system shall provide 37.71 m/s ΔV to support orbit maintenance activities.	Drag has to be countered with one re-boost. Further explained in the orbit maintenance strategy in Section 4.6.
REQ-PROP-O-SYS017-005	The propulsion system shall perform the ΔV commanded by the ground for orbit control with an accuracy better than the maximum of 5% of the ΔV magnitude along the commanded direction and 0.005 m/s.	To ensure predictable orbit control and prevent longitudinal orbit errors.
REQ-PROP-O-SYS017-006	The propulsion system shall perform the ΔV commanded by the ground for orbit control with an accuracy better than the maximum of 5% of the ΔV magnitude on the perpendicular directions (parasitic impulses) and 0.005 m/s.	To limit parasitic impulses that could degrade orbit accuracy and attitude stability.
REQ-PROP-C-LAUN007-001	The propulsion system shall not be bigger than 414 mm in the x-direction.	Derived from internal spacecraft structural and launcher clearance constraints.
REQ-PROP-C-LAUN007-002	The propulsion system shall not be bigger than 663 mm in the y-direction.	Derived from internal spacecraft structural and launcher clearance constraints.
REQ-PROP-C-001	The propulsion system shall be aligned with the spacecraft's CoG.	To ensure that no parasitic torques or sudden tumbling of the spacecraft occur during manoeuvres.

Table 8.1: List of requirements for the design of the Propulsion subsystem

8.2. Assumptions

For the propulsion subsystem design, several assumptions have been made. These assumptions are listed in Table 8.2, along with their design impact and potential consequences if they prove to be invalid.

Table 8.2: List of assumptions for the propulsion subsystem

Assumption ID	Assumption / input	Justification	Design Impact	Consequences if Invalid
ASSU-PROP-01	The Vega-C launch vehicle will inject the spacecraft into the target orbit altitude of 550 km with an accuracy of ±15 km.	This accuracy is consistent with the typical SSMS insertion performance of Vega-C as provided in launcher documentation [19].	If injected into a lower orbit, the propulsion system must correct the orbit to meet mission lifetime requirements.	An additional ΔV would be required, increasing propellant mass, propulsion system size, and spacecraft bus size.
ASSU-PROP-02	The Vega-C launch vehicle will inject the spacecraft into the target inclination of 45° with an accuracy of ±0.1°.	This accuracy is consistent with the typical SSMS insertion performance of Vega-C as provided in launcher documentation [19].	We do not size propellant for big inclination correction burns, so the ΔV budget stays much smaller.	Inclination correction manoeuvres would be required, leading to a large increase in ΔV demand and propellant mass.
ASSU-PROP-03	The propulsion system is not required to provide ΔV for de-orbiting at the EOL.	At less than 475 km, the spacecraft will de-orbit within the 5-year ECSS time-frame. More on this in Section 4.7.3.	Decreasing propellant needed during the mission lifetime, lowering subsystem mass and volume.	The propulsion system would require additional ΔV capability.
ASSU-PROP-04	A configuration of four thrusters is sufficient to compensate for unknown CoG offsets and thrust misalignments.	A symmetric four-thruster configuration allows thrust vector balancing and reduces sensitivity to CoG uncertainties.	With four thrusters, we can better balance forces and reduce unwanted torques, making it easier for AOCS to keep the spacecraft stable during burns.	Residual torques could be introduced during burns, increasing AOCS load and reducing manoeuvre accuracy.
ASSU-PROP-05	Propulsion performance parameters are assumed to be theoretical values taken from manufacturer data sheets.	Public performance data is an accurate estimate for the early design stage.	Sizing calculations are based on nominal thrust, Isp and impulse bit values, simplifying the early design phase.	Lower-than-expected performance would require additional propellant or longer burn durations.
ASSU-PROP-06	The propulsion system is not used for attitude control or momentum dumping.	AOCS is designed to fully handle attitude control and wheel momentum management, so PROP is only needed for orbit control and translational manoeuvres.	Thrusters and plumbing are sized and placed for ΔV manoeuvres only, without needing continuous small torques for attitude control.	If PROP is needed for attitude or dumping, it would increase firings, propellant usage, operational complexity, and could drive a different thruster configuration.
ASSU-PROP-07	The Centre of Mass (CoM) of the propulsion system is assumed to remain constant over the mission lifetime.	Propellant is assumed to be equally redistributed on the tank surface by surface tension and the self-pressurised mechanism of Dawn.	Thruster alignment and disturbance torque analyses assume a fixed propulsion CoM.	A varying CoM could introduce unexpected torques during burns, degrading ΔV accuracy and increasing AOCS load.
ASSU-PROP-08	Both propellant tanks are assumed to be depleted at the same pace, resulting in no CoM shift for the spacecraft in the y-direction.	No detailed information has been provided by Dawn on propellant depletion behaviour; for preliminary design, this assumption is sufficiently accurate.	The propulsion system does not introduce induced torques throughout the mission.	Uneven depletion could induce torques, degrading attitude stability during burns.
ASSU-PROP-09	For the selected B20 thruster, exactly 50% of the length consists of the valve assembly and 50% of the nozzle.	Based on visual inspection of the B20 thruster [29] and interpretation of available data from Dawn Aerospace.	Used for preliminary internal volume allocation and external thruster sizing.	Violation of internal volume or external envelope constraints, requiring structural redesign.
ASSU-PROP-10	The valve assembly is located on the inside of the spacecraft, with only the nozzle protruding externally.	There is no available data from Dawn on how its SatDrive thrusters are implemented.	This assumption determines how much of the thruster fits inside the bus and how much protrudes, which affects both packaging and launcher clearance.	If the valve block must be outside, the external envelope increases and the current integration concept may not fit, forcing a redesign of the propulsion placement.
ASSU-PROP-11	Density of the N_2O & C_3H_6 propellant mixture is assumed to be 720 kg/m^3.	The exact mixture density is not yet confirmed by Dawn, so a representative preliminary value is used for early tank sizing.	Directly sets the required tank volume, thereby driving the propulsion envelope and spacecraft packaging.	If the true density is lower, the required tank volume increases, and the current packaging may not close; if higher, the design is conservative but may be oversized.
ASSU-PROP-12	A 2% residual fraction is included as unusable propellant in the tank(s).	Some propellant is always left due to trapped volume and operational cut-off; 2% is used as a standard early-design allowance.	Increases loaded propellant mass above usable propellant and slightly increases the required tank volume.	If residuals are higher, usable ΔV margin reduces, and CAM/re-boost requirements may not be met; if lower, the design is slightly conservative.
ASSU-PROP-13	The tanks of the propulsion module shall be sized plus 10 %.	From the ESA mass margin requirement R-M2-9	Increases tank volume relative to propellant volume and drives packaging/envelope sizing.	If the margin is higher, the tank volume must increase; if lower, the design is conservative and could be reduced.

8.3. Final Design

8.3.1. Architecture

To fulfil the propulsion roles, an integrated chemical bi-propellant propulsion system from Dawn Aerospace is selected as the subsystem architecture. Their propulsion system can be modulated according to the customer's preferences and mission parameters. As our spacecraft falls in the SmallSat group, it will be a customised SatDrive design. This design is a suitable solution for our mission because it can deliver high thrust over short burn durations, which are required for time-critical CAMs. This has been the primary driver in choosing this propulsion system, as it requires the spacecraft to perform high-thrust manoeuvres and ensure safe mission continuation.

Reviewing other types of propellants that could fit the mission profile, electrical propulsion was a viable option because it has a high specific impulse and low mass and volume, but after consultation with space propulsion expert A.Cervone [26], it became clear that performing CAMs with this type of propulsion increases the collision risk if the debris is not detected with enough time upfront. It is orders of magnitude lower in thrust than chemical propulsion and will not be able to rapidly achieve a velocity change. Hydrazine, a common propellant in the space industry, is highly reliable but very toxic, corrosive, and relatively heavy, making it unsuitable for our small satellite sustainable mission profile. Lastly, green monopropellants and other bipropellants were also options, but have limited heritage, and the thrusters that use these propellants have not been developed in the 10-100 N thrust range needed for our mission. This level of thrust was advised by A.Cervone, due to the importance of the CAMs requirement. An overview of green mono- and bi-propellants can be seen in Table 8.3. This overview has been added because if development reaches a higher TRL, these propellants would be good candidates for the propulsion system.

Thruster name	Propellant type	Max thrust per thruster	Heritage (TRL)
HPGP	LMP-103S	22 N	Only 1 N thruster (7) [33]
GR-22	ASCENT	25 N	GPIM had GR-1 (7) [88]
Ocelot	HTP & Alcohol	22 N	SHERPA-LTC2 (9) [117]
B20	N2O & C3H6	18.11 N	>100 thrusters flown in space (9) [29]

Table 8.3: Green mono- and bi-propellant options

The other bi-propellant, HTP & Alcohol, used by the Ocelot thruster, has only flown on one mission, so its heritage is worse than Dawn's B20 thruster. The customised propulsion system is fully integrated, making it easy to adapt to our satellite. It consists of 4 main components, as shown in Table 8.4 along with their purposes.

Table 8.4: Propulsion system components and important characteristics

Component	Purpose
B20 thruster (4x)	Provides thrust for orbit, injection correction, CAMs and one re-boost.
Self-pressurised tank system	Stores bipropellant and provides it to the feed system.
A feed-and-valve manifold	Distributes propellant from tanks to thrusters and acts as a common control and safety point for propellant flow.
Propulsion Control Unit (PCU)	Interfaces the propulsion subsystem with the spacecraft's C&DH and EPS subsystems, executes thruster commands and valve control, and monitors propulsion system health and status.

The thruster set consists of four B20 thrusters (bi-prop and cold-gas capability), each equipped with four normally-closed solenoid valves (2 for firing, 2 for redundancy), a spark igniter, and integrated sensing (thermocouple, pressure sensor) [29]. The bi-propellant is in a self-pressurising system using nitrous oxide (N_2O) as oxidiser and propylene (C_3H_6) as fuel. Propellants are stored separately and maintained at their respective vapour pressures (no pressurant tanks or pumps). Operationally, the system is constrained to the stated temperature ranges (operational: -5°C to 30°C; survival: -30°C to 40°C) [7].

In Figure 8.1, the internal interfaces between propulsion subsystem components and the external interfaces with the EPS and C&DH are shown.

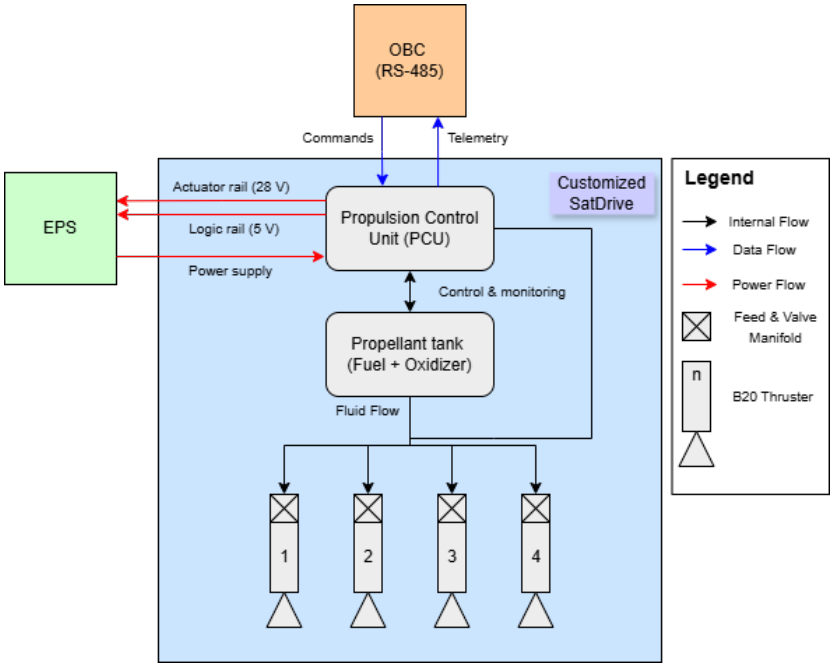

Figure 8.1: Hardware block diagram of the Propulsion system

Two electrical power interfaces are provided by the EPS: a 5 V logic rail and a 28 V actuator rail. The logic rail supplies continuous power to the PCU and associated low-power electronics, enabling monitoring, communication, and command processing at all times. The actuator rail provides power to high-power loads, such as thruster valves, igniters, and heaters, and is required only during propulsion-related operations.

Internally, the PCU distributes control signals to the feed-and-valve manifold and to the thrusters, while simultaneously collecting sensor data from these components. These internal interfaces are supplier-managed and abstracted at the spacecraft level, with the propulsion subsystem treated as a single functional unit. This architecture limits the number of spacecraft-level interfaces, reduces integration complexity, and isolates propulsion-specific functionality from the rest of the spacecraft avionics.

Internally, the PCU distributes control signals to the feed-and-valve manifold and to the thrusters, while simultaneously collecting sensor data from these components. These internal interfaces are supplier-managed, with the propulsion subsystem treated as a single functional unit. The PCU is integrated into the custom SatDrive, so Dawn Aerospace will be the supplier of this component. This architecture limits the number of spacecraft-level interfaces and reduces integration complexity.

8.3.2. Sizing

Based on the selected propulsion architecture, the subsystem is sized to satisfy the requirements in Table 8.1. The mission ΔV budget is the primary driver and, together with the assumed propulsion performance in Table 8.2 and the spacecraft dry mass, is translated into required propellant mass and tank volume, with tank volume driving the subsystem envelope and integration.

Sizing is performed with a Python tool to enable rapid iteration as the ΔV budget and dry mass mature [140]. Due to limited supplier response time, several configuration details remain assumptions; however, the same tool can later be updated with detailed inputs or even adapted to alternative chemical architectures. Based on mission needs and discussions with SRON, including potential cost reduction via sponsorship, Dawn Aerospace remains a strong candidate supplier.

The model follows a top-down chain from ΔV to the packaged envelope. Usable propellant mass is computed with the rocket equation from total ΔV and effective I_{sp}, using the spacecraft dry mass including the 20 % ESA system margin. Loaded propellant mass is then obtained by adding 2 % residuals, and tank volume is derived

from the assumed density and fill fraction, followed by an additional 10 % tank-volume margin [82].

For the bi-propellant system, the loaded propellant is split into oxidiser and fuel using an assumed O/F ratio of 8 (representative of Dawn's off-the-shelf tanking approach). Oxidiser and fuel volumes are converted into preliminary tank geometries using a thin-walled cylindrical approximation (1 mm shell thickness) with an outer diameter constrained by lateral spacecraft packaging. With diameter fixed, the required tank lengths along the thrust axis are calculated directly; consistent with SatDrive layouts, the tanks are treated as stacked, so total tank length equals $L_{\text{ox}} + L_{\text{fu}}$.

Because the detailed geometry of the feed-and-valve manifold and Power Conditioning Unit (PCU) is unavailable for the customised configuration, the overall propulsion envelope is closed by analogy with an SD15-class SatDrive, which best matches the current propellant mass and total impulse. The SD15 allocation is used to verify fit: adopting a 20 cm diameter constraint and a 54 cm reference length (from visual interpretation of SD15 dimensions), the computed stacked tank length of 44.6 cm remains within the SD15-class envelope after rearranging the tanks to match the spacecraft bus constraints, consistent with Dawn's modular approach.

A bottom-up dry-mass build-up is not performed due to the lack of public part-level data and limited supplier-specific information within the project timeframe. Instead, subsystem dry mass is closed using SD15-class heritage and updated to replace B1 thrusters with B20 thrusters; thrusters are assumed to be externally mounted near the spacecraft centre of mass to reduce induced torques and support manoeuvre accuracy. From usable propellant and I_{sp}, total available impulse is derived, and the model also reports EPS power requirements (steady/peak) for the most power-demanding firing configuration (four thrusters). Steady power is the continuous demand to keep the propulsion system enabled for command, telemetry and monitoring, while peak power is the maximum instantaneous demand, typically during ignition.

The propulsion sizing outputs that are used throughout the remainder of the spacecraft design are summarised in Table 8.5.

Table 8.5: Propulsion System Sizing outputs

Parameter	Value
Propulsion subsystem dry mass	13.04 kg
Loaded propellant mass	8.91 kg
Required tank volumes	12.09 L (Ox) / 1.51 L (Fu)
Propulsion envelope (rearranged SD15)	0.25 (X) x 0.54 (Y) x 0.25 (Z) m
Total usable impulse I_{tot}	23227 N s
Total thrust (4 firing at max thrust)	72.44 N
Firing power (steady / peak)	6.08 / 141.68 W

8.3.3. ΔV Execution Accuracy Analysis

The ΔV execution accuracy requirements state that the realised Δv shall be within

$$\epsilon_{\text{max}} = \max(0.05\,\Delta V_{\text{cmd}},\, 0.005) \quad [\text{m/s}] \tag{8.1}$$

Here, ΔV_{cmd} denotes the manoeuvre magnitude commanded by ground operations, and the execution accuracy requirements bound the deviation between realised and commanded ΔV. For small commanded manoeuvres ($\Delta V_{\text{cmd}} \leq 0.1$ m/s), the requirement is therefore dominated by the fixed floor of 0.005 m/s. This will be the case in a CAMs where the incoming debris is notified way upfront, so a minimal amount of ΔV is needed. To verify compliance analytically at the current design maturity, a pulse-mode error model is applied. This error model has also been added to the Python sizing model [140]. In the commanded direction, the dominant limitation is the discrete impulse delivery caused by the Minimum Impulse Bit (MIB). When N_f thrusters fire simultaneously, the effective system impulse bit increases linearly,

$$\text{MIB}_{\text{sys}} = N_f\,\text{MIB}_{\text{thr}}, \tag{8.2}$$

and the corresponding velocity step per pulse becomes

$$\Delta V_{\parallel,\text{pulse}} = \frac{\text{MIB}_{\text{sys}}}{m}. \tag{8.3}$$

Since only an integer number of pulses can be commanded, the smallest achievable commanded-direction accuracy is limited by quantisation. A bound is obtained by assuming a rounding of half a pulse:

$$\epsilon_{\parallel} \leq \frac{1}{2}\Delta V_{\parallel,\text{pulse}}. \tag{8.4}$$

For the current design, the transition point for bi-propellant operation with $N_f = 4$ occurs at $\Delta V_{\text{cmd}} = 0.102$ m/s, where the scaled requirement $0.05\,\Delta v_{\text{cmd}}$ becomes equal to the half-pulse bound. For manoeuvres above this threshold, the commanded-direction quantisation error remains below the requirement limit, meaning that ΔV execution accuracy is compliant for both two- and four-thruster firings. Consequently, the baseline operational approach is to execute nominal manoeuvres with two thrusters, while keeping two additional thrusters for redundancy.

In the perpendicular direction, parasitic ΔV is modelled as a small-angle cross-axis component caused by thruster alignment and attitude pointing errors during firing. These are combined into an effective angle $\theta_{\text{eff}} = \sqrt{\theta^2_{\text{align}} + \theta^2_{\text{point}}}$. From Table 9.9, the pointing error is 26.13 arcsec, which corresponds to $\theta_{\text{point}} = 0.00726°$. The thruster alignment error is assumed to be $\theta_{\text{align}} = 0.5°$ [128] together they are used to project $\Delta V_{\perp,\text{pulse}} = \Delta V_{\text{pulse}} \sin\theta_{\text{eff}}$, which is accumulated over the pulses required to realise ΔV_{cmd}. Table 8.6 summarises the model outputs that drive pass/fail for representative commanded manoeuvres and firing configurations.

Table 8.6: Results of the ΔV execution accuracy analysis

Mode	N_f	ΔV_{cmd} [m/s]	Req. limit [mm/s]	$\epsilon_{\parallel}$ [mm/s]	$\Delta V_{\perp,\text{tot}}$ [mm/s]
Bi-prop	4	0.10	5.0	5.050 **(FAIL)**	0.882 **(PASS)**
Bi-prop	4	0.20	10.0	5.050 **(PASS)**	1.763 **(PASS)**
Bi-prop	2	0.10	5.0	2.525 **(PASS)**	0.882 **(PASS)**
Bi-prop	2	0.20	10.0	2.525 **(PASS)**	1.763 **(PASS)**
Cold gas	4	0.10	5.0	0.052 **(PASS)**	0.882 **(PASS)**
Cold gas	4	0.20	10.0	0.052 **(PASS)**	1.763 **(PASS)**

8.3.4. Functions and Operations

The propulsion system is designed around a symmetric thruster arrangement aligned with the velocity vector to minimise disturbance torques during a commanded parallel manoeuvres. To re-boost to a higher altitude for orbit maintenance, it is preferred to fire all four thrusters to maximise thrust and minimise burn time, thereby limiting disturbance effects and time in burn mode. This also provides the best geometric symmetry, reducing the sensitivity to thrust inaccuracies and alignment errors. These could otherwise introduce parasitic torques, where AOCS has to correct more, which is undesirable. If bi-prop is preferred to achieve high thrust in short burn times, a practical baseline is to ignite two thrusters in a symmetric configuration, with the other two as redundancy. The best firing strategy mainly depends on the required burn time, the total thrust level, and the urgency of the manoeuvre. For short-notice CAMs, the key driver is the available response window: the burn must be feasible within the available time and reduce the collision probability below the chosen safety threshold. Rapid CAMs methods therefore focus on optimising burn timing, direction, and duration under tight constraints, rather than assuming low thrust is always better [108]. Lower thrust can be useful when there is enough warning time, but very short-notice cases may require higher thrust. Also, coarse ΔV control is mainly driven by minimum impulse bit, timing and pointing errors, not thrust alone. A detailed rapid CAM optimisation study (as in Reiter) could not be conducted within the DSE time frame. Since CAMs are critical for spacecraft survival, this should be addressed in further research.

Using the propulsion system follows a specific burn sequence: preparation, execution, and recovery, as explained in the following sections.

Burn preparation

Before any manoeuvre, the spacecraft is transitioned into a dedicated propulsion-ready state:

1. Planning: The commanded ΔV vector magnitude and execution window are generated.
2. AOCS alignment: attitude is aligned with commended thrust direction.
3. Thermal conditioning: hardware is brought to operational range [-5°C, 30°C] using the available tank/feed line heating capability.[29]
4. Checks: electronics are enabled, and health checks are performed. Temperature in range, voltages stable, no fault flags from PCU. Valves remain closed until T0, the start of the burn execution.

Burn execution

During burn execution, there are three coupled flows happening at the same time:

1. Data flow: at a planned time, the C&DH fires a command to the PCU. That command defines which thrusters fire and how the impulse is delivered (continuous or pulse sequence). In parallel, telemetry is returned for monitoring. Key parameters are the temperature in the thruster and lines, and pressure or health flags. AOCS continuously runs to keep the thrust vector aligned to the commanded direction.
2. Power flow: as explained Section 8.3.1, the PCU sits on the low-voltage logic rail and is processing at all times at low power. For burn execution, the actuator rail is used, where each valve actuation has a short 'hit' event to open the valve, followed by a low 'hold' power to keep it open. Ignition is transient to start the bi-prop mode. This is why the propulsion power profile has a short peak during pulsing and a low steady-state power during a continuous burn.
3. Propellant mass flow: oxidiser and fuel are stored separately and flow through the feed system towards the selected thruster(s). When a burn starts, the PCU opens relevant valves so that oxidiser and fuel flow in the following sequence: tanks -> feed-and-valve manifold -> combustion chamber. In bi-prop mode, the igniter is engaged at startup to initiate combustion, and the thruster produces hot-gas thrust. In cold-gas mode, the igniter is not engaged, and the system delivers low impulse bits for fine control. Same flow path but without combustion. If errors occur in, for example, attitude, thermal or propulsion control, the burn is aborted by closing valves and returning to a normal state.

Post-burn recovery

1. Safing: valves close (normal state), igniter disabled and propulsion return to inhibited state.
2. Thermal stabilisation: heaters return to standby; for larger ΔV executions, they may remain active between burns to avoid repeated cold starts.
3. Verfication: orbital parameters updated to estimate achieved ΔV and decide if a correction (often cold-gas) is required.

Propulsion manoeuvres are executed in Orbit Maintenance Mode and are entered from Standby. Safe Mode is only used as an abort path in case of a critical fault. For CAMs, the operational sequence is optimised for short response time while allowing the firing configuration to be selected based on the commanded ΔV. After a CAM request is received, the spacecraft first slews to the burn attitude and stabilises to the required pointing tolerance. In parallel, the propulsion subsystem is prepared by running the required health and readiness checks and transitioning to a 'ready-to-fire' state. The burn is then executed at the planned time, after which the propulsion subsystem is safed and the spacecraft returns to its nominal science attitude. Finally, orbit determination is updated using post-burn tracking/telemetry to reconstruct the achieved ΔV and confirm that the manoeuvre objective was met. If a critical fault is detected during preparation or firing, the burn is aborted (valves closed, ignition disabled) and the spacecraft transitions to Safe Mode and subsequently Troubleshooting Mode for recovery.

For the planned re-boost manoeuvre, the sequence is executed as a two-impulse Hohmann transfer from 475 km to 540 km altitude. First, the spacecraft slews to the burn attitude and holds pointing while the propulsion subsystem is prepared for the first burn. After Burn 1, the spacecraft enters a coast phase towards apogee, during which the propulsion system remains standby-ready and conditioned for a second ignition while AOCS maintains the required attitude constraints. Near apogee, the spacecraft re-establishes the burn attitude, the propulsion subsystem is re-armed, and Burn 2 is executed to circularise the orbit. After the second burn, the propulsion subsystem is safed and post-burn orbit determination is performed to verify the achieved orbit before returning to nominal operations.

8.4. Risk Assessment

Table 8.7 shows an FMEA of the propulsion subsystem. These include risks associated with the final design as well as those that influenced its decisions. The latter were addressed throughout Section 8.3 and will be related to redundancy and operational mitigations in Section 8.5.

Table 8.7: FMEA for Propulsion

Risk ID	Failure Mode	Effect	Cause	L	S	Risk	Mitigation
R-SUB-PROP-001	PCU failure	Propulsion cannot be commanded or monitored correctly; manoeuvre is delayed or aborted.	Electronics fault, software fault, radiation upset, harness/interface issue.	A	3	A3	Safing by default (valves closed), watchdog/FDIR, health telemetry and clear recovery procedure.
R-SUB-PROP-002	Single thruster failure	Reduced thrust and symmetry; longer burn and higher disturbance torques.	Thruster internal fault, degradation, contamination.	A	2	A2	Two- and three-thruster symmetric firing options, validated burn templates, acceptance testing.
R-SUB-PROP-003	Ignition failure / misfire	Burn start is delayed or missed; CAM timing margin reduces.	Propellant thermal/-pressure transient after previous burn reduces immediate restart readiness	B	3	B3	Switch to cold-gas mode for small manoeuvres, delay manoeuvre if allowed, pre-burn go/no-go checks.
R-SUB-PROP-004	Valve failure (single valve)	No significant loss of function at the thruster level due to redundant valves per thruster.	Electronics failure, mechanical sticking, contamination.	B	1	B1	Valve redundancy at thruster level (two valves per B20 thruster), plus monitoring to detect degraded behaviour.
R-SUB-PROP-005	Propellant leak	Reduced propellant budget; fewer CAMs possible and reduced margin for reboost and disposal.	Manufacturing or assembly defect, seal/weld defect, mechanical damage. Driven by customised tank volume and integration.	B	3	B3	Proof and leak testing, pressure trending in operations, strict propellant bookkeeping with reserved disposal budget.
R-SUB-PROP-006	Late CAM notification	Less time to plan and execute an efficient CAM; higher fuel use or reduced achievable collision probability.	Late conjunction data, delayed ground decision, delayed command uplink. Operationally driven.	B	3	B3	Minimum notification-time threshold, pre-approved CAM templates; for short-notice events prioritise collision probability reduction; maintain propellant margin.
R-SUB-PROP-007	Insufficient ΔV for disposal	Disposal may take longer or require a less optimal strategy; occurs after mission objectives are met.	Budget growth, unexpected propellant usage, leak, lower performance than assumed.	A	2	A2	Apply ΔV margin and keep a dedicated disposal reserve sized for the 5-year compliance strategy.
R-SUB-PROP-008	Δv accuracy below threshold	Very small manoeuvres may be less accurate, increasing the chance of an additional trim manoeuvre; fine burns are expected to be infrequent.	MIB quantisation, thruster misalignment, attitude pointing error during firing.	A	2	A2	Two-thruster symmetric firing & cold-gas for fine burns. Increase allowance of thruster alignment error & attitude error. On-ground alignment measurement and on-orbit calibration.
R-SUB-PROP-009	Subsystem does not fit the spacecraft bus	Late re-layout impacts schedule and mass properties.	Custom tank envelope uncertainty and remaining unknown dimensions in packaged SatDrive. Driven by customisation and interface maturity.	B	3	B3	Envelope margin, SD15-based packaging reference, early fit checks when detailed data is available.

8.5. Redundancy

The propulsion redundancy approach is driven by the risk assessment and follows the same single-point-failure-avoidance philosophy as the other subsystems. This means redundancy is applied only to functions whose loss would prevent meeting key mission needs, mainly collision avoidance and the ability to perform reboost and

end-of-life disposal. Failures that only reduce performance but do not end the mission are mainly handled through monitoring and operations rather than adding extra hardware. The need for redundancy is judged by the combination of mission impact and likelihood. For the selected Dawn Aerospace architecture, many component-level risks are already reduced because the SatDrive and B20 hardware are flight-proven and delivered as an integrated, tested unit. Therefore, propulsion redundancy is mostly achieved through features built into the SatDrive and thrusters, and through spacecraft-level operational flexibility that avoids a single failure directly removing the propulsion function.

At spacecraft level, redundancy is mainly achieved through how the subsystem is used. For large or time-critical burns, four thrusters can be fired to minimise burn time and maintain symmetric thrust geometry. If one thruster degrades, the spacecraft can switch to symmetric two-thruster firing to maintain controlled manoeuvring with reduced thrust. For very small manoeuvres where finer accuracy is required, cold-gas mode can be used to decrease the ΔV resolution at the end of the manoevre.

At thruster level, redundancy is present in the valve design. Each B20 thruster contains two cold-redundant valves, so a single valve failure does not render the thruster inoperable. The thruster also provides temperature and pressure telemetry, which supports health monitoring and helps detect abnormal behaviour early. In addition, the B20 can operate in both bi-prop and cold-gas mode. This provides a practical fallback for small manoeuvres and cases where ignition is not preferred, thereby improving the robustness of manoeuvre execution.

For the PCU, redundancy is implemented as fault-tolerant behaviour rather than duplicated hardware. The default safe state is that valves remain closed unless a valid command is issued. If a command fault occurs, the manoeuvre is aborted safely and can be repeated after reset and recovery, using the available pressure and temperature telemetry to confirm readiness. For the propellant tanks, no true hardware redundancy is assumed. A tank leak is therefore treated as a real single-point failure. The mitigation is focused on fault avoidance and early detection. A dedicated disposal reserve is maintained so that credible leak or usage growth scenarios reduce margin but still preserve ΔV compliance.

Finally, any post-burn changes in temperature or pressure are treated as operational limitations, not as hardware failures. The mitigation is to only allow a burn when the system is “ready”, meaning key temperatures and pressures are within safe limits and stable. If the conditions are not met, the burn is delayed until the system returns to the allowed range. For sequential burns, the system is kept warm and pressurised between burns, allowing a second burn to be executed without a full shutdown and reactivation. This provides temporal redundancy, as the manoeuvre can be safely postponed and retried rather than forcing immediate execution.

8.5.1. Compliance Check

The propulsion subsystem meets the mission ΔV requirements, as the propellant mass and tank volume are explicitly sized to the required ΔV budget, and the Python outputs were cross-checked against hand calculations. The execution accuracy results in Section 8.3.3 show that, using a conservative half-pulse quantisation bound and a 1° thruster misalignment/pointing assumption, the commanded- and cross-axis accuracy requirements are met for CAMs operations with two thrusters firing, and also for four-thruster firings for manoeuvres above $\Delta V_{\text{cmd}} = 0.102$ m/s. Finally, the structural dimension requirements are verified by inspection, as the integrated propulsion system packaging remains within the spacecraft bus allocation and the launcher envelope constraints.

9
Attitude & Orbit Control System

The AOCS is responsible for maintaining the spacecraft's attitude to ensure survivability and mission performance. From Chapter 2, it can be concluded that pointing performance is a key driver for the science observations. This chapter first presents the key requirements and the assumptions made during the AOCS design in Section 9.1 and Section 9.2, respectively. Section 9.3 explains the selected AOCS architecture, along with a discussion of the method that results in the final design. Section 9.4 the different AOCS modes and the associated mode-switching logic. A FMEA is performed in Section 9.7, which leads to redundancy in Section 9.8. Finally, a compliance check of the key AOCS requirements is performed in Section 9.9.

9.1. Key requirements

Table 9.1 shows the key requirements that were used to size the AOCS subsystem. Using these key requirements, an initial sizing of the actuators was conducted. Following this initial sizing, a compliance check was performed to verify the design's adherence to all AOCS requirements. One note is that REQ-AOCS-F-SYS008-007 has sister requirements, namely REQ-AOCS-F-SYS008-008 and REQ-AOCS-F-SYS008-009. These are the same requirements, but about the Y and Z axes, respectively.

Table 9.1: Key requirements for AOCS design

Requirement ID	Requirement text	Rationale
REQ-AOCS-F-SYS008-003	The AOCS shall limit the line-of-sight pointing stability to less than 15 arcseconds Root-mean-squared (RMS) over any 1 s interval during nominal science observations.	A stability requirement to ensure accurate science measurements.
REQ-AOCS-F-SYS008-004	The AOCS shall maintain the line-of-sight pointing accuracy to within ≤ 150 arcsec (3σ) of the commanded boresight during nominal science operations.	An accuracy requirement to ensure accurate science measurements.
REQ-AOCS-F-SYS008-005	The AOCS shall limit the pointing drift relative to the initial boresight to ≤ 37.5 arcsec over any continuous 2400-second science observation.	An accuracy requirement to ensure accurate science measurements.
REQ-AOCS-F-SYS008-006	The AOCS shall provide reconstructed attitude knowledge such that the Attitude Knowledge Error (AKE) is ≤ 75 arcseconds (3σ) during nominal science observations.	An accuracy requirement to ensure accurate science measurements.
REQ-AOCS-F-SYS008-007	The AOCS shall provide the capability to perform attitude manoeuvres 180 degrees on $X_S C$ axis in less than 150 seconds, including the tranquillisation phase	Minimise time lost during target switching.
REQ-AOCS-F-SYS003-010	The AOCS subsystem shall ensure the spacecraft autonomously avoids any attitude that leads to insufficient power generation, thermal instability, or instrument compromise, throughout all mission phases and system modes.	To ensure spacecraft survival.
REQ-AOCS-F-SYS003-012	The AOCS shall autonomously transition the spacecraft to a safe attitude within 30 minutes of Launch Vehicle (LV)-separation or upon the detection of a major anomaly resulting in control loss.	To ensure spacecraft survival and limit the risk of battery discharge during eclipse or loss of communication.

9.2. Assumptions

In Table 9.2, a list of assumptions is given, which were used in the design process. It includes a justification of the assumption, its impact on the design and the consequences if it is deemed invalid.

Table 9.2: List of assumptions made during AOCS sizing

Assumption ID	Assumption/input	Justification	Design Impact	Consequences if Invalid
ASSU-AOCS-1	Circular LEO at an altitude of 475 km is used for disturbance and sizing simulations	This is the worst-case scenario in the current operational envelope	Allows the AOCS to be sized for a worst-case scenario using a representative orbital period.	If altitude differs, AOCS actuators need to be resized as the disturbance torque will be different.
ASSU-AOCS-2	The solar maximum atmospheric density is taken as a fixed worst-case value during sizing, equalling $8.28 \times 10^{-12}\,\mathrm{kg/m^3}$ (Table 4.2)	A conservative approach is taken, considering density, because density in reality varies and does not remain at its worst-case value for the entire orbit.	Conservative estimate of the atmospheric drag torque.	If the density is a lot lower, then there is a slower momentum build-up. This means that the actuators could be sized too large.
ASSU-AOCS-3	The external geometry of the spacecraft (bus faces and solar panels) can be represented by facets with forces applied at facet centroids.	This enables traceable torque estimations using a simplified model.	It is not an exact representation of how external forces interact with the spacecraft, so there is some over- or underestimation.	This directly influences the sizing of the actuators. Once there is a more exact model, the actuators will need to be resized.
ASSU-AOCS-4	The CoM location is constant for sizing simulations	This is a model simplification.	Allows disturbance torques to be computed about a fixed CoM	If CoM shifts (i.e. due to propellant usage), the disturbance torque affects change, and actuator sizing will be different.
ASSU-AOCS-5	Two attitude cases are considered for the simulations: inertial fixed and sun-pointing mode (in positive X).	This simplifies the analysis utilising attitudes commonly employed in science and safe mode.	Allows for generating torque histories without an attitude simulation.	If actual attitude profiles differ, it will influence the worst-case disturbance torques and thus the sizing of the actuators.
ASSU-AOCS-6	A simplified bus shadowing model is implemented for the Solar Radiation Pressure (SRP) where a facet is removed from the calculation if the vector to the sun intersects the bus bounding box.	This reduces the model complexity and is determined to be a conservative approach after analysis.	It allows the SRP torque to be conservatively estimated.	If shadowing is over- or underestimated, it will mainly affect mean drift torque and Magnetorquers (MTQ) sizing.
ASSU-AOCS-7	Magnetic disturbance torque is modelled using a constant residual dipole m_{res} of $2.0\,\mathrm{Am^2}$	A technical report from NASA provides a method to estimate the residual dipole [122].	This assumption provides a conservative estimate which can also be used for MTQ unloading analysis.	If this value increases, magnetic disturbance and unloading demand rise. This influences MTQ sizing.
ASSU-AOCS-8	Reaction Wheel (RW)s are arranged in a 4-wheel pyramid scheme, with a skew angle of $\approx 54.7°$.	This is a commonly used configuration and provides a balanced torque authority [132].	Meet three-axis control and redundancy goals and reduces required per wheel torque/momentum.	Per wheel loading may increase, or a single wheel failure could prevent full three-axis control.
ASSU-AOCS-9	For slews, a bang-bang slew profile is used to generate peak torque and momentum during slew.	This is a conservative approach for sizing as it requires more momentum storage from the system.	It mainly sizes the RWs conservatively, requiring more momentum storage than if it were a bang-coast-bang profile. The science time is estimated more optimistically due to this assumption.	If the slew profile is different, it will affect the RW sizing and also the available science time.
ASSU-AOCS-10	Continuous momentum management during nominal science operation is feasible using low-bandwidth MTQs unloading while RWs reject high-frequency disturbances.	Literature shows that continuous magnetic control can manage slow dynamics (i.e. drift) [125].	This assumption supports the concept of no scheduled desaturation windows and continuous bounded RW momentum	If MTQs cannot be used during science (i.e. due to magnetic cleanliness), then science time will be negatively affected.
ASSU-AOCS-11	Jitter due to RW unbalance is assessed using a rigid-body model, and flexible structural amplifications are neglected.	The structural model is not mature enough to assess flexible structural amplifications.	A first-order Loss of Signal (LoS) stability compliance check can be made.	If flexible modes amplify jitter, then REQ-AOCS-F-SYS008-003 could not be met.
ASSU-AOCS-12	The spacecraft tumble rate after LV-separation is taken as $1.5\,°$.	This is stated in the Vega-C manual [20].	This value is used to perform a compliance check for REQ-AOCS-F-SYS003-012.	If this value is higher due to issues during LV-separation, then current RW could saturate, and REQ-AOCS-F-SYS003-012 could not be met.
ASSU-AOCS-13	The RW mount has a mass of 25% of the RW mass.	This is a first-level approximation from SMAD [137].	This impacts the Mass Moment of Inertia (MMOI) of the spacecraft and thus the sizing of the actuators.	A re-sizing of the actuators would need to be conducted to account for the change in mass.
ASSU-AOCS-14	Large slews happen one axis at a time.	REQ-AOCS-F-SYS008-007 and its sister requirements state this, but not that they should be combined.	It reduces the sizing requirements of the RWs.	If a large combined slew is performed, RWs could saturate.

9.3. Final Design

9.3.1. Sensor selection

In order to select the sensor hardware for the AOCS system, first, the reference vectors needed for the mission must be identified. The focus of the NEBULA-Xplorer mission is the X-ray binaries. This implies that the primary attitude reference must be inertial, such as stars. They are the most accurate references and are the standard option for fine inertial pointing [10]. This is opposed to using Earth as a reference, for instance, as it is mainly fit for Earth observation missions. Fine sensing is necessary for missions needing < 0.5 deg accuracy [10].

From the different types of star trackers, a fixed-head star tracker is the most appropriate in comparison to gimbal star trackers, or star scanners [10]. Gimbal star trackers are also less reliable due to their moving mechanism. Section 9.8 about redundancy discusses the reasoning behind using multiple start trackers. A star tracker can provide discrete measurements of attitude at a limited update rate. Furthermore, star trackers may be blinded during slews due to the Sun or due to fast movement. They may also become unavailable during safe mode, post-separation and other anomalies. These constraints introduce non-compliance with the requirement REQ-AOCS-F-SYS008-003, REQ-AOCS-F-SYS008-004 and REQ-AOCS-F-SYS008-005. Therefore, other sensors must be introduced to support the subsystem and meet the requirements.

A system of gyroscopes can be introduced to enable continuous attitude determination. Together with a simple kinematic model, it can measure the angular rate and translate it to attitude parameters. This propagated attitude from the gyroscopes predicts which stars should be visible, which reduces the star identification problem for the star tracker [10]. The attitude and gyroscope bias are corrected, such that the propagation continues with improved parameters. Furthermore, the gyroscopes can measure angular rates during slews to control and stop rotations together with the actuators.

A solution is also needed for the post-separation stage, when the attitude is still unknown. There is no high confidence in the gyroscope bias, as they are not calibrated, and a first inertial reference is needed. Star identification is computationally expensive, so an initial attitude estimation is helpful. This first estimation can be done with a system of coarse sensors and magnetometers. The sun sensors and the magnetometer can provide a reference vector each. This system can provide a three-axis attitude determination during initial acquisition or during safe mode [10].

The mission also has a requirement for accurate orbital position knowledge, for which an additional navigation receiver is needed, such as a GNSS receiver. It is not an attitude sensor, but it supports the AOCS with accurate measurements of orbital position and velocity knowledge. It also aids with star tracker blinding avoidance and generating the best attitude profiles for science observations. Finally, a radiation sensor will be included in the design due to the need of detecting dangerous space environments. This is included in the AOCS because the AOCS Processing Unit (PU) is active during radiation protection mode (Section 5.3).

Table 9.3: AOCS Sensor Suite and Functional Roles

Sensor	Off-the-shelf component	Mass per unit [g]	Power consumption per unit [W]
Multiple-head Star Tracker	PST3S-H4	95	1
Gyroscope Set	WIS210Y	75	1.5
Coarse Sun Sensors	Bradford CSS	215	NIL
Magnetometer	PEGASUS-1	87	0.735
GNSS receiver	GNSS-701	160	0.9
GNSS antenna	GNSS L1/E1 Bands Antenna	119	0
Radiation sensor	SPACEDOS01	0.033	0.030

9.3.2. Actuator selection

For this mission, the combination of RWs and using MTQs for desaturation is used. This combination is used due to its heritage in similar missions. As the main drivers for the AOCS are the pointing requirements, this

combination of actuators should perform optimally. An investigation into another actuator, namely micro-thrusters, was conducted. This option was dismissed due to the high-drag characteristic and longevity of the mission.

Before components are selected, the minimum requirements for the components must be computed. This was done using a simulation [139]. First, the disturbance torques must be defined, and the worst case must be identified. After this, the torque and momentum required to reject the worst case disturbance torques must be compared to REQ-AOCS-F-SYS008-007, REQ-AOCS-F-SYS008-008 and REQ-AOCS-F-SYS008-009 to find the overall worst case. This case shall then be used to size the RWs and MTQs. With this sizing, COTS components are selected. Using the parameters of those components, a compliance check is performed to check if all other AOCS requirements are fulfilled. For the actuator sizing, the following MMOI are used: I_{xx} = 75.971 kgm^2, I_{yy} = 63.307 kgm^2, I_{zz} = 49.657 kgm^2.

Simulation framework

A simplified spacecraft model is used to perform orbit simulations. The results are used for disturbance torque estimations, momentum management strategy analysis and a compliance check. The relevant assumptions can be found in Table 9.2, but this section will summarise the modelling approach and how the spacecraft is represented. All parameters used for the simulation can be found in Appendix A.

The external geometry of the spacecraft is represented by facets (ASSU-AOCS-3). Each facet corresponds to a face of the bus or a solar panel and is defined by its area, centroid location, surface normal vector, and its reflectance factor. With this model, external forces are evaluated by applying them at facet centroids. The torques are then computed around the CoM. The location of the CoM is treated as an input parameter, as this shifts throughout the design process. A simplified bus-shadowing model is implemented, where the bus can shadow incoming external forces. If an external force vector towards a facet centroid first intersects the bounding box of the bus, that entire facet is omitted from the torque computation. This conservative approach was taken due to the time and resources available during this project, and a more precise model can be created for future work.

An orbit is simulated to evaluate the disturbance torques. This is done by computing the external environment vectors (e.g. velocity direction) needed by each disturbance model. A time-history is created, which produces the necessary time-varying vectors. The simulation is run for at least one orbit, such that the periodic behaviour of the environment is estimated. Next to evaluating disturbance torques, the orbit simulation is also used to run specific scenarios to verify that the spacecraft complies with certain requirements and for momentum strategy analysis.

Disturbance torque estimation

This section explains how the disturbance torques were used to size the AOCS actuators. Following SMAD, the total disturbance torque was modelled by summing the 4 main contributors: SRP, aerodynamic drag, gravity gradient and the magnetic dipole torque [137]. The combined disturbance torque history will be used to extract (i) the peak disturbance torque per axis for wheel torque authority and (ii) the accumulated torque for wheel momentum build-up and MTQ sizing. Figure 9.1a shows the simulation results over a full orbit. Here, it is clear that drag is the dominating force. This is because the worst-case orbit with an altitude of 475 km at a solar maximum is used. Figure 9.1b shows the direction of the total disturbance torque over one full orbit.

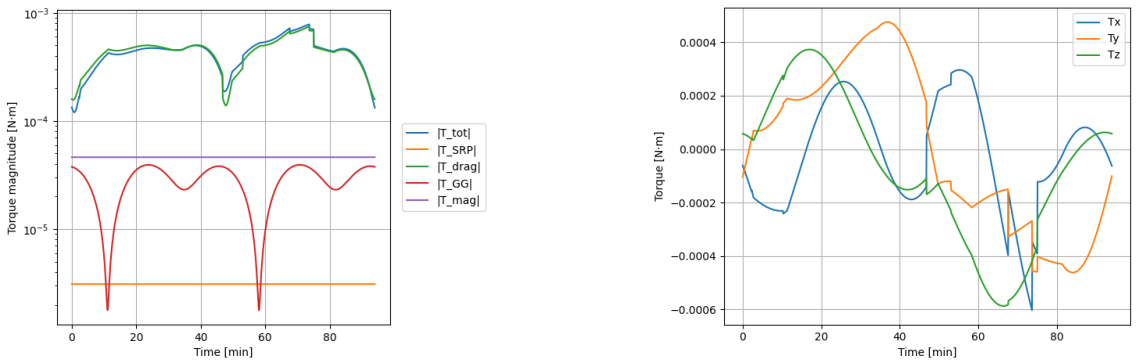

(a) Magnitude of disturbance torques on the spacecraft

(b) Direction of disturbance torques on the spacecraft

Figure 9.1: Disturbance torque graphs over one orbit

RW sizing

The RW sizing is performed to satisfy torque authority and momentum storage requirements of the most limiting case. The largest order of magnitude in Figure 9.1a is 10^{-4} for the total disturbance torque magnitude. This is compared to the required torque for slew, which has been derived from the slewing requirement (REQ-AOCS-F-SYS008-007) and the spacecraft geometry, and it is equal to 4.243×10^{-2} Nm. This is two orders of magnitude larger than the disturbance torques, so slew will drive the RW torque sizing and thus becomes the body torque requirement.

The wheel momentum storage must be sufficient to prevent saturation of the wheels due to slew and disturbance-driven momentum accumulation over time. For the sizing, the worst-case is defined as the maximum accumulated momentum during one orbit, followed directly by a maximum slew. Assuming a bang-bang slew profile, performing a slew according to REQ-AOCS-F-SYS008-007 contributes a peak body momentum of 3.182 Nms. The momentum build-up due to disturbance torques is obtained by integrating the disturbance torque history. This history is decomposed into a mean (drift) and a zero-mean component. The mean is assumed to be managed by the MTQs, which will be discussed in the next section. The remaining de-trended momentum determines the required wheel momentum capacity together with the peak slew momentum. This is a valid approach, provided that the MTQs are sized to reject the mean drift torque with margin and that desaturation is performed regularly. After adding the de-trended disturbance peak to the peak slew momentum, it results in a combined peak body momentum requirement of 4.771 Nms about the Y-axis. This value includes a 20% margin.

Table 9.4 shows a summary of the calculated sizing requirements above. It also includes the design values of a COTS component from Blue Canyon Technologies that meets the sizing requirements [133]. Do note that there is an important distinction between the required and selected values. Namely, the required values are for the body, and the selected values are per wheel. The required body value can be met by choosing an appropriate configuration of RWs.

Table 9.4: Summary of the RW sizing requirements and chosen design

Req.	Required (body-level)	Selected wheel capability
Body torque requirement [Nm]	4.243×10^{-2}	0.25
Peak body momentum requirement [Nms]	4.771	4.0

The RWs will be configured in a 4-wheel pyramidal configuration. This design of this configuration can be seen in Chapter 15. This configuration is commonly used as it has practical advantages, such as managing momentum saturation and ensuring reliability. Following ASSU-AOCS-8, the spin axes of the reaction wheels are oriented at an angle of approximately 54.7 ° from the spacecraft principal axis. This results in a well-balanced system. There are, however, studies that show optimisation methods for this skew angle to minimise power usage and angular momentum [3]. The application of this research was for a different class of spacecraft,

so further investigation can be done to apply it to this mission.

MTQ sizing

The MTQs are sized to counteract the mean (drift) torque, and the resulting design is then checked for its momentum removal capabilities per orbit and used for the momentum management analysis. From the disturbance torque simulation, the mean disturbance torque vector and magnitude are concluded, with the magnitude equalling 7.355×10^{-5} Nm. This result represents the value that would cause long-term momentum build-up.

Given the margins stated in Table 9.2, a total dipole of 9.88 Am^2 is computed. For this design, three orthogonally placed MTQs are used. This translates to a per rod requirement of 5.70 Am^2 using the following relation:

$$m_{max} = \sqrt{m_x^2 + m_y^2 + m_z^2} = \sqrt{3} m_{rod} \tag{9.1}$$

Because unloading can be dominated by one axis and the usable dipole depends on the B-field geometry, a larger per rod dipole is selected. A COTS component from Zarm Technik was selected, which provides a magnetic dipole of 10 Am^2 per rod [112]. This higher dipole also helps bias the RWs away from saturation. Section Momentum management uses the selected MTQ design and discusses how the momentum management is tackled.

Momentum management

As science time is one of the driving requirements for this mission (REQ-MIS-F-012), momentum management is performed continuously during science operations and not in scheduled dumps. The MTQs are continuously active to keep the RWs away from saturation. To preserve pointing stability, MTQ commands have a derated authority, such that RWs remain responsible for rejecting high-frequency disturbances (ASSU-AOCS-10). At the same time, MTQs remove only the low-frequency momentum trend. In the sizing analysis, this is captured by applying a 50% derated MTQ unloading torque during science, ensuring drift cancellation capability without introducing significant control jitter.

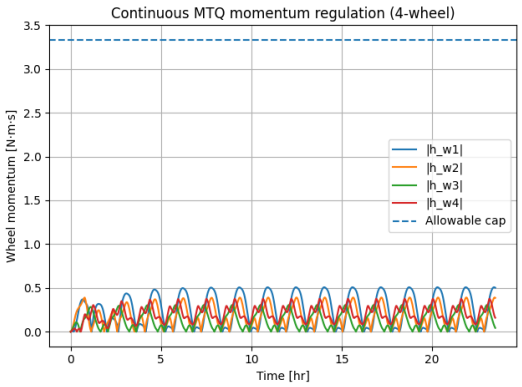

Figure 9.2: Wheel momentum using 4 wheels while MTQs continuously regulate momentum over a 24h period

Simulation results show that continuous momentum regulation by the MTQs keeps the RW momentum bounded. A graph depicting the wheel momentum of each wheel while the MTQs continuously regulate the momentum is Figure 9.2. During nominal 4-wheel operations, performing a worst-case slew while RWs were close to the momentum bound remained within the allowable capacity of the RWs. The peak momentum of the worst wheel is then 1.942 Nms, which gives some headroom. Doing the same analysis with 3-wheels resulted in degraded slew performance because the wheels would otherwise saturate. This will be further analysed in Section 9.7.
To conclude the actuator sizing, Table 9.5 shows the chosen actuator components with some key parameters.

Table 9.5: AOCS components specifications per unit

Component Type	Component Name	Quantity	Total mass [kg]	Total power (nominal) [W]
RW	BCT RW4	4	12.8	40
MTQ	MT10-2-H	3	1.05	3

9.4. AOCS Modes of Operation

The AOCS subsystem, like the system itself, operates in different modes. The system modes describe what the system is doing and how it adapts to different situations and needs, while the AOCS modes of operation

describe how the spacecraft will control its attitude to support these activities. The AOCS modes are: Launch, Acquisition, Orbit Control, Slew, Safe, Fine Pointing and Standby. Table 9.6 has an overview of all these modes with their purpose, key activities, active components, triggers and exit conditions. It also shows that safe mode consists of two sub-modes. SAFE_DETUMBLE and SAFE_SUN_POINTING are there because these are the primary objectives of AOCS during this mode. If safe mode is entered in the AOCS, it flags the OBC to enter the system into safe mode. This also highlights that the subsystem is unable to switch between modes when in safe mode, which is why sub-modes are implemented. Table 9.7 summarises how these modes support the system modes, showing which AOCS modes are active during which system modes.

This structure of modes allows the AOCS to autonomously respond to changes instead of having to rely on ground commands. The triggers for entry in a mode are not only OBC commands, but also measured conditions such as thresholds for angular rate, loss of fine sensing, power and/or thermal violations, etc. This allows the AOCS to continuously change the control strategy to maintain safe attitudes throughout all mission phases. For instance, if certain thresholds are violated during the mission (such as large tumble rates, loss of fine sensing or power-negative situations), the subsystem will automatically transition into Safe mode. This will ensure rate reduction strategies, stabilising into a power-positive attitude and sun acquisition using coarse sensing, without prioritising fine sensing.

The exit condition thresholds regarding tumble rates are derived from the detumble capabilities of the actuators, and mainly the RWs over a short period. The identified constraint for detumbling is RW saturation. Using the selected wheel momentum capability in Table 9.4, the maximum starting tumble rate that this design can detumble from can be computed. To define the threshold, a three-wheel case is examined in case of failure. This is justified because the thresholds should still be applicable in this case. The following relation holds for a three-wheel pyramidal geometry case:

$$H_{min} \approx 0.816 H_{wheel} \tag{9.2}$$

This relation is derived from Markley's approach to defining a momentum envelope [83]. This, combined with rigid-body dynamics, results in a maximum starting tumble rate of 2.56 deg/s. For the threshold to enter safe mode, an exit condition of >1.5 deg/s for 15 seconds is chosen for margin.

Table 9.6: AOCS modes, purposes, activities, triggers, exit conditions, and active components

AOCS Mode	Purpose	Key Activities	Triggers	Exit Conditions	Active Components
Launch	Keep the spacecraft safe during launch.	Detect spacecraft rough state during launch; keep all actuators disabled.	Launch command.	Launch vehicle separation detected.	Gyroscopes.
Initial Acquisition	Perform detumbling and initial attitude acquisition after launch vehicle separation.	Detumble spacecraft to a safe attitude; acquire initial attitude estimate.	Launch vehicle separation.	Tumble rate <0.1 deg/s for 30 s; consistent attitude measurements for 30 s.	Gyroscopes; Sun sensors; Star trackers (if available); Reaction wheels; Magnetorquers.
Standby	Maintain a stable attitude while waiting for instructions.	Hold current attitude; maintain low body rates and stable pointing.	Command from the OBC.	Command from the OBC; tumble rate >1.5 deg/s for 15 s (transition to Safe Mode).	Gyroscopes; Sun sensors; Star trackers (eclipse fallback); Reaction wheels; Magnetorquers.
Safe	Regain and maintain a safe, power-positive attitude following anomalies.	Detumble spacecraft (SAFE_DETUMBLE); acquire sun vector and initiate sun pointing (SAFE_SUN_POINTING); maintain steady safe attitude.	Tumble rate 1.5 deg/s for 10 s; loss of attitude knowledge for 30 s; system Safe Mode entry or OBC command; thermal or power violations flagged by TCS or EPS.	Tumble rate < 0.1°/s for 30 s; spacecraft power-positive; spacecraft temperature stabilised.	Gyroscopes; Sun sensors; Reaction wheels; Magnetorquers.
Slew	Reorient the spacecraft to a new target attitude.	Execute controlled attitude change; regulate body rates during rotation; settle spacecraft before mode handover.	New target attitude command from OBC; system mode transitions requiring attitude change (e.g. Standby to Science, Downlink, or Orbit Maintenance).	Attitude error below threshold; body rate below threshold; mode handover complete.	Star trackers; Gyroscopes; Sun sensors; Magnetometers; Reaction wheels; Magnetorquers.

Continued on next page

AOCS Mode	Purpose	Key Activities	Triggers	Exit Conditions	Active Components
Orbit Control	Maintain a stable attitude during orbit maintenance manoeuvres.	Hold burn attitude; monitor attitude and rate limits during burn; trigger abort or fallback if limits are violated.	Command from OBC; preconditions satisfied (low rates, correct burn-pointing attitude).	Burn complete; desired ΔV achieved; command from OBC to return to Standby.	Gyroscopes; Star trackers; Sun sensors; Magnetometers; RWs; MTQs.
Fine Pointing	Provide high-accuracy attitude control for science observations and Earth-pointing during downlink.	Maintain fine pointing; minimise jitter and drift; perform momentum management; monitor pointing performance.	Command from OBC; operational preconditions satisfied.	End of observation; new attitude target requiring Slew; entry into SAA; degraded fine pointing; OBC command.	Star trackers; Gyroscopes; Sun sensors; Magnetometers; Radiation sensors; Reaction wheels; Magnetorquers.

Table 9.7: Mapping between system modes and AOCS modes

AOCS Mode / System Mode	LEOP	COM	TROUB	SAFE	ORBIT	RAD	STANDBY	DOWNLINK	SCIENCE
Launch	X								
Initial Acquisition	X								
Orbit Control					X				
Slew					X		X	X	
Safe				X					
Fine Pointing								X	X
Standby		X	X			X	X		X

9.5. Final Subsystem Architecture

Figure 9.3 shows the data handling diagram of the AOCS system. This diagram has the goal of showing how the data flows in the diagram, therefore showing the dependencies of the components of the subsystem to each other and other parts of the system.

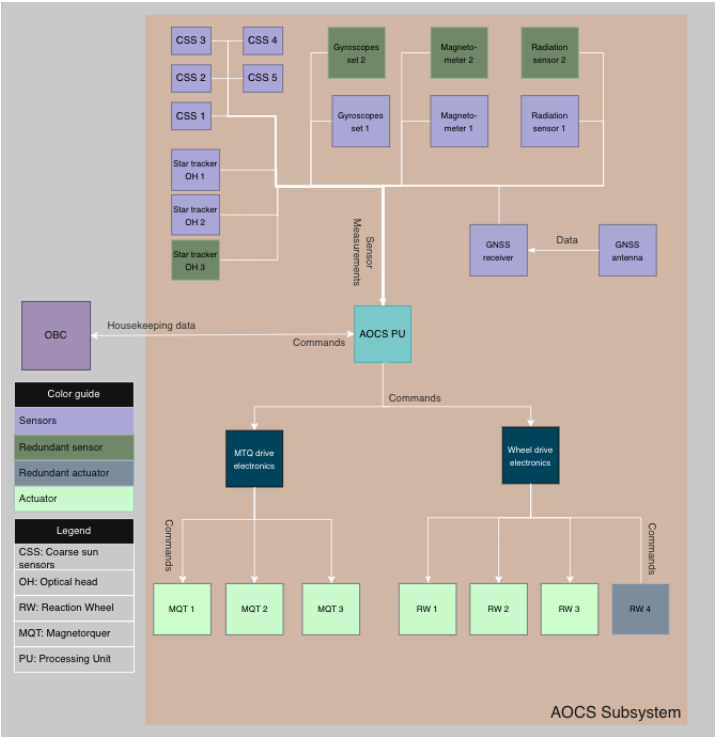

Figure 9.3: AOCS Data Handling Diagram

In the centre of the diagram, there is the AOCS PU, which is the sole point of connection of the OBC to the subsystem. As shown in the diagram, the AOCS sends housekeeping data to the OBC and also receives commands from it. These commands can be, for instance, mode change requests or new attitude targets. The AOCS PU also receives measurements from the sensors, shown in the upper part of the diagram. These measurements include attitude, orbital, radiation and body rate values. The AOCS has the role of processing these discrete measurements and outputting continuous attitude and orbital knowledge of the satellite. For instance, following the launch, the PU will receive an initial acquisition value from the sensors, followed by a continuous measurement of the angular rate of the satellite from the gyroscopes. The PU will then combine these values to produce a continuous estimation of the attitude of the satellite, which will be updated by the star tracker during discrete times.

The PU is also connected to the drive electronics of the actuators to send commands. The drive electronics then have the role of converting such commands into motor current for the wheels, regulating the current to the requested value and measuring the actual current for the magnetometers. Overall, they have the job of protecting the actuators against over current, short circuits and looking out for thermal constraints.

9.6. Sensitivity analysis

During the design process, the mass properties of the spacecraft were evolving and affected the AOCS sizing majorly. An AOCS specific sensitivity analysis was performed to quantify the uncertainty of these values and what effect it has on the resulting final design. The analysis was conducted using the same model described in Simulation framework. Two parameters were altered one at a time. First, the CoM position was moved ±5 mm along each body axis. Then, the principal MMOI were perturbed ±5%. The magnitude of these changes is chosen because that change at this stage of the design would be significant. The total disturbance torque, mean (drift) torque, the RW torque and momentum requirements, and the required MTQ dipole per rod were the recorded outputs.

The CoM shifts cause small but measurable changes to the peak disturbance torque, which varies a maximum of 1.22% with respect to the baseline. The RW sizing is barely affected, but this is to be expected as the RW sizing is mainly driven by slew. The mean torque has changed by 0.27% compared to the baseline. The MTQ dipole requirement varies the same amount because it is designed to counter the mean torque.

The MMOI sensitivity analysis shows that there is a large dependency of the RW sizing on the maximum principal inertia. In this case, altering I_{xx} by ±5% changes the RW torque and momentum requirements by ±5% and ±4.21%, respectively. This makes sense as I_{xx} is the largest principal inertia. Perturbing the MMOI does not affect the MTQ sizing.

A Monte Carlo simulation was also set up to assess the sensitivity of the AKE to sensor specification uncertainties and variations. In each run, the attitude of the spacecraft was propagated with a gyroscope estimator with star tracker updates. The gyroscope random walk and white noise, and the star stacker angular nose were changed independently within +-10% of their nominal values. Furthermore, the star tracker update rate was randomly selected from a set between 8Hz and 30Hz. The motion of the spacecraft was kept fixed. The results show that all cases meet the pointing requirement, with the maximum just before the star tracker updates staying below 16.6 arcsec in 95% of runs. Therefore, the attitude performance is affected by the star tracker update rate mostly, while the variations in the gyroscope's specifications (such as noise and bias) have a negligible effect in the conditions simulated.

9.7. Risk Assessment

Table 9.8 shows an FMEA of the AOCS subsystem. These include risks of the final design as well as risks that influenced decisions in the final design. The latter was explained throughout Section 9.3 and will be related to redundancy in Section 9.8.

Table 9.8: FMEA of the AOCS

Risk ID	Failure Mode	Effect	Cause	L	S	Risk	Mitigation
R-SUB-AOCS-001	Single wheel failure.	Reduced slew rates and pointing requirements cannot be met.	Motor drive failure, electronics failure, or overheating.	A	5	A5	Include a redundant wheel so 3-axis control remains possible after single wheel failure.
R-SUB-AOCS-002	Excessive wheel microvibration.	Degraded pointing stability and LoS jitter. Payload performance is reduced.	Bearing wear, operating frequency near structural resonance or manufacturing tolerances.	A	3	A3	Avoid operating at wheel speeds that align with structure modes.
R-SUB-AOCS-003	Reaction wheel saturation.	RWs lose control authority. This means degraded pointing, slews and risk of tumbling.	Magnetometer or MTQ failure.	B	2	B2	If due to magnetometer failure, a prediction model of the magnetic field can be used to control the MTQs. If one MTQ rod fails, there are still two rods that can desaturate less efficiently.
R-SUB-AOCS-004	MTQ single rod failure.	Reduced unloading capabilities and increased wheel saturation risk.	Electronics failure, coil insulation failure or overheating.	A	2	A2	The rods should be sized such that the remaining rods can still perform with less efficiency.
R-SUB-AOCS-006	Failure of all the star tracker heads.	Loss of high-accuracy attitude knowledge; science pointing requirements cannot be met.	Common-mode failure, radiation damage, or contamination.	A	5	A5	Fallback to gyroscopes and sun sensors; transition to Safe or Standby modes.
R-SUB-AOCS-007	Failure of one gyroscope axis.	Loss of rate information about one axis; increased estimation uncertainty, jitter, and reduced pointing stability.	Sensor degradation or electronic failure.	A	3	A3	Reduce controller bandwidth and rely on star tracker updates.
R-SUB-AOCS-008	Partial failure of sun sensors.	Reduced Sun vector acquisition in certain orientations; slower and less reliable initial acquisition.	Sensor failure, degradation, or obstruction.	A	2	A2	Sun sensors should be distributed on different faces of spacecraft; use remaining sensors and gyroscopes for coarse attitude recovery.
R-SUB-AOCS-009	Severe sun sensor failure.	Reduced autonomy and robustness of Safe Mode recovery, especially if star trackers are unavailable.	Multiple sensor failures or limitations due to eclipse.	A	3	A3	Rely on gyroscopes and MTQ detumbling; ground intervention if required.
R-SUB-AOCS-010	Magnetometer failure.	MTQ become less effective; risk of RW saturation.	Sensor failure or calibration loss.	A	5	A5	Operational constraints to limit wheel momentum build-up; have a redundant magnetometer available.
R-SUB-AOCS-011	GNSS failure.	Loss of high-accuracy orbit determination; degraded attitude constraint management and mission availability.	Receiver failure or signal loss.	A	3	A3	Periodic orbit updates and conservative attitude constraint margins.

9.8. Redundancy

The selection of the redundant components of the AOCS subsystem is driven by the risk assessment outlined in Section 9.7.

9.8.1. Redundancy in sensor configuration

In this context, the redundancy will be introduced for sensors that, when failed, would result in critical AOCS requirements not being met or lead to mission loss. Therefore, sensors that only degrade the performance but do not compromise the mission when failed are not going to have redundancy.

The need for redundant components, therefore look into the severity of the mission impact in case of failure and the likelihood of the failure happening. The latter factor is influenced by the TRL of the components. All sensors chosen for the AOCS are off-the-shelf and flight-proven units with a TRL of 9, which indicates a very low risk of failure as outlined in Chapter 17. Still, considering the high consequences associated with certain sensor failures, redundancy will be selectively implemented to mitigate single-point failures in the subsystem.

Particularly, the failure of one or more star tracker optical heads would directly compromise the satellite's ability to meet the critical AOCS requirements, thus making science operations infeasible. To avoid this, three star tracker optical heads will be included in the design. Two heads are to be used in nominal operations to ensure enough sky coverage and avoid complete blindness, while the third head will provide functional redundancy in the event of a failure, so the mission is not compromised. This way, in case one of the optical heads fails, there will still be two available. Similarly, redundant sets of gyroscopes and magnetometers will be included. Even though the components have a high TRL, their failure would significantly affect important factors such as the high-bandwidth control, momentum management and safe mode recovery. The redundancy in these components, therefore, will make sure there is compliance with the critical AOCS requirements.

Other sensors whose failure would only result in reduced autonomy or performance instead of mission loss will not be redundantly implemented. This included the GNSS receiver and the coarse sun sensors. The failure of such sensors introduces a medium risk but can be mitigated through degraded operational modes and ground support.

9.8.2. Redundancy in actuator selection

Same design redundancy alongside hot redundancy is used for the actuators. These are explained in Section 6.4 in more detail. Derived from risk R-SUB-AOCS-001 in Table 9.8, same design redundancy is implemented such that three-axis control is not lost after a single wheel failure because that would lead to mission failure. Next to this, the redundant reaction wheel is chosen to be a hot redundant wheel. Hot redundancy distributes actuator commands across all RWs, and can immediately re-allocate control in case of failure. There will be a reduced performance with respect to REQ-AOCS-F-SYS008-00 in case of failure. If a slew is performed at a point when the wheel momentum is at a maximum in Figure 9.4, the peak slew momentum may only be 2.564 Nms instead of 3.182 Nms. This means a bang-coast-bang profile is used, which increases the slewing time and thus decreases the science observation time.

The current MTQ design consists of three orthogonally placed rods. The same redundancy philosophy is used here, as with the RWs. In case of a single rod failure, the mission can continue without degraded performance. This will roughly be an 18.4% loss, as the torque authority ratio between two and three rods equates to 0.816 using Equation 9.1. This loss is compensated for by selecting a higher design dipole per rod than required.

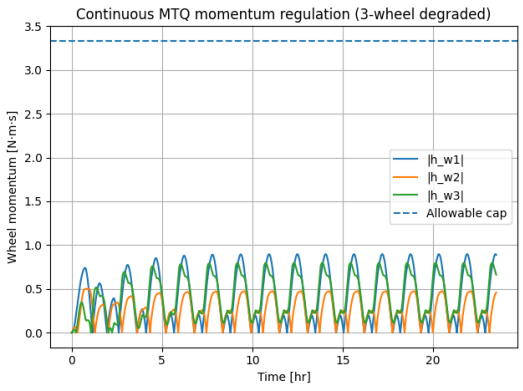

Figure 9.4: Wheel momentum using 3 wheels while MTQs continuously regulate momentum over a 24h period

9.9. Compliance check

Table 9.9 shows a compliance check of the key requirements stated in Table 9.1. The design values are results of simulations conducted to check the compliance, which are explained below. The limitations of the model are explained in Simulation framework and Table 9.2.

Table 9.9: AOCS compliance check of key requirements

ID	Required value	Design value
REQ-AOCS-F-SYS008-003	< 15 arcsec	6.45 arcsec
REQ-AOCS-F-SYS008-004	< 150 arcsec	26.13 arcsec
REQ-AOCS-F-SYS008-005	≤ 37.5 arcsec	3.72 arcsec
REQ-AOCS-F-SYS008-006	≤ 75 arcseconds	11.32 arcsec
REQ-AOCS-F-SYS008-007	180°/150s	180°/150s
REQ-AOCS-F-SYS003-012	≤ 30 min	36.5 seconds

REQ-AOCS-F-SYS008-003 requires an analysis of the
static and dynamic imbalance of the RWs, as the micro-vibrations lead to increased jitter. Using ASSU-AOCS-11, a rigid-body model. Because the wheel disturbance spectra were unavailable, the jitter is modelled as a single-frequency sinusoidal model:

$$\mathbf{T}(t) = T_{pk}\sin(2\pi f t)\hat{\mathbf{u}} \tag{9.3}$$

Here, T_{pk} is the peak disturbance torque amplitude. The single-wheel torque amplitude is computed by summing the torque produced by the static and dynamic imbalance. f is the wheel spin frequency. Due to unavailable data, a frequency sweep from 500rpm to 6000rpm was conducted to find the worst case. Finally, $\hat{\mathbf{u}}$ is the torque direction in the body frame. In this case, the torque was computed about the X and Y axes, because those axes produce the largest LoS error with the LoS in the +Z direction.

For REQ-AOCS-F-SYS008-004, the output of the jitter, AKE and drift were combined to find the Absolute Pointing Error (APE). These values are summed by treating bias terms, such as drift, as added linearly. Random terms such as jitter and AKE are combined by Root-sum-squared (RSS) following ECSS standards [120].

REQ-AOCS-F-SYS008-005 is checked by simulating multiple 2400s orbits to find the worst-case drift. The simulation replays the disturbance torque history and measures how far the boresight drifts over any continuous 2400s window. For this compliance check, continuous MTQ desaturation is included. A simple Proportional-derivative (PD) controller is used to simulate the closed-loop RW pointing hold. This is done by first sweeping through a range of controller frequencies and then choosing the value which satisfies the requirement.

REQ-AOCS-F-SYS008-006 is checked through a simulation that models how the star tracker and gyroscope work together to provide fine sensing measurements. The simulation uses specifications such as the star tracker's update rate and the measurement noise, and the gyroscopes' bias random walk and bias white noise. With these values, the simulation of the 'attitude sensing loop' can be set up, where the star tracker provides accurate measurements and corrects the gyroscope's drift, with the attitude knowledge error (AKE) staying within the required constraints.

REQ-AOCS-F-SYS008-007 is satisfied because the actuators are sized to be able to perform such a slew. This requirement, however, cannot be met in the event of a single-wheel failure. This is discussed in Section 9.8.

The compliance with key AOCS requirements REQ-AOCS-F-SYS003-010 and REQ-AOCS-F-SYS003-012 can be justified through the modes of operation of the subsystem, as explained in Section 9.4. The modes allow the system to autonomously identify dangerous attitudes, avoid them and adopt control strategies to mitigate violations. A simulation is run for detumbling requirement REQ-AOCS-F-SYS003-012, where detumbling is performed from a starting value of 1.5 deg/s (ASSU-AOCS-12). Here, the body torque requirement defined in Table 9.4 is used to compute the detumble time.

10 Electrical Power System

The Electrical Power System includes the generation, storage, conversion and distribution systems of the spacecraft. This subsystem is designed to deliver adequate power for every mode throughout the mission lifetime. Section 10.1 contains the requirements dictating the EPS design, and in Section 10.2, the assumptions are stated. Section 10.3 covers the configuration and components of the solar array. Section 10.4 discusses the selection and properties of the battery pack, while Section 10.5 details the power management, including power distribution and conversion. Sensitivity and risk analyses are performed to assess robustness and risk of the final design using the established components and architecture.

10.1. Key requirements

Table 10.1: Key requirements for EPS design

ID	Requirement	Rationale
REQ-EPS-F-MIS007-001	The EPS shall be able to supply sufficient power to the active components in every mode during its lifetime.	The spacecraft must power all active components to function nominally.
REQ-EPS-F-SYS007-003	The EPS shall provide continuous power measurements of all power buses.	Continuous monitoring is required to maintain safe and reliable power system operation.
REQ-EPS-F-SYS007-004	The EPS shall provide continuous voltage measurements for all spacecraft power buses.	Voltage monitoring is required to ensure compatibility with subsystem operational limits.
REQ-EPS-F-SYS009-005	The EPS shall be able to provide 170 W to the LEXI payload when in science mode.	The payload requires this power level to operate nominally.
REQ-EPS-F-SYS009-011	The EPS shall be able to provide 80 W to the heaters of the optical bench of the LEXI instrument.	Thermal conditions must be kept within operational limits.
REQ-EPS-F-SYS009-006	The EPS shall be able to provide 80 W to the HEXI payload when in science mode.	The payload requires this power level to operate nominally.
REQ-EPS-F-SYS018-009	The EPS shall be able to discharge batteries at end-of-life.	This prevents the risk of space debris due to a battery explosion.
REQ-EPS-F-SYS005-012	The EPS shall be able to generate sufficient power to fully charge the battery before eclipse.	In an eclipse, the system must operate without power generation.
REQ-EPS-F-SYS005-013	The battery system shall be able to store sufficient energy to power the spacecraft during eclipse.	In eclipse, the system must operate without power generation.
REQ-EPS-F-SYS005-014	The battery system shall have a sufficient discharge rate to power the spacecraft during eclipse.	The system needs sufficient power in eclipse.
REQ-EPS-F-SYS005-015	The power conditioning and distribution system shall be able to deliver generated power to the battery, subsystems, and payload.	Power connections are required from solar arrays to all consumers.
REQ-EPS-F-SYS005-016	The power conditioning and distribution system shall be able to deliver stored power to the subsystems and payload.	Power connections are required from the battery to all consumers.
REQ-EPS-F-SYS005-017	The battery shall have a maximum charging rate equal to or exceeding the maximum solar array power generation.	To ensure safe and complete battery charging.
REQ-EPS-F-SYS005-018	The power conditioning and distribution system shall convert generation and battery voltages into component-compatible voltages.	Subsystem input voltages must remain within safe operational limits.

10.2. Assumptions

Table 10.2: List of assumptions made during the preliminary design for EPS

ID	Assumption	Justification	Design Impact	Consequences If Invalid
ASSU-EPS-01	The maximum eclipse fraction is 0.39.	Conservatively rounded from Section 11.4.4	Determines required power generation and storage	Insufficient power storage at EoL
ASSU-EPS-02	The orbit duration is 1.5917 h.	See Section 11.4.4	Determines required power storage	Insufficient power storage at EoL
ASSU-EPS-03	Primary targets are located in the plane of the Milky Way.	See Section 2.2	Limits attitude range	Lowered science value
ASSU-EPS-04	Primary targets have a designated observation window, while secondary targets do not.	See Section 2.2	Limits attitude range	Lowered science value
ASSU-EPS-05	The pointing angle changes due to the satellite and Earth's orbit can be neglected for the attitude of the solar array relative to the Sun.	Targets are very far away compared to distances from the satellite to the Earth and Sun.	Limits attitude range	Lowered science value
ASSU-EPS-06	The AOCS system can optimise the solar array incidence angle through slewing with negligible error.	Chapter 9	Needed to define feasible options	Insufficient power generation
ASSU-EPS-07	The power conditioning and distribution efficiency from power generation to subsystems and payload is at least 90%.	Preliminary design fraction [6]	Determines required power generation and storage	Insufficient power generation and/or storage
ASSU-EPS-08	The conditioning and distribution efficiency from power storage (including discharge) to subsystems and payload is at least 85%.	Preliminary design fraction [6]	Determines required power generation and storage	Insufficient power generation and/or storage
ASSU-EPS-09	The conditioning, distribution and charging efficiency from power generation to power storage is at least 90%.	Preliminary design fraction [6]	Determines required power generation and storage	Insufficient power generation and/or storage

10.3. Solar Array Design

The solar array was designed to provide adequate power while minimising risk, mass and cost. Using general wattage over area numbers, the effective area necessary for the worst-case operating conditions was devised. These worst-case operating conditions were quantified using a power budget, taking into account degradation, efficiencies and possible panel attitudes. A trade-off was performed between feasible configurations, after which the chosen design was assessed in more detail using an orbit condition model.

10.3.1. Initial sizing

To perform an initial sizing to select configurations and components, some rough estimates were be taken. These estimates include load path efficiencies and degradation and eclipse fraction values, shown in Table 10.3.

Table 10.3: Initial estimates

Initial estimate	Estimated value	Justification
Cell degradation	<2.0% per year	Based on empirical data for GaAs cells in [75]
Efficiency: Array → Battery & system	First level estimate [6]	Taken from design handbook [6]
Efficiency: Battery → System	First level estimate [6]	Taken from design handbook [6]
Maximum power consumption system	438 [W]	Subsystem level power budget [63]

To perform the initial sizing of the solar array, the power needed at EoL was calculated using these estimates. The Science Mode power consumption was determined to be limiting[63], and was thus used in conjunction with the maximum eclipse fraction of 0.39 [63]. This led to an initial power generation requirement at EoL of 955 [W], which corresponds to a BoL power requirement of 1056 [W] using the worst-case degradation estimate [63]. The initial estimates will be replaced through detailed analysis further in the design process.

10.3.2. Array configuration

As has been mentioned in Section 2.2, the possible attitudes of the spacecraft are limited by the science targets, with the spaceraft being able to slew only around the instrument pointing vector to optimise power generation Section 10.2. The range of attitudes limits the feasible array configurations, driving the design. As per assumption 4 of Section 10.2, the spacecraft must generate adequate power while being able point at any point in the plane of the Milky Way. In combination with assumption 1, this yields a range of attitudes that the EPS must be able to operate at. Because of the orientation, the power requirement is scaled with the incidence loss incurred when the satellite is pointing in-line with the plane of Earth's orbit around the sun, and at the furthest point from the galactic plane. This gives a conservative $\sin(30)$ incidence loss for (a part of) the array, as can be inferred from Figure 10.1.

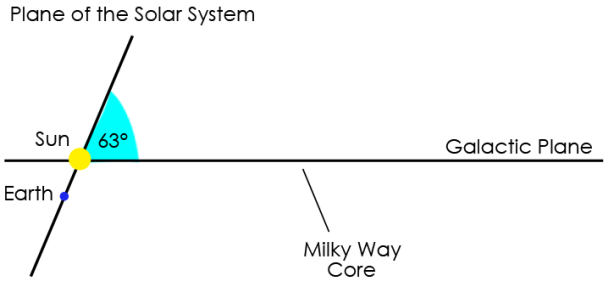

Figure 10.1: Solar system in the Galactic plane [109]

Two techniques were considered to manage these operating conditions: continuously rotatable panels and panels at different angles. This lead to three configuration candidates, shown in Figure 10.2.

(a) Array stowed

(b) Array folded out

Figure 10.2: Array folding

Option 1 is a combination of wall-mounted and fold-out panels, where part of the fold-out is at an angle. This adds to the solar array area which can fit in the launcher in stowed position, and increases the effective area for different solar incidence angles while having the same blanket area compared to only flat panels. As can be seen in Figure 10.2, the wall-mounted panel and fold-out panels stick out from the bus when stowed. Standard values are used for specific power, area over power and volume [6].
Option 2 was devised using the same rhetoric, though for this option, more fold-outs are used. This means the panels do not stick out when stowed, and less support structure is needed to endure launch loads. For this option, COTS components are readily available, and relevant values were inferred from datasheets.
Option 3 uses Solar Array Drive Assembly (SADA) in combination with fold-outs, decreasing blanket mass. The mass of the SADA mechanisms was based on the maximum array power, using a relation given by [118]. For these options, mass, area and specific dimensions were calculated using handbook estimation techniques [6], and averaging of historic data [124] and vendor datasheets [31] for certain metrics such as specific power and power density.

Table 10.4: EPS option descriptions

Option	Elements	Mass [kg]	Area [m^2]	Cost [k€]
Option 1: Rigid Deployable Combination	Wall-mounted panel; Fold-out flat part; Fold-out angled part	67.6	5.3	757
Option 2: Fold-out Deployable Combination	Wall-mounted panel; Front side fold-outs; Side fold-out flat; Side fold-out angled	58.2	6.3	670
Option 3: Rotating Fold-outs	Folding side panel; Rotational mechanism	65.7	4.3	771

The selection of the EPS preliminary design configuration was driven by an assessment of mass, complexity, TRL, and cost. Among the three options, Option 2 was chosen.
Option 2 outperforms the other configurations in mass, TRL, and cost. It is the lightest option due to reduced panel and structural mass, achieves the highest TRL through the exclusive use of COTS components, and benefits from lower cost as a result of large-scale COTS component production.
The only criterion in which Option 2 does not outperform the others is complexity; while less complex than Option 3, it is more complex than Option 1 due to its sequential folding mechanism. Despite this, the higher complexity was considered acceptable, and Option 2 was selected.

10.3.3. Component Selection

As the configuration was chosen with the availability of COTS components as an advantage, multiple component options were available to choose from. A high preference was given to high-TRL components with a large design heritage for missions. Using these differentiators together with the required panel sizes to fit the spacecraft, Sparkwing was chosen as the supplier of the solar panels. Another reason for this choice was the client's partiality to collaboration with Dutch companies. Sparkwing offers a multitude of panel sizes, of which the following were chosen:

Table 10.5: Solar panel characteristics at nominal conditions (BOL, 28°C, 0° incidence, 50 V)

Panel type	Dimensions [m]	Mass [kg]	Power [W]	Number used
1.1 × 0.75	1.10 × 0.75	3.66	244	4
1.1 × 0.91	1.10 × 0.91	4.03	305	3

The Sparkwing deployment is mechanical and spring driven, with mechanisms latching in place. The deployment hinge torques depend on the wing and panel designs. Further design steps, taking into account hinge torques and deployment sequencing, should be taken in collaboration with Sparkwing, as additional expertise and information about the panels are necessary to ensure design compatibility. The deployment and panel placement leaves free area between the fixed and fold-out panels, which can be used for placement of the S-band antenna and sun sensors.

10.3.4. Design Analysis

The power generation of the array design was modelled to show compliance, quantifying the effects of changing operating conditions. It was determined that the main parameters driving EPS performance are solar cell temperature, charged particle fluence, and battery charging voltage. Additionally, the relation between operating voltage and current had to be estimated for different conditions. With this model, the initial estimates will also be replaced by more specific values. To quantify performance throughout orbit and lifetime, approximations had to be used, which will be justified hereafter. Additionally, failure modes associated of the configuration were assessed.

Approximation I-V curve

The I-V curve, physically dictated by the diode equation:

$$I = I_{ph} - I_0 \left[\exp\left(\frac{V + IR_s}{nV_t} \right) - 1 \right] - \frac{V + IR_s}{R_{sh}} \tag{10.1}$$

This equation governs the current generated by solar cells at different operating voltages. Since parameters such as R_s and $R_s h$ are unknown, an approximation was used.

A modelling technique pioneered by Pindado et al. [103] using solar cell datasheets was implemented:

$$I = \begin{cases} I_{sc}\left[1 - \left(1 - \frac{I_{mp}}{I_{sc}}\right)\left(\frac{V}{V_{mp}}\right)^{\frac{I_{mp}}{I_{sc} - I_{mp}}}\right], & V \leq V_{mp}, \\ I_{mp}\frac{V_{mp}}{V}\left[1 - \left(\frac{V - V_{mp}}{V_{oc} - V_{mp}}\right)^{\eta}\right], & V \geq V_{mp}. \end{cases} \tag{10.2}$$

It was concluded that this approximation is tailored to this design stage with the available specifications.

Cell temperature

From datasheet specifications, the established I-V curve and experimental data, relations were established to approximate solar array voltage and current. The input coefficients from the datasheet are specified in Table 10.6. Panel voltage and current at the nominal temperature of 28 °C are taken from Table 10.5.

Table 10.6: Cell coefficients

Coefficient	Output	Value
α_{Voc}	Open Circuit Voltage	-0.0067
α_{VMP}	Maximum Power Point Voltage	-0.0072
α_{Isc}	Short Circuit Current 1	0.00099
α_{IMP}	Maximum Power Point Current	0.00072

α_{Voc} and α_{VMP} are assumed constant for temperatures above 200 [K]. This matches experimental data for solar cells [79], as the linearity of α_{Voc} and α_{VMP} only starts breaking down blow $< 100[K]$[79]. The same assumption is done for α_{Isc} α_{IMP}, as the associated temperatures have been shown to follow an approximately linear path throughout the entire temperature range [80].

Cell Degradation

For long-duration missions, degradation is a significant driver in the solar array design, and should be taken into account at every design stage. To obtain the Beginning-Of-Life (EOL) required power generation, the efficiency reduction of the array must be quantified based on in-depth understanding of the dominant degradation processes.

Charged particles are the most significant contributor to solar cell degradation in LEO [14]. These particles can displace atoms in the cell crystal lattice, leading to a drop in efficiency. A commonly used method is to calculate the equivalent 1-MeV electron fluence of a radiation environment. However, damage caused by particles does not scale linearly with their energy. Additionally, proton and electron flux cause different levels of damage, as heavier particles have a higher probability of displacing an atom. This is quite different from the way radiation damage is quantified for electronic components Section 4.2, which requires a different method for devising this equivalent fluence. An appropriate metric to scale with is the Linear Energy Transfer (LET) of particles. A modelling framework using the was proposed by A. Nayaka Nikicio et al. to derive maximum cell degradation [11]. This study includes an assessment of the AZURSPACE 3G30A solar cells for a 50 °inclination orbit at an altitude of 550 [km]. Since higher inclination orbits experience more radiation due to time spent in the SAA, this provides a conservative modelling case for the mission. The analysis produced maximum equivalent fluences for the open circuit voltage, short circuit current and the efficiency, as these parameters are impacted differently. The simulated values for the power was determined to be $1.5 * 10^{14}$ [MeV e-] per year. For the five-year mission duration, this translates to a $7.5 * 10^{14}$ [MeV e-] equivalent fluence. In the datasheet for the solar cells, a rated cell efficiency of 26.9% is given for the maximum radiation degradation value of $1 * 10^{15}$ [MeV e-] [119]. This produces an upper bound on the total degradation of 7.24%, which corresponds to 1.5% per year. This confirms the validity of the earlier 2.0% upper bound and confirms compliance with the initial budget.

Failure modes

Thanks to the independent deployable panels, the chosen configuration has partial redundancy; with deployment failure or failure in power transfer, only part of the power will be lost. The power lost is determined by

the specific failure and attitude. Because the configuration is designed to provide power for the two limiting attitudes defined in Section 10.3.2, the spacecraft can change it attitude in case of failure of deployment failure of a single panel stack. This means that the science time requirement can still be reached, but the possible targets will be limited. Another option is to limit the science time by not using the instruments throughout the entirety of the orbit. Too little is known at this point about the locations of the targets and their scientific value to quantify the science loss in the first scenario, while the loss of science time in the second scenario could be quantified for every panel deployment failing. This was deemed outside of the scope of this project phase, because this would require an extensive analysis of the attitudes throughout the orbit for given targets and failure modes, as AOCS would optimise attitude for every failure mode in a different way. However, it can be concluded that the most significant deployment failure would be of the deployment of the panel folding out towards to positive Z-direction (defined in Chapter 15). This would prevent this panel and the two panels below from generating any power, severely limiting science time and possible targets. It is recommended that these failure modes are assessed in more detail in the following phases.

10.3.5. Updated Budget

Using the updated estimated values, the required power generation was calculated for the two limiting solar incidence cases, defined by solar vectors along the positive z-axis and along the positive x-axis of the spacecraft Chapter 15. The final values were determined to be 1029 [W] for the positive z-direction and 1189 [W] for the positive x-direction. The distinction comes from the case detailed in Section 10.3.2, taking into account incidence losses for this case. It was determined that the panel combination fits this budget, validating the design under the assumption that nominal power can be assumed throughout the orbit. The validity of this assumption is assessed in Section 10.5.1.

10.4. Battery Pack Design

To provide adequate power during eclipse, a battery pack was selected, using the limiting mode power consumption Section 14.4, degradation data and voltage ranges as input. The initial battery design estimates, which will be analysed and replaced with more accurate values in Section 10.4.2, are stated in Table 10.7.

Table 10.7: Initial battery design estimates

Initial estimate	Estimated value	Justification
Capacity degradation (30%Depth of Discharge (DoD))	<2%/year	Experimental studies for LEO show values around 1%/year for higher DoD[12]
Max energy used per eclipse	376 [Whr]	Calculation using subsystem level power consumption esimates [63] 1%/year for higher DoD[12]

10.4.1. Component Selection

The selection of the battery pack was driven by design heritage, component mass and integration with the solar array design. The product which fulfils the required specifications while optimising these aspects was determined to be the ABSL 8s16p Li-ion Rechargeable Battery. This option has a TRL of 9, having over 20 years of continuous in-orbit heritage [5]. This option also has a relatively low mass of 7.8 [kg], adding to its advantages compared to other battery packs.

10.4.2. Design Analysis

The charge and discharge ranges of the battery pack are given in Figure 10.3, leading to an charging voltage between 31 and 34 [V], given the assumed DoD of 30%.

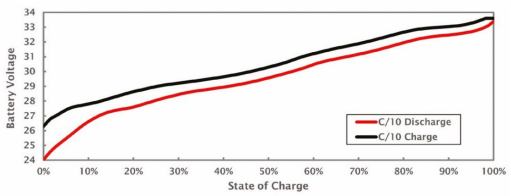

Figure 10.3: State of Charge (SoC), charge and discharge voltage battery pack [5]

The nominal capacity is stated to be 1628 [Whr]. The estimated maximum degradation and eclipse energy assumptions stated in Table 10.7 were used to estimate a maximum DoD of 25.5%. This is well below the maximum of 30% on which the degradation assumption was based.

10.5. Power Management

The power management of the satellite is defined by how the system controls the flow of power, which includes component functions and interactions. As this aspect of the power system is essential for prolonged safe operation, this section focuses on safeguards, command structure and redundancy. The conditioning of the power generated by the arrays can be realised using several techniques; each having different implications on the generation efficiency, cable loss, mass and complexity of the system. This yielded several options to be considered for the EPS architecture. These design options were assessed, and the most feasible architecture was defined in terms of functions and hardware.

MPPT versus DET

One of the main defining characteristics of an EPS system is the use of either MPPT or Direct Energy Transfer (DET) architectures. MPPT systems, which regulate the variable voltage used by the system by varying the conversion factor, allow the solar array to operate very close to its Maximum Power Point Voltage (VMPP). This increases efficiency at the cost of added mass and complexity. DET systems do not have this feature, which is why these systems have lower array efficiencies.

The difference in output can be quantified by assessing variability in VMPP and battery charging voltage, which clamps the output voltage of the solar array [103]. To model this output difference, the panel temperature, being the main driver, was used as the input variable for the Maximum Power Point Voltage. while the charging voltage range, mainly varying with the SoC of the battery, was taken from the battery pack datasheet [5]. A 1.1x0.91 panel was modelled, using the power at nominal operating conditions [124]. By using the fluctuations in temperature given in Section 11.4.6 together with the VMPP temperature coefficient of the solar cells, the VMPP range was modelled. The panel folding out in the positive Z-direction (defined in Chapter 15) was taken, with a 0-degree incidence. These model parameters were chosen because this panel was determined to have the largest variability in temperature, under these conditions determined in Section 11.4.6. The 0-degree incidence corresponds to the limiting attitudes. The VMPP temperature coefficient was taken for the worst case equivalent fluence upper bound of $1 * 10^{15}$ [MeV e-], determined in Table 10.3.4, leading to Figure 10.4.

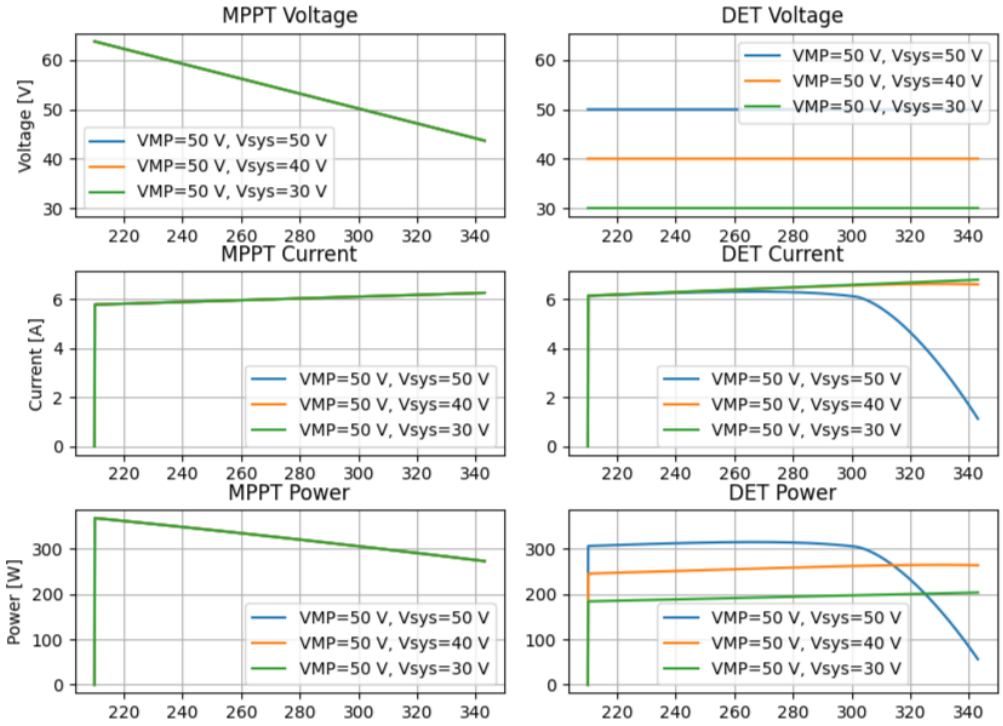

Figure 10.4: Voltage, current and fractional power loss DET vs MPPT

Different system voltages were assessed, as varying system voltage can lead to large DET losses. As system voltage is determined by battery voltage, values from the range of Section 10.4 were used. VMP_{nom} in the figure refers to the VMPP for nominal operating conditions, at 28°C. The figure clearly shows lower currents of DET with respect to MPPT increase when moving further from the temperature at which VMPP matches the system voltage. Another observation is that while a system voltage far below the nominal VMPP is less efficient, a system voltage equal to the nominal VMPP is also not preferred. Losses rise quickly with increasing temperature in this case, as the VMPP drops below the system voltage.
From the thermal model of Chapter 11, panel temperatures throughout the orbit were imported to produce Figure 10.5, which shows the power and fractional difference for MPPT and DET at different system voltages.

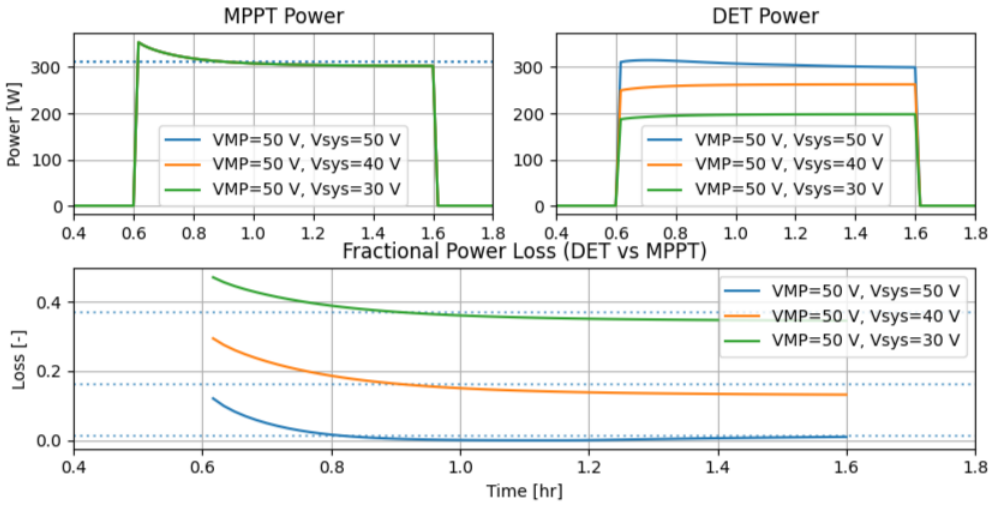

Figure 10.5: Voltage, current and fractional power loss DET vs MPPT

Using this model, it was determined that with system voltages matching the selected battery voltage range of 31-34 [V] Section 10.4, DET architecture would limit the power output to such a degree that the power budget could not be met throughout the mission orbit. Power generation would be especially limited when the spacecraft comes out of eclipse, when the panel temperature is lowest. Actual fractional power output would lie between the green ($V_{sys} = 40V$) and blue ($V_{sys} = 30V$) lines. Thus, an MPPT architecture was chosen.
Using the MPPT architecture, the simulated average power generated over the orbit 311.6 [W] for this panel, which can be attributed to a higher efficiency for lower temperatures. This result complies with other studies [103]. The model validates the design with respect to the power generation requirements, as more energy is generated per orbit than at constant nominal conditions, affirming that the power production of this design is sufficient.

Unregulated versus Regulated

Unregulated and regulated system architectures are also a defining feature of the power management design. With the availability of COTS components being a limiting factor, this choice was incorporated into the component selection.

10.5.1. System Architecture

A hardware diagram was constructed to show the system architecture using the defined components, providing an overview of components and connections in the EPS subsystem. This diagram, shown in Figure 10.6, is also used to identify components with single-point failures and provide a framework for adding redundancies.

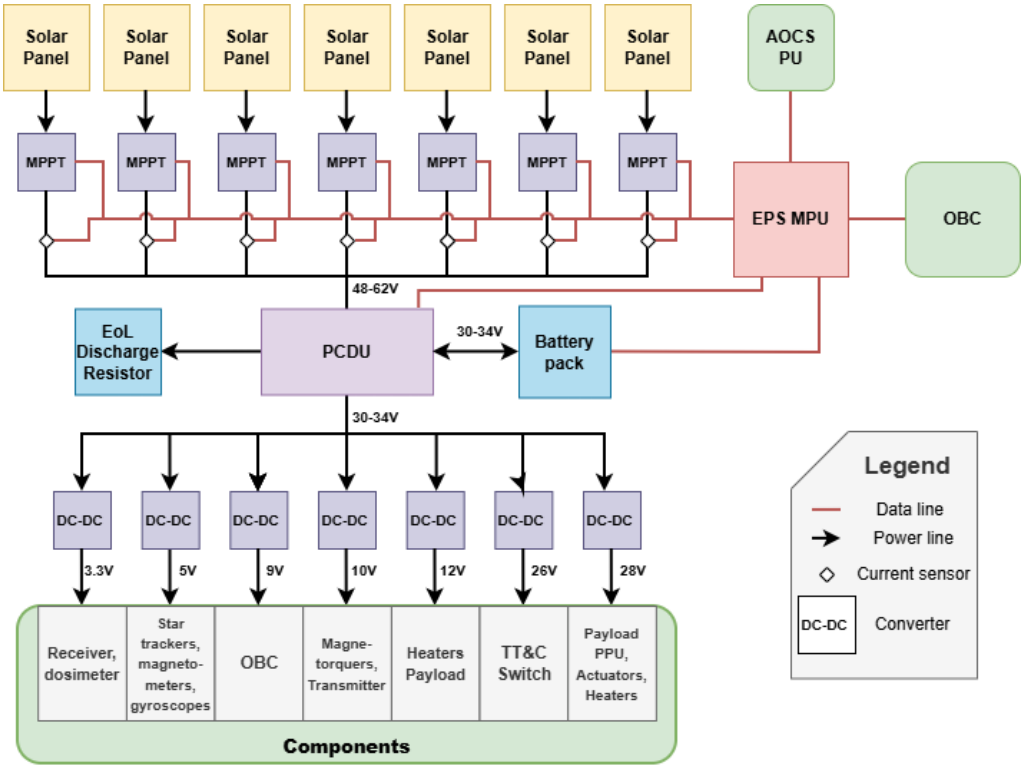

Figure 10.6: Hardware Diagram EPS

Redundancies

In accordance with the redundancy philosophy and risk assessment Figure 10.5.1, components in need of redundancy were identified. The COTS components are stated to be in accordance with ECSS standards, which means single points of failure do not propagate, and redundancy is already embedded in the design. This includes the data interface of the EPS PU with the On Board Computer (OBC) and AOCS PU. These connections are essential to the safe operation of the spacecraft, as they are needed to enter safe mode and control currents. The power cabling was determined to carry less risk, and adding redundancies here has more drawbacks than for the data wire connections. Examples of these drawbacks include mass penalties, higher volume and routing complexity. Instead, the recommendation is to include sufficient derating, radiation protection, and margins in the final component selection. Unlike cabling, converters have a well-documented history of in-orbit failure, attributed to vulnerability to single-event latch-ups and upsets. Because of this, cold redundancy should be added for every converter. For redundancy of the PU, the algorithms controlling the flow of current and the MPPTs should be able to run on the OBC in case of EPS PU failure.

Component Selection

Using these considerations, the Medium Power Power Conditioning and Distribution Unit (PCDU) from Airbus was chosen [30]. This component combines the functionality of the array power conditioning and the power distribution for an unregulated system. A need to select converters to change the unregulated bus voltage into the component voltages arises with this system architecture.

The specific choice of PU, wiring and converters was deemed outside of the scope of this project phase. As these choices are less driving to the system design and depend on unknowns such as specific cable connectors, it is recommended that these components are selected while designing the detailed spatial power harness, in collaboration with the structures team.

Standard conservative fractions were taken to produce the masses in Table 15.1, which were concluded to fit the budget. The selected components should be used to confirm and more precisely define the efficiency estimates used in Table 10.3. More detailed analysis could use current mass per meter estimates to produce cable, converter and PU masses according to standards [13].

10.6. Risk Analysis

A risk analysis was conducted to identify aspects needing risk mitigation or handling. The analysis was conducted throughout the EPS design process, with risk levels varying as the design furthered. Risks shown may have been higher earlier in the design, before mitigation was applied. Risk rating levels shown are determined by the final design, including mitigation measures, presented in this report. Further risk management may be necessary at later design phases, for which this analysis should be utilised.

Table 10.8: FMEA for EPS

Risk ID	Failure Mode	Effect	Cause	L	S	Risk	Mitigation
R-SUB-EPS-001	Solar panel string failure	Reduced or lost power generation	Cell degradation due to radiation, micrometeoroid damage	B	4	B4	Implement multiple panel strings; apply EOL power margin
R-SUB-EPS-002	MPPT failure	Loss of power harvesting from affected solar panel	Single-point failure in MPPT electronics or control logic	B	4	B4	Distribute power generation across multiple independent MPPTs
R-SUB-EPS-003	MPPT control instability	Bus voltage oscillations affecting loads	Faulty control loop tuning	A	4	A4	Perform control stability analysis; include voltage clamping and watchdogs
R-SUB-EPS-004	PCDU failure	Loss of regulated power distribution to all subsystems	Internal electronics failure or latch-up event	A	5	A5	Implement current limiting and latch-up protection; use high components
R-SUB-EPS-005	Battery pack failure	Loss of eclipse power and degraded mission availability	Cell degradation, internal short circuit, or manufacturing defect	A	5	A5	Use space-qualified cells; include cell balancing and protection circuitry
R-SUB-EPS-006	Battery overcharge	Thermal runaway or permanent battery damage	MPPT or charge control failure	A	5	A5	Implement redundant over-voltage protection and hardware charge cut-off; use high TRL components
R-SUB-EPS-007	Battery undervoltage	Inability to power loads during eclipse	Excessive DoD or inaccurate SoC estimation	A	4	A4	Enforce conservative DoD limits; use redundant voltage sensing
R-SUB-EPS-008	DC-DC converter failure	Loss of regulated voltage rail to connected components	Component failure or radiation-induced latch-up	B	4	B4	Separate critical loads; include current limiting and reset capability, use high- components
R-SUB-EPS-009	Bus overvoltage	Damage to sensitive electronics	Regulation failure or load shedding transient	A	4	A5	Implement transient suppression and overvoltage protection
R-SUB-EPS-010	EPS-MPU communication failure	Loss of telemetry and command capability for EPS	Data bus fault or MPU software failure	C	3	B4	Implement redundancy and autonomous safe-mode behaviour
R-SUB-EPS-010	EPS-PU AOCS communication failure	Safe mode not triggered by flag from AOCS sensors	Damage to sensitive EPS electronics due to SEE	B	4	B4	Implement redundancy and autonomous safe-mode behaviour
R-SUB-EPS-011	Current sensor failure	Incorrect power monitoring and load management	Sensor degradation or calibration drift	B	2	B2	Cross-check measurements using voltage and power trends
R-SUB-EPS-012	Panel deployment failure	Reduced or lost power generation, thermal management impeded	Sensor degradation or calibration drift	B	5	B5	Collaborate with the manufacturer to install safeguards and sequence deployment
R-SUB-EPS-013	Power cable failure	Improper strain relief, fatigue	Loss of (part of) power	A	5	A5	Stress-testing, using components rated for space

11 Thermal Control System

This chapter focuses on the thermal control subsystem of the NEBULA-Xplorer spacecraft. For optimal operations of the satellite, key components need to be kept at operational temperature ranges. In Section 11.1 and Section 11.2, the key requirements and assumptions are defined, which were used as guidelines for the final TCS architecture. Section 11.3 covers the final design of TCS, consisting of both passive and active thermal regulation methods. In Section 11.4 the thermal analysis is performed to determine the performance of selected TCS architecture. Section 11.5 and Section 11.6 cover the risk and redundancy of the TCS respectively.

11.1. Key requirements

The design of the spacecraft TCS is driven by several key requirements. Chapter 3 includes a comprehensive list of all requirements, however for the purpose of this chapter only key requirements associated with TCS are mentioned. The compiled list of relevant requirements is shown in Table 11.1.

Table 11.1: Key requirements for TCS design

Requirement ID	Requirement text	Rationale
REQ-TCS-F-SYS004-001	The TCS shall maintain the system within the survival temperature range passively.	The spacecraft needs to be able to survive during shutdown.
REQ-TCS-F-SYS004-002	The TCS shall perform thermal control operations autonomously.	The spacecraft needs to perform its functions autonomously.
REQ-TCS-F-SYS004-003	The TCS shall maintain the system within the operational temperature range actively.	The spacecraft needs to maintain required subsystem temperature ranges.
REQ-TCS-C-LAUN004-007	The spacecraft shall be designed for a ground operating temperature of 23 ± 2 °C.	The spacecraft needs to withstand conditions of the launch site.
REQ-TCS-C-LAUN004-008	The spacecraft shall be designed for a (ground operating) relative humidity of 55 ± 5%.	The spacecraft needs to withstand conditions of the launch site.
REQ-TCS-F-SYS007-009	The TCS shall provide temperature measurements of all subsystems.	The spacecraft thermal data is needed as part of housekeeping data and correct mode switching.
REQ-TCS-F-TCS001-010	The TCS shall maintain the Instrument Readout Unit (IRU) within the -60 to 125 °C temperature range passively.	The payload has its own thermal regulation system, however the electronics of this system need to be kept in this temperature range.
REQ-TCS-F-TCS001-011	The TCS shall maintain the Instrument Focal Plane (IFP) within the -40 to 85 °C temperature range passively.	The payload has its own thermal regulation system, however the electronics of this system need to be kept in this temperature range.
REQ-TCS-F-TCS003-012	The TCS shall maintain the IRU within the -40 to 105 °C temperature range actively.	The payload has its own thermal regulation system, however the electronics of this system need to be kept in this temperature range.
REQ-TCS-F-TCS003-013	The TCS shall maintain the IFP within the -35 to 80 °C temperature range actively.	The payload has its own thermal regulation system, however the electronics of this system need to be kept in this temperature range.
REQ-TCS-F-MIS007-14	The payload shall experience a temperature difference of less than 5 °C during a single orbit.	The quality of data is dependent on payload temperature changes.

11.2. Assumptions

For the design process of the TCS several assumptions had to be made. These assumptions are listed in Table 11.2.

Table 11.2: List of assumptions made during the preliminary design for TCS

ID	Assumption	Justification	Design Impact	Consequences If Invalid
ASSU-TCS-01	Right Angle of Ascending Node (RAAN) is assumed to be 0° for initial orbital parameters.	The exact orbit insertion executed by the launch vehicle is unknown.	Initial orbital conditions are known.	The dates for which the spacecraft will experience a given thermal environment are shifted on the timeline due to a shift in the RAAN.
ASSU-TCS-02	The rate of change of RAAN is constant.	It is difficult to predict exact rate of change without telemetry.	The eclipse starting points are known in advance with high accuracy.	The rate at which the beta angle changes will be different.
ASSU-TCS-03	The thermal conductivity of material/component is uniform in all directions.	The materials can be modelled as quasi-isotropic.	The thermal conductance is not dependent on material orientation.	The thermal analysis will differ for components that are not really isotropic.
ASSU-TCS-04	The orbit's inclination stays constant throughout mission lifetime.	The variations in orbit inclination are hard to model without telemetry.	The change in beta angle and eclipse fraction is predictable.	The variation in eclipse fraction is different than if the inclination was changing.
ASSU-TCS-05	The internal black body radiation of S/C components is negligible compared to thermal conductance.	The rate of heat exchange from thermal conduction is much higher compared to radiation between internal components [67].	The emission characteristic is not included, therefore the equilibrium states are different.	The actual thermal fluctuations of components will differ from simulation.
ASSU-TCS-06	The geometry of components can be modelled as cuboids.	The exact geometry for several components is unavailable, the main source of heat exchange is conductance.	Simplified geometry affects the calculations for thermal emissions of exposed components.	The actual geometry of components affects the heat transfer between components.
ASSU-TCS-07	Initial component temperatures are set to 280 K.	To perform simulation the initial conditions must be stated.	Initial temperature values will heavily fluctuate and do not represent real scenario.	The initial temperature will be dependent on spacecrafts condition just after the deployment.
ASSU-TCS-08	For Earth's IR emissions, it is considered to be a perfect black body.	This level of simplification is often performed for LEO missions.	Overestimation of Earth's IR power output.	The incoming Earth's IR heat will vary based on location.
ASSU-TCS-09	LEXI generates 286.0 W of waste heat during peak operations.	All of power consumed by payload was assumed to be converted to heat as seen in clients NEBULA-Xplorer Design Description [132].	Overestimation of waste heat generated by LEXI.	LEXI will experience lower temperatures.
ASSU-TCS-10	HEXI generates 44.0 W of waste heat during peak operations.	All of power consumed by payload was assumed to be converted to heat as seen in clients NEBULA-Xplorer Design Description [132].	Overestimation of waste heat generated by HEXI.	HEXI will experience lower temperatures.
ASSU-TCS-11	The propulsion module has an in-built temperature regulation unit.	See Chapter 8.	The propulsion module does not require external temperature control methods.	The propulsion module may experience inoperable/unsurvivable temperature ranges.
ASSU-TCS-12	The battery discharge efficiency is assumed to be 87%	See Chapter 10.	Simplified waste heat generation from battery discharge.	The waste heat during battery discharge will fluctuate.
ASSU-TCS-13	The operational and survival temperature ranges of AOCS components are known.	See Chapter 9.	The TCS is designed to maintain AOCS components in these temperature ranges.	The components may sustain damage from overheating or freezing.
ASSU-TCS-14	The operational and survival temperature ranges of EPS components are known.	See Chapter 10.	The TCS is designed to maintain EPS components in these temperature ranges.	The components may sustain damage from overheating or freezing.
ASSU-TCS-15	The operational and survival temperature ranges of TT&C components are known.	See Chapter 12.	The TCS is designed to maintain TT&C components in these temperature ranges,	The components may sustain damage from overheating or freezing.
ASSU-TCS-16	The operational and survival temperature ranges of C&DH components are known.	See Chapter 13.	The TCS is designed to maintain C&DH components in these temperature ranges.	The components may sustain damage from overheating or freezing.

11.3. Final Design

The final TCS architecture consists of both passive and active systems as a way to facilitate individual components operational temperature ranges.

11.3.1. Passive Systems

The outer surface of the spacecraft's main bus is covered in MLI made out of Indium Tin Oxide (ITO) coated 2 mil Aluminised Polyimide that provides moderate absorptivity and emissivity coefficients, whilst also preventing the build-up of electric charge on the surface. Additionally, a main and secondary radiators are placed on the back and side panels, respectively, to facilitate heat dissipation for the payload and solar panels. The radiator's surface was chosen to be ITO coated 5 mil Silvered Teflon. In both cases, the ITO layer is characterised by low degradation caused by atomic oxygen mentioned in Section 4.3, as stated by NASA's report titled "Space Exposure of Indium Tin Oxide Coatings" [93]. The back sides of solar panels are coated in AZ-93 white paint that provides additional IR emissions with low absorptivity levels. Both LEXI and HEXI are covered in 5 mil Aluminised Polyimide, aluminium side outwards, to minimise the radiative emissions inside the spacecraft. A compiled list with thermo-optical properties of used materials can be seen in Table 11.3, for which the data and properties of MLI materials were taken from Sheldahl Inc. Materials Red Book [71].

Table 11.3: Thermo-optical properties of used materials [4], [71], [119], [134]

Material	Absorptivity [α]	Emissivity [ϵ]
ITO Aluminized Polyimide 2 mil	0.49	0.71
Aluminized Polyimide 5 mil	0.14	0.035
ITO Silvered FEP 5 mil	0.14	0.75
AZ-93 White Paint	0.17	0.89
Z307 Polyurethane Black Paint	0.97	0.89
3G30A Solar Cells	0.91	0.81
Aluminium 6061 T6	0.2	0.13

To conduct heat from internal components to radiative surfaces a combination of thermal straps and interface materials was used to dissipate unwanted heat. Pyrolytic Graphite Film (PGF) thermal straps manufactured by Technology Applications Inc. [18] were selected due to extensive flight heritage and high thermal conductivity. The thermal properties of materials used for the passive system are listed in Table 11.4.

Table 11.4: Thermal properties of used materials

Material	Thermal Conductivity [$Wm^{-1}K^{-1}$]	Specific Heat Capacity [$Jkg^{-1}K^{-1}$]
Pyrolitic Graphite Film (PGF)	1500	850
Aluminium 6061 T6	167	897
Aluminium 5056	117	904
CFRP	10-100	938

A compiled list was made that features all components that comprise the passive system of the TCS architecture. The radiator surface area was acquired through iterative design via thermal analysis, which is described in detail in Section 11.4. The cost estimations were derived using "Spacecraft Thermal Control Handbook, Volume I: Fundamental Technologies" by D. G. Gilmore [59] due to the proprietary nature of such values. The list is featured in Table 11.5.

Table 11.5: Passive system components specifications per unit [71] [59] [18]

Component Type	Component Name	Quantity	Mass [kg]	Surface Area [m^2]	Volume [m^3]	Estimated Cost [k€]
MLI	ITO Aluminized Polyimide 2 mil	-	2.26	3.18	$1.63 \cdot 10^{-3}$	1.8
MLI	Aluminized Polyimide 5 mil	-	0.70	4.03	$4.89 \cdot 10^{-4}$	1.2
Main Radiator	ITO Silvered FEP 5 mil	1	3.24	0.400	$1.20 \cdot 10^{-3}$	1.2
Secondary Radiator	ITO Silvered FEP 5 mil	2	1.90	0.234	$7.02 \cdot 10^{-4}$	0.7
Thermal Strap	PyroFlex PGF	6	0.35	-	$1 \cdot 10^{-3}$	0.4

11.3.2. Active Systems

High priority components were equipped with dedicated temperature sensors that will gather measurements as part of housekeeping data. The use of thermistors was deemed adequate due to their high TRL and low power consumption. A UTC Aerospace Systems sensor [131] was selected, which creates a potential differential given the change in resistivity from temperature variation. The generated electrical signal is converted through the use of ADC connected to the TCS processing unit which sends and receives data from the spacecraft's OBC. From that information basic logic is applied to the central heater controller which manages the temperature of battery pack, LEXI and HEXI electronics. Simple etched foil polyimide flexible heaters manufactured by Zoppas Industries [72] were selected due to their high TRL and low mass. The active system components and their key specifications per unit are listed in Table 11.6.

Table 11.6: Active system components specifications per unit [131][72][59]

Component Type	Component Name	Quantity	Mass [g]	Power Consumption [W]	Estimated Cost [$k€$]
Temperature Sensor	MODEL 0118MM	124	0.35	0.046	0.15 - 0.35
Electric Heater	Zoppas Flexible Heater	6	2.2	4	0.12 - 0.45

11.3.3. TCS H/W Diagram

A hardware diagram was constructed, which can be seen in Figure 11.1. It showcases the connections and their types between TCS components and other subsystems.

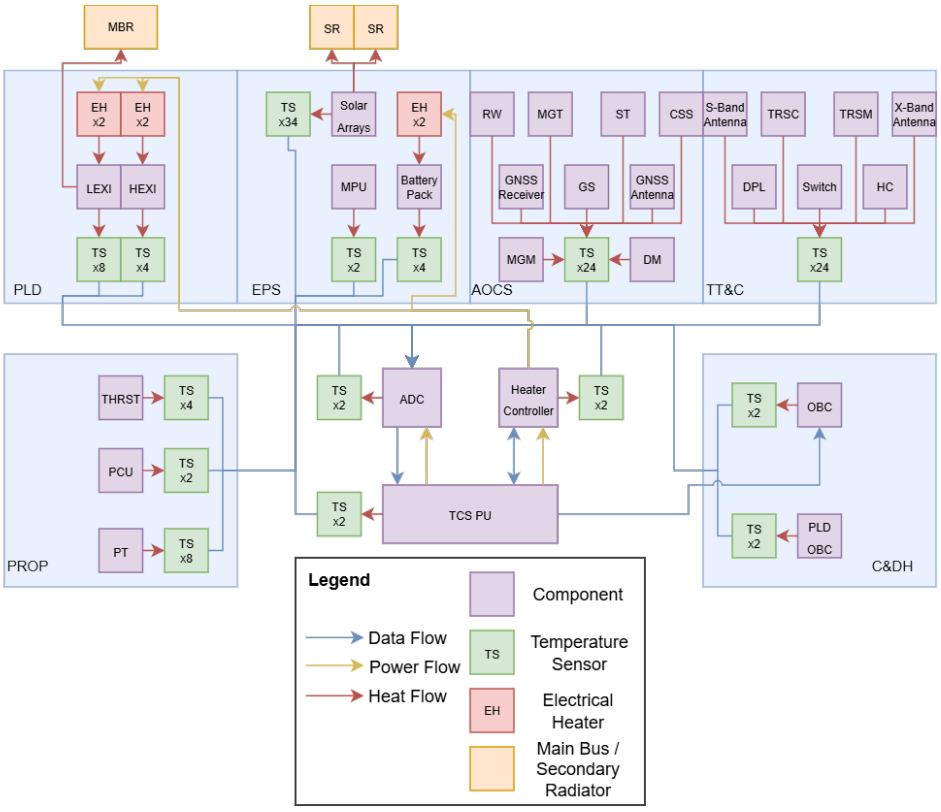

Figure 11.1: TCS H/W Diagram

11.4. Thermal Analysis

To perform thermal analysis of the selected TCS architecture and if it does comply with the imposed requirements relating to spacecrafts thermal performance, firstly the radiative environment has to be studied. After that the computational method can be devised followed by simulation set-up showcasing the temperature progression over time.

11.4.1. Radiative Environment

To determine the radiative environment and therefore identify hot and cold cases, the spacecrafts orbit geometry evolution is analysed. The beta angle analysis conducted in Section 4.4.1 is used to determine eclipse fractions experienced by the spacecraft. As a source for the TSI experienced around Earth's orbit, the ECSS-E-ST-10-04C Space Environment [36] standard was used resulting in a TSI range of 1316 to 1407 Wm^{-2}. Another potential source of heat is Earth's IR emissions and albedo effect. The Earth's IR temperature fluctuates between 250 and 260 K, whilst its albedo factor ranges from 0.19 to 0.40 is derived from "Guidelines for the Selection of Near-Earth Thermal Environment Parameters for Spacecraft Design" [17]. The compiled variables for both hot and cold cases are presented in Table 11.7.

Table 11.7: Hot & Cold Case Variables

Variable	Hot Case	Cold Case
TSI [Wm^{-2}]	1407	1316
Earth's IR Temperature [K]	260	250
Albedo Factor	0.40	0.19
Eclipse Fraction	0.0	0.38

11.4.2. Transient State

With spacecrafts relatively short orbital period, a simple steady state approach would not showcase the temperature fluctuations associated with transition between sunlit and eclipse phases of the orbit. Therefore a transient state approach was chosen to confirm whether the current TCS architecture meets all associated requirements. From relevant celestial bodies and internal heat generation, the total incoming power was estimated

$$\begin{aligned} P_{\text{Solar}} &= \alpha \cdot A_S \cdot I \cdot \cos(\theta) & P_{\text{Earth}} &= \alpha \cdot A_E \cdot \sigma \cdot T_{\text{Earth}}^4 \cdot \cos(i) \\ P_{\text{albedo}} &= \alpha \cdot A_S \cdot I \cdot a \cdot \cos(i) & P_{\text{total}} &= P_{\text{Solar}} + P_{\text{albedo}} + P_{\text{Earth}} + P_{\text{internal}} \end{aligned} \tag{11.1}$$

where:

- P – effective incoming power [W]
- α – material absorptivity [-]
- A_S – surface area exposed to sunlight [m^2]
- A_E – surface area exposed to Earth view [m^2]
- I – solar irradiance [$W\,m^{-2}$]
- θ – Sun incidence angle [rad]
- i – Earth incidence angle [rad]
- σ – Stefan–Boltzmann constant [$W\,m^{-2}K^{-4}$]

The only way for spacecraft to lose waste heat is through radiation. The effective radiation emission is tied to the temperature of the emitting object and the background it is emitting onto. For a full hemispherical view, the spacecraft and its radiators would be emitting unobstructed thermal radiation towards empty space, which on average can be considered to have temperature of around 2.73 K as stated in ESA article titled "Planck and the cosmic microwave background" [45].

$$P_{out} = \epsilon \cdot A \cdot \sigma \cdot (T_{SC}^4 - T_{space}^4) \tag{11.2}$$

The ϵ denotes a materials given effective emissivity coefficient, which dictates how well it emits thermal radiation. With Equation 11.1 and 11.2 the thermal changes for each geometrical surface were calculated, however the conductance between surfaces and components needs to be taken into account.

$$\dot{Q} = k \cdot A \cdot \frac{\delta T}{\delta x} \tag{11.3}$$

Above equation showcases the heat flow between two objects depending on the thermal conductivity k [$Wm^{-1}K^{-1}$], the contact surface area A and the temperature gradient $\frac{\delta T}{\delta x}$ [Km^{-1}].

11.4.3. Computational Model

To perform numerical analysis, an adequate computational model had to be chosen. The backward Euler method was selected due to it being an implicit computational method, which allows for larger time steps

while providing unconditional stability and high levels of accuracy.

$$T^{n+1} = T^n + \Delta t f(T^{n+1}) \tag{11.4}$$

Stefan-Boltzmann equation linearisation was performed for correct application with backward Euler method.

$$P_{out} = \epsilon \cdot \sigma \cdot A \cdot ((T^{n+1})^4 - T_{space}^4) \tag{11.5}$$

$$\approx \epsilon \cdot \sigma \cdot A \cdot ((T^n)^4 - T_{space}^4) + 4\epsilon \cdot \sigma \cdot A \cdot (T^n)^3 \cdot (T^{n+1} - T^n) \tag{11.6}$$

All temperature dependent terms are linearized and the backward Euler method is applied. A system matrix was constructed consisting of component heat capacity, conductance and thermal radiation terms, from which a solution vector for a given time was calculated. A uniform time step of 60 seconds was deemed adequate for the purposes of this model.
For any additional information regarding computational methods such as backward Euler the book ”Numerical Methods for Partial Differential Equations” [74] is recommended.

11.4.4. Simulation Setup

A simple geometrical model of the spacecraft was created that includes critical components along the supporting TCS architecture. The main driving aspects of radiator placement were the sunlight exposure, proximity to components and unobstructed view of outer space. The code to perform the simulation was written in Python programming language [139].

11.4.5. Best and Worst Case Scenario

The best and worst case scenarios had to be devised to determine the conditions the spacecraft will potentially find itself in. For that the section on detailed modes of operations in Section 14.4 was used as a guideline. The downlink mode was deemed to be the driving mode for the worst case scenario due to the limits imposed on spacecrafts attitude and possible exposure of unwanted surfaces to the sunlight. For the best case scenario the science mode was chosen as its the mode the spacecraft will experience the most time in. Additionally the thermal response of both LEXI and HEXI was analysed after the spacecraft exits SAA, to determine the wait time required for temperature stabilisation.

Science Mode

During science mode the spacecraft will prioritise maximizing power generation to support the operations of both LEXI and HEXI. The incoming sun vector will positioned in positive x direction at small angle. An example of such condition can be seen in Figure 11.2, where the yellow vector denotes incoming sunlight, whilst the blue vector shows the Earth direction.

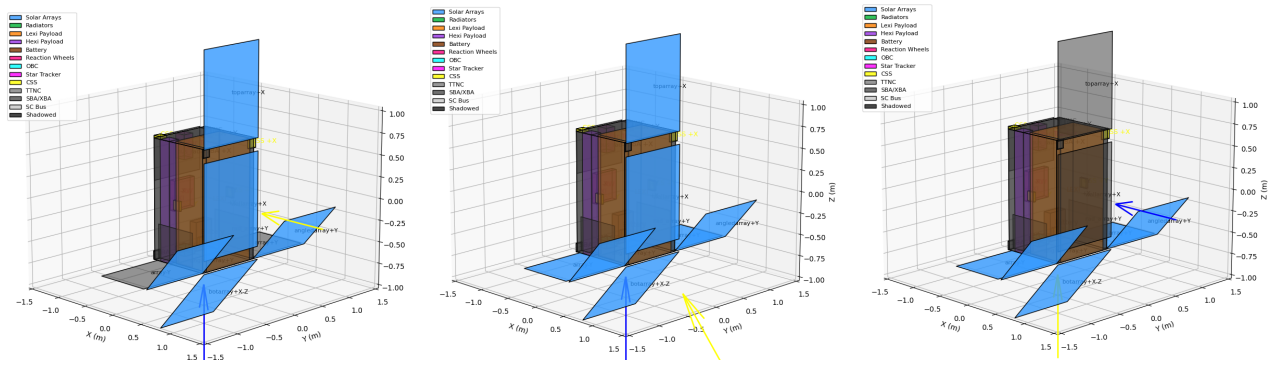

(a) Science mode at 0 degree Y-axis Sun angle **(b)** Science mode at 45 degree Y-axis Sun angle **(c)** Science mode at 90 degree Y-axis Sun angle

Figure 11.2: Spacecraft attitude configurations for Science Mode

Communication Mode

During communication mode the S/C will orient itself to point the X-band antenna to provide downlink capability with the ground station segment. During that period the S/C can be vulnerable to sun exposure of

unwanted elements. An example of such condition is shown in Figure 11.3, with the corresponding vector colours for incoming sunlight and Earth direction being the same as for Science Mode example.

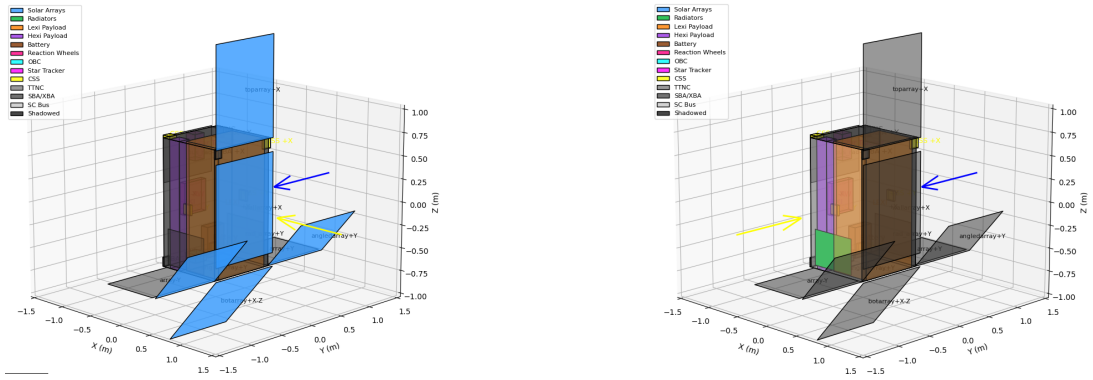

(a) Communication mode at 0 degree Z-axis Sun angle

(b) Communication mode at 90 degree Z-axis Sun angle

Figure 11.3: S/C attitude configurations for Communication Mode

11.4.6. Simulation Results

A simulation was performed using the previously derived hot and cold cases, modes of operation scenarios and the derived computational model. As per NASA's Thermal Control Engineering Guidebook [89] a temperature margin of 5 K was applied to the component thermal operational ranges as a way to predict uncertainties of the model. Additionally a ±1 K margin was imposed on thermal fluctuations for both payloads. The graphs displaying temperature changes for payloads in both hot and cold cases can be seen in Figure 11.4. The resulting values for minimum, maximum, mean temperatures and worst ΔT fluctuation are compiled in Table 11.8. From these results it can be seen that the TCS meets payloads operational requirements stated previously in Section 11.1. The previously described communication mode was also analysed, with no thermal operational limits being breached following the downlink time estimations performed in Section 12.4.

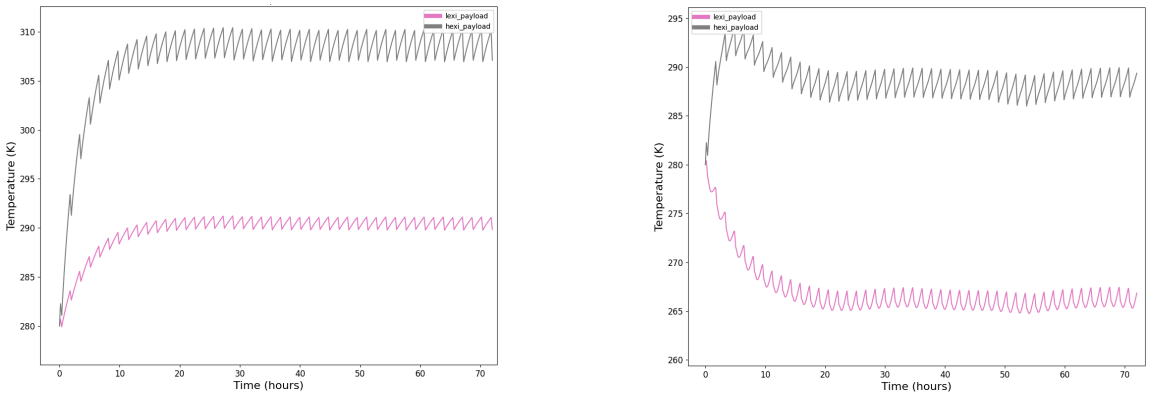

(a) Hot Case

(b) Cold Case

Figure 11.4: Payload temperature graphs for Science Mode

Table 11.8: Thermal Simulation Payload Results for Science Mode

Payload	Minimum Temperature [K]	Maximum Temperature [K]	Mean Temperature [K]	Worst ΔT Fluctuation [K]
LEXI (Hot Case)	289.65	291.22	290.49	1.27
HEXI (Hot Case)	306.95	310.42	308.75	3.15
LEXI (Cold Case)	264.76	267.57	265.96	2.08
HEXI (Cold Case)	285.99	290.12	288.15	3.10

11.4.7. Simulation Verification

As part of the simulation model, a verification process was performed to determine whether the model follows the underlying physical equations stated previously in Section 11.4.2. A simplified case of rectangular plate was performed where a steady state solution was acquired both from hand calculations and the simulation. The simulation solution for final temperature was within acceptable error compared to the analytical solution, therefore verifying the main underlying method used for simulation calculations.

11.5. Risk Assessment

To determine the risks associated with the TCS architecture a high level FMEA was performed, using the methodology presented in Chapter 17, with scoring metrics applied from Section 17.2. Subsystem level FMEA is summarized in Table 11.9.

Table 11.9: FMEA for TCS

Risk ID	Failure Mode	Effect	Cause	L	S	Risk	Mitigation
R-SUB-TCS-001	LEXI cooling failure	LEXI experiences temperatures above its operational regime	Reduced/Severed thermal connection to main bus radiator	A	5	A5	Implement hot parallel redundancy by subdividing thermal connection into separate independent connectors
R-SUB-TCS-002	HEXI cooling failure	HEXI experiences temperatures above its operational regime	Reduced/Severed thermal connection to main bus radiator	A	5	A5	Implement hot parallel redundancy by subdividing thermal connection into separate independent connectors
R-SUB-TCS-003	Radiator overheating	Radiator experiences temperatures above its operational regime	Reduced effective emittance of radiator surface	C	4	C4	Implement resistant coating; Apply margins on radiator sizing
R-SUB-TCS-004	Surface Discharge	Arcing between outer components causing damage	Build-up of surface charge causes potential differential.	C	3	C3	Implement charge dissipating coating
R-SUB-TCS-005	Internal Discharge	Arcing between inner components causing damage	Build-up of internal charge causes potential differential.	C	3	C3	Implement grounding of internal components
R-SUB-TCS-006	Battery pack heating failure	Battery experiences temperatures below its operational regime	Failure/Damage to battery pack assigned electrical heater	B	5	B5	Implement cold parallel redundancy for battery pack heaters
R-SUB-TCS-007	LEXI heating failure	LEXI temperature below operational regime	Failure/Damage to LEXI assigned electrical heater	B	5	B5	Implement cold parallel redundancy for LEXI heaters
R-SUB-TCS-008	HEXI heating failure	HEXI temperature below operational regime	Failure/Damage to HEXI assigned electrical heater	B	5	B5	Implement cold parallel redundancy for HEXI heaters

11.6. Redundancy

The identified risks in Section 11.5 and the associated mitigation plans, result in implementation of redundancy across both passive and active systems for TCS. The redundancy philosophy first explained in Section 6.4 is used as the basis for the selection process and justification for showcased redundant components.

11.6.1. Passive Systems Redundancy

For passive systems a 10% margin was taken on radiator sizing to allow for loss in radiative efficiency over mission lifetime.

11.6.2. Active Systems Redundancy

As part of redundancy measures a combination of parallel hot and cold components was used. In case of temperature measurements, each measured component has at least two active sensors wired in parallel providing continuos data flow in case one of the units fails. For electrical heaters, there is an additional cold spare wired in parallel for each of the main units in case it experiences failure. The redundant heaters will not consume power until failure confirmation of main unit is processed.

12 Telemetry, Tracking & Command

This chapter explains the final design and design choices for the TT&C subsystem, which is responsible for communication with the ground station. Key requirements and assumptions, which were used during the design process, are listed in Section 12.1 and Section 12.2, respectively. Section 12.3 shows the final design of the subsystem and in Section 12.4 the design process is explained. A risk assessment is performed in Section 12.5 and mitigation strategies are explained in Section 12.6.

12.1. Key requirements

The key requirements that drive the design of the TT&C subsystem are listed in Table 12.1.

Table 12.1: List of requirements for the design of the TT&C subsystem

Requirement ID	Requirement Text	Rationale
REQ-TT&C-C-SYS012-001	HKTM data shall be downlinked with a frequency of 2200–2290 MHz	The downlink frequency will define the available bandwidth, ground station compatibility and what data throughput is achievable. Therefore, this requirement constrains how much telemetry data can be returned during each contact period
REQ-TT&C-C-SYS011-002	Payload data shall be downlinked with a frequency of 8025–8500 MHz	The downlink frequency will define the available bandwidth, ground station compatibility and what data throughput is achievable. Therefore, this requirement constrains how much payload data can be returned during each contact period
REQ-TT&C-C-SYS009-003	The spacecraft shall downlink 408 Gbit of payload data within 18 minutes every 24 hours	To maximise available time for science operation, the downlink window is reduced to 18 minutes with 20% margin
REQ-TT&C-F-SYS012-004	The spacecraft shall downlink 2.64 Gbit of HKTM data every 24 hours	This requirement ensures that sufficient HTKM is returned to the ground to enable continuous monitoring of spacecraft health.
REQ-TT&C-F-SYS012-005	The downlink data rate for HKTM data shall be at least 0.45 Mbits	This requirement ensures that the data is sent back to the ground station within the available contact time
REQ-TT&C-F-SYS012-006	The TT&C subsystem shall ensure an effective downlink BER of 10^{-8} for telemetry and payload data after error correction	The delivery of telemetry and payload data needs to be accurate and reliable in order to monitor the spacecraft health and to meet science mission objectives.
REQ-TT&C-C-SYS013-007	Telecommands shall be uplinked with a frequency of 2025–2110 MHz	This requirement constraints how much data can be uplinked during each contact period as the frequency will define the available bandwidth, ground station compatibility and what data throughput is achievable
REQ-TT&C-F-SYS013-008	Up to 264 Mbit of telecommands shall be uplinked every 24 hours	This requirement ensures sufficient uplink capacity to support commanding and software updates.
REQ-TT&C-F-SYS013-009	The uplink data rate for telecommands shall be at least 45 kbit/s	This requirement ensures that the telecommands can be sent to the satellite within the available contact time
REQ-TT&C-F-SYS013-010	The TT&C subsystem shall ensure an effective BER of 10^{-8} for command reception after error correction	Having a reliable command reception is important for the operations of the spacecraft to be safe and continuous.

12.2. Assumptions

Assumptions made during the design of the TT&C subsystem are shown in Table 12.2.

Table 12.2: List of assumptions made during the preliminary design for TT&C

Assumption ID	Assumption/input	Justification	Design Impact	Consequences if Invalid
ASSU-TT&C-1	A roll-off factor of 0.25 is supported by the ground station	A roll-off factor of 0.25 is commonly supported by modern ground stations	Defines occupied bandwidth and spectral efficiency for TT&C links; used in bandwidth allocation and regulatory compliance analysis	A higher roll-off factor would increase occupied bandwidth, potentially violating spectrum allocation limits or requiring a lower data rate
ASSU-TT&C-2	Link margin is 5dB	Consistent with link margin values reported in example link budgets in SMAD[137]	Used to account for uncertainties in propagation, pointing, and hardware performance in the TT&C link budget	A lower margin would reduce robustness to uncertainties and could lead to reduced link availability
ASSU-TT&C-3	AOCS line-of-sight accuracy is within < 150 arcsec	See Chapter 9	Used to assess antenna pointing losses	Degraded pointing accuracy would increase pointing losses and could lead to link outages
ASSU-TT&C-4	The maximum supported downlink data rate by SpaceFibre is 4.5 Gbit/s	See Section 13.2.2	Ensures that internal data handling does not limit the downlink capability	If lower than the required data rate, onboard buffering or reducing the data rate would be required
ASSU-TT&C-5	S-band patch antenna receiving system noise temperature is <190 K	Value adopted from Maral & Bousquet, Satellite Communications Systems[81]	Used in uplink link budget calculations	Higher system noise temperature would degrade uplink SNR
ASSU-TT&C-6	Ground station maximum isotropic gain is 35 dBi	Provided in the Leaf Space Network Deployment Plan[77]	Directly affects uplink and downlink link budgets	Lower antenna gain would reduce link margin
ASSU-TT&C-7	Ground station maximum antenna input peak power is 15 dBW	Provided in the Leaf Space Network Deployment Plan[77]	Limits the maximum achievable uplink margin	Lower antenna input peak power would reduce link margin
ASSU-TT&C-8	Ground station antenna G/T at 5° elevation is 12.53 dB/K (S-band) and 24.65 dB/K (X-band)	Provided in the Leaf Space Network Deployment Plan[77]	Used in link budget calculations	A lower value would increase the required SNR
ASSU-TT&C-9	Ground station antenna G/T at 10° elevation is 12.93 dB/K (S-band) and 25.45 dB/K (X-band)	Provided in the Leaf Space Network Deployment Plan[77]	Used in link budget calculations	A lower value would increase the required SNR
ASSU-TT&C-10	Ground station antenna supports RHCP polarisation	Obtained from the datasheet of the Gaia100 antenna[100]	Ensures polarisation matching and minimizes polarization mismatch losses	Polarisation mismatch would introduce additional losses, degrading link margin
ASSU-TT&C-11	The ground station supports OQPSK and 32-APSK modulation schemes with concatenated CC+RS and Low-Density Parity-Check (LDPC) FEC codes	Leaf Space confirmed support for the selected modulation scheme and FEC codes.	Enables adoption of the selected modulation and coding schemes	If unsupported, a different modulation scheme or FEC code would have to be chosen
ASSU-TT&C-12	The implementation loss is 1.5dB	Consistent with representative example link budgets in Sklar[115]	Included in link budget calculations to avoid optimistic performance estimates	Underestimated implementation losses would reduce effective link margin and may necessitate late-stage redesign
ASSU-TT&C-13	The maximum allowed occupied bandwidth on S-band is 1.2 MHz for a data rate of 10 to 60 kbps	Stated in ESA PSS-04-105[47]	Constrains the choice of modulation and coding rate for the S-band TT&C downlink	Exceeding the allowed bandwidth could result in non-compliance with regulations and denial of frequency allocation
ASSU-TT&C-14	The maximum allowed occupied bandwidth on X-band is 142 MHz	No mission-specific regulatory constraint on X-band bandwidth has been identified at this stage; the value is used as a preliminary placeholder	Enables high-rate payload downlink and drives RF front-end and filtering design	Reduced allowed bandwidth would limit achievable data rates

12.3. Final Design

After completion of the detailed design phase, the final TT&C system architecture was defined. The selected configuration and associated hardware are summarised below.

12.3.1. Command and Housekeeping Data

To downlink HKTM data and uplink TC, the S-band frequency range will be used. The architecture consists of 2 NANOlink(-S)-boost-dp units, two Single-pole Double-throw (SPDT) RF switches and two low-gain patch antennas.

The NANOlink [116] integrates a transceiver, amplifier, diplexer and a splitter. The transceiver provides for

modulation and demodulation of both uplink and downlink signals and controls the modes of operations of the subsystem. It supports Offset Quadrature Phase Shift Keying (OQPSK) modulation and concatenated Forward Error Correction (FEC) consisting of a rate-1/2 convolutional code and a Reed–Solomon code to improve link robustness. It also uses multiple, independent buffers to properly manage data for transmission and reception. In addition, the transceiver provides encryption of uplink TC to prevent unauthorised commands from being accepted by the spacecraft.
The power amplifier boosts the RF signal to meet the required transmit power. The diplexer is a filtering component that couples the receiver and transmitter signals together onto a single RF cable. Downstream of the diplexer, the splitter divides the RF signal between two antenna ports, both of which are capable of transmitting and receiving data.
An additional NANOlink unit is included for redundancy. The receiver of the redundant unit operates in hot redundancy, allowing for immediate switchover in the event of a failure without loss of spacecraft command ability. The transmitter is maintained in cold redundancy, as a short loss of downlink capability does not significantly increase overall mission risk. To enable the antennas to switch between the nominal and redundant NANOlink units, SPDT switches are used.
Two low-gain S-band patch antennas are employed to communicate with the ground station. These antennas have hemispherical coverage and are mounted on opposite sides of the spacecraft to achieve omnidirectional antenna coverage. This configuration allows HKTM downlink and TC uplink without the need for spacecraft pointing, thereby maximising time available for science operations.
A list of S-band subsystem components, along with their associated mass and power requirements, is provided in Table 12.3.

Table 12.3: S-band subsystem components specification

Component Type	Component Name	Quantity	Mass [g]	Power Consumption
Transceiver	Skylabs NANOlink(-S)-boost-dp	2	409	Rx+Tx at max output power: 17 W; Rx only: 1.9 W
Switch	Radiall low-power coaxial SPDT (lay down with pins)	2	62	N/A
S-band Antenna	EnduroSat S-band wideband patch antenna	2	113	N/A

12.3.2. Payload Data

Payload data downlink is performed using the X-band to accommodate the higher required data rate. The X-band communication architecture consists of two transmitters, an SPDT RF switch, and a high-gain patch antenna.
The transmitter is responsible for encoding and modulating the payload data stream and converting it to the required X-band frequency for transmission. In Section 12.4.2, 32-APSK (Amplitude and Phase Shift Keying) modulation is selected, together with a LDPC code with a rate of 4/5 for forward error correction. Redundancy is implemented through two transmitters, with one operating nominally while the other is kept in cold redundancy. An SPDT switch routes the RF output from the active transmitter to the antenna, enabling selection between the nominal and redundant units.
A high-gain patch antenna is used to transmit the payload data to the ground station. In contrast to the low-gain S-band antennas, the antenna has a significantly narrower Half-power Beam Width (HPBW) and therefore requires pointing toward the ground station to close the communication link. The antenna is body-mounted on the spacecraft, requiring spacecraft pointing to achieve line of sight.
A complete list of X-band components is provided in Table 12.4. Figure 12.1 illustrates the hardware architecture for both the S-band and X-band communication subsystems.

Table 12.4: X-band subsystem components specification

Component Type	Component Name	Quantity	Mass (g)	Power Consumption
Transmitter	Cubecom HDRTX	2	250	25W
X-band Antenna	EnduroSat X-band 8×12 patch antenna	1	400	N/A
Switch	Radiall low-power coaxial SPDT (lay down with pins)	1	62	N/A

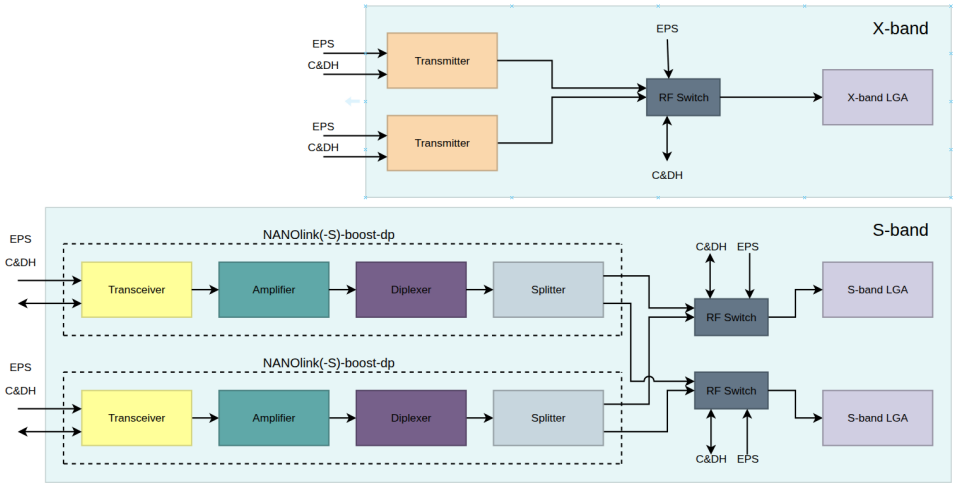

Figure 12.1: TT&C subsystem architecture

12.3.3. Ground Station Network

The recommended ground station network for the mission is the Leaf Space network. It contains nine suitable ground stations for the mission. According to the ConOps report [22], Leaf Space supports up to 24 contact opportunities per day, providing more than sufficient contact time for both uplink and downlink operations. Each contact window has an average pass duration of 7.74 minutes.

In total, twelve ground station passes are required per day. Of these, two passes have a duration of at least 7.5 minutes and are allocated for payload data and HKTM downlink via the X-band antenna, as well as TC reception via the S-band. Passes with a longer duration are chosen for downlinking with the X-band antenna to minimise spacecraft slews, thereby reducing interruptions to science observations. The remaining ten passes are used exclusively for routine HKTM downlink and TC reception via the S-band antennas and should total to at least 75 minutes. The required power of the TT&C subsystem during the two X-band passes is 26.9W, whereas the power required during the S-band passes is 18.9W.

During the ten passes used for HKTM and TC only, the spacecraft will start downlinking from an elevation of 5°. For X-band operations, a higher minimum elevation angle of 10° is adopted to mitigate atmospheric attenuation.

The TT&C subsystem remains operational for an orbit inclination of 60°, using the Leaf Space network. As an alternative, the ground station network of KSAT was also analysed. For orbit inclinations of 45°, and 60°, this configuration still provides sufficient downlink capacity to meet mission requirements.

The downlink link budgets for the S-band and X-band, as well as the S-band uplink link budgets, are presented in Table 12.5.

12.4. Communications Analysis

This section presents the analyses performed to verify compliance of the TT&C subsystem with the mission requirements shown in Table 12.1. The analysis includes a link budget assessment to verify link closure, an evaluation of antenna placement, and an assessment of ground station contact opportunities.

12.4.1. Link budget

Before choosing the antennas, the required transmit power and gain should be calculated. The primary drivers are the required data rate, derived from the data volume and available downlink time, and the target Bit Error Rate (BER).

A Python script was set up to allow rapid iteration by varying key parameters, including downlink time, minimum elevation angle, and link losses. The tool also allows selection of various modulation and FEC schemes, which determine the required energy-per-bit to noise-density ratio (E_b/N_0) for the specified BER.

The required E_b/N_0 corresponding to the required BER is then used to derive the carrier-to-noise ratio (C/N0) along with the data rate, implementation losses and link margin [68]:

Table 12.5: Uplink and downlink link budgets

Parameter	S-band DL	X-band DL	S-band UL
Data size	2.2 Gbit	51.44 Gbit	264 Mbit
Link time (min)	75	15	90
BER	10^{-8}	10^{-8}	10^{-8}
Information bit rate	0.489 Mbps	457.24 Mbps	48.89 kbps
Modulation	OQPSK	32-APSK	OQPSK
FEC	Conv. 1/2 + RS	LDPC 4/5	BCH(56)
Coded data rate	1.12 Mbps	571.56 Mbps	55 kbps
Transmit power [dBW]	1.24	2.3	1.62
Tx passive loss [dB]	0.12	0.12	1
Tx antenna gain [dBi]	5	24	35
EIRP [dBW]	5.81	27.5	36.1
Path loss [dB]	-166.16	-175.89	-166.16
Atmospheric loss [dB]	-1.6	-3.5	-1.6
Other losses [dB]	-11	-1.588	-5
Minimum elevation [deg]	5	10	5
Ground antenna G/T [dB/K]	12.53	25.45	—
Receive antenna gain [dBi]	—	—	-5
Receive system noise [K]	—	—	200
Required E_b/N_0 [dB]	2.7	8	10.75
Link margin [dB]	5	5	5

$$\frac{C}{N_0} = \frac{E_b}{N_0} + 10\log_{10}(R_b) + L_{\text{imp}} + M \tag{12.1}$$

where $\frac{C}{N_0}$ is the carrier-to-noise density ratio (dB-Hz), $\frac{E_b}{N_0}$ the energy-per-bit to noise density ratio (dB), R_b the data rate (bit/s), L_{imp} the implementation loss (dB), and M the link margin (dB).

As discussed by Sklar[115], the required link margin depends on the designer's confidence in the accuracy of the link budget entries. For systems employing new technology or new operating frequencies, one needs more margin than for systems that have been repeatedly built and tested. In this analysis, a link margin of 5 dB is adopted as a conservative design choice. The selected margin is consistent with spacecraft link design practice as described in SMAD[137].
Implementation loss is the loss in performance due to the difference between theoretical detection performance and the actual performance due to imperfections such as timing errors, frequency offsets, finite rise and fall times of waveforms, and finite-value arithmetic.
The effective isotropic radiated power (EIRP) is then calculated as[68]:

$$\text{EIRP} = \frac{C}{N_0} - \frac{G}{T} + 10\log_{10}(k) + L_{\text{path}} + L_{\text{atm}} + L_{\text{point}} + L_{\text{pol}} \tag{12.2}$$

where EIRP is the effective isotropic radiated power [dBW], $\frac{C}{N_0}$ the carrier-to-noise density ratio [dB-Hz], $\frac{G}{T}$ the receiver antenna gain-to-noise-temperature ratio [dB/K], k the Boltzmann's constant (1.38×10^{-23} J/K), L_{path} the free-space path loss [dB], L_{atm} the atmospheric loss [dB], L_{point} the pointing loss [dB], and L_{pol} the polarization loss [dB].

Atmospheric attenuation was modelled using the ITU-Rpy[104] Python library, which implements ITU-R propagation recommendations. The model accounts for attenuation due to atmospheric gases, rain and other forms of precipitation, clouds, scintillation and multipath effects, as well as attenuation caused by sand and dust storms. For a minimum elevation angle of 5° and a time exceedance probability of p = 3%, the maximum atmospheric attenuation is estimated as 1.6, dB in S-band and 6.4, dB in X-band. Increasing the elevation to 10° reduces the maximum atmospheric attenuation in the X-band to 3.5 dB.

Pointing losses were evaluated based on antenna radiation characteristics. For the S-band antenna, a maximum pointing error of 90 degrees was taken to ensure link closure over a 180° field of view. For the X-band antenna,

the maximum pointing error is the sum of the maximum AOCS pointing error and the ground station pointing error. Both the spacecraft and ground station antennas employ right-hand circular polarisation (RHCP) for S-band and X-band, resulting in negligible polarisation mismatch and a polarisation loss of 0 dB.

The free space path loss can be found using the selected frequency and the maximum distance between the satellite and the ground station, which is dependent on the orbit altitude and elevation angle[68]:

$$\mathrm{L}_{\mathrm{path}} = 20\log_{10}(d) + 20\log_{10}(f) + 32.44 \tag{12.3}$$

where L_{path} is the free-space path loss [dB], d the transmitter–receiver distance [km], f the carrier frequency [MHz], and the constant 32.44 accounts for unit conversion in the free-space loss formula. Finally, the required transmit power can be found using:

$$P_{\mathrm{dBW}} = \mathrm{EIRP} - G_{\mathrm{T}} + L_{\mathrm{feed}} \tag{12.4}$$

where P_{dBW} is the received power at the receiver input [dBW], EIRP the effective isotropic radiated power [dBW], G_{T} the receiver antenna gain [dBi], and L_{feed} the receiver feed and waveguide loss [dB].

Transmit-side feed losses include contributions from the diplexer, RF splitter, RF switch, and interconnecting cables. In addition, the S-band architecture introduces an inherent 3 dB power division loss due to splitting the signal between two antennas. The NANOlink unit provides 5W output power after the amplifier, this is reduced to approximately 1.4 W per antenna port after accounting for the losses induced by the diplexer and splitter.
The required transmit power and antenna gain could then be plotted as shown in Figure 12.2. Figure 12.2a shows the required transmit power and gain for the S-band antenna. Figure 12.2b shows the result for the X-band antenna.

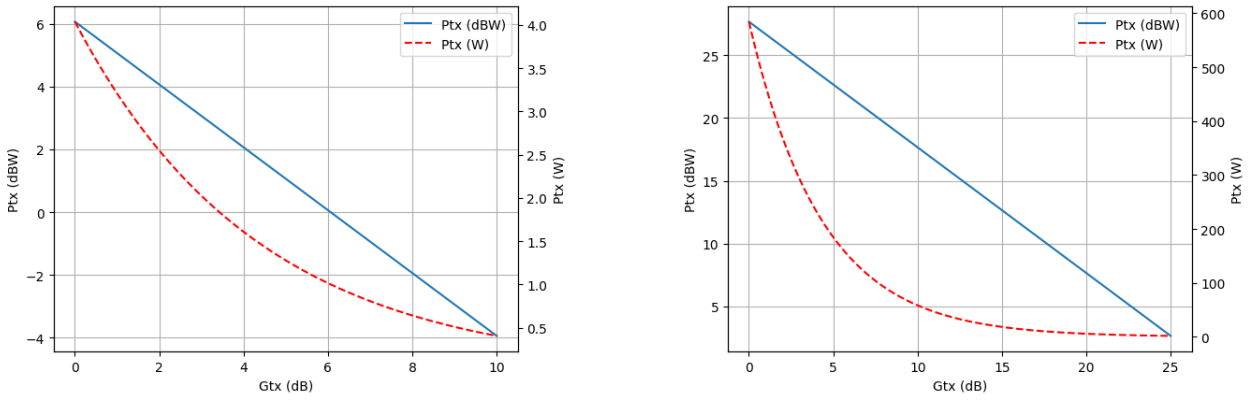

(a) Required transmit power and gain for S-band downlink

(b) Required transmit power and gain for X-band downlink

Figure 12.2: Required antenna transmit power and gain for S-band and X-band downlinks

12.4.2. Forward Error Correction and Modulation

FEC techniques are employed to mitigate transmission errors and to reduce the required E_b/N_0. Several FEC schemes exist, of which the most common are convolutional codes, Reed–Solomon (RS) codes, LDPC codes, and turbo codes. These coding schemes are recommended in Consultative Committee for Space Data Systems (CCSDS) 130.1-G-3 [27]. Convolutional and Reed–Solomon codes can be concatenated to improve error-correction performance; the recommended configuration by CCSDS consists of an RS outer code followed by a convolutional inner code.
According to CCSDS 131.0-B-5 [28], turbo codes are primarily intended for links beyond low Earth orbit, providing high coding gains at the cost of increased bandwidth expansion and greater demodulation and decoding complexity. For this reason, turbo coding was excluded from the design, and only convolutional, Reed–Solomon, and LDPC codes were considered. Performance curves from CCSDS 130.1-G-3[27] and from the LDPC-coded modulation performance analysis reported by Hamkins[66] were used to determine the required

E_b/N_0 for a given target BER.
Among the considered schemes, LDPC codes offer the highest coding gain, but they also introduce higher complexity, increased latency, and reduced robustness compared to convolutional and Reed–Solomon codes. Therefore, convolutional and RS coding are preferred whenever they are sufficient to close the link. If this is not achievable, a higher-performance coding scheme such as LDPC becomes necessary. Additionally, FEC codes are available with different code rates: lower code rates provide higher coding gain but increase occupied bandwidth, which must be carefully considered during system design.

Modulation

Modulation schemes determine how information is mapped onto a carrier signal. BPSK and QPSK are commonly used at lower data rates due to their robustness against noise and interference and their relatively low implementation complexity. However, they occupy more bandwidth compared to higher-order modulation schemes such as 8-PSK, 16-APSK and 32-APSK, which offer improved spectral efficiency at the cost of a higher required E_b/N_0.
Usually, a satellite mission can't use the entire operational frequency band because it's shared with other users. Therefore, there are often constraints on the maximum allowed bandwidth, and it's important to make efficient use of the available bandwidth. The maximum allowable bandwidth occupation is derived from the ESA PSS-04-105 [47] standard. For the 2200–2290 MHz S-band frequency range and symbol rates between 10 and 60 kbit/s, the maximum occupied bandwidth is 1.2 MHz. For the 8025–8400 MHz X-band frequency range, the applicable bandwidth constraint has not yet been specified. In addition, the ground station operator was contacted about any further bandwidth limitations; however, no response was received at the time of this study. Consequently, the design prioritizes minimizing bandwidth occupation while ensuring reliable link closure.
The required bandwidth, symbol rate, required gain and transmit power were then calculated for various combinations of modulation schemes and FEC codes. Options that could not close the link or had an unrealistic symbol rate were emitted first. The remaining options were then filtered on bandwidth. It was found that for the S-band architecture, a concatenated FEC scheme consisting of a rate-1/2 convolutional code and a Reed–Solomon (255,223) outer code is the most suitable, combined with OQPSK modulation. This configuration results in an occupied bandwidth of 0.737 MHz, which is well within the bandwidth constraint of 1.2 MHz. For the X-band architecture, a rate-4/5 LDPC code was selected together with 32-APSK modulation. This configuration results in an occupied bandwidth of 142 MHz. If further bandwidth reduction becomes necessary, several mitigation options exist, including selecting an antenna with increased gain, reducing the roll-off factor, selecting a higher-order modulation scheme, or lowering the data rate by increasing the downlink time. Moreover, moving to Ka-band would be an option as well because it has a wider spectrum allocation, relaxing bandwidth constraints.

12.4.3. Communication Windows

From the link budget analysis, it was found that 75 minutes per day is required to downlink HKTM data through the S-band and 15 minutes per day is required to downlink HKTM and Payload data on the X-band. HKTM is downlinked during payload downlink passes to reduce the peak power usage of the subsystem. TC reception is maintained simultaneously via the S-band. In total, 90 minutes of contact time is required with the ground station.
From the ConOps [22], information was collected on the Leaf Space and KSAT ground station networks, including ground station locations and maximum supported data rates. Antenna specifications for the Leaf Space ground stations were available; however, no equivalent data were provided for KSAT. KSAT was contacted to request this information, but no response was received during the course of the project. Consequently, in this analysis, it is assumed that KSAT employs antennas with performance characteristics comparable to those used by the Leaf Space network.
The Leaf Space network provides nine suitable ground stations for the missions, supporting up to 24 contacts per day. KSAT recommended licensing three ground stations, supporting up to 16 contacts per day. Network contact metrics for both networks were calculated using the General Mission Analysis Tool (GMAT) and processed with a Python script to obtain the metrics and visualise the contact windows as shown in Figure 12.3. The resulting network contact metrics for Leaf Space and KSAT are presented in Table 12.6. Analyses were performed for orbital inclinations of 45° and 60°.
For the 45° and 60° inclinations, all nine Leaf Space ground stations were utilised. For the KSAT network, the selected stations for the 45° orbit were Athens (GR), Awarua (NZ), and Hartebeesthoek (ZA). For the 60°

orbit, Awarua (NZ), Punta Arenas (CL), and Inuvik (CA) were used. All results assume a minimum elevation angle of 5°.

Table 12.6: Comparison of network contact metrics for Leaf Space and KSAT

Orbit Inclination	Metric	Leaf Space	KSAT
60°	Average pass duration [min]	6.83	8.90
	Maximum pass duration [min]	10.3	10.3
	Passes per day	48	17
	Total network contact per day [min]	327.97	151.26
	Maximum no-contact gap [min]	92.33	92.65
45°	Average pass duration [min]	7.74	7.90
	Maximum pass duration [min]	10.3	10.3
	Passes per day	55	19
	Total network contact per day [min]	425.83	150.18
	Maximum no-contact gap [min]	106.22	202.39

Both networks support the required downlink time of 90 minutes that is needed for downlinking the HKTM data. The orbit inclination will have an effect on total network contact time, however, it never drops below the required 90 minutes per day. Based on the average pass duration, daily contacts required are 11-14. The ConOps report, however, advices to use the Leaf Space network over KSAT because of reduced costs. For the selected 550 km orbit with a 45 degree inclination, the Leaf Space network provides an average pass duration of 7.74 minutes. To obtain the 90 minutes of required data, this would require 12 contacts per day.
For X-band, it's preferred to start downlinking at a higher elevation of 10 degrees to mitigate high atmospheric attenuation. Additionally, it's preferred to downlink the payload data in a minimum number of contact windows to reduce the required slews. Using GMAT, the ground contact times for the selected orbit with the Leaf Space network were calculated again. It was found that there are many available contact windows of at least 7.5 minutes at this minimum elevation. Therefore, downlinking with the X-band antenna will happen during dedicated communication windows of at least 7.5 minutes.

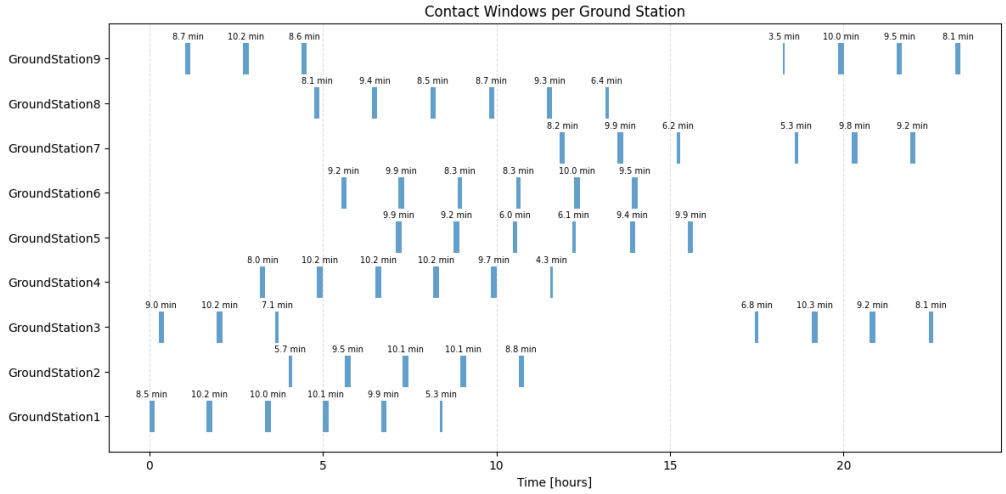

Figure 12.3: Contact windows with Leaf Space Network for a 550 km altitude, 45 degree inclination orbit at a minimum elevation of 5 degrees.

12.4.4. Antenna Placement

To determine the optimal placement of the omnidirectional S-band antennas on the spacecraft, a ray-casting analysis was performed using Blender. The method simulates antenna radiation by emitting a large number of uniformly distributed rays from the antenna location and evaluating line-of-sight obstruction by spacecraft structures. Multiple candidate antenna positions were evaluated to minimise radiation blockage by the satellite body and deployed components.
Based on the results, the first antenna is placed on the -X face of the spacecraft. In this configuration, no

blockage by solar panels or other structural elements occurs, ensuring full hemispherical coverage. The second antenna is placed on the +X face of the spacecraft, centred between the deployed solar panels. In this location, the side-mounted solar panels introduce the least amount of blockage.
The analysis indicates that the vast majority of directions remain unobstructed. The first antenna provides full hemispherical (180°) omnidirectional coverage. For the second antenna, two small localised dead zones are observed, caused by blockage from the solar panels. These blocked regions form narrow bands on the radiation sphere and together account for approximately 0.08% of the total solid sphere. The resulting radiation coverage for the second antenna is shown in Figure 12.4.
In addition to the localised nulls resulting from solar panel blockage. The resultant sum pattern of the antennas will experience significant nulls in the regions where the antenna patterns meet and combine destructively according to SMAD[137].

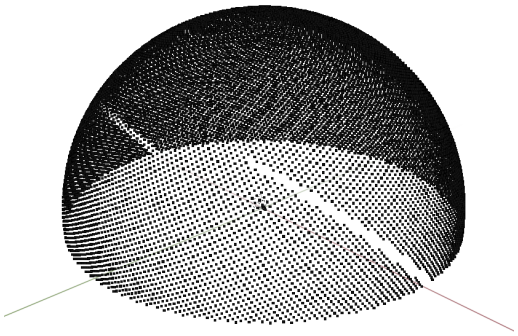

Figure 12.4: Antenna radiation coverage visualisation showing two obstructed regions produced by a single S-band antenna.

The X-band antenna will be mounted on either the +Y or −Y face of the spacecraft. Placement along the +Z direction is avoided, as the X-ray instrument is aligned with this axis. Locating the antenna on the +Z face would require large spacecraft attitude manoeuvrers when switching between science observations and communication with the ground station. Installation on the −Z face is also not feasible, as this face is occupied by the launch vehicle adapter and does not provide sufficient available volume. The ±X faces are largely allocated to the solar panels and propulsion subsystem, leaving limited mounting space. Consequently, the ±Y faces represent the most suitable locations for antenna installation. The selected configuration ensures an unobstructed field of view for the X-band patch antenna, which has a narrow beamwidth of 18°, with no spacecraft structures intersecting the beam.

12.5. Risk Assessment

Table 12.7 presents the high-level FMEA performed on the TT&C subsystem. It identifies common failure modes, their potential effects on mission operations, causes of the failure modes, and corresponding mitigation strategies. Scoring metrics from Section 17.2.2 were used to assess the risk.

Table 12.7: High-level FMEA taking into account common failures for the TT&C subsystem

Risk ID	Failure Mode	Effect(s)	Cause(s)	L	S	Risk	Mitigation
R-SUB-TT&C-001	Transceiver or Diplexer failure	Loss of uplink and downlink communications	Radiation effects, thermal or power stress, component or connector failure	B	5	B5	Redundant transceiver, radiation-tolerant parts, thermal control
R-SUB-TT&C-002	Transmitter failure	Loss of payload data	Radiation effects, thermal or power stress, component or connector failure	B	5	B5	Redundant transmitter, radiation-tolerant parts, thermal control
R-SUB-TT&C-003	Antenna mis-pointing	Reduced link margin; intermittent or lost communications	AOCS line-of-sight pointing errors	B	4	B4	Wide-beam antennas, pointing constraints

Continued on next page

Risk ID	Failure Mode	Effect(s)	Cause(s)	L	S	Risk	Mitigation
R-SUB-TT&C-004	Wrong frequency	Loss of lock; no data or high bit error rate	Frequency drift, temperature variation, configuration error	B	4	B4	Temperature compensation, wide acquisition bandwidth
R-SUB-TT&C-005	Command loss(uplink TC not received)	Inability to control spacecraft; delayed response to anomalies	Low uplink margin, interference, ground station outage	B	3	B3	Multiple ground stations, uplink margin, command retries
R-SUB-TT&C-006	Unauthorised command acceptance	Execution of unsafe or incorrect commands	Weak command validation, RF interference	C	5	C5	Command authentication
R-SUB-TT&C-007	Telemetry dropout/-packet loss	Incomplete situational awareness; missed anomalies	Low SNR, antenna nulls, scheduling or link interruptions	D	3	D3	Telemetry buffering, priority housekeeping
R-SUB-TT&C-008	Excessive RF interference	Degraded uplink/downlink performance; intermittent link loss	Onboard EMC issues, payload interference	B	4	A4	EMC testing, filtering, separate antennas
R-SUB-TT&C-09	Ground segment outage	Missed passes; delayed commanding and data reception	Ground station failure, network outage, scheduling error	A	2	A2	Redundant ground stations, automation

12.6. Redundancy

To mitigate the unacceptable risks found in Section 12.5, several mitigation methods have been implemented into the design.

12.6.1. Redundant components

The primary risks to the subsystem are associated with the transceivers, diplexers, and transmitters. To address these risks, the S-band architecture employs two NANOlink units, each integrating a transceiver and diplexer. Both S-band patch antennas are connected to the two units via an SPDT RF switch, allowing either antenna to be routed to either unit. In the event of a failure in one NANOlink unit, the antennas can be reconfigured to operate with the remaining unit, preserving TT&C functionality. For the X-band architecture, two transmitters are implemented with an RF switch that enables the selection of the alternate transmitter in the event of a failure. These redundancies reduce the likelihood of a complete loss of S-band or X-band communications.

12.6.2. Encryption

Unauthorised or unintended command acceptance is mitigated through the use of cryptographic protection on the S-band uplink, implemented by the NANOlink-S-boost-dp. The unit supports the CCSDS Space Data Link Security (SDLS) protocol, providing cryptographic authentication of TC using the AES-GCM-256 algorithm. This ensures that only commands generated by the authorised ground segment and protected with the correct cryptographic keys are accepted by the spacecraft.

12.6.3. Telemetry dropouts

Telemetry dropouts are primarily driven by antenna pattern nulls. To mitigate this risk, the spacecraft implements telemetry buffering, allowing HKTM to be stored onboard during periods of reduced link quality and transmitted once a stable downlink is re-established. Buffering is supported by the NANOlink(-S) transceiver that's chosen for the design. In addition, critical telemetry data is prioritised over non-critical data to ensure that essential spacecraft health information is downlinked whenever communication is available.

13
Command & Data Handling

This chapter will describe the final design of the C&DH. First, an overview of the subsystem requirements and used assumptions is given. This is followed by an overview of the components, the data handling architecture and the communication bus definition. Additionally, a risk assessment is done to justify the applied redundancy techniques. The chapter is concluded with an overview of key hardware characteristics.

13.1. Key Requirements

The C&DH subsystem for the NEBULA-Xplorer was designed in compliance with the requirements in Table 13.1 below. The requirements used at this stage define data throughput, data storage and reliability measures that shall be taken.

Table 13.1: List of requirements for the design of the C&DH subsystem

Requirement ID	Requirement Text	Rationale
REQ-C&DH-C-SYS025-01	The C&DH subsystem shall not contain any single point failure in the data buses leading to loss of command reception and telemetry generation	The spacecraft must remain recoverable and capable of communicating with ground for the full required mission lifetime
REQ-C&DH-F-SYS025-02	The C&DH subsystem shall implement an autonomous and independent mechanism to detect software freezes and restore nominal operations	To increase reliability and prevent a software lock-up from causing permanent loss of spacecraft functionality
REQ-C&DH-F-SYS021-03	The C&DH subsystem shall collect housekeeping data from each subsystem	Housekeeping is data is used for verifying spacecraft status and mode switching
REQ-C&DH-C-SYS010-004	The C&DH system shall have at least 408 Gbit of onboard non-volatile mass memory for science data storage	To prevent loss of science data when downlink is not available, the data output for a full day of observations should be stored on board
REQ-C&DH-C-MIS003-005	The C&DH system shall have at least 2.64 Gbit of onboard non-volatile mass memory for housekeeping data storage	To enable autonomous operations when ground contact is unavailable, the system must store housekeeping data for onboard decision-making
ReEQ-C&DH-C-TT&C008-006	The data interfaces between the stored payload data and the TT&C system shall handle a data throughput of 380 M bit/s	This data throughput is required to meet the downlink time target set to maximise observation time
REQ-C&DH-F-SYS006-007	Data interface between spacecraft bus and payload shall handle a data throughput of 6 Mbit/s for payload data	The LEXI and HEXI payload have a total peak data rate of 5 Mbit/s and 4Mbit/s. The Interface must maintain signal integrity during data transmission (6Mbit/s includes 20% margin)
REQ-C&DH-F-SYS007-008	Data interface between subsystems shall handle a data throughput of 4 kbit/s for housekeeping data	Interfaces between subsystems and the OBC shall be capable of maintaining signal integrity during data transmission
REQ-C&DH-C-SYS024-009	The C&DH subsystem shall support RS485 communication between the OBC and the CPDU	CPDU will have an RS485 interface
REQ-C&DH-C-LAUN009-010	The spacecraft shall be programmable after integration via electrical interface	During integrated testing, bugs can be found or updates might be required
REQ-C&DH-C-LAUN009-011	Watchdog timer shall be disabled during programming	Will prevent the watchdog from rebooting the system during programming of the OBC

13.2. Assumptions

For the design of the C&DH subsystem, several assumptions have been made. These assumptions are listed in Table 13.2 below, accompanied by their impact.

Table 13.2: List of assumptions made during the preliminary design for C&DH

Assumption ID	Assumption/input	Justification	Design Impact	Consequences if Invalid
ASSU-C&DH-01	Processing units in bus diagrams contain the transceivers for the selected protocol	This is often the case in COTS components	Simplification of bus topology diagrams and selecting specific components	Transceivers must be added
ASSU-C&DH-02	The accumulated payload data for 24 hours, 408 GB (REQ-C&DH-C-SYS010-006) is the complete data volume including overhead.	No additional data volume needs to be downlinked to account for overhead	Downlink data rate is calculated by dividing data volume by available downlink time	Faster data rates will be required or time needs to be allocated to transmit the same data volume
ASSU-C&DH-03	The practical upper limit for bit rate for a SpaceWire interface is 130 Mbit/s	See Section 13.2.1	The theoretical limit of 400 Mbit/s cannot be used resulting in a lower data throughput	If lower, lower data throughput. If higher SpaceWire might be suitable
ASSU-C&DH-04	The spacecraft will be able to downlink all accumulated science and housekeeping data every 24 hours	Demonstrated in Chapter 12	justifies the required capacity of 408 Gbit in REQ-C&DH-C-SYS010- 004	If this is not the case more data storage capacity would be needed
ASSU-C&DH-05	Telemetry data from every subsystem is required for health status monitoring and autonomous mode transitions	Explained in Section 14.4	Implies the need for housekeeping data gathering by the C&DH subsystem	Other ways triggers will have to determine autonomous mode switching
ASSU-C&DH-06	The smallest reliable connector for RS485 is a D-SUB 9 pin connector.	Stated in ECSS-E-ST-50-15C if RS485 is used as a physical layer for CAN[41]	Limits the range of available connectors to D-sub 9 or larger/other types and increases number of wires used	Spacecraft is heavier than needed
ASSU-C&DH-07	For non SpaceWire or Fibre cables a density of 10 g/m was added to account for a protective Electromagnetic Interference shielding (EMI) shielding/isolation sleeve [135]	SpaceWire and Fibre already have shielding defined	This adds 10 g/m to the cable weight	Cables weight should be reassessed
ASSU-C&DH-08	Power cables are excluded from the C &DH harness and are included in the EPS design	See Chapter 10	The harness mass calculated in C&DH design will include mass of data lines only	Power and data lines might be combined in cables
ASSU-C&DH-09	The practical upper limit for the bit rate for a SpaceFibre interface is 4.5 Gbit/s	See Section 13.2.2	The theoretical limit of 6.25 Gbit/s can not be used for the design	Similar consequences as for ASSU-C&DH-03
ASSU-C&DH-10	The satellite can be powered through the umbilical connector	See Chapter 10	Satellite will not need to use battery for last software updates before launch	Other means of power supply are needed during software updates before launch
ASSU-C&DH-11	Inhibits such as separation switches or microswitches disable the EPS subsystem, keeping the watchdog inactive	See Chapter 10	This cancels the need for a disable watchdog separation switch since power to the watchdog is cut	Additional inhibits required for disabling watchdog until separation from LV
ASSU-C&DH-12	The transceivers used in the uplink chain buffer uplink data until GPIO signal is detected	See Chapter 12	Allows for longer response time of the OBC on commanding the transceiver to send data	Uplink data might be partially lost
ASSU-C&DH-13	Data rate produced by the payloads includes overhead	Technolution stated 38 to 40 bits of overhead were included per packet	Sets 5 Mbit/s as total required throughput	Higher throughput required for overhead
ASSU-C&DH-14	Power is provided to components by the EPS unless specifically specified elsewhere	See Chapter 10	Splits data lines and power lines in the design documentation	Should account for additional power lines within the cables

13.2.1. SpaceWire Practical Limit

According to ECSS-E-ST-50-12C [40] standards on SpaceWire, a SpaceWire interface has a theoretical ceiling of 200 Mbit/s instead of the 400 Mbit/s that is often mentioned in data sheets. According to clause 5.4.3.1 from the ECSS, a character shall be encoded in 10 bits, consisting out of one parity bit, a data control bit and eight bits of actual data. Therefore, from the 200 Mbit/s, only 160 Mbit/s is actual science data. This would be an upper theoretical limit. From STAR-Dundee Ltd.'s short paper on Testing over Ethernet with the SpaceWire

GbE Brick[86] average values of 130 Mbit/s are found for SpaceWire throughput.

13.2.2. SpaceFibre Practical Limit

According to ECSS-E-ST-50-11C [39] standards on SpaceFibre, data rates up to 6.25 Gbit/s are achievable. Since SpaceFibre uses the same packet format again, only eight per ten bits contain actual data, resulting in a maximum theoretical ceiling of 5 Gbit/s, when using one lane. ECSS-E-ST-50-11C provides an example showing approximately 93 % user-data efficiency for SpaceFibre under representative large-frame conditions. This results in a practical limit of 4.65 Gbit/s, here 4.5 Gbit/s was taken as a conservative value.

13.3. C&DH Architecture

The C&DH subsystems uses a dual OBC design to split up the responsibilities of satellite bus control and operations and the instrument control and operations. Additionally, this separation of responsibilities simplifies qualification activities by reducing component complexity and minimising functional coupling. A main OBC is used to run the flight and contains a Central Processing Unit (CPU), PCU, program memory, working memory, watchdog timer and a dual-image boot loader. It will command the satellite subsystems, collect telemetry and handle incoming commands from the ground station. The payload control and operations are done by the second OBC, which is included in the CPDU. The CPDU consists of a mission-specific carrier board and a CPDU Core board. The Core Board takes care of payload data processing and encrypting. The carrier board will house all required transceivers for the interfaces to the payloads, TT&C subsystem and the spacecrafts OBC. Furthermore, it will house the Mass Memory Unit (MMU) including two redundant MMU's that each can store the payload data set from a full day of science data collection, 408 Gbit. The CPDU will be designed by the Technolution group, however, it is included in the C&DH design to smooth the integration of the unit once it enters a more advanced design stage. The interfaces between the CPDU, the TT&C subsystem, the Payloads and the OBC can therefore be treated as recommendations from this design studyFigure 13.1 provides an overview of how the subsystems are wired to the OBC and the CPDU. Table 13.3 provides a definition of the buses used in the C&DH architecture.

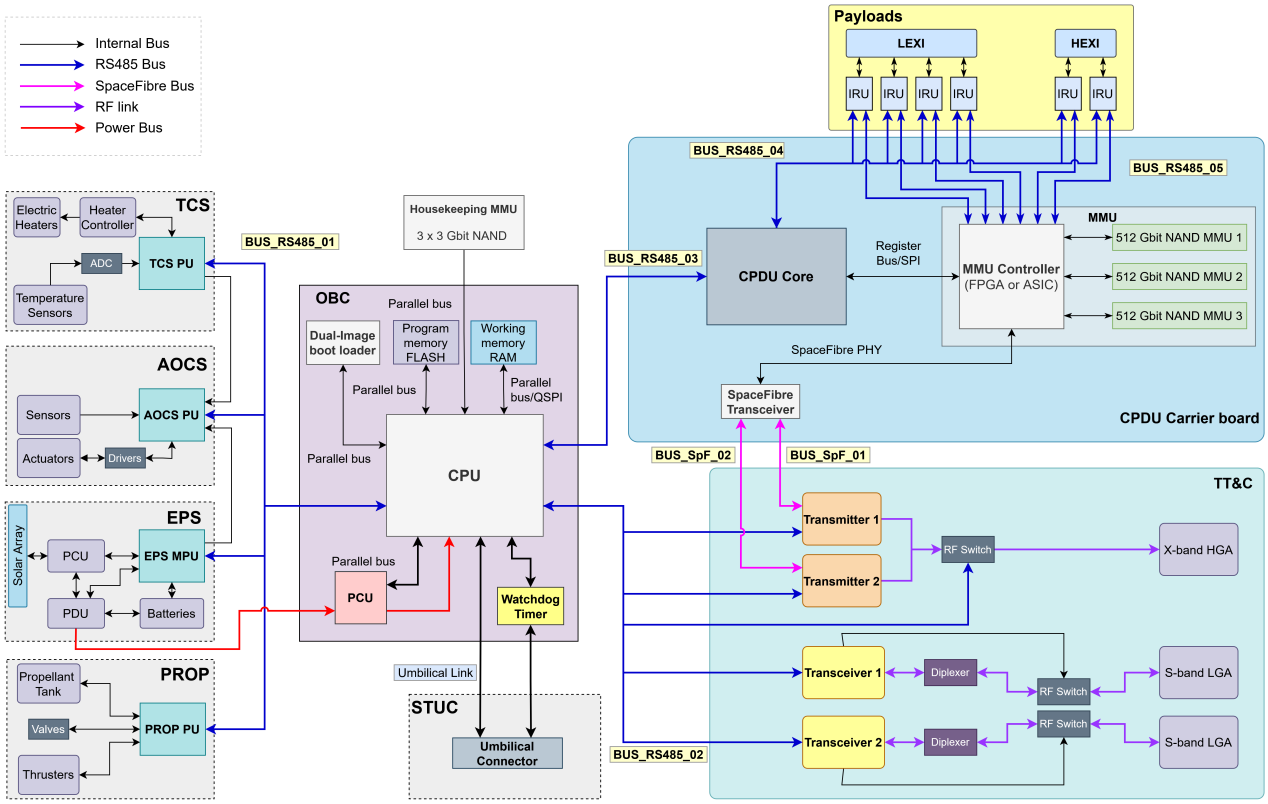

Figure 13.1: C&DH subsystem architecture containing the main data buses with respective labels

Table 13.3: On-Board Communication Bus Overview

Bus ID	Connected Subsystems	Purpose	Master/Controller
BUS_RS485_01	OBC, EPS, AOCS, PROP, TCS	Commanding subsystems and collecting housekeeping data	OBC
BUS_RS485_02	Transmitter 1, Transmitter 2, Transceiver 1, Transceiver 2, RF Switch	Transmission of uplink and downlink data between TT&C and C&DH, control of RF switch and gathering housekeeping data from the TT&C system	OBC
BUS_RS485_03	OBC, CPDU	Commanding the CPDU and collecting housekeeping data from the payloads and CPDU. Provide a data path between ground segment and payloads	OBC
BUS_RS485_04	CPDU Core, LEXI IRU's (4), HEXI IRU's (2)	Commanding IRU's and collecting housekeeping data	CPDU Core
BUS_RS485_05	MMU Controller, IRU	Payload data bus to transport date to the MMU for storage	MMU Controller
BUS_SpF_06	MMU Controller, Transmitter 1	Transport stored payload date to the downlink RF chain	MMU Controller
BUS_Spw_07	MMU Controller, Transmitter 2	Transport stored payload date to the downlink RF chain	MMU Controller

13.3.1. BUS_RS485_01

The main satellite bus acts as a data path for commanding spacecraft bus subsystems and collecting housekeeping data. TT&C is not included on this bus in order to separate incoming commands from the ground station and telemetry downlink to the ground station from the housekeeping and commanding bus. This decoupling of the external communications from internal control prevents internal bus traffic from impacting command reception and telemetry downlink performance The main satellite bus will connect the EPS, AOCS, TCS and Propulsion (PROP) subsystems to the OBC. The OBC will monitor housekeeping data from the subsystems to monitor the satellite's health and operational status. This data will be input for the flight software state machine that controls mode switching. When subsystems need to be commanded, the OBC will send commands via this bus as well.

Operational Concept and Data Flow

BUS_RS485_01 uses a typical master-slave configuration for a multi-drop bus, where the OBC is the master and the other subsystems are slaves. To prevent bus contention, a polling scheme will be used in which the OBC will command each subsystem sequentially to send housekeeping data. When a subsystem is commanded the polling scheme is interrupted until the command has been executed.

Bus Topology

To comply with REQ-C&DH-F-SYS007-004 and REQ-C&DH-F-SYS007-005 from Table 13.1, an RS485 multi drop bus topology was used the realize this bus. Besides that RS485 provides the required bit rates, it is also widely used in industry and radiation-tolerant transceivers are available. Figure 13.2 shows the half-duplex topology for the bus. Besides this additional discrete lines connected to GPIO on the OBC are shown to allow for the assertion of failsafe flags. These failsafe flags are asserted when mission endangering anomalies are detected within the EPS, AOCS and TCS subsystems. Dedicated lines are used to bypass the soft real-time latency associated with the RS485 bus's polling structure.

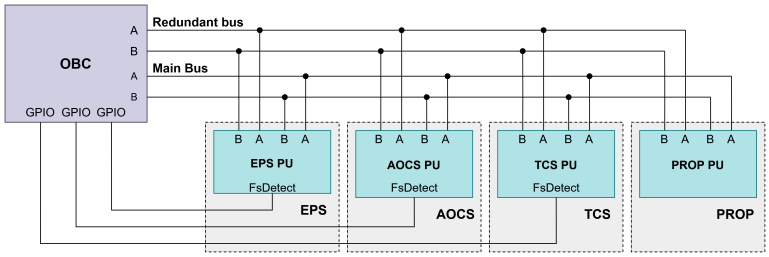

Figure 13.2: Topology of BUS_RS485_01, including the different lines and a redundant bus

In the figure, a main bus and a redundant bus are shown, both are exactly equal and connect to separate transceivers on both the OBC side and the subsystems processing units. The RS485 bus shall adhere to standards as defined in the RS485 design guide [76] and the ECSS-E-ST-50-15C[41]. It should be noted that RS485 only defines the physical layer of the communication protocol used for this bus as RS485 standardizes electrical characteristics such as signalling levels and bus loading, but does not define data framing, addressing, or access control. Deferring protocol selection to later phases allows the communication concept to be refined once subsystem interfaces are fully defined. According to the RS485 design guide by Texas Instruments[76], it is possible to have up to 32 Unit Load (UL) connected on a single bus. However, including fail-safes to prevent LoS caused by open circuits, short circuits or idle buses takes up 20 UL[76]. This leaves a total available loading of twelve UL. Assuming typical transceivers with a 1 UL loading, this leaves space for twelve transceivers on this bus. Besides the five used for the OBC and subsystems, this leaves room for bus growth of seven UL to include more subsystems or add redundant processing units to a subsystem on this bus.

13.3.2. BUS_RS485_02

The goal of the BUS_RS485_02 is to provide a data path between the TT&C subsystem and the OBC. This bus is used for the transfer of telemetry data to the TT&C subsystem for downlink to the ground segment, as well as for the reception of commands from the ground station delivered via the TT&C subsystem.

Operational Concept and Data flow

For BUS_RS485_02 a similar polling strategy is used as for BUS_RS485_01, however, incoming data from the ground segment is considered to be an event driven traffic. To prevent bus contention the transceivers used in the uplink RF chain shall be able to buffer uplinked data (ASSU-C&DH-012) until it is retrieved by the OBC via master-initiated bus transactions. To increase responsiveness, a GPIO pin is used as an attention signal witch triggers the OBC to stop periodically collecting telemetry housekeeping data and initiate retrieval of the buffered uplink data from the transceiver. For this bus, a soft real-time latency was deemed to be sufficient since delays in data flow do not cause immediate failure.

Bus Topology

As can be seen from Figure 13.3, the OBC connect to the five nodes: Transmitter 1, Transmitter 2, transceiver 1, transceiver 2 and the RF switch, and acts as master to these five nodes, attaining a typical master-slave multi drop bus topology. In addition, each transceiver has an added path to send an uplink detection signal to the OBC in case of an uplink event. Besides this, again a redundant bus is also implemented. This bus contains six nodes (including the OBC), allowing for potential bus growth of six additional UL's.

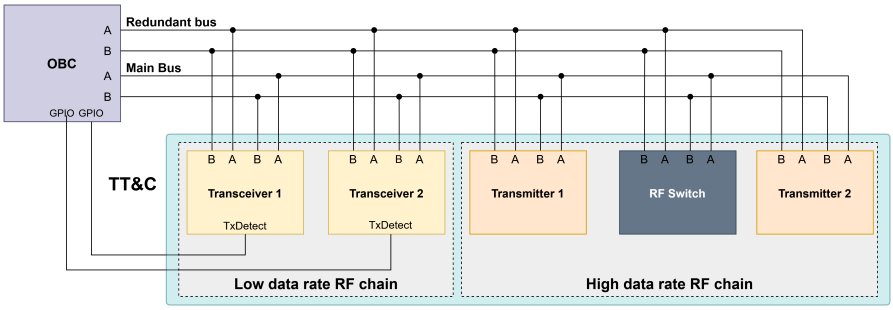

Figure 13.3: Topology of BUS_RS485_02, including the differential lines, additional GPIO's for pending uplink detection and a redundant bus

13.3.3. BUS_RS485_03

The third RS-485 bus is the direct connection between the CDPU and the main OBC. This bus extends the uplink connection from the ground station via the main OBC towards the payload. This bus is used to command the payload initiate payload data downlink and to receive telemetry housekeeping data from the payload via the payload OBC.

Operational Concept and Data flow

A similar operational concept is used for BUS_485_03 as for BUS_485_01.

Bus Topology
The bus connecting the OBC and the CPDU again uses a half duplex RS485 connection. It differs from the other buses since now it is implemented as a point to point connection, opposed to a multi drop bus.

13.3.4. BUS_RS485_04
BUS_RS485_04 serves as a connection between the IRU and the CPDU and provides a data path for commands to the payload and collecting housekeeping data. Although the interface between the CPDU and the payloads lies outside the scope of this design, as both are developed by other student groups, the on-board data handling diagram must still include the data path between the payloads and the satellite bus for completeness. The interface described between these subsystems can therefore be seen as a design recommendation.

Operational Concept and Data flow
This RS485 bus follows the same principle as for polling and commanding as BUS_RS485_01 and BUS_RS485_02 by using periodic polling for gathering housekeeping data and interruptus for commanding.

Bus Topology
Again, a multi drop RS485 bus was used to realize this bus since it offers sufficient data rates for commanding the IRU's and for gathering housekeeping telemetry. Again, a redundant bus was added as well as can be seen in Figure 13.4

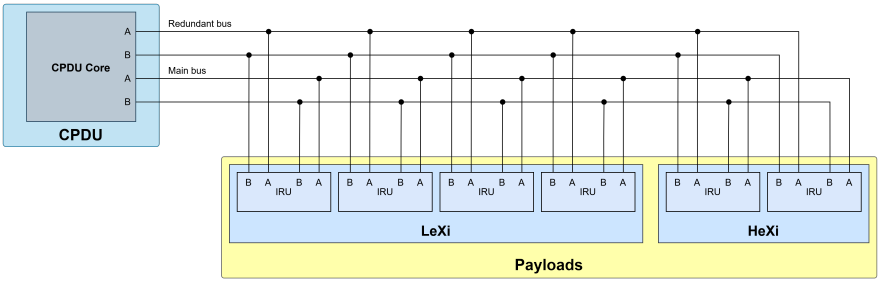

Figure 13.4: Multi drop bus for commanding and telemetry collection between the CDPU core and the IRUs from the payloads

13.3.5. BUS_RS485_05
For storing payload data on the MMU, each IRU will have a direct connection to the MMU controller on the CPDU. These are BUS_RS485_05_01 to BUS_RS485_05_06 grouped in this report underneath BUS_RS485_05. They are grouped because they are exactly similar both in topology and function and connect to the same unit, the MMU controller.

perational Concept and Data flow
When the payloads are operational, the IRUs will send data towards the MMU. This flow is initiated by a command from the CPDU core via BUS_RS485_04 when the payload is gathering data.

Bus Topology
The buses are point to point RS485 lines to allow for simultaneous data transmission from each IRU to the MMU and to support the required data rate of 5 Mbit/s from REQ-C&DH-F-SYS006-003. One of these buses is illustrated in Figure 13.6 below.

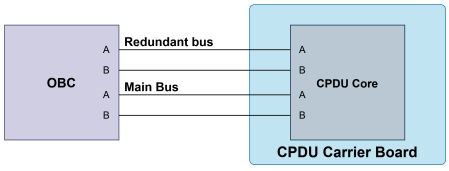

Figure 13.5: Topology of BUS_RS485_03

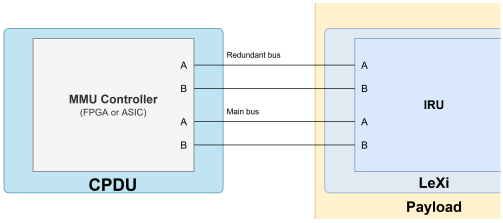

Figure 13.6: Point to point connection of one IRU (out of six) to the MMU controller.

13.3.6. BUS_SpF_06 & BUS_SpF_07

Buses BUS_SpF_05 and BUS_SpF_06 are combined in this section because they are identical buses in terms of purpose and topology. The buses purpose is to send payload data from the MMU to the TT&C subsystem, which makes it part of the downlink connection between the payload and the ground station.

Operational Concept and Data flow

The buses both provide a point to point connection and have as their only purpose to transport science data stored on the MMU to the transmitters for downlinking. Despite the bus only transmitting data from the MMU to the transmitter, still an Rx line is required for receiving, flow control credits, acknowledgements/retry control, link state and health information, time-codes and control symbols, which are built into the SpaceFibre protocol. A downlink is initiated by a command from the OBC to the CPDU via BUS_RS485_03, the CPDU will subsequently command the MMU controller to start the transmission.

Bus Topology

The SpaceFibre buses facilitate a point-to-point connection between the MMU controller and the transmitters within the TT&C subsystem. The redundant transmitter is considered to be a redundancy within the TT&C subsystem, therefore the BUS_SpF_02 is not considered to be a redundancy for the BUS_SpF_01. For example, a failure of transmitter 2 and BUS_SpF_01 will result in a failure of high-speed downlink functionality. Therefore, a redundant lane is used per bus. Each lane consists of a pair of optical fibres, one for Tx (data from A → B) and one for Rx (data from B → A) as defined for Type-A flight fibre optic cable assemblies in ECSS-E-ST-50-11C [39].

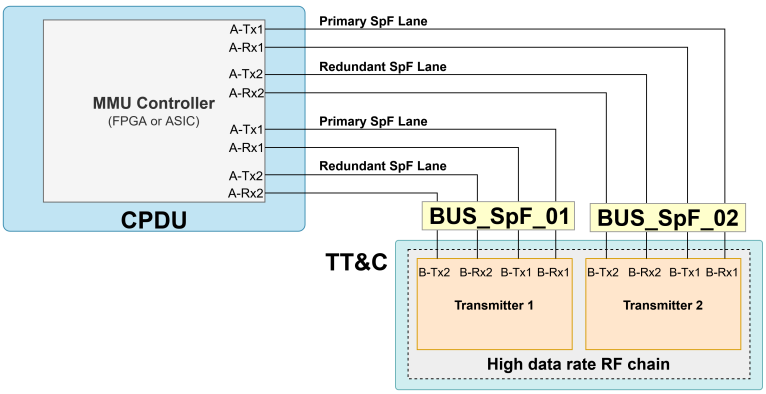

Figure 13.7: SpaceFibre buses BUS_SpF_01 and BUS_SpF_02 connecting the MMU controller to primary and redundant transmitters for transporting payload data to the downlink RF chain

13.3.7. Umbilical Connection

From the launcher requirement REQ-LAUN-C-MIS001-009, two additional requirements on the C&DH system were identified: REQ-C&DH-C-LAUN009-010 and REQ-C&DH-C-LAUN009-011, which specify the electrical connection required between the launcher and can be seen in Table 13.1. An umbilical connection is therefore included which will allow the flash software to the satellite via an electrical connection before launch. The protocol via which this is done has not been chosen in this stage of the project. Besides this, an additional GPIO is connected via which the watchdog will be disabled while the programming connector is plugged in. This will prevent the watchdog from booting the system during the flashing of software. The umbilical connection will have no more than 34 pins as stated in REQ-C&DH-LAUN009-012. In the Figure 13.1 the data lines of the umbilical connector as well as the watchdog inhibit are implemented within the structures subsystem.

13.3.8. Non-Volatile Memory

The payload data volume can be stored on the MMU present on the CPDU. It contains three independent units containing four 128 Gbit FLASH NAND memory modules from 3D Plus Inc. [1] This leads to having three units of 512 Gbit capacity, where two are there as a redundancy. This complies with requirement REQ-C&DH-C-SYS010-004. To store the housekeeping data volume of 2.64 Gbit, an additional mass memory unit containing three modules of using three 1 Gbit FLASH NAND chips from Micron Technology, Inc[85].

is included in the OBC. This complies with REQ-C&DH-C-MIS003-005. Besides their storage capabilities, the components for both memory units were picked because of their flight heritage and radiation tolerance, because of the environmental conditions and reliability needs mandated by requirements REQ-MIS-C-002and REQ-MIS-O-003.

13.4. Risk Assessment

To allow for a fault-tolerant design, a risk assessment in the format of a high-level FMEA was computed, using the scoring metrics from Section 17.2.2. Subsystem level FMEA is summarised in Table 13.4.

Table 13.4: High-level FMEA taking into account common failures for the C&DH subsystem

Risk ID	Failure Mode	Effect(s)	Cause(s)	L	S	Risk	Mitigation
R-SUB-C&DH-001	OBC latch-up	Short circuits, voltage drops, thermal runaway, subsystem wide brownouts	Parasitc structures caused by heavy ions, protons and neutrons (SEL/SEU	C	4	C4	Power cycling combined with fast detection methods
R-SUB-C&DH-002	Boot Failure	OBC can not reach/run operating software after reset/power on	Corrupt boot image by SEU, memory aging/degradation, human error	B	5	B5	Dual-image boot loader, protected boot memory
R-SUB-C&DH-003	Software Freeze	Software gets stuck in an operation, operations gets halted	Software bugs, deadlocks, stack overflow, memory corruption	B	4	B4	Time bound operations defined in software, watchdog timer
R-SUB-C&DH-004	Bus contention	Temporary no communication between nodes, loss of data	Protocol error, node talking when it is not supposed to, transceiver failure	B	2	B2	Redundant bus, bus recovery strategies (power cycling nodes)
R-SUB-C&DH-005	Data corruptions	Invalid telemetry or commands	SEU, EMI	B	3	B3	Shielding, differential signalling, packet validation
R-SUB-C&DH-006	Excessive bus loading	loss of data, latency issues	To high data rate, to many nodes, high parasitic capacitance	A	3	A3	Margin in bus bandwidth
R-SUB-C&DH-007	Loss of bus	Subsystems unresponsive	Transceiver fault, cable fault	C	5	B5	Add redundant buses
R-SUB-C&DH-008	Memory corruption	Loss of stored data	SEU in memory cells	B	3	B3	Error detection and correction devices, shielding
R-SUB-C&DH-009	Memory overflow	Data loss after generation	Wrongly estimated data volume or storage size	A	2	A2	Include margins, more frequent downlink
R-SUB-C&DH-010	MMU failure	No payload data storage	MMU contains a single string, memory controller failure	B	5	B5	Redundant storage modules, separation of modules, cross wiring
R-SUB-C&DH-011	Complete OBC failure	Loss of mission	Overstress due to Electro Static Discharge (ESD), manufacturing defect, destructive SEE	A	5	A5	Redundant OBC, functional redundancy in CPDU

13.5. Implemented Redundancies

The main risks identified in the previous section resulted in the selection of several redundancies within the C&DH subsystem. A failsafe methodology was used where recovery after failure instead of failure prevention was deemed appropriate to comply with requirements REQ-C&DH-C-SYS025- 01.

Bus redundancies

A risk of B5 was assigned to the loss of a bus, therefore according to the proposed actions in Table 17.3 mitigations must be allocated. Depending on the cause of the failure, recovery might be possible, for example, if one of the transceivers of a node causes the issue, it could be disabled, leading to a significant loss of functionality. Since the design is well below the mass requirement, a redundant bus was added for all buses.

Dual-Image boot loading

A dual-image boot loader is implemented on the OBC since a risk of B5 was assigned to boot failure caused by a corrupted boot image. Adding a redundant loader in case of boot failure reduces the risk.

Redundant Mass Memory Units

The MMU consists of three separate modules that each can store the payload data volume collected over 24 hours of payload operation. This redundancy can be further enhanced if payload data duplication is used for storing copies of the collected data.

Watchdog Timer
A watchdog timer was implemented as an Fault Detection, Isolation and Recovery (FDIR) mechanism to reduce the risk of failure due to software freezes. The Watchdog Timer is implemented as an autonomous IC on the OBC which makes it independent at board level in compliance with REQ-C&DH-F-SYS0025-02.

Latch-up detection
A risk magnitude of C4 was identified for the OBC latch-up failure mode. Over current detection should be implemented in subsequent design phases to allow for fast detection and power cycling.

Redundant OBC
Risk R-C&DH-011 could result in mission failure and is given a severity of A5. Possible mitigations such as a redundant OBC or functional redundancy by using the CPDU as OBC when this failure occurs is considered to be a too rigorous measure for the likelihood. Adding a redundant OBC would result in increased bus complexity and high added cost. Using the CPDU as a backup OBC would require extensive cross-strapping to all subsystems. Additionally, the added functionality to the CPDU would increase the amount V & V procedures associated with the qualification of the component itself, since it is still under development, and of the spacecraft itself. It was concluded that this is not a proportional mitigation for an ESA class III mission.

13.6. Final Design Hardware Characteristics
To conclude the design overview of the C&DH subsystem, relevant hardware characteristics that will be included in the spacecraft's wide budgets such as mass, power and volume, are presented. The mass, power, dimensions and operating voltages of the main OBC and the CPDU can be found in Table 13.5. The main OBC for the subsystem is realized by the Q8 OBC by Xiphos [138], which was picked because it contains sufficient RS485 interfaces, offer a 30 Krad TID radiation tolerance and has an extensive flight heritage. Which makes it comply with the bus architecture and reliability considerations derived from the life time and environment requirements, REQ-SYS-F-MIS003-001 and REQ-SYS-F-MIS003-004.

Table 13.5: Main budget parameters for the main OBC and the CPDU

Component	Manufacturer	Mass [kg]	Power [W]	Operating Voltage [V]	Dimensions [mm]
OBC (Q8 OBC)	Xiphos	0.957	14	9	167.3 x 182.6 x 91
CPDU	Technolution BV	3.9	10	28	100 x 100 x 30

Besides the mass of the processing units in Table 13.5, the mass of the harness should also be accounted for. Half duplex RS485 needs 2 datalines, however, since the smallest reliable connector is a D-SUB 9 pin connector as stated in ASSU-C&DH06, nine 24 AWG wires of 3.86 g/m [60] are used besides an additional 10 g/m [135] for a shielding sleeve as stated in ASSU-C&DH-07. The other seven lines can be used for Ground (GND)s, logic level voltages and additional GPIOs for failsafe detection lines as discussed in Section 13.3.1. For the SpaceFibre links a mass of 30 g/m and a connector mass of 8 g as stated in [16]. By estimating the cable length, a cable harness mass of 1.620 kg was found. This includes all redundant buses plus a 20% margin. The contribution of the cable harness mass to the spacecraft's inertia tensor is not explicitly modelled at this stage of the mission design. While the cable mass does contribute to the total spacecraft mass, its effect on the inertia properties is expected to be limited due to its low mass fraction and distribution throughout the spacecraft. The impact of the harness mass should therefore be treated as a model uncertainty that should be assessed in a later design phase of the mission when detailed harness routing and mass properties are finalised.

14 Interface Design

Having established the detailed design of the seven spacecraft subsystems in the preceding chapters, this chapter transitions to their integration through interface design. As the interface architecture fundamentally defines the functionality of the spacecraft, it serves as the concluding phase of the spacecraft system design. Section 14.1 provides an overview of all interfaces in the form of an N2 chart. The subsequent sections give a more detailed interface design through the application of interface diagrams. Section 14.2 shows all the hardware interfaces, some of which have already been displayed in previous chapters. Section 14.3 addresses software interfaces by referencing the data handling diagram shown in Section 13.3 and by establishing the necessity for the in-depth modes of operations analysis found in Section 14.4. After this, a final time budget can be derived in Section 14.5.

14.1. N2 Chart

Interfaces within the spacecraft are documented using an N2 chart, which can be seen in Figure 1. The subsystems of the spacecraft are positioned on the diagonal. To provide a higher level of detail, the subsystems are divided into their main components. The rows indicate that an interface is an output from the component or subsystem, whereas a column defines an input. The interfaces are given a code according to the ID system presented in Table 14.1 such that they remain traceable. A description of each interface in the N2 chart can be found in Table 14.2

Table 14.1: ID system for the interfaces within the N2 chart

SUB1-SUB2-X-YY		
SUB	**X**	**YY**
PLD	D = Data	01-99
C&DH	P = Power	
TT&C	M = Mechanical	
EPS		
PROP		
AOCS		
TCS		
STUC		

Description:
An ID is made up out of 4 sections the two subsystems that are connected are SUB1 and SUB2. SUB1 is the subsystem corresponding to the output. SUB2 is corresponding to the input. The type can be data, power and mechanicaland, and is represented with by plugging in a letter for X. The ID is concluded with its number using numbers 01-99 at YY.

Example:
Housekeeping data/command responses from EPS MPU to OBC is: EPS-C&DH-D-01

Table 14.2: Spacecraft interface list defining interfaces specified in the N2 chart in Figure 1

Interface ID	Description	Physical implementation
C&DH-PLD-D-01	Commands from CPDU to LEXI IRU's	BUS_RS485_04 (cable harness)
C&DH-PLD-D-02	Commands from CPDU to HEXI IRU's	BUS_RS485_04 (cable harness)
PLD-C&DH-D-01	Housekeeping data/command responses from LEXI to CPDU	BUS_RS485_04 (cable harness)
PLD-C&DH-D-02	Housekeeping data/command responses from HEXI to CPDU	BUS_RS485_04 (cable harness)
PLD-C&DH-D-03	Housekeeping data/command responses from LEXI to MMU	BUS_RS485_05_01 to 04 (cable)
PLD-C&DH-D-04	Housekeeping data/command responses from HEXI to MMU	BUS_RS485_05_05 to 06 (cable)
C&DH-PLD-P-01	Power supply for IRU's (CPDU distributes power from 28V satellite bus)	Power cables
C&DH-PLD-P-02	Power supply for IRU's (CPDU distributes power from 28V satellite bus)	Power cables
C&DH-C&DH-D-01	Housekeeping data/command responses from MMU to CPDU	Register bus on CPDU PCB
C&DH-C&DH-D-02	Commands from CPDU to MMU	Register bus on CPDU PCB
C&DH-C&DH-D-03	Housekeeping data/command responses from CPDU to OBC	BUS_RS485_03 (point to point cable)
C&DH-C&DH-D-04	Commands from OBC to CPDU	BUS_RS485_03 (point to point cable)
C&DH-C&DH-M-01	12, 128 Gbit memory modules mounted on CPDU PCB	SMD soldered
C&DH-C&DH-P-01	Power plane in CPDU PCB	PCB traces

Continued on next page

Interface ID	Description	Physical implementation
C&DH-TT&C-D-01	Payload data from MMU to Transmitters for downlink	BUS_SpF_06 (point to point cable)
C&DH-TT&C-D-02	Commands from OBC to Transmitters and RF switches	BUS_RS485_02 (cable harness)
C&DH-TT&C-D-03	Command from OBC to Transceivers RF switches	BUS_RS485_02 (cable harness)
STUC-C&DH-M-01	Main OBC mounted to the structures internal panel inside the radiation box	Bolts
STUC-C&DH-M-02	Main OBC mounted to the structures internal panel inside the radiation box	Bolts
TT&C-C&DH-D-01	Housekeeping data/command responses from Transmitters to OBC	BUS_RS485_02 (cable harness)
TT&C-C&DH-D-02	Housekeeping data/command responses and uplink commands from Transceivers to OBC	BUS_RS485_02 (cable harness)
TT&C-C&DH-D-03	Uplink detection GPIO line	BUS_RS485_02 (cable harness)
EPS-C&DH-D-01	Housekeeping data/command responses from EPS MPU to OBC	BUS_RS485_01 (cable harness)
EPS-C&DH-D-02	Failsafe detection GPIO line	BUS_RS485_01 (cable harness)
EPS-C&DH-P-01	9 V supply voltage from EPS to OBC	Power cable
EPS-C&DH-P-02	28 V supply voltage from EPS to CPDU	Power cable
AOCS-C&DH-D-01	Housekeeping data/command responses from AOCS PU to OBC	BUS_RS485_01 (cable harness)
AOCS-C&DH-D-02	Failsafe detection GPIO line	BUS_RS485_01 (cable harness)
TCS-C&DH-D-01	Housekeeping data/command responses from TCS PU to OBC	BUS_RS485_01 (cable harness)
TCS-C&DH-D-02	Failsafe detection GPIO line	BUS_RS485_01 (cable harness)
TCS-C&DH-M-01	Temperature sensors mounting on the C&DH subsystem	Addhesive bond(Epoxy)
PROP-C&DH-D-01	Housekeeping data/command responses from SatDrive PU to OBC	BUS_RS485_01 (cable harness)
C&DH-EPS-D-01	Commands from OBC to TCS MPU	BUS_RS485_01 (cable harness)
C&DH-PROP-D-01	Commands from OBC to SatDrive PU	BUS_RS485_01 (cable harness)
C&DH-AOCS-D-01	Commands from OBC to AOCS PU	BUS_RS485_01 (cable harness)
C&DH-TCS-D-01	Temperature readings from sensors	Seperate cable
C&DH-TCS-D-02	Commands from OBC to TCS PU	BUS_RS485_01 (cable harness)
TCS-TCS-D-01	Temperature readings from sensors to TCS ADC and PU	Power cables
TCS-TCS-M-01	Temperature sensor mounting on the TCS PU	Addhesive bond(Epoxy)
TCS-TCS-P-01	28 V supply voltage from TCS PU to the TCS active systems	Power cables
TCS-TCS-P-02	Power supply to the temperature sensors	Power cables
TCS-TCS-D-02	Bang-bang control of TCS active systems	Point to point cables
TCS-TCS-M-02	Mounting of electrical heater switchboard with TCS PU	Addhesive bond(Epoxy)
TCS-STUC-M-01	TCS PU mounted to the structures internal panel inside the radiation box	Bolts
TCS-STUC-M-02	Radiators are mounted to external structure on -X, +Y and -Y faces.	Adhesive bond
TCS-STUC-M-03	MLI connected to the external structure	Adhesive attachment
AOCS-TCS-D-01	Attitude data from AOCS PU to TCS PU	Data cable
TCS-PLD-M-01	Electrical heater mounting to HEXI	Adhesive attachment
TCS-PLD-M-02	Electrical heater mounting to LEXI	Adhesive attachment
TCS-PLD-M-03	Temperature sensor attachment to HEXI	Adhesive bonding(Epoxy)
TCS-PLD-M-04	Temperature sensor attachment to LEXI	Adhesive bonding(Epoxy)
TCS-PLD-M-05	MLI connected to HEXI	Adhesive attachment
TCS-PLD-M-06	MLI connected to LEXI	Adhesive attachment
TCS-EPS-M-01	Thermal strap connection from solar arrays to secondary radiators	Bolted
PLD-TCS-M-03	Thermal strap connection from LEXI to main radiator	Bolted
PLD-TCS-M-04	Thermal strap connection from HEXI to main radiator	Bolted
STUC-PROP-M-01	Thruster skeleton connected to the -X panel	Mounting structure
STUC-PROP-M-02	Propellant tank skeleton mounted on both the -X panel and the internal panel	Mounting structure
STUC-AOCS-M-01	External sun sensor mounting (5x)	Bolted
STUC-AOCS-M-02	External magnetorquers mounting (3x)	Bolted
STUC-AOCS-M-03	Star tracker hub on the +Z panel	Mounting structure
STUC-AOCS-M-04	Reaction Wheel Module mounted on the internal panel	Mounting structure
STUC-AOCS-M-05	Gyroscope mounting on the internal panel	Bolted
STUC-AOCS-M-06	GNSS receiver mounting on the -X panel	Bolted
STUC-AOCS-M-07	External GNSS antenna mounting on the -X panel	Bolted
STUC-EPS-M-01	Battery pack mounted to the structures internal panel inside the radiation box	Bolted
STUC-EPS-M-02	PCDU mounted to the structures internal panel inside the radiation box	Bolted
STUC-EPS-M-03	Solar Array Deployment Mechanism	Mechanism
STUC-EPS-M-04	Solar Array Clamping Mechanism	Mechanism
STUC-TCS-M-01	External main bus radiator mounting on the -X panel	Adhesive
STUC-TCS-M-02	External secondary radiator mounting on the -Y and +Y panel	Adhesive
STUC-TCS-M-03	MLI appliance on the outer structure	Adhesive

Continued on next page

Interface ID	Description	Physical implementation
STUC-TTC-M-01	External S-band antenna mounting on the +Y panel	Bolted
STUC-TTC-M-02	External X-band antenna mounting on the -X and +X panel	Bolted
STUC-TTC-M-03	TT&C module mounting on the -X panel	Bolted
STUC-PLD-M-01	Isostatic mounts	Clamping mechanism
EPS-PROP-P-01	5 V logic rail to the PCU	Power cable
EPS-PROP-P-02	28 V actuator rail to the valves/igniter/heaters	Power cable

Not all TCS interfaces were included in the above table. In order to keep the list as comprehensive as feasible, most of the interfaces between temperature sensors and other components were omitted. This is due to the repeatable description of these interfaces. As a short overview, the temperature sensors are mechanically connected to each component through adhesive bonding, while the received temperature read-out in the form of heat is interpreted as data which the sensors collect.

14.2. Hardware interfaces

14.2.1. Mechanical interfaces

Figure 14.4 shows all mechanical interfaces of the spacecraft. These represent the physical methods used to connect components to each other, to other subsystems or to the structure. Some interfaces require bolting or adhesives, while others demand further explanation.

Launch Adapter

In Section 7.3.1, the selection of the PSC Mk II MLB 24” adapter was explained. This forms the only mechanical interface with the launcher. The passive ring of the adapter will remain on the spacecraft during its entire lifetime, while the active ring will stay behind on the launcher. Because the launch loads are introduced through this adapter into the -Z panel, this panel has no other interfaces with subsystems.

Isostatic mounts

Section 7.3.2 gives a detailed description of the isostatic mounts, which are the only mechanical interface the payloads have with the spacecraft. They are designed to make the payload withstand launch loads and to prevent the payload from thermally expanding with the spacecraft.

Reaction Wheel Module

The RW module provides the mechanical interface between the four RW4 wheels. These need to be placed in a pyramidal configuration with an angle of 54.7°, as described in Section 9.3.2. The module accommodates this configuration and transfers the induced torques to the spacecraft. Figure 14.1 shows the RW module.

Propulsion system structure

As the entire propulsion system is one of the heaviest subsystems and has a complex geometry. It requires its own structural frame. This subsystem takes up the full depth (in X-direction) of the bus volume and is therefore connected to both the internal panel and the -X panel. This is done with a so-called ’skeleton structure’, minimising the total weight but still providing sufficient stiffness. The frame of the thrusters is connected to the -X panel, which has holes through which the thrusters fit. The frames of the tanks are connected to the thruster frame and the internal panel to hold the propellant tanks in place. The propulsion system structure can be seen in Figure 14.1.

Figure 14.1: Reaction Wheel Module and Propulsion system structures in the spacecraft

Star Tracker Hub

Section 9.3.1 explains the selection of PST3S-H4 Start Trackers, which need to be placed externally on the spacecraft, separated by an angle of 30° with respect to each other. The Star Tracker Hub forms the mechanical interface between the three star trackers, enabling the required angles. The star trackers consist of an external baffle and an internal circuit board, which is shielded by the hub. Figure 14.2 shows the final design.

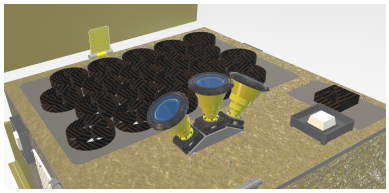

Figure 14.2: Star Tracker Hub

Solar Array Deployment- & Clamping Mechanisms

Section 10.3 describes the entire solar array design, including the deployment and clamping mechanisms, which are the mechanical interfaces with the structure. As Figure 14.4 shows, the panels have separate components interfacing with each other and with the structure. The two side panels (at ± Y), the upfold panel (at +X), and the angled downfold panel (at +X) are connected to the structure with a single root hinge (see Figure 14.3). The angled side panels are then connected to the side panels using interpanel hinges (Figure 14.3). The fixed panel is connected to the structure at both ± Z with a fixed root hinge, and by the Central Hold down mechanism (Figure 14.3). For the other panels, this is used as the clamping mechanism during launch. Besides the Central Hold down during clamped configuration, snubbers are placed in between the solar panels to keep them from vibrating.

Together with the simple joining methods, these mechanical interfaces have been summarised in the Mechanical Interface Diagram in Figure 14.4.

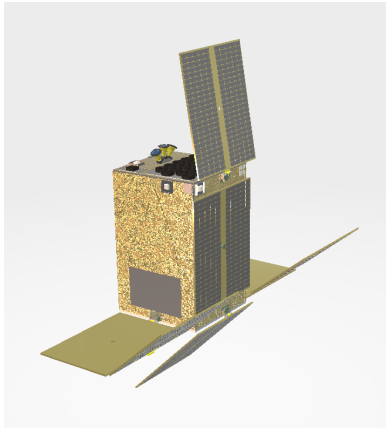

Figure 14.3: Solar Array Deployement- & Clamping Mechanisms

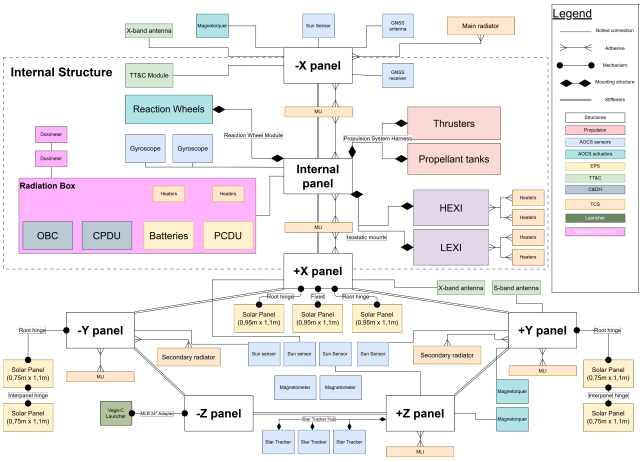

Figure 14.4: Mechanical interface diagram

14.2.2. Electrical interfaces

The electrical block diagram is presented in Section 10.5.1. It is mentioned here to provide directions to the reader.

14.3. Software Interfaces

14.3.1. Data Handling Interfaces

The data handling diagram is presented in Section 13.3. It is mentioned here to provide directions to the reader. Besides the data handling diagram, the software interfaces are defined by the modes of operation, which are explained in the next section.

14.4. Detailed Modes of Operations

The Modes Of Operations (MOO) were briefly introduced in Section 5.3. Now, the spacecraft design, including its subsystems, is defined, and detailed modes of operation are presented. This section will provide information on active subsystems, constraints, mode transitions, and transition triggers and will provide a mode switching diagram that could provide the structure for the main flight software state machines.

LEOP Mode

LEOP mode is the first mode initiated after launch, used to stabilise the Spacecraft (S/C) before commissioning. More specifically, it is triggered after LV-separation. This means that this mode is only used once in the lifetime of the S/C. The main activities during this mode are to detumble the S/C to a safe tumbling rate (defined in Section 9.4), acquire the Sun, start power generation, and initiate communication with the ground. To exit this mode, certain conditions must be met. These conditions include reaching a safe tumbling rate, the system being power positive and communications with the ground having been established. LEOP mode is estimated to last 3 to 5 days. The only mode the system can transition to after this is commissioning mode.

Commissioning Mode

This mode commissions the S/C, which must happen before the system can proceed with nominal operations. During this mode, the subsystems (including payload) are tested for functionality and calibrated one-by-one. The trigger to enter this mode is if all the exit conditions of the LEOP mode have been met. Similar to the LEOP mode, this mode is entered once in the lifetime of the S/C, and it is estimated to last 30 days. To exit this mode, all subsystems must be calibrated, and the system must be stable.

Safe Mode

The safe mode is triggered when an anomaly is detected that poses unacceptable risks to the spacecraft's or subsystem's survival. Examples of these conditions are power bus violations (over- or under-voltage), subsystems operating outside of their operational temperature and loss of attitude. As described in Section 13.3.2, the OBC monitors spacecraft health parameters via polling on BUS_RS485_01. To override the soft real-time latency associated to this polling mechanism, the AOCS, EPS, and TCS are equipped with dedicated hard-wired connections to the OBC for latency-critical flag raising. During safe mode, nominal operations are halted, minimising functionality to subsystems that are required for regaining a stable, safe state. When the system is power positive, has a stable attitude and has established ground contact, it is allowed to transition to Troubleshooting Mode for further diagnosis and recovery. The spacecraft can enter safe mode from any mode, except for Radiation Protection mode and EOL mode, and will exclusively exit safe mode to enter troubleshooting mode. When the system is rebooted, it will always start up in safe mode.

Radiation Protection Mode

During the Radiation Protection mode, all subsystems, except for the AOCS and EPS, are powered off to prevent radiation induced damage from SEE, such as SEU and SEB in the electronics of spacecraft. The spacecraft will contain radiation sensors in its AOCS subsystem, which will alert the OBC to transition to radiation protection mode when the switching threshold of [value] is reached. Orbital position is also checked and can be used to initialise the switch in case of a radiation sensor failure. The EPS stays powered during the SAA to power the AOCS system and start up the OBC upon exciting the radiation protection mode. Based on the orbital environment analysis presented in Chapter 4, the maximum duration of a single SAA passage is 27.83 minutes. Including a safety margin, a timeout of 34 minutes is implemented within the EPS as a backup mechanism to power on the OBC in case of failure of the primary transition mechanism within the AOCS.

Trouble Shooting Mode

The Troubleshooting mode is used for diagnostics and recovery after an anomaly has occurred. When an anomaly which does not pose an immediate risk to mission survival occurs, the spacecraft directly transfers from its current mode to troubleshooting mode. When the anomaly is more severe, the spacecraft will first enter Safe mode in order to regain a safe status before computing diagnostics and recovery. Another functionality of the Troubleshooting mode is executing software updates sent from the ground segment.

Standby Mode
Standby mode is used to keep the spacecraft in a stable and operation-ready status. It is also used as a fallback mode to transition between different modes. When a command is given to perform an operation, the spacecraft will initialise the relevant subsystems and prepare for the mode transition. Target acquisition is carried out in this mode to minimise the power required by the AOCS during Science Mode, in which the payloads consume the majority of the available power budget. This lowered the requirement on power generation REQ-EPS-F-MIS007-001.

Orbit Maintenance Mode
The Orbit Maintenance is used for orbit correction manoeuvres and space debris mitigation. This mode includes aligning the spacecraft thrust vector in the required direction for the executed manoeuvre.

Science Mode
Science mode is the dedicated operational mode for operating the payloads. During this mode, the payloads gather data on the observed target and store it in the MMU. AOCS functionality is reduced to maintain target acquisition, which lowers the power consumption since no large slews will be executed. To switch between targets, the spacecraft will first switch back to standby mode, in which it performs the slew manoeuvre for power budgeting.

Downlink Mode
The spacecraft is susceptible to uplink commands via the S-band antennas during all modes except for the Radiation Protection mode. For downlinking payload data, however, the spacecraft must be rotated to align the fixed X-band antenna with the ground station. This mode will occur at least once every 24 hours to downlink the accumulated payload data. Because the spacecraft attitude is optimised for antenna line of sight, no observations are possible during this mode.

EOL Mode
After completion of the operational lifetime, the spacecraft performs a manoeuvre using the remaining on-board propellant to lower the orbit and initiate atmospheric re-entry. Following the final manoeuvre, the propulsion system is passivated by venting the pressurised lines and tanks where applicable. The AOCS is then used to maximise aerodynamic drag by orienting the spacecraft such that the maximum cross-sectional area is presented to the velocity vector. Finally, the spacecraft is electrically passivated by isolating the battery and disabling power generation and distribution, ensuring that all stored energy sources are rendered safe prior to re-entry.

14.4.1. Subsystem Activation per Operational Mode
As stated before, the MOO are used to limit functionalities of the spacecraft to the required functions during specific operations. To provide an overview of the subsystems powered per mode, Table 14.3 is shown. An important note is that a subsystem can be turned on, but this does not mean that it is operating at peak power. In science mode, the TT&C subsystem is turned on for being able to receive uplink, which is a large difference in power consumption compared to when the system is turned on during downlink mode for transmitting the payload data volume.

Table 14.3: Overview of active subsystems during each mode

Mode	AOCS	EPS	C&DH	TCS	TT&C	PROP	CPDU	PLD
LEOP	✓	✓	✓	✓	✓			
Commissioning	✓	✓	✓	✓	✓	✓	✓	✓
Safe	✓	✓	✓	✓	✓			
Radiation Protection	✓	✓						
Trouble Shooting	✓	✓	✓	✓	✓			
Standby	✓	✓	✓	✓	✓			
Orbit Maintenance	✓	✓	✓	✓		✓		
Science	✓	✓	✓	✓	✓		✓	✓
Downlink	✓	✓	✓	✓	✓		✓	
EOL	✓	✓	✓		✓	✓		

14.4.2. Mode Transition Logic

A high-level transition map defining how the spacecraft's modes change throughout its mission phases is provided to combine both the information of the ConOps and the MOO, which can be seen in Figure 14.5 below. The diagram starts at the top left corner with separation from the Vega-C, starting with the first mission phases of the space segment, LEOP and Commissioning, respectively. Since these modes together with the EOL mode only happen during certain mission phases, they are grouped together in Phase-Specific Operational Modes as indicated by their colour in the transition map. After commissioning, the Nominal Operational Modes can be attained by the spacecraft. From Standby mode, acting as the default mode, the Orbit Maintenance, Science, and Downlink modes can be attained. To switch between the latter three, the spacecraft will first need to switch back to Standby mode. The spacecraft operated in these modes during the Nominal Operation phase and potentially during its Extended Life Phases. Within these mission phases, Fault and Environment Interrupts can trigger a mode transition towards the Contingency Modes. These include the Safe, Troubleshooting and Radiation Protection modes. This transition can happen from any mode, except EOL and Radiation Protection mode. At the end of the spacecraft's extended life, the spacecraft will transition to its EOL phase and dedicated mode.

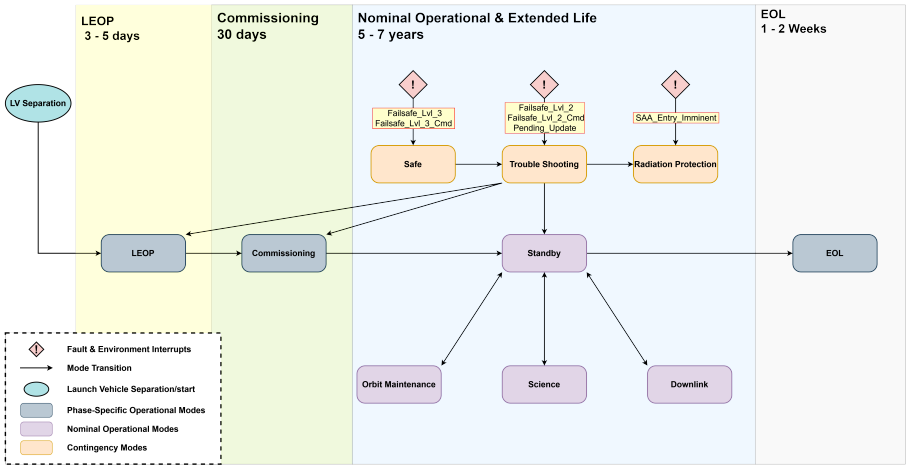

Figure 14.5: Mode transition map, indicating how switch transition logic throughout the mission life time at high-level

14.4.3. Mode Transition Triggers and Conditions

Mode transitions in the spacecraft are triggered by flags. Flags are software indicators maintained by the OBC that can represent the current status of the spacecraft, its subsystems and the occurrence of events. These flags are collected by the OBC via housekeeping data and via additional detection lines for mission survival critical flags that require a hard real-time latency as described in Section 13.3.1. The on-board flight software uses these flags in its mode management and fault-handling logic to determine in what mode the spacecraft should operate. This logic is implemented as a state machine, in which transitions between modes are triggered

when predefined flag conditions are satisfied. Flags that trigger mode transitions are listed in Table 14.4. The corresponding mode transfers can be found in Table 14.5. To enable an appropriate response to detected anomalies, a subset of flags is further classified. The onboard fault-handling logic distinguishes between three failsafe levels, based on the anomaly severity. Failsafe level 1 corresponds to minor anomalies that do not create an immediate risk to the spacecrafts safety. At this level flight software will start temporal redundancy operations by retrying commands and spacecraft reconfigurations to increase the operation success probability upon retry. Failsafe level 2 is raised for anomalies that require subsystem level isolation in order to perform diagnostics and recovery strategies. When a Failsafe level 2 flag is raised the system is not allowed to sustain its nominal operations while executing the dedicated contingency methods, making it switch to Trouble Shooting mode. Failsafe level 3 is triggered when the anomaly needs immediate mitigation to prevent mission failure. When this flag is asserted the spacecraft will switch to safe mode. Together, this flag-based state machine and the distinguished failsafe level hierarchy form a base layer for the flight software enabling autonomous mode transitions that will increase continuity of the mission.

Table 14.4: List of high-level flags that are capable of triggering mode transitions

Flag	Description	Assertion condition
LV_SEP	Separation from launcher vehicle	Separation switches are decompressed enabling the separation signal
LEOP_Complete	All LEOP success criteria satisfied	The spacecraft detumbled to below 1.5 [deg/s], became power positive, established communications
Commisioning_ Complete	All commissioning success criteria satisfied	subsystems are calibrated, payloads are calibrated, system is running nominal
Safe_Conditions_Met	Spacecraft is safe to exit safe mode	Subsystems within operational limits, power positive, software operational, tumbling rates not above 1.5 [deg/s] for 15 [s]
Safe_Exit_Authorized	Safe mode exit override from ground station	Command from ground station to exit safe mode has been received and is confirmed through a secondary override approval command as part of a two-step verification procedure
SAA_Exited	Spacecraft is outside of the SAA	AOCS radiation sensors detect lower threshold defining safe condition confirmed by predicted orbital positions or back up EPS timer trips a restart
Anomaly_Resolved_Commissioning	Anomaly that caused safe mode trigger during commissioning mode is resolved	Nominal operation restored for that subsystems that triggered the fail-safe
Anomaly_Resolved_LEOP	Anomaly that caused safe mode trigger during LEOP mode is resolved	Nominal operation restored for that subsystems that triggered the fail-safe
Anomaly_Resolved	Anomaly that caused safe mode trigger is resolved	Nominal operation restored for all subsystems that triggered the fail-safe
OBC_Reset	OBC reset initiated	Watchdog timer initializes reset or OBC reboot for completion of software update
Orbit_Maintenance_Ready	All necessary conditions apply for a ΔV manoeuvre after command from ground has been received	Spacecraft is pointed and payload is turned off
EOL_Reached	End of life	Based on housekeeping data the predicted remaining operational lifetime of the spacecraft is less than two weeks
Premature_EOL_Reached	End of life constraint by ground control	EOL sequence initiated by the ground control
SAA_Entry_Imminent	Spacecraft approached the SAA passage	Radiation measurements or orbital position confirm approach to the SAA with safety margin
Pending_Update	System has received a software update	Software update package has been successfully received from the ground segment and is pending installation
Primary_Target_Acquired	Payloads point at the primary target	AOCS has attained a stable attitude pointing the payloads at the primary target
Secondary_Target_Acquired	Payloads point at the secondary target	AOCS has attained a stable attitude pointing the payloads at the secondary target
Ground_Xlink_Acquired	X-band link with ground station established	AOCS points X-band antenna at ground station and communication link is established
Manoeuvre_Completed	ΔV manoeuvre is completed	Burn is completed and actuators are disabled
Switch_Primary	Payload cannot observe secondary target	Secondary target is within obscurance range
Switch_Secondary	Payload cannot observe primary target	Primary target is within obscurance range

Continued on next page

Flag	Description	Assertion condition
Ground_Xlink_Lost	Transmission is not received	Loss of sight or link degradation causing unsuccessfully transmission
Data_Transmission_Complete	Payload data volume is sent down	MMU sent all data to the RF chain and data receipt has been confirmed by the ground station
Ground_Xlink_Interrupt	Ground station operations halted	Interrupted due to operational constraints from ground station
Failsafe_Lvl_2	Failure level 2 detected	Detection of anomalies that do not impose immediate risk of mission survival
Failsafe_Lvl_3	Failure level 3 detected	Detection of anomalies that impose direct risk on the spacecrafts survival such as attitude loss, bus voltage violations and thermal limits violations
Failsafe_Lvl_2_Cmd	Failsafe level 2 override from ground control	Ground command requesting entry into troubleshooting mode
Failsafe_Lvl_3_Cmd	Failsafe level 3 override from ground control	Ground command requesting entry into safe Mode

Table 14.5: Summary table containing mode switches and their triggers

Current Mode	Next Mode	Trigger	Control Authority
IDLE	LEOP	LV_SEP	Autonomous
LEOP	Commissioning	LEOP_Complete	Autonomous
Commissioning	Standby	Commissioning_Complete	Autonomous
Safe	Trouble Shooting	Safe_Conditions_Met	Autonomous
Safe	Trouble Shooting	Safe_Exit_Authorized	Ground control
Radiation Protection	Safe	SAA_Exited	Autonomous
Trouble Shooting	Commissioning	Anomaly_Resolved_Commissioning	Autonomous
Trouble Shooting	LEOP	Anomaly_Resolved_LEOP	Autonomous
Trouble Shooting	Standby	Anomaly_Resolved	Autonomous
Trouble Shooting	Safe	OBC_Reset	Autonomous
Standby	Orbit Maintenance	Orbit_Maintenance_Ready	Autonomous
Standby	EOL	EOL_Reached	Autonomous
Standby	EOL	Premature_EOL_Reached	Ground Control
Standby	Trouble Shooting	Pending_Update	Ground control
Standby	Science	Primary_Target_Acquired	Autonomous
Standby	Science	Secondary_Target_Acquired	Autonomous
Standby	Downlink	Ground_Xlink_Acquired	Autonomous
Orbit Maintenance	Standby	Manoeuvre_Completed	Autonomous
Science	Standby	Switch_Primary	Autonomous
Science	Standby	Switch_Secondary	Autonomous
Downlink	Standby	Ground_Xlink_Lost	Autonomous
Downlink	Standby	Data_Transmission_Complete	Autonomous
Downlink	Standby	Ground_Xlink_Interrupt	Ground control
Any mode [1]	Trouble Shooting Mode	Failsafe_Lvl_2	Autonomous
Any Mode [1]	Safe	Failsafe_Lvl_3	Autonomous
Any Mode [1]	Trouble Shooting	Failsafe_Lvl_2_Commanded	Ground control
Any Mode [1]	Safe	Failsafe_Lvl_3_Commanded	Ground control
Any Mode [1]	Safe	OBC_Reset	Autonomous
Any Mode [2]	Radiation Protection	SAA_Entry_Imminent	Autonomous

14.5. Time budget

Table 14.6 and Table 14.7 show the estimated time budget per orbit for a typical science measurement and downlink orbit, respectively. These budgets are conservative, as worst-case values were taken.

[1] Except for Radiation Protection mode and EOL mode
[2] Except for EOL mode

Table 14.6: Science-orbit time budget per system and AOCS mode.

System mode	AOCS mode	Time [min]	% of orbit	Notes
Science	Fine pointing	71.33	74.30	
Standby	Slew	2.92	3.04	Based on target overview (Section 2.2)
Standby	Standby	6.00	6.25	Worst-case temperature regulation
Radiation protection	Standby	10.95	11.41	Worst-case
Mode switching	–	4.80	5.00	Assumed
Total	–	**96**	**100**	–

Table 14.7: Downlink-orbit time budget per system and AOCS mode (every 24 h).

System mode	AOCS mode	Time [min]	% of orbit	Notes
Science	Fine pointing	54.25	56.51	–
Standby	Slew	5.00	5.21	2×180
Standby	Standby	6.00	6.25	Worst-case temperature regulation
Downlink	Fine pointing	15.00	15.63	Section 12.4.3
Radiation protection	Standby	10.95	11.41	Worst-case
Mode switching	–	4.80	5.00	Assumed
Total	–	**96**	**100**	–

For a science orbit, the slew duration is estimated by the time it takes to switch targets. In Section 2.2, it is explained that the targets are assumed to be within the galactic plane and clustered towards the galactic centre. The assumption is made that no slewing is required perpendicular to the galactic plane. A max slew of 30 ° is required in the axis parallel to the galactic plane, as the targets are most likely clustered towards the centre of the galaxy. About the Z-axis, a worst-case slew of 180 ° is assumed. Following REQ-AOCS-F-SYS008-007, the slew time was computed. It is also assumed that only one target switch takes place during an orbit, as the aim is to maximise the observation time. For the downlink orbit, the slewing time is estimated by two 180 ° slews (one to aim the antenna to the ground and one to point back to the target). In this orbit, it is assumed that there is no target switching.
To estimate the scientific observation time, a simulation framework is established. First, the latitude/longitude coordinate mesh is generated using SPENVIS for the 475km and 550km altitude limits. Then, the corresponding proton flux environment tables are generated for the solar minimum and maximum periods. Using a Python program [139], the orbit of NEBULA-Xplorer is simulated over a year, with passage through the regions' proton flux larger than 10 MeV being timed. For this, a constant SAA environment and orbit altitude were assumed, and the average annual time spent in the SAA was conservatively estimated for the boundaries of the altitude envelope. For a 550km altitude, a solar maximum of 10.87% and solar minimum of 11.41% SAA time was estimated, and for 475 km altitude, a solar maximum of 9.03%, and solar minimum of 9.39% SAA time was estimated.
According to Section 4.7.1, the spacecraft is expected to perform approximately 43 CAMs over the mission lifetime. Each CAM burn lasts only a few seconds, but requires preparation and post-burn recovery time. For budgeting purposes, a CAM was assumed to take about 10 minutes in total, which results in roughly 430 minutes of CAM activity. In addition, one re-boost manoeuvre was assumed, during which the spacecraft would remain in standby for about half an orbit to perform the second burn and recover afterwards, bringing the total orbit-maintenance time to approximately 480 minutes. This overall time consumption is small compared to the mission timeline and does not justify setting up a dedicated time budget for an orbit-maintenance mode. This estimate excludes any injection correction manoeuvre, since it would be handled before any science observation is done.
To verify compliance with REQ-SYS-F-MIS007-009 a full mission time budget was worked out. This time budget will show the expected percentage of the mission life time spent in each mode. For this the time budgets for the science and downlink orbit presented in Table 14.6 and Table 14.7 were averaged and added to the additional modes that were not considered in the two typical orbits.

The mission lifetime budget for the nominal life time of 5 years is presented in Table 14.8. It can be seen that with the current modes of operations an operating time of 71% of the life time of the spacecraft can be reached, complying with REQ-SYS-F-MIS007-009. if the operational life time could be expanded up to seven years, an operating time fraction of 71.59% could be reached, assuming the times spent in safe mode and trouble shooting mode scale linearly. This is also shown in Table 14.9.

Table 14.8: Mission lifetime budget for 5 years of operational life

System mode	Time [days]	% of total lifetime
LEOP	5.00	0.27
Commissioning	30.00	1.64
Safe	15.00	0.82
Radiation protection	208.23	11.41
Trouble Shooting	20.00	1.10
Standby	164.24	9.00
Orbit Maintenance	0.18	0.01
Science	1295.81	71.00
Downlink	18.13	1.04
EOL	14.00	0.77
Mode stabilizing	54.40	2.98
Total	1825	100.00

Table 14.9: Mission lifetime budget for 7 years of operational life

System mode	Time [days]	% of total lifetime
LEOP	5.00	0.20
Commissioning	30.00	1.17
Safe	21.00	0.82
Radiation protection	291.53	11.41
Trouble Shooting	28.00	1.10
Standby	233.11	9.12
Orbit Maintenance	0.26	0.01
Science	1829.15	71.59
Downlink	25.74	1.01
EOL	14.00	0.55
Mode stabilizing	77.21	3.02
Total	2555	100.00

The duration of the mission phases and modes, LEOP, Commissioning and EOL, could directly be added from Chapter 5 as their duration is defined there. From the ΔV analysis performed in Section 4.7 is was found that over the life time duration of 5 years, the orbit maintenance mode will only account for 0.01% of the operational lifetime. To determine the estimated amount spent in safe mode and troubleshooting mode data from other missions was used. Imken et al.(2018) [69] analysed a dataset containing 21 space mission recording 240 mission anomalies that triggered a safe mode. From this, it was concluded that roughly 12 safe mode triggering anomalies occur during per mission over the spacecraft life time. For the NEBULA-Xplorer this would mean 2.4 per year. Most missions in the dataset are deep space missions, which are not fully representable for the a LEO mission. Considering the differences in mission profile, a conservative margin was applied, and the expected number of safe-mode events for the NEBULA-Xplorer mission was rounded up to three events per year. The time spent in Safe Mode can vary widely between different anomaly scenarios and missions. From an article on the recovery of ESA's Integral spacecraft [52], it was found that the first recovery steps had to be completed within three hours. The total duration of the recovery process is not mentioned. From Gravity Probe B mission [61] it was found that to go from safe mode to nominal operations a full day was required. Larger durations are used for some missions, but these are typically non-LEO with less contact time. Therefore a full day was taken as an estimate, resulting in the spacecraft spending 15 days in total in safe mode during its nominal life time of five years. Since every time the spacecraft enters safe mode it will exit to trouble shooting mode at least 15 switches to troubleshooting modes should be accounted for as well. Based on the recovery time of the Gravity Probe B mission [61], one day was again used as the duration per event. Taking into account that troubleshooting mode is also used for failsafe level 1 and software updates, five more days were added, leading to a total of 20 days in troubleshooting mode. Furthermore, it should be noted that mode switching itself occurs instantaneously. Operations to prepare for this switch happen mostly during the standby mode, and are accounted for within this mode. To allow for stabilizing, a 3% margin per orbit was added in the budget under 'mode stabilizing'. This is purely a margin, since reaching stable attitude, slewing manoeuvres and stable temperatures, is already accounted for in the standby mode. The stabilizing happens during the operational mode the of the spacecraft itself.

15
Final Design

Having defined the interfaces, the spacecraft design is now finalised, marking the completion of the system-level design. This chapter presents a comprehensive overview of the spacecraft, beginning with a detailed CAD visualisation in Section 15.1. Section 15.2 provides the engineering rationale behind the specific placement of each subsystem. Section 15.3 shows the mass budget and CoG calculations to verify compliance with the launcher requirements. The chapter concludes with the power budget in Section 15.4.

15.1. CAD model

Figure 15.1 and Figure 15.2 show an external and internal view of the spacecraft.

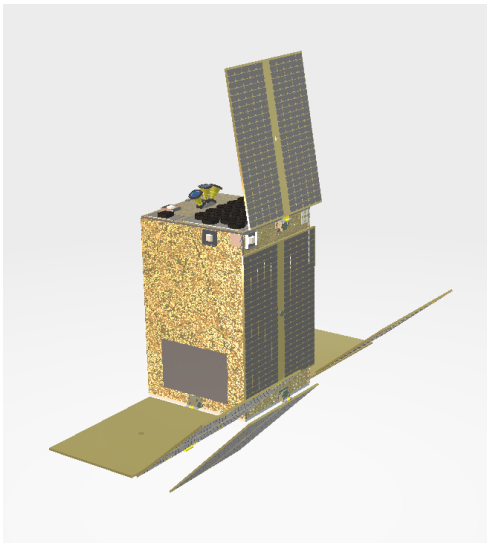

Figure 15.1: Isometric view of the NEBULA-Xplorer's external architecture

Figure 15.2: Front view of the NEBULA-Xplorer's internal architecture

15.2. Subsystem placement

In the final design, all subsystem components have been placed to optimise their own functionality but also to comply with (sub)system requirements. Figure 15.2 shows the overview of all subsystems and their location. This section provides reasoning for the placement of subsystem components.

15.2.1. Propulsion

The propulsion system is placed internally with its four thrusters protruding from the -X panel. The most important requirement for the thrusters is that they are aligned with the spacecraft CoG, to prevent induced torques. Therefore, by balancing other subsystems, the spacecraft CoG is placed in the exact middle of the four thruster configuration square. As explained in Section 8.2, this configuration also accounts for any unknown CoG offsets. Section 15.3.1 goes further into detail on the CoG values.

15.2.2. AOCS actuators

Reaction Wheel Module

The MMOI of the S/C is a key driver for the RW sizing. The RW module is placed as close to the CoG as possible. This is because it is a heavy component and indirectly affects its own sizing due to the change in

MMOI. Due to its mass, the module is attached to the internal panel directly above the propulsion system.

Magnetorquers

As explained in Section 9.3.2 (MTQ sizing), three orthogonally placed MTQs are used, where each rod is placed along one of the body axes. The -X,+Y,+Z corner of the S/C is reserved for this three-axis configuration. Each MTQ has a magnetic dipole of 10 Am^2, which converts to 17.3 Am^2 in total. These actuators produce a magnetic field, and thus also an electric field. For this reason, they are placed as far from the payload electronics as possible. The relationship between distance and the magnetic field strength is $1/R^3$ as it follows the inverse cube law.

15.2.3. AOCS sensors

As mentioned in Section 9.3.1, there are five kinds of AOCS sensors, each in different quantities. The first being the Start Trackers, placed on the Start Tracker Hub (see Section 14.2.1. The hub is placed on the top panel to reduce the launch loads induced on the hub's structure, and on the edge in the -X direction to minimise blockage by the solar panels. The gyroscopes are placed internally, as close as possible to the reaction wheels, due to their constant data exchange. The other internal component is the GNSS receiver, which is placed away from the reaction wheels electronics to prevent interference. It is located at the bottom of the -X panel, directly opposite to the externally placed GNSS antenna. The five sun sensors are placed on each side of the spacecraft except the launch adapter panel. The sun sensors on the +Z, +Y and -Y panels are placed on the -X direction edge to minimise solar panel blockage. On the -X panel, it is placed below the propulsion system. The sun sensor on the +X panel is placed in between the slit of the solar panels. The two magnetometers are placed next to each other, as one is redundant. They are placed opposite to the MTQs, to minimise magnetic disturbance.

15.2.4. EPS

As the battery pack and the PCDU are two of the heavier components, they have been placed to balance the CoG in the Y direction and lower the CoG in the Z direction. They have been placed close to the OBC and CPDU to fit all of them inside the radiation walls. The wires of the EPS system are placed all around the spacecraft and are, for now, assumed to be uniformly distributed (see Table 7.2). The location and orientation of the solar arrays are explained in Section 10.3.

15.2.5. TCS

Section 11.3 goes into detail on all the component placement where Section 11.3.1 explains the positioning of the radiators. Important to mention is that the secondary radiators (on the ± Y sides) fit under the solar arrays in stowed configuration. The main bus radiator is placed on the -X panel, above the thrusters.

15.2.6. TT&C

The TT&C components can be split into three kinds: the TT&C module (containing the transceiver/diplexer, transmitter and switches), the S-band antennas and the X-band antenna. Section 12.4.4 explains that the S-band antennas are placed on the ±X panels. On the +X panel, it is placed in the slit between the solar panels (see Section 10.2). On the -X panel, it is placed such that the TT&C module can be placed on the opposite side of the panel, internally. The X-band antenna is placed on the +Y panel (instead of the -Y panel), as this enables easier connection with the TT&C module.

15.2.7. C&DH

The OBC and CPDU are, just as the EPS components, placed to balance the CoG. They are placed in the radiation walls as protection. The same assumptions is made for the wiring, where the wires are uniformly distributed across the whole spacecraft (see Section 13.6).

15.3. Mass Budget

Table 15.1 presents the spacecraft mass budget. Following ESA's margin philosophy, the dry mass at launch was calculated, including a 20% system-level margin applied to the nominal launch dry mass, where the nominal value was obtained by summing the masses of all spacecraft components. Additionally, equipment-level design-maturity margins were applied when forming the nominal mass: 5% for off-the-shelf items, 10% for off-the-shelf items requiring minor modifications, and 20% for newly developed items or items requiring major modifications [82].

Table 15.1: Final Mass Budget Breakdown

(a) Structures

Component	Mass [kg]	± %
X-braced panels	40.74	44.82
CFRP face sheets	35.37	38.91
Honeycomb cores	3.002	3.302
Launcher panel	26.21	31.45
Launch adapter	5.1	5.355
Isostatic mounts	2.544	3.053
Sunshades	4.612	5.073
Total	**117.6**	**132.0**

(b) Propulsion

Component	Mass [kg]	+ %
Thrusters (4x)	2.78	2.919
Prop. tanks	1.78	1.958
Feed/manifold	8.1	8.91
Total	**12.66**	**13.79**

(c) AOCS

Component	Mass [kg]	+ %
Reaction wheels	12.8	13.44
RW mount	3.2	3.84
Magnetorquers	1.05	1.1
Star Tracker	4.2	4.41
GNSS receiver	0.16	0.17
Magnetometer	0.17	0.18
Total	**21.58**	**23.14**

(d) EPS

Component	Mass [kg]	+ %
Solar Panels +X	14.7	16.17
Solar Panels ±Y	12.6	13.86
Battery pack	7.8	8.19
PCDU	3.1	3.255
Converters	1.8	2.16
Wires	8.1	9.72
Sensors	0.4	0.48
Total	**48.5**	**53.84**

(e) TCS

Component	Mass [kg]	+ %
MLI	2.96	3.26
Thermal straps (6x)	0.35	0.39
Main radiator	3.24	3.50
Sec. radiator (2x)	1.9	2.1
Elec. Heaters (6x)	2.2e-3	2.3e-3
Temp. sensors (124x)	3.5e-4	3.5e-4
Total	**12.15**	**13.41**

(f) TT&C

Component	Mass [kg]	+ %
Transceiver (2x)	0.818	0.8589
S-band Ant. (2x)	0.226	0.2373
Transmitter (2x)	0.5	0.525
Switch (3x)	0.182	0.1953
X-band Ant.	0.8	0.84
Total	**1.726**	**1.817**

(g) C&DH

Component	Mass [kg]	+ %
OBC	0.95	1.00
CPDU	3.9	4.29
Harness	1.62	1.782
Total	**6.47**	**7.072**

(h) Other

Component	Mass [kg]	+ %
HEXI	80	88
LEXI	10	11
Dosimeter	0.066	0.693
Total	**90.07**	**99.70**

(i) Total spacecraft

Subsystem Group	Mass [kg]	+ %
(a) Structures	117.6	132.0
(b) Propulsion	12.66	13.79
(c) AOCS	21.58	23.14
(d) EPS	48.5	53.84
(e) TCS	12.15	13.41
(f) TT&C	1.726	1.817
(g) C&DH	6.47	7.072
(h) Other	90.07	99.70
System Total	**310.7**	**344.7**

15.3.1. Center of Gravity

With all component masses, the exact location of the CoG can be computed. The computed values in launch configuration (stowed solar panels) are (x[mm], y[mm], z[mm]) = (-28, 0, 577) and for flight configuration (deployed solar panels) the computed values are (x[mm], y[mm], z[mm]) = (-7, 0, 543). Note that these values are measured from the centre of the launch adapter. The static imbalance in launch configuration is $\sqrt{x^2 + y^2} = \sqrt{28^2 + 0^2} = 28mm$. This means the static imbalance is less than 30mm and the CoG height is less than 900mm. Therefore, the spacecraft complies with requirements REQ-STUC-C-LAUN003-006 and REQ-STUC-C-LAUN003-007. Y_{cog} and Z_{cog} in flight configuration are exactly aligned with the propulsion system, meaning no torques will be induced.

15.4. Power Budget

Table 15.2 shows the power budget of the spacecraft. The budget is given for the science mode as this is the most limiting mode (see Section 14.4). The EPS power generation fits this power budget, as it was sized for a power consumption of 438 W (see Section 10.3.2).

Table 15.2: Final Power Budget Breakdown For Science Mode

(a) AOCS

Component	Power [W]
Reaction wheels	40
Magnetorquers	3
Star Tracker	1.4
GNSS receiver	0.9
Magnetometer	0.74
Total	**46.10**

(b) TCS

Component	Power [W]
Elec. Heaters (6x)	12
Temp. Sensors (124x)	5.7
Total	**17.7**

(c) TT&C

Component	Power [W]
Transceiver	Tx: 17; Rx: 1.9
Transmitter	25
Total	**1.172**

(d) C&DH

Component	Power [W]
OBC	7.5
CPDU	10
Total	**17.5**

(e) Other

Component	Power [W]
HEXI	80
LEXI	250
Dosimeter	0.06
Total	**330.06**

(f) Consolidated System Power Budget

Subsystem Group	Power [W]
Subsystems	412.532

16
Cost Analysis

The objective of this chapter is to provide a transparent and reproducible cost estimate that can be updated in later project phases. Since the mission is still in Phase 0, the focus is not on producing accurate cost estimates, but on establishing a clear cost scope and a consistent Cost Breakdown Structure (CBS) that remains traceable to its assumptions and key inputs. The chapter first defines the ground rules and assumptions, then describes the estimation methodology, and finally presents the resulting CBS and a brief sanity check.

16.1. Groundrules and Assumptions

Since NEBULA-Xplorer is currently in Phase 0, the design maturity does not support a detailed bottom-up costing. Instead, the analysis focuses on two things: defining clear cost boundaries and establishing a consistent CBS with traceable assumptions.

Scope

During discussions with the client, it became clear that the €4M budget cap was inherited from the earlier Falcon 9–based reference design and was therefore not treated as a binding, mission-driving requirement in this phase. Instead, it was primarily used as a consistency and granularity check, guiding which cost elements were included or excluded. Therefore, this cost analysis is limited to the spacecraft bus and the minimum set of programmatic and test activities needed to realise the bus product within the defined project boundaries. The following elements are included in the scope of this cost analysis:

- Spacecraft bus subsystems: Structures, EPS, AOCS, Propulsion, TCS, TT&C, and C&DH
- Assembly, Integration & Test/Verification (AIT/AIV)
- Program level activities
- Ground Support Equipment (GSE) and other costs (test facilities, travel & transport)

The following elements are explicitly excluded from the scope:

- Payload (instrument) development and procurement
- Launch services and launcher-specific hardware procurement
- Ground segment and mission operations (including mission centre)
- System-level margin/contingency, outreach and science exploitation
- Construction of facilities or major facility upgrades (CoF)

These exclusions follow directly from REQ-MIS-C-5 and are consistent with the project-level cost scope described by SRON [64]. They must be considered when extending this estimate to a full mission life-cycle cost in later phases.

Model Philosophy

For verification and validation, an Engineering Model (EM) and a Protoflight Model (PFM) are chosen, as discussed in more detail in Chapter 18. Dedicated flight spares are treated as out-of-scope for this Phase 0 estimate. The CBS is structured by development phases to remain compatible with SRON's budgeting logic and to allow updates when design maturity improves.

Costing Approach

A hybrid analogy- and parametric-based approach is applied. Analogy-based estimates are used where costs are dominated by organisational choices and available reference budgets (e.g. student-led program context), while parametric Cost Estimating Relationships (CER) are used as high-level models when technical drivers are identifiable. A detailed engineering build-up is not performed due to low design maturity [137]. The primary goal is reproducibility and traceability rather than component-level accuracy.

Student-led Project
NEBULA-Xplorer is a student-led mission where most engineering work is performed in-kind by students, and out-of-pocket staff costs are primarily limited to coaching and supervision. SRON's planning baseline assumes this coaching effort scales with the number of active students and is distributed across SRON and industrial partners, with additional support from educational institutions [127]. Although this effort is not explicitly costed in the CBS, as time and rate data are not known, its scale remains significant. SRON reports that at the start of 2026, more than 70 students have already contributed to the project, and this number will continue to grow in the coming years.

Financial Factors
All reported values were expressed in EUR 2025. The starting point for the spacecraft bus estimate was already available in EUR, and therefore, no explicit currency conversion or inflation correction was required in the main calculation. Parametric relations from SMAD [137] were still used, but only to derive relative distributions between cost elements and to support sanity checks. Because these relations were applied as percentages rather than absolute currency outputs, the cost year and currency of the original CER datasets did not directly propagate into the final reported values.

16.2. Cost Estimation Methodology
This cost estimate is designed to be transparent and reproducible for later phases rather than to provide a high-accuracy budget. As NEBULA-Xplorer is still in Phase 0, the design maturity does not support bottom-up costing; costs are therefore derived using a simplified combination of analogy-based scaling and parametric guidance [111]. The SRON Project Management Plan provides the main reference for the costing logic and the level of detail appropriate at this stage [127].

The spacecraft bus cost is estimated by analogy, assuming that for comparable architectures and verification philosophies the total bus cost scales primarily with dry bus mass. The baseline is therefore scaled in proportion to the current dry bus mass using the SRON reference, avoiding additional Phase 0 tuning factors [111]. The result is treated as an order-of-magnitude value that can be rescaled as the design matures.

Subsystem-level costs are not based on procurement lists in this phase. Instead, the total bus cost is allocated based on relative subsystem mass contributions from the NEBULA-Xplorer mass budget and the small-satellite subsystem CERs from SMAD, ensuring a realistic split while reflecting the current design [137]. These allocations can be replaced by component-level budgets in later phases.

Non-hardware elements are treated separately. AIT/AIV is kept as a dedicated line item because it depends strongly on the final verification approach; in Phase 0, it is retained as a placeholder until the test campaign and facilities are defined. Programme activities follow the staffing model in the CBS; student-led execution and in-kind support mean these costs are not treated as standard industrial overhead. GSE and other out-of-pocket items are included as separate entries based on SRON order-of-magnitude inputs.

Key inputs and drivers are: dry bus mass for analogy scaling, subsystem mass budget for allocation, model/verification philosophy for scope interpretation, the SRON costing baseline in EUR 2025 [127], and SMAD small-satellite distributions for allocation and sanity checks [137]. Overall, the structure is straightforward to update: re-scale the bus with mass, replace allocations with detailed subsystem budgets, and refine AIT/AIV once the integration and verification plan is fixed.

16.3. Cost Breakdown Structure
This section presents the CBS for the NEBULA-Xplorer spacecraft within the cost boundaries defined in Chapter 16. The CBS was structured to remain compatible with the SRON budgeting breakdown by development phase, while limiting scope to the spacecraft bus and supporting activities that remained within REQ-MIS-C-5.

16.3.1. Staffing
The NEBULA-Xplorer mission was organised as a student-led project, with most engineering work performed by students. The staffing costs in the previous section, the program-level activity costs, have been omitted,

assuming that this coaching effort scaled with the number of students active in each development phase and was distributed across SRON and participating industry partners, with additional support from educational institutions. In the SRON planning baseline, the estimate was based on roughly 40 students per half-year, with an average coaching load of approximately 2 hours per week per student, corresponding to approximately 2.5 FTE of coaching support per year (excluding margin) over the project duration up to launch [127].

16.3.2. Out-of-pocket Costs

Having estimated staffing costs in the previous section, the program-level activity costs have been omitted from the CBS below. Table 16.1 summarises the out-of-pocket costs for the spacecraft bus only within the defined scope: Phase C is taken as the client-provided EM cost assumption, while Phase D is a first-order subsystem allocation derived from a scaled reference Phase D bus cost. While Phase C/D 'bus development' implicitly includes some integration and test effort from the reference baseline, AIT/AIV is not modelled as a separate cost element because the SRON Falcon 9 baseline did not separate spacecraft-level AIT/AIV and it cannot be quantified reliably at this design stage. Although SMAD suggests AIT/AIV shares of roughly 20–30% [137], feedback from Michel van Pelt (ESA) [102] indicated that these models tend to overpredict for modern small-satellite projects, so the percentage uplift was not applied; AIT/AIV is therefore deferred to later phases once the verification approach is defined in more detail.

Phase C: Engineering Model (EM) bus development	
Engineering Model (EM) bus development	€ 2,500,000
Phase D: Protoflight Model (PFM) bus development	
EPS	€ 1,833,000
AOCS	€ 1,381,000
Propulsion	€ 541,000
C&DH	€ 291,000
TCS	€ 232,000
TT&C	€ 104,000
Structures	€ 2,187,000
Subtotal Phase C & D bus development	**€ 9,089,000**
Other	
Ground Support Equipment (GSE)	€ 107,710
Test facilities (ROM)	€ 161,570
Travel (ROM)	€ 40,000
Transport, insurance	€ 50,000
Subtotal Other	**€ 359,290**
Total	**€ 9,448,290**

Table 16.1: Cost Breakdown Structure

16.3.3. Consistency Check

A consistency check was performed to confirm that the estimate was internally consistent and that no unrealistic allocations were introduced by the scaling and breakdown approach. The subsystem-level cost split was checked for plausibility by comparing the mass-based allocation and the SMAD-derived typical cost distributions: SMAD was not used to set the total bus cost, but it provided a reference for whether the relative subsystem shares were reasonable for a small satellite.

In conclusion, this Phase 0 cost analysis provided a traceable estimate of a similar order of magnitude to the SRON Falcon 9 baseline from which REQ-MIS-C-5 was originally copied, and it offered a reproducible starting point for updating the requirement and refining the budget in later phases. Since heritage cost references and SMAD-style CER do not fully reflect modern small satellite mission guidelines, a follow-up meeting with ESA cost engineer Michel van Pelt is recommended to review the cost breakdown and agree on a more appropriate estimation approach.

17
Technical Risk Assessment

This chapter focuses on the identification and management of potential risks the mission may encounter followed by a Reliability Availability Maintainability and Safety (RAMS) analysis. The main goal of technical risk assessment is to support designing a spacecraft capable of achieving designated mission parameters, whilst meeting the imposed top level requirements in a safe and efficient manner. This chapter is subdivided into sections that focus on key aspects of this task. In Section 17.1 the procedure undertaken for risk assessment is described in detail, followed by risk identification and categorisation in Section 17.2. An extensive mitigation guideline is constructed in Section 17.3, which then is applied to the identified for both system and sub-system level risks compiled in the risk log in Section 17.4. The contingency framework in Section 17.5 is designed to accommodate potential gaps in mitigation strategy. The RAMS analysis is performed in Section 17.6.

17.1. Risk Procedure

The risk management strategy can be summarized in four steps [42]:

1. Define risk management implementation requirements
2. Identify and assess the risks
3. Decide and act
4. Monitor, communicate and accept the risks

This process was followed throughout all design phases of the project, with multiple iterations taking place within each phase.

17.2. Risk Identification and Categorisation

To ensure the risk assessment is complete, both system and sub-system level risks were identified and classified in a systematic manner in the risk log of Section 17.4. The classification is two-fold: by rating and category.

17.2.1. Categorisation

The categorisation of risks was performed both system and sub-system level wise. The system risks were divided into a corresponding domain, them being: Science, Operational, Schedule and Cost. For sub-system risks the corresponding sub-system is declared as the corresponding domain.

17.2.2. Likelihood and Severity Metrics

The ranking schemes for likelihood and severity metrics were devised such that an accurate risk rating can be evaluated. Due to risk likelihood being intertwined with the reliability metric of the system, a so called Heritage Based Likelihood Metric (HBLM) was constructed using the ESA's HERA mission risk assessment as an inspiration [44]. The severity metric corresponds to ECSS-M-ST-80C [42]. With that information both likelihood and severity metrics are presented in Tables 17.1 and 17.2 respectively.

Table 17.1: HBLM System

Score	Likelihood	TRL	Heritage-Based Interpretation
E	Very High	1 - 2	Failure is **expected** due to lack of validation; concept relies on unproven assumptions with no representative testing or flight heritage.
D	High	3 - 4	Failure is **likely** due to limited experimental evidence; major uncertainties remain and system behaviour is not yet fully understood.
C	Medium	5 - 6	Failure is **possible**; design is based on known principles but significant configuration or environmental extrapolation is required.
B	Low	7 - 8	Failure is **unlikely**; system largely derived from proven designs with limited and well-understood modifications.
A	Very Low	9	Failure is **improbable**; design is well proven in flight with extensive heritage and minimal changes.

Table 17.2: Severity Metric System [25], [42]

Score	Severity	Science	Operational	Schedule	Cost
5	Catastrophic	Failure leading to the impossibility of accomplishing the stated scientific goals	Loss of system, launcher or launch facilities	Schedule delay leading to cancellation	Cost overruns leading to cancellation
4	Critical	Failure results in a critical reduction of the mission's science return	Loss of mission	Critical launch delay (24-48 months)	Critical cost increase (400 k€–800 k€)
3	Major	Failure results in major reduction of mission's science return	Major degradation of the system	Major launch delay (6-12 months)	Major cost increase (160 k€–400 k€)
2	Significant	Failure results in significant reduction of mission's science return	Minor degradation of the system	Significant launch delay (3 - 6 months)	Significant cost increase (40 k€–160 k€)
1	Negligible	Failure results in no/negligible reduction of mission's science return	No/negligible consequences	Minimal launch delay (1 - 3 months)	Negligible cost increase (< 40 k€)

17.2.3. Risk Index

Combining the risk likelihood and severity, each risk can be defined with a Risk Index (RI). As an example, a risk with medium likelihood and critical severity would have a risk index C4. In Table 17.3, the magnitude of every possible RI is displayed and linked to one of five risk magnitudes (ranging from "Very Low" to "Very High", based on ECSS risk management philosophies [42]): only risks that have a low or very low risk magnitude are considered acceptable for the design; risks with a magnitude of medium or higher need to be mitigated to acceptable risk levels.

Table 17.3: Risk Magnitude Designations and Proposed Actions [42]

Risk Index	Risk Magnitude	Proposed Actions
E4, E5, D5	Very High	Unacceptable risk: implement new team process or change baseline, implement mitigation actions, seek project management attention at appropriate level
E3, D4, C5	High	Unacceptable risk: see above
E2, D3, C4, B5	Medium	Unacceptable risk: aggressively manage, consider alternative team process or baseline, implement mitigation actions
E1, D1, D2, C2, C3, B3, B4, A5	Low	Acceptable risk: control, monitor
C1, B1, B2, A1, A2, A3, A4	Very Low	Acceptable risk: see above

17.3. Mitigation

As part of risk assessment, mitigation strategies were devised for every single identified risk. These strategies take different forms ranging from redundancy as described in Section 6.4, to procedural safeguards, conservative design margins, and operational constraints aimed at reducing both the likelihood and impact of potential failures. The mitigation plans are then applied to a risk map to see the shift in likelihood and severity metrics for every single identified risk. The resultant heat maps are shown in Figure 17.1.

17.4. Risk Log

In order to provide a clear overview of main risks, a risk log was created in tabular form that contains each risks ID, failure condition, pre-mitigated risk index, mitigation plan and finally the post-mitigated risk index. For the labelling of the risk ID's, a division between system and subsystem is used. System level risks follow the label R-SYS-DOMAIN-###, with the domain being either COST (cost); SCI (science); TECH (technical) or SCHD (schedule). Subsystem level risks follow the label R-SUB-TYPE-###, with the type referring to which subsystem the risk is related to: PROP (propulsion subsystem); EPS (electrical power subsystem); TT&C (TT&C subsystem); C&DH (C&DH subsystem); AOCS (AOCS subsystem); TCS (TCS subsystem); STUC (spacecraft structure); LAUN (launcher-related risks). To keep the table concise, only system level and unacceptable subsystem level risks are included.

Table 17.4: Risk Log

Risk ID	Failure Mode	Effect	Cause	Risk	Mitigation	Mitigated Risk
R-SYS-SCI-001	The system can not operate both payloads simultaneously during the entire orbit.	Reduced scientific data output	The system can not handle the strain imposed by both payloads at the same time	C3	Implement correct margin estimations as detailed in ESA handbook [82]	B3
R-SYS-OP-001	The spacecraft is not able to maintain operations without communication for 72 hours.	Reduced mission lifetime; Narrowed operational window	Autonomous operations logic is being inhibited by one or more subsystems	C5	Verify and validate the autonomous operations mode; Ensure compatibility between relevant subsystems.	B4
R-SYS-SCI-002	The spacecraft is not able to protect the payload.	Payload lifetime reduced; Inability to collect scientific data	Subsystems do not meet the requirements imposed by the operational environment	C5	Implement correct margins on thermal, mechanical, or radiation protection measures for the payload. Apply additional protection measures beyond current assumptions.	B4
R-SYS-OP-002	The spacecraft can not withstand the operational environment.	spacecraft lifetime reduced; Spacecraft can not operate.	Subsystems do not meet the requirements imposed by the operational environment	B5	Implement correct margins on thermal, mechanical, or radiation protection measures for the system. Include subsystem level redundancy measures where applicable.	A5
R-SYS-SCHD-001	The spacecraft does not finish decommissioning phase within 5 years of the end of the mission.	Creation of space debris; Violation of ESA requirements.	Orbital decay will proceed outside predicted bounds, preventing timely completion of decommissioning.	A3	Implement correct Δ V margins for the propulsion system in accordance with ESA guidelines [82]. Use high reliability and TRL components. Investigate potential passive orbital decay methods.	A2
R-SYS-SCHD-002	The project phase A/B/C/D schedule is delayed beyond the launch date in 2030.	Rescheduling the launch and operations phase of the spacecraft; Increased costs.	Unexpected additional or extended design, production, or test activities will delay the project schedule.	D4	Implement internal schedule-control measures per ECSS-M-ST-10 [35] and ECSS-M-ST-80 [42], including adding realistic internal schedule margins, locking design freeze dates, and enforcing strict configuration/change control to prevent scope creep.	C2
R-SUB-STUC-005	Crack propagation	Propagation of pre-existing flaws (cracks, voids, delamination) to a critical size, causing collapse or rupture	Manufacturing defects	C5	Inspection and implementing Safe Life, meaning undetected flaws cannot propagate to failure	B4
R-SUB-AOCS-005	Actuator misalignment.	Pointing bias, degraded control authority and unexpected momentum behaviour.	Mechanical tolerances or thermal distortion.	C4	Perform on-ground and on-orbit calibration.	B4
R-SUB-EPS-012	Panel deployment failure	Reduced or lost power generation, thermal management impeded	Sensor degradation or calibration drift	B5	Collaborate with the manufacturer to install safeguards and sequence deployment	A4
R-SUB-TCS-003	Radiator overheating	Radiator experiences temperatures above its operational regime	Reduced effective emittance of radiator surface	C4	Implement resistant coating; Apply margins on radiator sizing	B4
R-SUB-TCS-006	Battery pack heating failure	Battery experiences temperatures below its operational regime	Failure/Damage to battery pack assigned electrical heater	B5	Implement cold parallel redundancy for battery pack heaters	A5
R-SUB-TCS-007	LEXI heating failure	LEXI temperature below operational regime	Failure/Damage to LEXI assigned electrical heater	B5	Implement cold parallel redundancy for LEXI heaters	A5
R-SUB-TCS-008	HEXI heating failure	HEXI temperature below operational regime	Failure/Damage to HEXI assigned electrical heater	B5	Implement cold parallel redundancy for HEXI heaters	A5
R-SUB-TT&C-001	Transceiver or Diplexer failure	Loss of uplink and downlink communications	Radiation effects, thermal or power stress, component or connector failure	B5	Redundant transceiver, radiation-tolerant parts, thermal control	A5
R-SUB-TT&C-002	Transmitter failure	Loss of payload data	Radiation effects, thermal or power stress, component or connector failure	B5	Redundant transmitter, radiation-tolerant parts, thermal control	B4

Continued on next page

Risk ID	Failure Mode	Effect	Cause	Risk	Mitigation	Mitigated Risk
R-SUB-TT&C-006	Unauthorised command acceptance	Execution of unsafe or incorrect commands	Weak command validation, RF interference	C5	Command authentication	B4
R-SUB-TT&C-007	Telemetry dropout/packet loss	Incomplete situational awareness; missed anomalies	Low SNR, antenna nulls, scheduling or link interruptions	D3	Telemetry buffering, priority housekeeping	C3
R-SUB-C&DH-001	OBC latch-up	Short circuits, voltage drops, thermal runaway, subsystem wide brownouts	Parasitc structures caused by heavy ions, protons and neutrons (SEL/SEU	C4	Power cycling combined with fast detection methods, over current detection, shunt resistors	C3
R-SUB-C&DH-002	Boot Failure	OBC can not reach/run operating software after reset/power on	Corrupt boot image by SEU, memory aging/degradation, human error	B5	Dual-image boot loader, protected boot memory	A4
R-SUB-C&DH-007	Loss of bus	Subsystems unresponsive	Transceiver fault, cable fault	B5	Add redundant buses	B3
R-SUB-C&DH-010	MMU failure	No payload data storage	MMU contains a single string, memory controller failure	B5	Redundant storage modules, separation of modules, cross wiring	B3

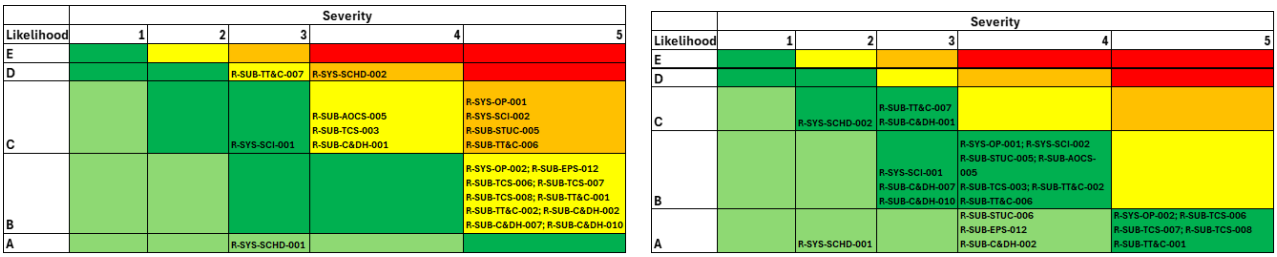

(a) Pre-Mitigation

(b) Post-Mitigation

Figure 17.1: Risk Heat Maps

17.5. Contingency

For risks where it was possible, contingency measures were put in place to alleviate the consequences of a risk event taking place. This ties closely into detailed modes of operation described in Section 14.4. Based on trigger events such as component failure, the spacecraft can switch into safe mode preventing further consequences from taking place. From this status, a so called ”Plan B” can be initiated that allows for further mission operations despite the altered state of satellites functionality.

17.6. RAMS Analysis

Reliability Availability Maintainability and Safety (RAMS) analysis is usually performed for manned missions as a way to quantify and outline the procedures used to estimate failure rates, up-times and maintenance of individual subsystems, with a goal of extending their lifetime. Therefore, it should be noted that applying RAMS analysis to the NEBULA-Xplorer mission is rather challenging.

17.6.1. Reliability

Reliability describes the probability of a component executing a given function successfully. This parameter is closely intertwined with the risk assessment due to its influence on risk likelihood. System reliability estimation on a quantitative level is an extremely challenging task, which is usually performed by experienced teams of engineers over long periods of time. This approach is beyond the scope of this project, therefore a qualitative approach was undertaken which aims at identifying key aspects that influence system level reliability. This closely ties to redundancy philosophy as described in Section 6.4, which details the available redundancy options that can be implemented throughout the system.

17.6.2. Availability
Availability describes the capacity of components to execute their functionality if a need arises. This parameter is closely coupled with modes of operation and mission time budget, which dictate the different operational modes the spacecraft is capable of to execute a given task and time allocation for its completion. Both of these aspects are expanded upon in Section 14.4 and Section 14.5.

17.6.3. Maintainability
Maintainability describes the capacity of activities that can be performed to ensure optimal component performance throughout mission lifetime. In case of the NEBULA-Xplorer any physical interaction with the spacecraft is highly unlikely. However, with the implemented capability of establishing uplink with the ground segment, future software updates can be performed to possibly add new functionality. Additionally, in case of performance loss due to component degradation/failure, modification to pre-existing modes of operation can be done to facilitate new status quo. A more in depth explanation for communication handling can be found in Chapter 12.

17.6.4. Safety
The safety part of RAMS analysis takes into consideration the impact of the spacecraft on personnel and civilians during its pre-launch preparations at the launch site, operations and end of life decommissioning. The safety of aforementioned groups is paramount during whole mission implementation and execution.

Pre-Launch
During the preparation of the spacecraft at launch facilities, local personnel will be susceptible to any components chosen for the final design including hazardous materials on-board the spacecraft. To avoid negligence and potentially harmful events the chapters on Guiana Space Center and Safety Assurance from Vega-C User's Manual [20] are followed to maintain necessary safety standards. These chapters detail the safety procedures followed on the launch site and the handling of spacecraft while it's being prepared for the launch.

Operations
During spacecraft operations, there is a risk of generating additional space debris as described in Section 8.4. This generation of additional space debris raises safety concerns for LEO operations of other missions, both current and future ones. There are several ways for spacecraft to generate debris, these include propellant tank explosion, improper battery discharge and collision either with already existing debris or some other spacecraft. To adhere to guidelines imposed by ESA and ECSS, the spacecraft will perform avoidance manoeuvres in case of high enough risk of collision with a detected object.

End of Life
As part of decommissioning procedure for LEO satellites, the spacecraft needs to be de-orbited which poses safety concerns in case of uncontrolled re-entry in Earth's atmosphere. The risk of unburnt debris that may threaten populated regions needs to be taken into account. To perform this analysis the ORIUNDO tool provided by ESA was used to determine the casualty cross-section threshold incorporating United Nation's world population predictions for the worst case de-orbiting year of 2042. This resulted in cross section of 4.6 m^2 for re-entry debris as the limit. By assuming the whole spacecraft bus excluding solar arrays as a solid body that survives reentry, the cross-sectional area was calculated to be around 3.28 m^2 resulting in casualty risk value of $7.57 \cdot 10^{-5}$ satisfying the requirements. The maximum cross sectional area of debris is dependent on types of materials used and component location in the spacecraft. Components containing titanium, inconel, stainless-steel and composites are more likely to partially survive the burn-up sequence. A simulation using ESA's SARA tool was performed to assess the component-wise survivability of the most critical components. The model does not take into account how parts are connected to each other and the shielding effects that may result from the attitude during re-entry. Estimating the exact risk of casualty is complex and a more detailed analysis is required to be performed to get a meaningful estimate. Hence, this is included as a recommendation that needs to be looked into.

18 Verification and Validation

This chapter has the goal of outlining the verification and validation plan for the NEBULA-Xplorer mission. Firstly, the adopted V-model framework will be explained and how it fits in with the mission phases. Following that, the different Verification and Validation (V&V) procedures relevant to the mission and the differences between them will be detailed. The model philosophy adopted will be described, and the purpose of each model in the V&V activities. Finally, the timeline for the next phases in the mission lifecycle will be discussed, highlighting where important reviews will take place and the usage of the models, and how risks introduced by the V&V procedures will be mitigated.

18.1. Framework

For the framework of the V&V procedures, the V-model will be used. This choice was made because the V-model is a linear framework that easily allows for the full traceability of requirements throughout the project phases. In this scenario, traceability means the ability to track the requirements from their origin up until the check that they are being complied with. This is beneficial because it makes it easier to conduct both V&V procedures, which have the goal of checking if the model complies with the requirements, but also if the requirements are really compatible with what the stakeholders had asked for. The V-model Diagram can be seen in Figure 18.1 [106].

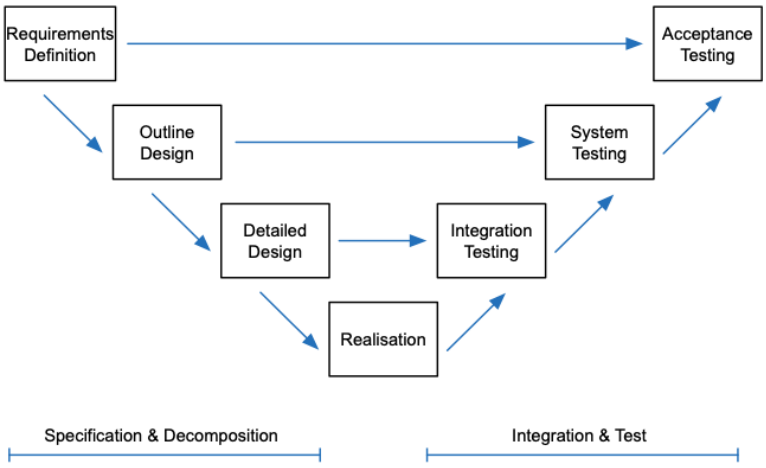

Figure 18.1: V-model Diagram [106]

The V-model helps recognise where the V&V procedures take place. On the top left of the V-model, one can identify the requirements definition step. Following this, the validation of the requirements, outlined in Section 18.3.1 occurs. The product and model verification, outlined in Section 18.3.2 and Section 18.3.4 respectively, takes place bottom-up through the right side of the V-model. Finally, the product and model validation, explained in Section 18.3.3 and Section 18.3.4 respectively, happen at the top right of the V-model, at the system-level.

18.2. Model Philosophy

The model philosophy has the goal of providing high confidence in the success of the mission while keeping cost, schedule and risks under control. The choice of model philosophy has a big impact on the mission timeline, especially in the event of anomalies during testing. Adding additional models can mitigate technical risk,

but it also leads to an increase in cost quite drastically. Therefore, a balance between risk mitigation and costs must be found.

For the NEBULA-Xplorer mission, two model philosophies can be taken into account: the PFM and the Prototype/Flight Model (PM/FM) philosophies. Under the PFM philosophy, a single model is used for both the test campaign and as the flight unit, after being certified as flight-ready. This approach is contrasting with a PM/FM philosophy, in which two different models are manufactured. The PFM is used for qualification testing and potentially discarded if damaged, and the Flight Model (FM) goes through acceptance testing and is ultimately launched. The Prototype Model (PM) can be subjected to tougher qualification-level tests and for longer durations, such as worst-case scenarios, thus providing a higher level of confidence in the design. The PFM cannot go under the same test severity, as any damage could add severe risks to the mission. Therefore, the PFM is limited by the qualification environment tests applied during acceptance-level durations.

However, while the PM/FM philosophy provides greater confidence in the mission for the reasons stated, the cost of the mission would increase drastically, and is therefore used only in missions with higher risk classes. The NEBULA-Xplorer mission does not have such a high risk; according to ESA's mission classification, the mission has "Medium Criticality" [65]. Therefore, the PFM philosophy is selected as the most balanced approach, as the most cost-effective solution without introducing unacceptable risk.

As mentioned before, the PFM will undergo qualification and acceptance testing, but an additional model is required to support early testing activities. It is also needed to verify compliance of the design with requirements. This will be fulfilled by an EM, which consists of representative hardware used to evaluate performance, interfaces and operational aspects of the design. The EM does not have a complete spacecraft configuration like the PFM, as it includes only the hardware necessary to verify the requirements that need to be addressed through testing. The addition of an EM in the model philosophy further increases confidence in the design while limiting cost and scheduling risk.

An approach that can be used for the EM is the so-called "Flat Sat", a high-fidelity, cost-effective alternative that uses flight hardware for integration, software and operations testing. In this set-up, the system components are laid out on a bench and connected as they would in the final system, just not mechanically integrated [15].

Finally, a Flight Spare (FS) can be added to the model philosophy. Its primary role is to reduce the risks introduced with the PFM philosophy, since any damage experienced during the test campaign can directly compromise the launch readiness of the spacecraft. The FS usually is made of selected critical components rather than being a full spacecraft replica, and serves as a contingency to mitigate potential schedule delays and additional costs that would otherwise happen if a FM had to be rebuilt. Therefore, the FS provides targeted risk reduction while avoiding the expenses of a full FM.

18.3. Approach

There are different types of V&V procedures. The goal of this section is to outline those that are relevant for this mission, including the model philosophy implementation. The life cycle of a space mission is divided into 7 phases and described by the ECSS standards [42]. The design detailed in this report is contained within Phase 0, which is responsible for identifying a mission concept which is input for the subsequent mission phases. Therefore, the V&V procedures that can be performed during this phase have the aim of ensuring the design concept is in accordance with the system requirements and mission objectives. Further and more detailed V&V strategies will be implemented in subsequent mission phases, as described in Section 18.4, but planned for in advance.

18.3.1. Requirements Validation

Before any of the design tasks take place, the validation of the requirements must take place. This validation procedure has the goal of making sure that all requirements, outlined in Chapter 3, follow the VALID criteria. These criteria make sure all requirements are Verifiable, Achievable, Logical, Integral and Determined, which not only ensures that they are good enough to be used in the design process, but also facilitates checking the compliance of the requirements. This validation procedure took place once all the requirement discovery

activities were finished. At this stage, no models are used.

18.3.2. Product Verification

The verification of the product has the goal of answering the question of whether the product was built in compliance with all the requirements. Looking at the V-model, the product verification happens bottom-up on the right side, where the verification activities will move from a component- and subsystem-level to system-level. In order to check the requirement compliance, every single requirement is assigned a verification method. This method can either be inspection, analysis, review-of-design, or testing [35]:

- Inspection: Verifies compliance through direct visual examination.
- Analysis: Verifies compliance through theoretical and numerical evaluation.
- Review-Of-Design: Verifies compliance through examination of design documentation (schematics, models, descriptions, drawings, etc).
- Testing: Verifies compliance through controlled testing under pre-defined conditions.

The verification method was assigned to each requirement and can be seen in the Compliance Matrix [32]. The compliance with the requirements of each subsystem, achieved by using the relevant verification method, has been detailed in their respective chapters.

The EM is introduced for this purpose and is used for the requirements that need to be tested. Requirements that are considered critical for achieving the mission objectives, such as the pointing accuracy, can also be verified through two methods: review of design (by obtaining specifications from off-the-shelf components) and testing to achieve high confidence.

18.3.3. Product Validation

Validation is done in order to answer the question of whether the right product was built, meaning if the product aligns with the mission goals and stakeholder expectations. The system can be validated by exposing the system and subsystem elements to interfaces, data exchange and tests representative of the operational mission and environment. It is the final line of defence against previously undiscovered risks for the mission.

A method of validating the product is by following the First Day, Best Day, Worst Day, Last Day scenario [137]. In this method, each day represents a different set of situations, with their corresponding environmental and operational scenarios. This way, the system is exposed to a wide range of circumstances that also allow the system to be qualified.

18.3.4. Model Validation and Verification

Any models of the spacecraft, such as 3D and numerical models, will have to go through V&V. The model verification aims to confirm that the physical principles and governing equations behind the model are implemented correctly. This can be achieved through sanity checks, comparison with analytical solutions, or cross-checking with independent modelling tools. The model validation aims to confirm that the models represent the system with enough accuracy. This can be done by comparing model outputs with supplier data, public test results or heritage data. Furthermore, the results of the sensitivity analysis also help to confirm physically consistent behaviour.

18.4. Project Design and Development

In accordance with the ECSS standards [42], the life cycle of space projects is typically divided into 7 phases:

- Phase 0: Mission analysis/need identification
- Phase A: Feasibility
- Phase B: Preliminary Definition
- Phase C: Detailed Definition
- Phase D: Qualification and Production
- Phase E: Utilisation
- Phase F: Disposal

The project detailed in this report deals with Phase 0, in which a preliminary concept of the mission is detailed. This phase and its contents will serve as input for the following phases of the project life cycle, which will delve into more expanded and detailed phases for the completion of the design.

18.4.1. Risk Management

When planning for the subsequent phases of the mission lifecycle, it is important to take into account the possible risks and account for mitigation strategies in the planning itself. This way, adequate scheduling margins can be introduced.

Firstly, issues discovered while testing with the EM (such as non-compliance) might not be completely solved before the scheduled manufacturing of the PFM. Testing the PFM also introduces many risks, such as equipment failure, incomplete test coverage or damage to the spacecraft. The FS will be able to mitigate some of these risks, but since it is only a partial replica, it cannot fully mitigate any great damage. Furthermore, other anomalies such as facility hazards, issues with handling, contamination or infrastructure limitations will affect the reliability of results and could therefore demand test repetitions, which naturally mean scheduling issues.

These risks can be mitigated through detailed test planning and maintaining a margin for the schedule to account for these possible issues. In the subsequent subsection, the time needed for each phase was taken into account with a margin of months. Furthermore, Test Readiness Reviews (TRRs) and Validation Readiness Reviews (VRRs) have been introduced in order to ensure that the readiness of procedures, facilities, systems, and documentation is fully checked before any activities take place.

18.4.2. Timeline

Figure 18.2 details the expected timeline for the NEBULA-Xplorer project life cycle, which culminates in 2030 with the launch of the satellite, thus giving a start to Phase E: Utilisation. The timeline showcases in which instances the model philosophy discussed in Section 18.2 is used (including where their manufacturing should start and in which instances they will be in use) and the timing of formal reviews. This timeline is based on the description of the mission phases (including all the necessary tasks, reviews and plans) as detailed in the ECSS standards [42]. The timeline also includes scheduling margins to take into account risks such as manufacturing delays and testing anomalies.

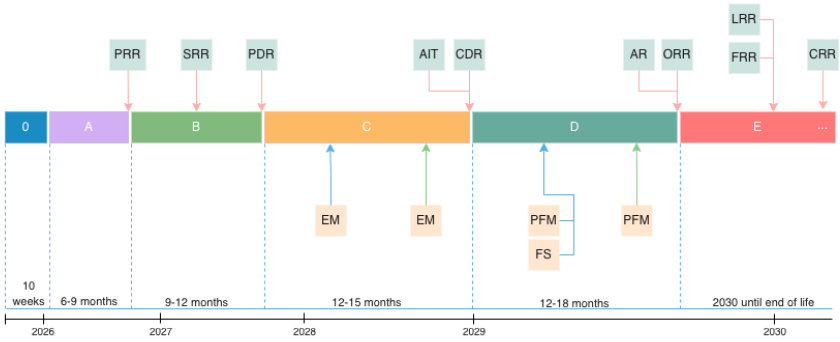

Figure 18.2: Project Timeline

Phase 0 The timeline starts on the left with the Phase 0, which has the total duration of the DSE project, thus 10 weeks. During this phase, as aforementioned, a preliminary concept has been worked into component-level design and will serve as input for the following phases. At this stage, a preliminary risk, cost and sustainability assessment, together with this V&V plan, is also drafted in order to understand possible scheduling risks that could violate the 2030 launch deadline.

Phase A Once concluded, it will give rise to Phase A, which culminates with the Preliminary Requirements Review (PRR). Phase A has a focus on conducting feasibility studies of the possible concepts, including the one proposed in Phase 0, through planning and risk assessments. The PRR will assess the work done during Phase

A, which includes preliminary management plans for the rest of the project lifecycle and the selection of system and operation concepts, which are used as inputs for Phase B. It is expected that Phase A will take 6 to 9 months.

Phase B Once approved, Phase B will carry on. Its goal is to develop in more detail the selected system and mission concept so that it can be translated into a preliminary design. A System Requirements Review (SRR) will be held during this phase in order to assess the consistency between the system requirements and the preliminary design. The phase will end with the Preliminary Design Review (PDR), which has the goal of confirming that the proposed design will meet the system requirements and that the project is ready to go into Phase C. It is expected that Phase B will take 9 to 12 months.

Phase C Next, Phase C will focus on completing the detailed design of the spacecraft. Therefore, all the interfaces, assemblies and components will be defined in detail. Critical elements will also be developed and tested according to the V&V plan and the model philosophy. Therefore, it is during this phase that the manufacturing and use of the EM will come into place, with the goal of reducing technical risks. Between its manufacturing and testing, a TRRs, as mentioned in Section 18.4.1 will take place. Furthermore, the assembly, integration and test (AIT) plans will be completed and the verification plan updated. Phase C will conclude with the Critical Design Review (CDR), which has the goal of making sure the detailed design is complete and ready for qualification and production. It is expected that Phase C will take 12 to 15 months.

Phase D Phase D will start after the approval for the CDR. During this phase, the qualification testing, manufacturing, assembly and integration will take place. This therefore marks the PFM, which will be manufactured and tested, as seen in the Figure 18.2. As mentioned in Section 18.4.1, VRRs will take place before it goes through qualification testing. A subsequent Qualification Review (QR) will take place to check verification results. The phase will end with an Acceptance Review (AR), which confirms the model is ready for delivery. Furthermore, the Operational Readiness Review (ORR) will verify that both space and ground segments are ready for Phase E. It is expected that Phase D will take 12 to 18 months.

Phase E Finally, Phase E will start, which signals launch preparations and subsequently the actual launch, early orbit operations, commissioning and nominal science operations. Still, before the launch, a Flight Readiness Review (FRR) and a Launch Readiness Review (LRR) will be held to confirm it is safe to launch. Finally, a Commissioning Result Review (CRR) will confirm that the nominal science operations may begin. Phase E will last as long as the spacecraft's lifetime, so it is expected to last 5 years.

19
Recommendations for Future Work

In this chapter, recommendations for future work are outlined, which have the goal of further maturing the design that has been developed in this report. As the activities performed are limited to Phase 0, the results are preliminary and based on simplified assumptions and early trade-offs. As the mission enters the next phases, the system definition will be refined with increased model fidelity, and additional analysis will be made to reduce technical uncertainty and risks. Therefore, the recommendations outlined here will ensure a smooth transition into Phase A, emphasising factors such as reliability quantification, increased detailed modelling of subsystems and validation using industry-standard tools.

Thermal Control System: For future mission phases, the TCS needs to be further analysed and developed by providing more accurate thermal models and heat exchange between internal components. A more detailed research into surface and internal charging should be performed, due to current uncertainties in the exact process occurrence and mitigation strategies. Also, validation using industry-approved tools should be performed.

Command and Data Handling: In the next design phase, the C&DH subsystem should be further developed by finalising the communication protocol layer to be used on the RS485 buses. Furthermore, the assumption that the cable mass contribution to the spacecraft inertia tensor is negligible should be verified with a more detailed model. Lastly, the CPU design should be finalised, including its full integration into the system architecture, to allow for a consistent interface definition.

Attitude and Orbital Control System: For the AOCS, higher-fidelity disturbance torque models should be used to better quantify disturbances such as environmental and internal disturbances. Additionally, a more detailed analysis of structural flexible modes is also recommended to support the jitter requirements. Finally, compliance checks against mission and system requirements will need to be done again once updated vendor specifications are available, as changes in the sensor and actuator performance will impact the performance margins.

Propulsion: For the propulsion subsystem, further work should focus on establishing contact with Dawn Aerospace in order to develop the customised SatDrive design in better detail. Additionally, it is recommended to clarify if Dawn Aerospace could support the mission with sponsorship, as this could significantly reduce procurement costs and impact overall feasibility in later mission phases.

Electrical Power System: In the next design phases, a design choice that could be reconsidered is the array configuration. The configuration was based on assumptions that >180°deployment angles are a possibility, while shadowing and three-panel fold-outs should be avoided if possible. While correspondence with Sparkwing engineers confirmed this, it was also established that this design is relatively uncommon and would require additional testing costs and complex deployment sequencing. A configuration was proposed that utilises the same number of panels, but with a triple 1.1x0.91 [m] fold-out, with a deployment angle of 45°from the positive x-axis wall. A double fold-out of the same size would be placed on the opposite wall, folding out 180 °toward the positive z-axis. This configuration should be analysed for performance within the operational attitude range, and the advantages of easier integration and deployment sequencing should be weighed against downsides, including the additional mass.

Cost Estimation: When it comes to cost estimation, the current approach based on heritage cost and SMAD-style CERs do not fully reflect modern small satellite mission guidelines. It is therefore recommended to review the current cost breakdown, assumptions and applicable scaling factors. This would lead to a more appropriate estimation approach.

References

[1] 3D-Plus. *3DFP128G08VS8308MB NAND Flash Memory Datasheet*. https://www.3d-plus.com/app/uploads/2023/04/3dfp_0308.pdf. Accessed: 2026-01-XX. 3D-Plus, 2023.

[2] 3DExperience. *User Assistance R2026x*. 2025. URL: https://help.3ds.com/2026x/English/DSDoc/SimXmplUserMap/xmpl-t-BracketSRD-AnalyzeResults.htm?contextscope=cloud&id=fa728e6b5480476890f97c3ede681ab3.

[3] F. F. Saberi A. Kasiri and M. Kashkul. "Optimisation of Pyramidal Reaction Wheel Configuration for Minimising Angular Momentum". In: *7th International Conference on Control, Instrumentation and Automation (ICCIA)* (2021), pp. 1–6.

[4] Nithin S. Abraham, Mark M. Hasegawa, and Sharon A. Straka. *Black Molecular Adsorber Coatings for Spaceflight Applications*. Tech. rep. NASA, 2014. URL: https://ntrs.nasa.gov/api/citations/20140017346/downloads/20140017346.pdf.

[5] ABSL. *Product Data SheetLi-ion Rechargeable Battery ABSL 8s16p 28V 56Ah*. https://www.enersys.com/49a094/globalassets/documents/product-documentation/absl/amer/amer-en-fly-absl-8s16p-3.5ah_0424.pdfy. 2024.

[6] *AE1222-II: Aerospace Design & Systems Engineering Elements I*. Course Reader. Delft University of Technology, Faculty of Aerospace Engineering, 2021.

[7] Dawn Aerospace. *SatDrive: Customized Propulsion Systems for Small Satellites*. https://www.dawnaerospace.com. 2024.

[8] Iklim Akay. *NEBULA DSE Pitch 2025-2026*. Technical report Issue 1. Delft University of Technology, Faculty of Aerospace Engineering, 2025.

[9] Iklim Akay. *Project guide: Design synthesis exercise, NEBULA-X.VC mission*. Course handbook Issue 7. Delft University of Technology, Faculty of Aerospace Engineering, Nov. 3, 2025.

[10] J. Wertz et Al. *Spacecraft Attitude Determination and Control*. Kluwer Academic Publishers.

[11] A. Nayaka Nikicio et al. "Radiation Analysis and Mitigation Framework for LEO Small Satellites". In: *IEEE International Conference on Communication, Networks and Satellite* (2017).

[12] Concha M. Reid et al. *Performance and Comparison of Lithium-Ion Batteries Under Low-Earth-Orbit Mission Profiles*. NASA Technical report NASA/TM—2007-214826. NASA, 2007. URL: https://ntrs.nasa.gov/api/citations/19710014805/downloads/19710014805.pdf.

[13] M. Malagoli et al. *Harness Optimization by Improvement of the Derating Standard ECSS-Q-ST-30-11C*. Tech. rep. Airbus Defence and Space, 2018. URL: https://www.spcd.space/proceedings/2018/1st%20Day/Normative%20System%20&%20Standards/Final%20Paper/SPCD_Harness_Sizing-Final01.pdf.

[14] Sheng-sheng Yang et al. *Displacement Damage Characterization of Electron Radiation in Triple-Junction GaAs Solar Cells*. Tech. rep. Lanzhou Institute of Physics, 2009. URL: http://esmat.esa.int/Materials_News/ISME09/pdf/2-Radiation/Poster%20Radiation%20and%20Charging%20Effects%20-%20Yang.pdf.

[15] D. Amason. *SDO FlatSat Facility*. 2008. URL: https://ntrs.nasa.gov/api/citations/20080023611/downloads/20080023611.pdf.

[16] AMGAB / Axon' Cable. *AXOMACH SpaceFibre links: High Data Rate Links for Faster Data Transmission*. https://www.amgab.se/wp-content/uploads/pdf-dir/AMGAB-Specialkabel-Axon-Axomach-Spacefibre-links.pdf. Accessed: 2026-01-05. AMGAB / Axon' Cable, 2018.

[17] B.J. Anderson. *Guidelines for the Selection of Near-Earth Thermal Environment Parameters for Spacecraft Design*. NASA. 2001. URL: https://ntrs.nasa.gov/api/citations/20020004360/downloads/20020004360.pdf.

[18] Technology Applications. *GRAPHITE & GRAPHENE SHEET THERMAL STRAPS*. Accessed: 19-01-2026. 2020. URL: https://www.techapps.com/graphene-pgs-thermal-straps.

[19] Arianespace. *Small Spacecraft Missions Servica Vega C User's Manual*. 2020.

[20] Arianespace. *Vega C User's Manual*. 2025.

[21] William Atwell et al. "Mitigating the Effects of the Space Radiation Environment: A Novel Approach of Using Graded-Z Materials". In: *AIAA SPACE 2013 Conference and Exposition*. 2013. DOI: 10.2514/6.2013-5385.

[22] J. Bijl et al. *NEBULA-Xplorer Concept of Operations*. Technical report Issue 1. Delft University of Technology, Faculty of Aerospace Engineering, 2025.

[23] V. Braun et al. "Probabilistic Orbit Lifetime Assessment with OSCAR". In: *6th International Conference on Astrodynamics Tools and Techniques (ICATT)*. Mar. 2016.

[24] Noah Brosch. *Sirius Matters*. Springer, 2008.

[25] *CDF Study Report ATHENA, Assessment of an X-Ray Telescope for the ESA Cosmic Vision Program*. European Space Agency, 2014.

[26] Angelo Cervone. *Personal communication on propulsion thrust sizing for CAMs*. Personal communication (meeting), Delft University of Technology. Jan. 2026.

[27] Consultative Committee for Space Data Systems. *TM Synchronization and Channel - Summary of Concept and Rationale*. Tech. rep. CCSDS 130.1-G-3. Consultative Committee for Space Data Systems, 2020.

[28] Consultative Committee for Space Data Systems. *TM Synchronization and Channel Coding*. Tech. rep. CCSDS 131.0-B-5. Consultative Committee for Space Data Systems (CCSDS), 2023.

[29] Dawn Aerospace. *B20 Thruster Data Sheet and Brochure*. Dawn Aerospace. New Zealand and The Netherlands, 2025.

[30] Airbus Defence and Space. *"Medium power PCDU"*. 2024. URL: https://satsearch.co/products/airbus-defence-and-space-medium-power-pcdu.

[31] DHV. *SOLAR PANELS FOR SMALLSATS*. https://dhvtechnology.com/products/solar-panels-smallsats/.

[32] DSE 2026 Nebula Xplorer Group 3. *Requirements Compliance Matrix*. Tech. rep. Internal project document. TU-Delft, Faculty of Aerospace Engineering, 2026.

[33] ECAPS and Bradford Space. *22 N High Performance Green Propellant Thruster (HPGP) – Small Satellite Catalog*. n.d. URL: https://catalog.orbitaltransports.com/content/brands/ECAPS/smallsat_catalog_22%20N%20flysheet.pdf (visited on 01/15/2026).

[34] *ECSS system Glossary of terms*. European Cooperation for Space Standardization, 2023.

[35] *ECSS-E-ST-10-02C Rev.1 – Verification*. European Cooperation for Space Standardization, 2018.

[36] *ECSS-E-ST-10-04C Space Environment*. European Cooperation for Space Standardization, 2020.

[37] *ECSS-E-ST-10C-Rev.1 - System engineering general requirements*. European Cooperation for Space Standardization, 2017.

[38] *ECSS-E-ST-32C Structural general requirements*. European Cooperation for Space Standardization, 2008.

[39] *ECSS-E-ST-50-11C, SSpaceFibre - Very high-speed serial link*. European Cooperation for Space Standardization, 2019.

[40] *ECSS-E-ST-50-12C, SpaceWire - Links, nodes, routers and networks*. European Cooperation for Space Standardization, 2019.

[41] *ECSS-E-ST-50-15, CANbus extension protocol*. European Cooperation for Space Standardization, 2015.

[42] *ECSS-M-ST-80C, Space Project Management, Risk Management*. European Cooperation for Space Standardization, 2008.

[43] *ECSS-Q-ST-70C, Space product assurance, Materials, mechanical parts and processes*. European Cooperation for Space Standardization, 2019.

[44] eoPortal. *Hera — the asteroid deflection mission of ESA*. https://www.eoportal.org/satellite-missions/hera#camera. Accessed: 2026-01-21.

[45] ESA. *Planck and the cosmic microwave background*. 2025. URL: https://www.esa.int/Science_Exploration/Space_Science/Planck/Planck_and_the_cosmic_microwave_background.

[46] ESA. *Building and testing spacecraft*. URL: https://www.esa.int/Science_Exploration/Space_Science/Building_and_testing_spacecraft.

[47] *ESA PSS-04-105, Radio Frequency and Modulation Standard*. European Space Agency, 1996.

[48] *ESSB-ST-U-007, ESA Space Debris Mitigation Requirements*. European Space Agency, 2023.

[49] European Cooperation for Space Standardization. *ECSS-Q-ST-60-15C: Space product assurance – Radiation hardness assurance – EEE components*. ECSS-Q-ST-60-15C. European Cooperation for Space Standardization, 2012.

[50] European Cooperation for Space Standardization. *ECSS-Q-ST-30C: Space product assurance – Dependability*. ECSS-Q-ST-30C. European Cooperation for Space Standardization, 2017.

[51] European Space Agency. *The cost of avoiding collision*. 2021. URL: https://www.esa.int/ESA_Multimedia/Images/2021/02/The_cost_of_avoiding_collision.

[52] European Space Agency. *Three hours to save INTEGRAL*. https://www.esa.int/Enabling_Support/Operations/Three_hours_to_save_Integral. Accessed: 2026-01-XX. European Space Agency, 2021.

[53] European Space Agency. *NewAthena Factsheet*. Accessed: 2025-11-14. 2024. URL: https://www.esa.int/Science_Exploration/Space_Science/NewAthena_factsheet.

[54] European Space Agency. *ESA Space Environment Report 2025*. https://www.esa.int/Space_Safety/Space_Debris/ESA_Space_Environment_Report_2025. 2025.

[55] European Space Agency. *ESA's Zero Debris approach*. https://www.esa.int/Space_Safety/Clean_Space/ESA_s_Zero_Debris_approach. 2025.

[56] European Space Agency. *Exploratory Call for a mini-Fast Mission Proposals*. Accessed: 2025-11-21. 2025. URL: file:///mnt/data/243d9a11-0341-4e63-8c23-0f412c7b807f.png.

[57] European Space Agency. *What are solar flares?* 2026. URL: https://www.esa.int/Science_Exploration/Space_Science/What_are_solar_flares (visited on 01/21/2026).

[58] The Nobel Foundation. *The Nobel Prize in Physics 2002*. URL: https://www.nobelprize.org/prizes/physics/2002/summary/.

[59] David G. Gilmore. *Spacecraft Thermal Control Handbook Volume I: Fundamental Technologies*. AIAA, 2002.

[60] Glenair, Inc. *Micro-D Connector Weights*. https://www.glenair.com/micro-d/pdf/a/micro-d-weights.pdf. Accessed: 2026-01-XX. 2013.

[61] Gravity Probe B Mission Team. *Gravity Probe B: Mission Status Update as of 30 December 2005*. https://einstein.stanford.edu/highlights/hl_123005.html. Accessed: 2026-01-XX. Stanford University / Einstein GP-B Project, 2005.

[62] Nebula-X DSE group. *NEBULA-Xplorer - Baseline Report*. Technical report Issue 1. Delft University of Technology, Faculty of Aerospace Engineering, 2025.

[63] Nebula-X DSE group. *NEBULA-Xplorer - Midterm Report*. Technical report Issue 1. Delft University of Technology, Faculty of Aerospace Engineering, 2025.

[64] Nebula-X DSE group. *NEBULA-Xplorer - Project Plan*. Technical report Issue 1. Delft University of Technology, Faculty of Aerospace Engineering, 2025.

[65] V. Gupta. *ESA Mission Classification: focus on RHA tailoring recommendations for COTS projects*. 2023. URL: https://indico.esa.int/event/445/contributions/8595/.

[66] Jon Hamkins. *Performance of Low-Density Parity-Check Coded Modulation*. Tech. rep. IPN Progress Report 42-184. Jet Propulsion Laboratory, California Institute of Technology, 2011.

[67] J.P. Holman. *Heat Transfet 10th ed.* McGraw-Hill, 2010.

[68] Leon W. Couch II. *Digital and Analog Communication Systems*. 8th ed. Pearson, 2013.

[69] Travis Imken et al. "Modeling Spacecraft Safe Mode Events". In: *2018 IEEE Aerospace Conference*. IEEE. 2018, pp. 1–13. DOI: 10.1109/AERO.2018.8396383.

[70] Aerospace Specification Metals Inc. *Aluminum 6061-T6 Material Properties*. URL: https://asm.matweb.com/search/specificmaterial.asp?bassnum=ma6061t6.

[71] Sheldahl Inc. *Sheldahl Materials Red Book*. 2015. URL: https://j-t-s.net/wp2023/wp-content/uploads/2023/02/Red-Book.pdf.

[72] Zoppas Industries. *FLEXIBLE HEATER FOR SPACE MARKET*. https://zoppasindustries.com/wp-content/uploads/2023/06/Catalogo-Flexible-Heaters-for-Space.pdf.

[73] International Telecommunication Union (ITU) and European Space Agency (ESA). *ITU and ESA agree on optimizing satellite communications*. International Telecommunication Union. Mar. 5, 2025. URL: https://www.itu.int/hub/2025/03/itu-and-esa-agree-on-optimizing-satellite-communications/.

[74] F. Vermolen J. van Kan A. Segal and H. Kraaijevanger. *Numerical Methods for Partial Differential Equations*. 1st ed. Delft Academic Press, 2019.

[75] Thomas Kerslake and Eric Gustafson. "On-Orbit Performance Degradation of the International Space Station P6 Photovoltaic Arrays". In: (Aug. 2003). DOI: 10.2514/6.2003-5999.

[76] Thomas Kugelstadt. *The RS-485 Design Guide*. Application report. Texas Instruments, 2008.

[77] Leaf Space. *Network & Deployment Plan*. Leaf Space. Nov. 2025.

[78] Dr. Carl Christian Liebe. *Star Trackers Attitude Determina tion*. Paper. Department of Electrphysics, Technical University of Denmark, 1995.

[79] P. Löper et al. "Analysis of the Temperature Dependence of the Open-Circuit Voltage". In: *Energy Procedia* 27 (2012). Proceedings of the 2nd International Conference on Crystalline Silicon Photovoltaics SiliconPV 2012, pp. 135–142. ISSN: 1876-6102. DOI: https://doi.org/10.1016/j.egypro.2012.07.041. URL: https://www.sciencedirect.com/science/article/pii/S1876610212012544.

[80] Ali.O.M. Maka and Tadhg S O'Donovan. "Effect of thermal load on performance parameters of solar concentrating photovoltaic: High-efficiency solar cells". In: *Energy and Built Environment* 3.2 (2022), pp. 201–209. ISSN: 2666-1233. DOI: https://doi.org/10.1016/j.enbenv.2021.01.004. URL: https://www.sciencedirect.com/science/article/pii/S2666123321000118.

[81] Gérard Maral, Michel Bousquet, and Zhili Sun. *Satellite Communications Systems: Systems, Techniques and Technology*. 6th. John Wiley & Sons, 2019. ISBN: 9781119382089.

[82] *Margin philosophy for science assessment studies*. European Space Agency, 2012.

[83] F. Landis Markley et al. *Maximum Torque and Momentum Envelopes for Reaction Wheel Arrays*. 2009.

[84] Richard H. Maurer et al. *Radiation Effects in Electronics: Single Event Effects, Total Dose, and Displacement Damage*. Technical Digest Volume 28, Number 1. Accessed: January 27, 2026. Johns Hopkins University Applied Physics Laboratory, 2014. URL: https://secwww.jhuapl.edu/techdigest/Content/techdigest/pdf/V28-N01/28-01-Maurer.pdf.

[85] Micron Technology, Inc. *M78A 1 Gb SPI NAND Flash Memory Datasheet*. https://www.micron.com/content/dam/micron/global/secure/products/data-sheet/nand-flash/70-series/m78a-1gb-spi-auto.pdf. Accessed: 2026-01-XX. Micron Technology, Inc., 2023.

[86] Stuart Mills et al. *Testing over Ethernet with the SpaceWire GbE Brick Test and Verification (Short Paper)*. Short Paper. STAR-Dundee Ltd, Space Technology Centre, University of Dundee, 2025.

[87] NASA. *Low Earth Orbital Atomic Oxygen Interactions With Spacecraft Materials*. 2004.

[88] NASA. *Green Propulsion Infusion Mission (GPIM): Final Report*. Tech. rep. NASA/TM–2017-219490. National Aeronautics and Space Administration, 2017. URL: https://ntrs.nasa.gov/api/citations/20170001286/downloads/20170001286.pdf (visited on 01/15/2026).

[89] NASA. *NASA Thermal Control Engineering Guidebook*. 2023.

[90] NASA. *Chandra X-ray Observatory*. Accessed: 2025-11-14. 2024. URL: https://www.nasa.gov/mission/chandra-x-ray-observatory/.

[91] NASA. *NICER Hardware and Patch Kit*. Accessed: 2026-01-12. 2024. URL: https://svs.gsfc.nasa.gov/14603/.

[92] NASA. *NICER Mission Overview*. Accessed: 2025-11-14. 2024. URL: https://science.nasa.gov/mission/nicer/.

[93] NASA. *Space Exposure of Indium Tin Oxide Coatings*. 2024.

[94] NASA. *XRISM Mission Overview*. Accessed: 2025-11-14. 2024. URL: https://science.nasa.gov/mission/xrism/.

[95] NASA. *The History of X-ray Astronomy: The Rough and Tumble Early Days*. URL: https://imagine.gsfc.nasa.gov/science/featured_science/forty/xray_anniversary1.html.

[96] NASA Goddard Space Flight Center. *About Solar Irradiance*. 2026. URL: https://earth.gsfc.nasa.gov/climate/projects/solar-irradiance/about.

[97] National Institute of Standards and Technology. *Stopping-Power & Range Tables for Electrons, Protons, and Helium Ions*. 2026. URL: https://www.nist.gov/pml/stopping-power-range-tables-electrons-protons-and-helium-ions.

[98] NOAA Space Weather Prediction Center. *Coronal Mass Ejections*. 2026. URL: https://www.swpc.noaa.gov/phenomena/coronal-mass-ejections.

[99] NOAA Space Weather Prediction Center. *F10.7 cm Radio Emissions*. 2026. URL: https://www.swpc.noaa.gov/phenomena/f107-cm-radio-emissions.

[100] Orbit Communication Systems. *Gaia™ 100 LEO/MEO Satellite Tracking Ground Stations*. Datasheet, version v0.05. Orbit Communication Systems Ltd.

[101] D. Vukobratovich P. Yoder Jr. *Opto-Mechanical Systems Design - DESIGN AND ANALYSIS OF OPTO-MECHANICAL ASSEMBLIES*. 4th ed. CRC Press, 2015.

[102] Michel van Pelt. *Rockets and Space Launches*. New York: Springer, 2012. DOI: 10.1007/978-1-4614-2243-1.

[103] Santiago Pindado and Javier Cubas. "Simple mathematical approach to solar cell/panel behavior based on datasheet information". In: *Renewable Energy* 103 (2017), pp. 729–738. ISSN: 0960-1481. DOI: https://doi.org/10.1016/j.renene.2016.11.007. URL: https://www.sciencedirect.com/science/article/pii/S0960148116309697.

[104] Inigo del Portillo. *ITU-Rpy: A python implementation of the ITU-R P. Recommendations to compute atmospheric attenuation in slant and horizontal paths.* https://github.com/inigodelportillo/ITU-Rpy/. 2017.

[105] Annelies Powell. *Press Release: Dawn Aerospace Unveils On-Orbit Docking and Refueling Capabilities*. https://www.dawnaerospace.com/latest-news/dftport. Aug. 2024.

[106] E. Puik. "Systems Engineering Tidbits: The V-Model". In: (2023). LinkedIn Article.

[107] Granta Edupack R2025x. *3.2mm 5056 Aluminium Honeycomb Material Properties*.

[108] Jason A. Reiter and David B. Spencer. "Solutions to Rapid Collision-Avoidance Maneuvers Constrained by Mission Performance Requirements". In: *Journal of Spacecraft and Rockets* 55.4 (2018), pp. 1039–1047. DOI: 10.2514/1.A33898. URL: https://www.researchgate.net/publication/325601836_Solutions_to_Rapid_Collision-Avoidance_Maneuvers_Constrained_by_Mission_Performance_Requirements.

[109] A. Rhodes. *A Photographer's Guide to the Milky Way*. 2026. URL: https://andrewrhodesphoto.wordpress.com/2014/01/19/a-photographers-guide-to-the-milky-way/ (visited on 01/25/2026).

[110] Ben Ricketts. *Scientific Targets NEBULA-Xplorer*. https://www.esa.int/Space_Safety/Space_Debris/ESA_Space_Environment_Report_2025. 2025.

[111] Michael Saing. *NASA and Smallsat Cost Estimation Overview and Model Tools*. NASA S3VI Webinar Talk Series. Jet Propulsion Laboratory, California Institute of Technology. June 10, 2020. URL: https://www.nasa.gov/wp-content/uploads/2020/05/saing_nasa_and_smallsat_cost_estimation_overview_and_model_tools_s3vi_webinar_series_10_jun_2020.pdf (visited on 01/19/2026).

[112] Satcatalog. *MT10-2-H*. 2025. URL: https://www.satcatalog.com/component/mt10-2-h/.

[113] Satellite Map. *Starlink Constellation*. 2026. URL: https://satellitemap.space/constellation/starlink (visited on 01/17/2026).

[114] Anna V. Shapiro et al. "Solar-cycle irradiance variations over the last four billion years". In: *Astronomy & Astrophysics* 636 (2020), A83. DOI: 10.1051/0004-6361/201937128.

[115] Bernard Sklar. *Digital Communications: Fundamentals and Applications*. 3rd ed. Prentice Hall, 2019.

[116] SkyLabs d.o.o. *NANOlink / NANOlink-S Interface Control Document*. Revision 2.1. SkyLabs d.o.o. Jan. 2025.

[117] Skyrocket Space Documentation. *Sherpa-LTC Spacecraft*. n.d. URL: https://space.skyrocket.de/doc_sdat/sherpa-ltc.htm (visited on 01/15/2026).

[118] *Solar Cell Array Design Handbook*. Handbook. NASA, 1976.

[119] Azur Space. *30% Triple-Junction (TJ) III-V Bare Solar Cells Assemblies*. 2025. URL: https://www.azurspace.com/media/uploads/file_links/file/bdb_00010892-01-00_tj3g30-advanced_8x8.pdf.

[120] *Space engineering Control performance*. European Cooperation for Space Standardization, 2008.

[121] Space.com. *SpaceX lowering orbits of 4,400 Starlink satellites for safety's sake*. 2025. URL: https://www.space.com/space-exploration/satellites/spacex-lowering-orbits-of-4-400-starlink-satellites-for-safetys-sake.

[122] *Spacecraft Magnetic Torques*. NASA, 1969.

[123] SpaceX. *Falcon User's Guide*. 2025.

[124] Sparkwing. *Sparkwing solar array datasheet*. https://sparkwing.space/?gad_source=1&gad_campaignid=23255665323&gbraid=0AAAAACRMJplhIhdgpbA3qCYw7B-PBjlIK&gclid=CjwKCAiA0eTJBhBaEiwA-Pa-hQfRRY5ECkFBMMlegDOmd8P0HaTH1tRhLcFDldTBGe-gsynN2g8T7RoCipUQAvD_BwE. 2024.

[125] Karthik Mysore Srinivasa. *SPACECRAFT ATTITUDE CONTROL USING MAGNETIC ACTUATORS*. Tech. rep. Michigan Technological University, 2015.

[126] SRON. *Nebula Payload Presentation*. 2025.

[127] SRON Netherlands Institute for Space Research. *NEBULA Xplorer Project Management Plan*. Internal project report SRON-NEBULA-PL-2024-006. Version v1.3. Utrecht, The Netherlands: SRON Netherlands Institute for Space Research, 2024.

[128] Scott R. Starin and John Eterno. *Attitude Determination and Control Systems*. Preprint 20110007876. NASA Goddard Space Flight Center, 2011. URL: https://ntrs.nasa.gov/citations/20110007876 (visited on 01/21/2026).

[129] Starlink. *Starlink Progress Report 2024*. 2024. URL: https://starlink.com/public-files/starlinkProgressReport_2024.pdf?srsltid=AfmBOorQbkKmfVSEDAeRa5nyRfCJdw_bFvpRP6JNINd4KQ9m1URb8GpL.

[130] Sustainable Impact Metrics Foundation (SIMF). *IDEMAT Database (2026 Version): Industrial Design & Engineering Materials Life Cycle Inventory*. https://nexus.openlca.org/database/IDEMAT. 2026.

[131] UTC Aerospace Systems. *ESA/SCC Screened Surface Temperature Sensor Model 0118MM*. https://www.rtx.com/collinsaerospace/-/media/CA/product-assets/files/commercial/power-controls-actuation/engine-power-systems/rosemount-model-0118mm-temperature-sensor.pdf?rev=6edfab217a284bb3b2e58aca1e134b34/1000.

[132] NEBULA Xplorer TEAM. *NEBULA-Xplorer Design Description Document*. Technical report Issue 1.1. SRON, 2025.

[133] Blue Canyon Technologies. *Blue Canyon Technologies Reaction Wheels*. 2025. URL: https://www.bluecanyontech.com/components/reaction-wheels/.

[134] AZ Technology. *AZ-93 White Thermal Control*. 2026. URL: https://www.aztechnology.com/product/1/az-93.

[135] Unkown. *BRAIDED WIRE PROTECTION Bulk tubular non-metallic braid for wire harness protection*. Data sheet Application. 3062 Glenair, Inc, 2017.

[136] Fred Wendorf and Romuald Schild. *Holocene Settlement of the Egyptian Sahara, Volume 2*. Kluwer Academic and Plenum Publishers, 2001.

[137] James R. Wertz and Wiley J. Larson. *Space Mission Analysis and Design*. 3rd ed. Microcosm Press and Kluwer Academic Publishers, 1992.

[138] Xiphos Systems. *Q8 On-Board Computer (OBC) Datasheet*. https://xiphos.com/hubfs/XIPHOS2025/Datasheets/Q8OBC_Datasheet_3.20.25.pdf?hsLang=en. Accessed: 2026-01-XX. Xiphos Systems, 2025.

[139] DSE Group 3 Nebula Xplorer. *Final Report Python Scripts*. ZIP file containing Python code. Delft University of Technology, Faculty of Aerospace Engineering, 2025.

[140] DSE Group 3 Nebula Xplorer. *Midterm Report Python Scripts*. ZIP file containing Python code. Delft University of Technology, Faculty of Aerospace Engineering, Dec. 10, 2025.

A Simulation parameters

Table A.1: Simulation constants and user-defined parameters used in the AOCS sizing and verification scripts

Category	Variable	Value	Units	Notes
Spacecraft & orbit (AOCS_FLOODFLOINK_2.py)				
Inertia	IXX	75.971	kg m^2	Principal inertia (body axes)
Inertia	IYY	63.307	kg m^2	
Inertia	IZZ	49.657	kg m^2	
Orbit	ALTITUDE	4.75×10^5	m	
Orbit	R_EARTH	6.371×10^6	m	
Orbit	MU_EARTH	3.986×10^{14}	m^3/s^2	
Orbit	R_ORBIT	6.846×10^6	m	$R_{EARTH+ALTITUDE}$
Orbit	T_ORBIT	5640	s	94×60
Environment	RHO_HOT	8.28×10^{-12}	kg/m^3	Hot density used in AOCS script
Environment	RHO_COLD	2.00×10^{-14}	kg/m^3	Cold density used in AOCS script
Environment	R_AU	1.0	–	1 AU scaling for SRP
Numerics	DT_SIM	5.0	s	Orbit disturbance sim timestep
Sun direction	S_HAT_I	[1, 0, 0]	–	Assumed constant over one orbit
Magnetic model	m_res_vec_body	$[D\_RESID, 0, 0]$	A m^2	Residual dipole vector definition
Disturbance / geometry constants (Disturbance_torque_functions_2.py)				
CoM	r_com	$[6\times10^{-3}, 0, 540\times10^{-3}]$	m	CoM in body frame
Magnetics	D_RESID	2.0	A m^2	Residual dipole magnitude
Magnetics	M_MAG	7.8×10^{15}	T m^3	Dipole surrogate (simple model)
Magnetics	LAMB	1.5	–	Latitude factor in model
Optics	Absorptance_MLI	0.14	–	
Optics	Absorptance_Panels	0.91	–	
Optics	Transmittance	0.0		Conservative assumption
Optics (derived)	q_MLI	0.86	–	$1 - \alpha_{MLI} - \tau$
Optics (derived)	q_panel	0.09	–	$1 - \alpha_{panel} - \tau$
SRP	C_LIGHT	299792458	m/s	Speed of light
SRP	SOLAR_FLUX	1366.0	W/m^2	Solar flux used
SRP (derived)	P_SRP_1AU	4.5565×10^{-6}	N/m^2	$SOLAR\_FLUX/C\_LIGHT$
Drag	C_D_DEFAULT	2.2	–	Drag coefficient
Geometry	deg_angled	45.0	deg	Panel/bus angled facet construction
Geometry	rad_angled	0.785398	rad	$\pi/4$
Geometry	L_panel1	1.1	m	
Geometry	W_panel1	0.91	m	
Geometry (derived)	A_panel1	1.001	m^2	$L\_panel1 \cdot W\_panel1$
Geometry	L_panel2	1.1	m	
Geometry	W_panel2	0.75	m	
Geometry (derived)	A_panel2	0.825	m^2	$L\_panel2 \cdot W\_panel2$
Bus	Bus_D	0.904	m	
Bus	Bus_W	0.853	m	
Bus	Bus_H	1.4	m	
RW sizing & momentum management knobs (AOCS_FLOODFLOINK_2.py)				
Slew sizing	THETA_SLEW_DEG	180.0	deg	Bang-bang slew sizing target
Slew sizing	T_SLEW	150.0	s	Bang-bang slew time
Wheel geometry	BETA_DEG	54.7356	deg	Pyramid cant angle
Wheel capacity	H_cap_actual	4.0	N m s	Per wheel datasheet capacity

Continued on next page

Category	Variable	Value	Units	Notes
Wheel capacity	`margin`	0.20	–	Requirement margin used for capacity check
Wheel capacity (derived)	`H_cap_allow`	3.33	N m s	$4.0/(1+0.2)$
Desat cadence	`N_ORBITS_BETWEEN_DESAT`	2	orbits	Used in degraded MTQ sensitivity block
Continuous unload	`USE_CONTINUOUS_MTQ`	True	–	Enables continuous momentum regulation
Continuous unload	`SCIENCE_MTQ_AUTHORITY`	0.50	–	MTQ authority factor during science
Continuous unload	`TAU_REG_ORBITS`	1.0	orbits	Regulation time constant
Duty	`duty_4wheel`	1.0	–	Availability (interpreted as duty)
Duty	`duty_3wheel`	1.0	–	Availability (interpreted as duty)
Cadence sim horizon	`Nmax`	15	orbits	This is approximately 24h
Detumble scenario parameters (AOCS_FLOODFLOINK_2.py)				
Detumble	`w0_deg_s`	1.5	deg/s	Initial tumble rate used
Detumble	`w_target_deg_s`	0.1	deg/s	Exit threshold used
Detumble	`t_max`	1800	s	$30 \cdot 60$
Detumble	`dt`	0.5	s	Integrator timestep
MTQ detumble	`m_rod_max`	10.0	A m^2	Per rod dipole cap
MTQ detumble	`k_bdot`	5×10^5	(A m^{2}s)/T	B-dot gain used
MTQ detumble	`geom_factor`	0.7	–	MTQ effectiveness factor
MTQ detumble	`b_perp_factor`	0.7	–	Accounts for $\tau \perp B$ limitation
RW assist	`use_rw`	True/False	–	Two runs: MTQ-only and MTQ+RW assist
RW assist	`T_rw_max`	0.25	N m	Body-equivalent max assist torque
RW assist	`H_rw_axis_max`	3.4	N m s	$4.0 \cdot 0.85$ (per-axis cap in detumble sim)
RW assist	`omega_deadband`	0.02	deg/s	RW assist turns off below this
Jitter / LOS stability check parameters (AOCS_FLOODFLOINK_2.py)				
LOS / requirement	`e_los_B`	[0, 0, 1]	–	LOS/boresight axis
LOS / requirement	`req_arcsec`	15.0	arcsec	RMS over any 1 s window
Wheel speeds	`rpms`	500, 1000, 2000, 3000, 4000, 5000, 6000	rpm	Discrete set tested due to missing information from vendor
Unbalance	`U_static_gmm`	6.0	g mm	Static unbalance input [133]
Unbalance	`U_dynamic_gmm2`	300.0	g mm^2	Dynamic unbalance input [133]
Numerics	`dt`	0.001	s	Jitter sim timestep
Numerics	`duration_s`	60.0	s	Jitter sim duration

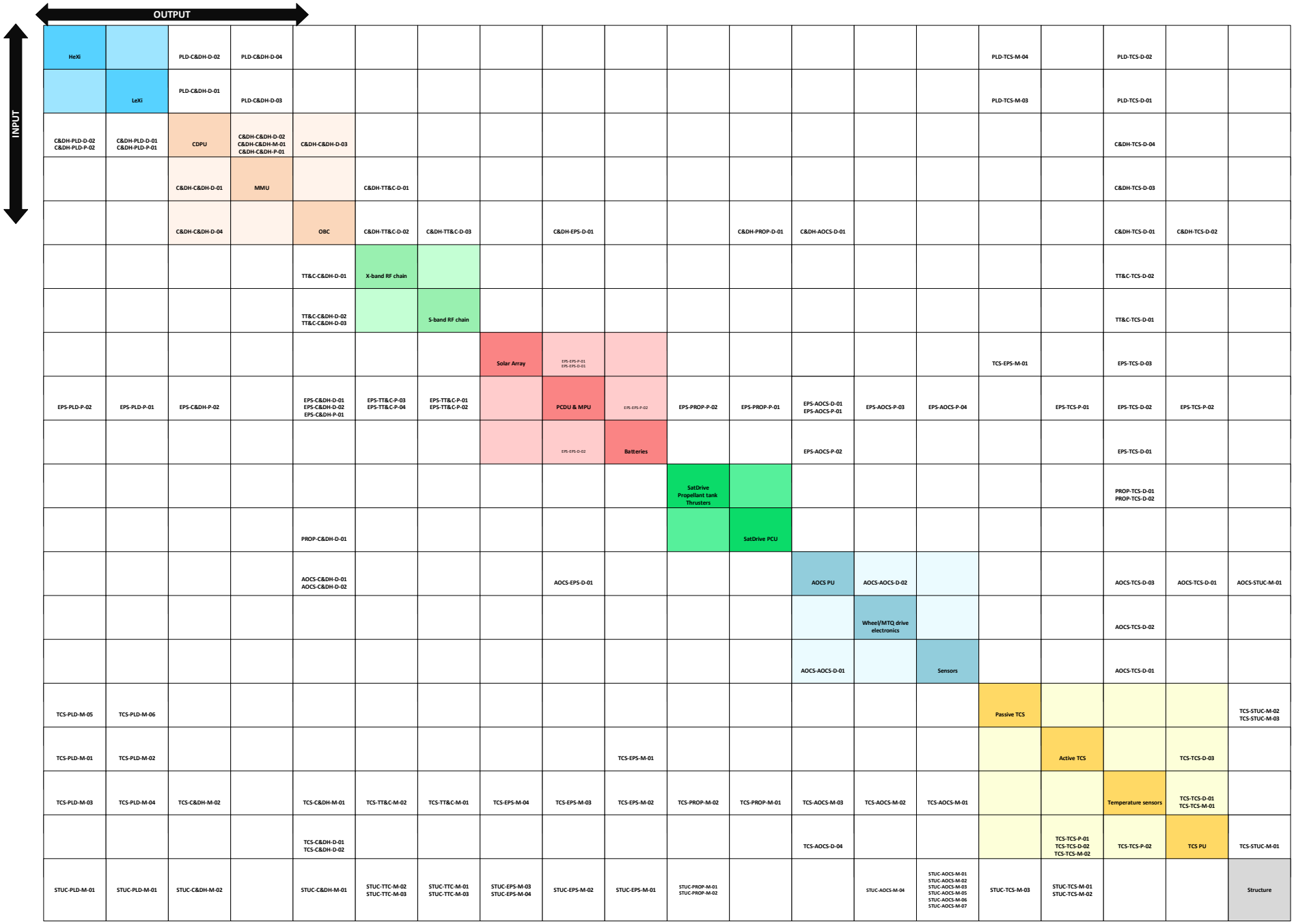

Figure 1: N2 chart containing the subsystems interfaces used for generating the hardware diagrams and data handling diagrams